Design and Evaluation of a Modular, Supercooling Phase Change Heat Storage Device for Indoor Heating

by

Louis Desgrosseilliers

Submitted in partial fulfilment of the requirements
for the degree of Doctor of Philosophy

at

Dalhousie University
Halifax, Nova Scotia
July 2016

TABLE OF CONTENTS

LIST OF TABLES

LIST OF FIGURES

ABSTRACT

Modular heat storage cells containing a supercooling salt hydrate phase-change heat storage material were developed for implementation into a portable electric thermal storage (ETS) indoor heating system. ETS systems can generate indoor heating cost-savings for customers using low-cost off-peak electricity for charging from time-of-day electricity rate pricing. The supercooling ability of the phase-change material (PCM) was used in this research to retain heat storage for extended periods of time (multi-day to multi-month) at room temperature without heat loss ($\geq$ 40 % of heat stored at 110 ˚C), and released on-demand using nucleation triggers built into each heat storage cell. An ETS system was developed to facilitate heat exchange with the heat storage cells using a circulated heat transfer fluid (HTF), exchanging heat also with a liquid-to-air heat exchanger to generate useful room heating.

An equimolar mixture of sodium acetate trihydrate and water (SAT PCM) was used in the heat storage cells to store thermal energy with combined sensible and latent heats resulting in charge capacities up to 475 kJ/kg between 20 ˚C and 110 ˚C. Heat discharge capacities up to 449 kJ/kg can be achieved with minor or no supercooling of the SAT PCM and continuous useful heat release from the SAT PCM $\geq$ 28 ˚C. Triggering heat release only after idle supercooling between 20 ˚C and 28 ˚C would result in a discharge heat capacity of 425 kJ/kg.

Heat storage cells underwent three design iterations, incrementally improving on leak-tightness, heat transfer performance, supercooling reliability, and nucleation-triggering strategies. This culminated in the Mark III modular, rectangular heat storage cell design developed in this research, containing 2.4 kg (0.3 kWh capacity at 110 ˚C) and equipped with pairs of plate heat exchangers. Stable supercooling was observed for 167 days before autonucleation, while repeated cycling (including supercooling and solidification) for a total of 131 cycles without noticeable degradation was observed. Although the minimum U values obtained exceeded the PCM-literature benchmark (0.03 kW m^{-2} K^{-1}), heat storage cells with twenty times the value of UA would be required to deliver an average heat transfer rate of 600 W to a liquid-to-air heat exchanger.

LIST OF SYMBOLS USED

Dimensional variables

$AMTD$	Arithmetic mean temperature difference (K)
$[A]$	Molar concentration of chemical species A (M)
a	Eq.(2.1) extent of reaction (mol)
A	Surface area (m^2)
b	Eq.(2.2) extent of reaction (mol)
$B3_1$	Supercooled Mark III '3' bottom thermocouple (B3) temperature prior to nucleation (K)
$B3_2$	Supercooled Mark III '3' bottom thermocouple (B3) temperature prior to nucleation (K)
C	Heat capacity (J/kg)
C_d	Discharge coefficient
C_p	Specific heat capacity (J kg^{-1} K^{-1})
D_o	Orifice diameter (m)
e	Fin depth (m)
E	Enclosure mid-depth (m)
F	Pattern-element half-length (m)
G	Relative Gibbs energy (J)
h	Individual convective heat transfer coefficient (W m^{-2} K^{-1})
H	Specific relative enthalpy (J kg^{-1})
$H_{SAT(aq)}$	Pure, aqueous SAT specific relative enthalpy (J kg^{-1})
$H_{SAT(s)}$	Solid SAT specific relative enthalpy (J kg^{-1})
$\widehat{H}$	Molar enthalpy (J mol^{-1})
ΔH_1	Total relative enthalpy of supercooled SAT PCM prior to nucleation (J kg^{-1})
ΔH_2	Total relative enthalpy of freshly nucleated SAT PCM (J kg^{-1})
I	Heat transfer equipment perimeter in horizontal 2-D plane (m)
k	Thermal conductivity (W m^{-1} K^{-1})
L	Characteristic length for heat diffusion (m)
L_1	Characteristic length for planar heat diffusion (m)

L_2	Characteristic length for radial heat diffusion (m)
L_3	Characteristic length for planar heat diffusion at the ends of the staggered fin arrangement (m)
m	Mass (kg)
$\dot{m}$	Mass flow rate (kg s^{-1})
MTD	Mean temperature difference (K)
$LMTD$	Log-mean temperature difference (K)
ΔP	Pressure difference (Pa)
P_i	Pressure at interval i (Pa)
P_{i-1}	Pressure at interval i-1 (Pa)
P	Pressure (Pa)
P_{vap}	Partial vapour pressure (Pa)
$P_{vap,i}$	Species 'i' partial vapour pressure (Pa)
P_{sat}	Saturated vapour pressure (Pa)
$P_{sat,i}$	Species 'i' saturated vapour pressure (Pa)
P_1	Internal pressure (Pa)
P_2	External pressure (Pa)
Q	Rate of heat transfer (J)
r	Radial length (m)
R	Thermal resistance (m^2 K W^{-1})
R_{air}	Air-gap thermal resistance (m^2 K W^{-1})
$R_{air,HX}$	Air-flow thermal resistance (m^2 K W^{-1})
R_{film}	Aluminized film thermal resistance (m^2 K W^{-1})
R_{HTF}	HTF thermal resistance in the heat exchange plate (m^2 K W^{-1})
$R_{HTF,HX}$	HTF thermal resistance in the liquid-to-air heat exchanger (m^2 K W^{-1})
R_{PCM}	SAT PCM thermal resistance (m^2 K W^{-1})
R_{plate}	Aluminum flow plate thermal resistance (m^2 K W^{-1})
R_{tube}	Tube/fin thermal resistance in the liquid-to-air heat exchanger (m^2 K W^{-1})
S	Cross-section area (m^2)
t	Time (s)
T	Temperature (K)

$\hat{T}$ Average hot fluid temperature (K)

$\hat{T}'$ Average cold fluid temperature (K)

T' Cold fluid temperature (K)

T_{air} Ambient air temperature of airflow to the liquid-to-air heat exchanger (K)

T_b Normal boiling point temperature (K)

T_h High temperature limit for charged-state (K)

T_i Temperature array ith element (K)

T_l Low-temperature limit for supercooled-state (K)

T_{liq} Liquidus line temperature (K)

T_{HTF} Nominal circulating HTF temperature (K)

T_{PCM} Nominal temperature of the SAT PCM (K)

U Overall heat transfer coefficient for heat exchangers (W m^{-2} K^{-1})

U_{cell} Heat storage cell overall heat transfer coefficient (W m^{-2} K^{-1})

U_{HX} Liquid-to-air heat exchanger overall heat transfer coefficient (W m^{-2} K^{-1})

UA Overall heat transfer capacity rate for heat exchangers (W K^{-1})

$\dot{V}$ Volumetric flow rate (m^3 s^{-1})

$\hat{V}$ Molar volume (m^3 mol^{-1})

W Pattern-element side length (m)

X Pattern-element repeat-distance (m)

v Solidification front expansion rate (m s^{-1})

z Inter-fin spacing (m)

Z Rectangular enclosure length (m)

Dimensionless variables

C_r Capacity ratio

Fo Fourier number

K_a Reaction quotient for hydrolysis of acetic acid

K_b Reaction quotient of Eq.(2.1)

K_w Reaction quotient of Eq.(2.2)

N_i Indexed ('i') binary array element recording charged-state

Nu Nusselt number

pH Aqueous solution acidic strength

pOH	Aqueous solution caustic strength
Pr	Prandtl number
Re	Reynolds number
S_i	Indexed ('i') binary array element recording the solidification process
x	Liquid-phase mole fraction
x_i	Species 'i' liquid-phase mole fraction
w	Mass fraction
w_{s1}	Solid mass fraction for supercooled liquid prior to nucleation
w_{s2}	Solid mass fraction for freshly nucleated SAT PCM
$w_{SA,liq}$	Saturated liquid mass fraction at T_{liq}
Y	Compressibility parameter

Greek symbols

α	Thermal diffusivity ($m^2\ s^{-1}$)
Γ	MTD correction factor
Ω	Equation (1) constant ($J\ mol^{-1}$)
ϕ	Pattern pitch angle (rad)
ρ	Density ($kg\ m^{-3}$)
σ	Surface tension ($N\ m^{-1}$)

Subscripts

ave	Mixture average property
l	In relation to pure, aqueous SAT
max	Maximum value
mix	Mixture-average property
s	In relation to solid SAT
SA	Sodium acetate anhydride
SAT	Sodium acetate trihydrate
trans	Relating to phase transitions
w	Water

ACKNOWLEDGEMENTS

First and foremost, I thank my partner, Jill. Her courage and tenacity have made it possible to become well established in our new home after six years of completing my graduate studies. I am perpetually excited about launching our venture together (incl. Jill) with Moe and improving the way Canadians live. Our cats, Rocky, George, Bridget, and Blacky always know how to make daily life enjoyable with their snuggles and antics, so thank you all.

Moe, my good friend, colleague, and business partner, many thanks for sharing my vision in launching our business together with Jill.

I am also grateful for the continued love and support from my parents who welcomed us to Halifax in 2010, along with aunt and uncle Jo-Anne and Shawn and cousin Danielle (and respective dogs and cats).

Dominic and Mary Anne, thank you both for supporting my efforts these past six years, through my research and many grant proposals made together. Also, thanks to my committee members, Dr. Swan and Dr. Donaldson, and external examiner, Dr. Gennady Ziskind.

Thanks to all of my office mates in both labs: Moe, Ben, Ali, Jonas, Tousif, Laura, Maha, Azad, John Noël, John Niven, Samer, Jan, Carl, Sarah, and Mike. Thanks also to former lab mates Trevor and Nick.

The continued support of Dr. Alain Joseph and James Thomspon at NSCC with our start-up venture has been instrumental in its early growth and in completing my PhD research, thank you both. Thanks also to Martha and Jeramy for their assistance with setting up and conducting experiments at NSCC. Many thanks to Angus MacPherson, whose vast mechanical design knowledge and kindness were able to make up for my absence of mechanical design training. Thanks also to Jon MacDonald and Peter Jones.

I am also very grateful for the scholarships awarded to me from NSERC and DREAMS, and project supports from Innovacorp, with special thanks to Amanda, Michael, Shelley, and MacKenzie.

Thanks also to the Mechanical Engineering Office at Dalhousie University: Kate, and formerly, Michelle and Selina. Another thanks goes out to Janet at DREAMS and my DREAMS colleagues, DREAMS professors, and for the funding awarded to me from the DREAMS program.

CHAPTER 1: INTRODUCTION

1.1 BACKGROUND AND MOTIVATION

1.1.1 INDOOR HEATING IN CANADA

Thermal energy used for indoor heating dominates the energy consumption of Nordic societies. Indoor heating in Canada accounts for 62 % of energy used on average (1990-2009) in the residential sector and 52 % in the commercial/institutional sector, with their sum equal to 18 % of national energy use (NRCan, 2012). It is clear that indoor heating energy consumption constitutes a major monetary cost in these sectors and is a significant factor affecting national economic performance. The primary heat sources available nationally in these sectors, in ascending order of nominal wholesale unit cost of energy are: natural gas, electricity, and furnace oil (NRCan, 2015b; NRCan, 2016). While electricity and furnace oil are available nation-wide in Canada, natural gas is only widely available where pipelines are present (i.e., only west of Quebec, (Snider, 2006)).

How is indoor heating characterized in the residential and commercial/institutional sectors? At first glance, indoor heating energy intensity of the Canadian residential sector in 2009 was 0.50 GJ/m^2 vs. 0.83 GJ/m^2 in the commercial/institutional sector[1] (NRCan, 2011; NRCan, 2012), while their respective average floor areas are 129 m^2 (NRCan, 2011) vs. 2,200 m^2 (NRCan, 2002). The number of households (13 M, (StatCan, 2013a)) far outnumbers the number of commercial/institutional buildings (137 k, (NRCan, 2002)) in Canada, indicating a distributed residential sector vs. a concentrated commercial/institutional sector. Notable factors affecting the national aggregate values of energy intensities of these two sectors are building occupation patterns and ingress/egress frequency of individuals through the building envelope. Residential occupation is typically characterized by daytime absences, largely during weekdays (vacant 40 h/w for 8 h workdays), whereas 70.7 % of commercial/institutional buildings are occupied 49 h - 168 h per week (NRCan, 2002).

Through what means can households and building owners reduce indoor heating costs? Energy efficiency upgrades to the building envelope or primary heating system

[1] Commercial/institutional space heating energy intensity is likely underreported due to the prevalence of office employees using individual space heaters year-round that are recorded as appliance loads rather than indoor heating.

have already realized energy savings over recent decades (NRCan, 2011), but these are only available to building owners (apartment owners excluded, e.g., condos) and efficiency improvements remain subject to the same unit cost of energy. Altering the unit cost of energy can be achieved by primary heat source conversion (i.e., conversion to natural gas) or by supplemental heating (e.g., heat pump, electric thermal storage (ETS), or renewable energy). While natural gas conversions are restricted by access to distribution networks (e.g., pipeline networks) and might require a retrofit to the indoor heating distribution system, supplemental heating solutions are widely available and do not generally require primary heating system retrofits. Supplemental heating installations are also scalable to budget and desired energy cost reduction and do not require primary heating system retrofits. Renewable energy and heat pump supplemental heating require penetration of the building envelope and support structure installation, while conventional ETS units require only indoor installation, although they are generally fixed or permanent. Portable supplemental heating (e.g., portable heat pumps) requires the least installation and is neither fixed nor permanent.

1.1.2 CANADIAN INDOOR HEATING BUILDING CHARACTERISTICS

How do residential and commercial/institutional customer segmentations affect access to these strategies and how are they distributed? Detailed characteristics of the Canadian residential sector are shown in Table 1-1, listing the age of the dwellings, ownership rates (relating closely to income distributions, (Snider, 2006)), dwelling types, and the prevalence of high-cost primary heat sources (e.g., electricity, furnace oil, wood). Older homes[2] require the most extensive retrofits to improve heating performance to that of newer ones. The ability to undertake a retrofit is dependent on the occupant's dwelling-ownership status and dwelling type since only the building owner (homeowners and apartment building owners) is permitted to alter the building envelope and only the dwelling owners (homeowners and condo owners) gain value from capital improvements to the dwelling. Conversion to natural gas heating is a strategy only affecting those using high-cost primary heat sources. As is shown in Table 1-1, there is a clear delineation between owners and renters in the Canadian residential sector and the prevalence of high-

[2] The heating intensity of homes built prior to 1981 is greater than those built afterward (StatCan, 2013b).

cost primary heat sources, with access to low-cost natural gas favouring owners over tenants, as well as with those residing in homes vs. apartments[3]. Despite increasing ownership trends in new apartment constructions (e.g., condos) (StatCan, 2013b), Table 1-1 shows that access to natural gas in these buildings remains unfavourable. The ability to heat with low-cost natural gas is also accentuated by income disparity, favouring the wealthy who can more easily afford home ownership (Snider, 2006) and conversions to natural gas.

Table 1-1: Dwelling characteristics in Canada

	Canada	Homes [a]	Apartments [b]
Households [c]	13,320,610	66.1 %	32.6 %
Owned [d]	69 %	86 %	21 %
Year of construction ≤ 1980	61.0 % [e]	-	-
Dwellings using high-cost primary heat sources [f]	50 % [g]	44 % [d]	66 % [d]

[a] Includes attached, semi-detached, and row-houses; [b] Includes low-rise and high-rise buildings; [c] (StatCan, 2013a); [d] (Snider, 2006); [e] (StatCan, 2007); [f] All heat sources excluding natural gas; [g] (StatCan, 2013cB)

While the owners of older homes can benefit from efficiency upgrades and those with high-cost primary heat sources could benefit by converting to natural gas, low-income homeowners (data unavailable), home renters (1.2 M households), and apartment dwellers (owners and renters, 3.4 M households) have either limited financial ability or are not permitted do so. Alternatively, homeowners can invest in supplemental heating to avoid major retrofits, but these are not usually suitable for home renters and apartment dwellers, and ETS units are only suitable for apartment owners, while portable supplemental heating is suitable for all segments, but especially for renters. As is illustrated, apartment dwellers and home renters are underserviced by conventional heating cost reduction strategies and would therefore benefit from the development of new, portable supplemental heating solutions.

[3] Electric heating is most widely used in apartment buildings due to inherent ease with which to meter the consumption of renters (Snider, 2006).

Detailed building characteristics in the Canadian commercial/institutional sector are found in Table 1-2. The latter explores the distribution of ownership types and key building attributes: floor area, year of construction, operating hours, and primary heat sources. Similarities can be drawn between commercial/institutional buildings and dwellings with respect to year of construction and the prevalence of high-cost primary heat sources. Access to large capital differs between ownership types, favouring individuals and non-profits the least, therefore favouring major retrofits and upgrades to those with the most capital; floor area impacts the scale of indoor heat consumption, favouring larger, centralized systems to heat larger buildings; and, operating hours serve as proxy for the duration of the primary heating periods (i.e., periods without temperature setback). As can be seen in Table 1-2, the commercial/institutional sector already enjoys a higher rate of natural gas use as the primary heating fuel than does the residential sector, but a significant number of buildings remain without natural gas across all ownership types. Of these buildings, those owned by individuals and corporations encompass the majority. Older buildings are equally prevalent across all ownership categories, but buildings owned by individuals are the most numerous. The largest proportions of older buildings are found in non-profit and individual ownerships, short operating hours are most common among non-profit and publicly owned buildings, and smaller floor area buildings ($\leq$ 464 m^2) constitute the majority of buildings owned by individuals only.

Table 1-2: Commercial/institutional building characteristics in Canada (NRCan, 2002)

	Canada	Individual ownership	Corporate ownership	Non-profit ownership	Public ownership
Buildings	137,039	39.4 %	36.4 %	12.0 %	12.2 %
Total floor area	302 km^2	19.6 %	43.0 %	9.3 %	28.1 %
Buildings ≤ 464 m^2	38.7 %	57.4 %	30.6 %	28.2 %	12.7 %
Year of construction < 1980	69.6 %	72.6 %	61.5 %	81.9 %	71.9 %
Operating ≤ 48 h/w	29.3 %	27.3 %	23.2 %	47.7 %	35.8 %
Buildings using high-cost primary heat sources [g]	36.2 %	38.8 %	36.8 %	29.6 %	32.5 %

[g] All heat sources excluding natural gas.

Due to the prevalence of newer buildings, large floor area buildings, and longer operating hours, public and corporate-owned buildings are primarily suited for efficiency upgrades and natural gas conversions, favouring supplemental heating to a lesser degree. Buildings owned by individuals are predominantly older, occupy smaller floor areas, operate longer than 48 h/w, and have the highest rate of high-cost primary heat sources. Buildings owned by non-profits are also predominantly older, but occupy larger floor areas, and operate for shorter durations. Despite the longer hours prevalent for buildings owned by individuals and larger floor areas occupied by non-profit owned buildings, both categories are most suitable for supplemental heating since these provide options for smaller, incremental installations that reduce the pressure on capital investments. It is also noted that franchise hotels (approx. 2,300 buildings with 230,000 rooms, (HAS, 2015)), included in corporate owned buildings, constitute a special, structurally[4] unique group that is most suitable for supplemental heating. Also, corporate lessees, for whom no data could be found, occupy buildings owned by individual and corporations. With corporate lessees, as with residential renters, only supplemental heating is available to reduce indoor heating costs.

1.1.3 INNOVATION POTENTIALS FOR SUPPLEMENTAL HEATING

Significant consumer segments, namely rental tenants (residential and commercial), apartment dwellers (including condos), capital-limited building owners (residential and commercial) and franchise hotels, have thus been identified in the Canadian residential and commercial/institutional sectors for which the option for indoor heating cost reduction is limited primarily to supplemental heating. Since their options are limited compared to those who are suited for efficiency upgrades and natural gas conversions, in what areas would new innovations in supplemental heating technologies show promise for adoption by renters, commercial lessees, and building owners alike, such as renewable energy generation, heat pumps, and ETS used to leverage time-of-day electricity pricing?

Is there significant opportunity in renewable energy generation? Renewable energy generation (solar thermal, photovoltaic, and wind), unless made very effective in a compact, inexpensive form, is not suitable for corporate lessees, renters, or apartment

[4] Individual room and suite heating systems are popular in franchise hotels.

dwellers, and are therefore too restrictive for further consideration. For instance, 44 m^2 of south-facing flat plate solar thermal panels are required on average per home in the Drake Landing Solar Community (DLSC), a 52 home district heating solar community operating since 2007 using underground seasonal heat storage situated in Okotoks, AB (Sibbitt et al., 2011). Using only diurnal heat storage instead of seasonal storage, these homes would each require 88 m^2 of flat plate solar panels (Pinel et al., 2011).

Even using the inherent seasonal storage capability of supercooling phase change materials (PCMs) to increase the heat storage density and efficiency of seasonal heat storage, the estimated heat storage system volume required onsite of 159 m^3 (Desgrosseilliers et al., 2014c) per home is excessive for urban and suburban homes, and altogether incompatible with rental tenancies. Dannemand and coworkers estimated needing only 36 m^2 of solar collectors and 10 m^3 of supercooling PCM seasonal heat storage to deliver a 100 % solar fraction for both indoor heating and domestic hot water supply of a single, high efficiency, Danish passive house, modelled numerically. In comparison, the modelled Danish passive house consumes 7.2 GJ/y for indoor heating (16.3 GJ/y including domestic hot water) in a climate of 3,000 ˚C-days (basis unknown) for heating vs. 5,200 ˚C-days (18 ˚C basis[5]) and 51.1 GJ/y on average for DLSC homes (Sibbitt et al., 2011; Desgrosseilliers et al., 2014c; Dannemand et al., 2015b), both of which are far below the Canadian residential average of 67 GJ/y (129 m^2 average Canadian home, (NRCan, 2011)). Differences also arise in the thermodynamic cycles[6] assumed for their supercooling PCM heat storage volumes, in PCM thermodynamic property validation[7], and in assumed system-based heat storage density[8] that account for the large difference in estimated seasonal heat storage volumes reported in both cases. In

[5] Heating degree-day is defined as sum of non-zero values of the basis value (temperature at which no heating is required) minus the daily-average temperature.
[6] Dannemand et al. (2015b) assumed initial and supercooled states of 20 ˚C and useful heat discharge from the PCM storage down to 20 ˚C, while Desgrosseilliers et al. (2014c) assumed 25 ˚C and 28 ˚C (actual operating conditions at DLSC), respectively.
[7] Desgrosseilliers et al. (2014c) used a thermodynamic PCM model validated against T-history measurements reported by Sandnes et al. (2006) and used to accurately reproduce the binary phase diagram for sodium acetate trihydrate in water reported by Green (1908).
[8] Desgrosseilliers et al. (2014c) imposed a 20 % void fraction to the heat storage to account for the balance-of-system, while Dannemand et al. (2015b) use the pure PCM heat storage density.

any case, 10 m^3 of seasonal heat storage in moderate climates remains largely impractical; therefore, only lower solar fractions are likely practicable.

Just as with seasonal solar heat storage, the opportunity is equally poor for the delivery of waste heat from industrial facilities. Delivery of waste heat requires either transportation and on-site storage of transportable heat storage modules or long pipelines installed to deliver the heat source directly to the end-user, not likely situated close by. Moreover, these strategies are incompatible with rental tenancies.

What opportunities are there with conventional heat pump technologies? Conventional ductless, air-to-air heat pumps are very effective at delivering energy savings[9] for supplemental heating and deliver heating, cooling, or dehumidification on-demand. However, cost and energy savings from heat pump usage is limited by climate suitability (compressor design and refrigerant dependent (NRCan, 2015a)), and outdoor installation, indoor installation, and building envelope penetration is required, restricting the locations of indoor heating units to proximity to outside facing walls. Conventional heat pump units are not suitable for renters and commercial lessees, but new portable air-sourced heat pumps are (Phillips, 2010; Honeywell, 2012). Although these units are not directly limited by outdoor climate, they are limited by the intake air temperature from the indoor air they are intended to heat ($\geq$ 4.4 ˚C for some, $\geq$ 12.8 ˚C for others), although only problematic in the absence of a primary heat source (Phillips, 2010) and when used in poorly insulated seasonal buildings (e.g., cottages) and seasonal rooms (e.g., sunrooms). Of larger concern is the rate of heat loss imposed by air drafts and/or mechanically ventilated makeup air needed to balance the direct outdoor venting of cool evaporator air from the unit. For units with an airflow capacity up to 7.5 m^3/min at STP (assuming 20 ˚C and 1 atm and $C_p \sim 1$ kJ/(kg K)) and a heating capacity of 3.2 kW (Honeywell, 2012), heat generation deficits would occur when makeup air temperatures are 22 ˚C below the indoor ambient air temperature (e.g., outdoor air temperatures $\leq$ -2 ˚C). As such, portable heat pumps cannot operate in the absence of another heat source enabled at all times and must use a window vent (increasing the risk of window drafts and reducing the thermal insulation of windows), limiting use only to rooms with suitable windows for venting kits and units can only be positioned in close proximity to

[9] This would economize between one half and two-thirds of the energy used by electric heaters.

such windows. Unlike conventional ductless air-to-air heat pumps for which the compressors are normally housed in outdoor units, portable heat pumps must also house all components indoors, and therefore generate additional indoor noise (31 dB(A) - 39 dB(A) for ductless heat pump indoor unit vs. ≥ 54 dB(A) for portable heat pumps, (Honeywell, 2012; LG, 2014)). All of these limitations and consequences of using portable heat pumps stem directly from their fundamental principles of operation; therefore, opportunities for innovations in these areas to improve ease-of-use and encourage adoption are limited.

Is there opportunity for innovation to increase adoption of ETS using time-of-day electricity pricing? Time-of-day (TOD, also called time-of-use) electricity pricing is an alternative pricing strategy to all-day fixed pricing that is offered by some electricity providers aimed to manage consumption patterns, also called demand-side management (OEB, 2015; NSPower, 2016; PSEG, 2016). This is accomplished by rewarding off-peak electricity consumption with discounted unit cost of energy rates in a pre-defined off-peak period and discouraging on-peak consumption with penalized unit cost of energy rates, while sometimes also charging a third-tier mid-peak rate, and typically offering off-peak rates throughout weekends and holidays (OEB, 2015; NSPower, 2016; PSEG, 2016). Thermal energy storage, by means of an ETS unit, is used to take advantage of the discounted off-peak electricity rates for indoor heating by delaying heat release until pre-defined mid-peak and on-peak periods. Access to TOD electricity rates is contingent on owning an ETS for some electricity providers (e.g., Nova Scotia Power, (NSPower, 2016)), either conventional brick ETS system (either room or central heating) or custom in-floor heating, and requires an electrical consumption smart meter to enable multi-rate billing (OEB, 2015). Regardless of the ETS technology used to deliver the primary cost reduction benefit of TOD electricity rates (i.e., indoor heating), all of the customer's electrical consumptions are also subject to TOD pricing. Additional cost savings can be realized by exercising either diligent timing, using automatic timing, or energy storage in the course of energy consumption from appliances, lighting, and hot water heating (if electrically heated), collectively contributing to the remaining 38 % of Canadian residential energy consumption and 48 % in the commercial/institutional sector (NRCan,

2012). Therein lies the value of supplemental heating using TOD electricity rates as opposed to all other indoor heating cost reduction strategies.

Conventional ETS units (see Figure 1-1) use masses of refractory bricks packaged into an insulated cabinet, heated directly by electrical heating elements, and cooled either passively by heat transfer through the cabinet walls (called 'static') or dynamically by air supplied from a blower or water/glycol solution delivered by pump (Romero, 2013; Dimplex, 2015; Steffes, 2016a). These systems deliver heat to the indoor space by either circulating the warmed air into the room or circulating the warmed solution to hydronic baseboard heaters, an in-floor hydronic heater, or a exchanging heat with a central-air heating system, respectively (Dimplex, 2015; Steffes, 2016a). Heating system integration and control varies between brick ETS manufacturers, but their principles of operation are long established and mature (Romero, 2013; NSPower, 2016)), therefore lacking significant opportunity for performance improvement and reduced form factor to generate appeal to rental occupants (residential and commercial).

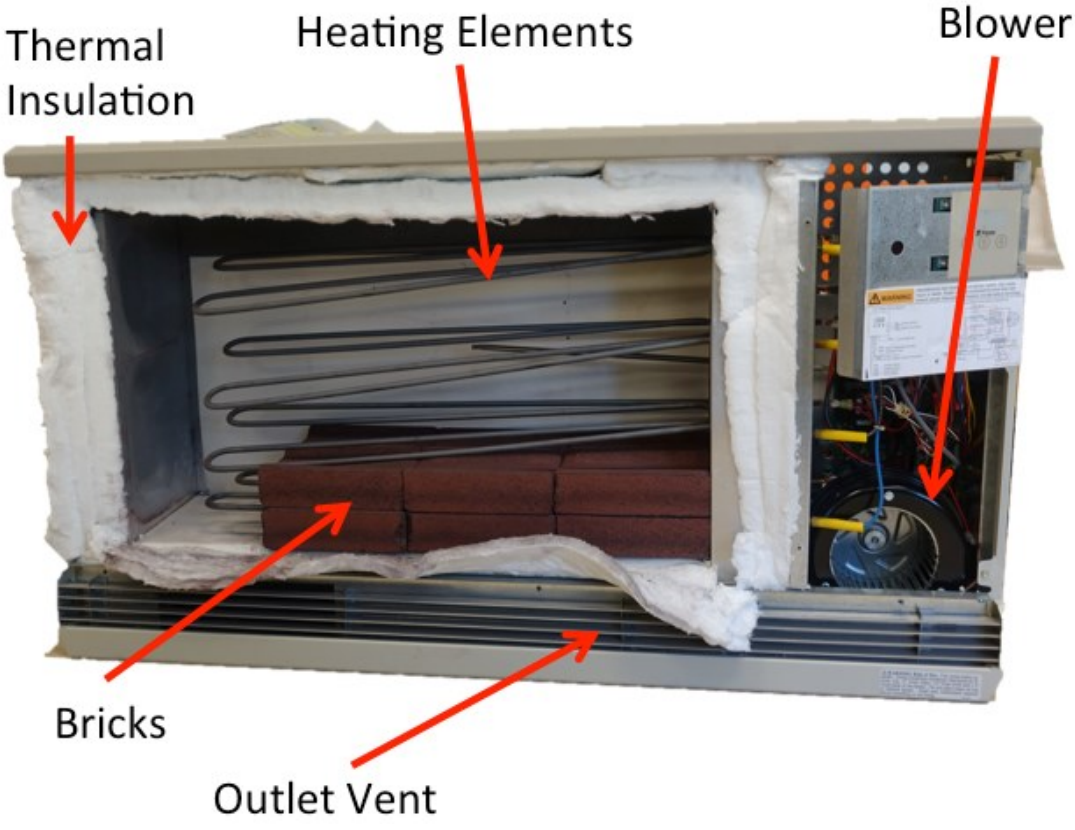

Figure 1-1: Internal view of a Steffes model 2104 brick ETS unit, storing up to 27 kWh of sensible heat (Steffes, 2016b).

Brick ETS units operate on the basis of sensible heat storage, meaning that they rely on large temperature differences in a bulk mass to generate useful heat storage. Brick ETS units typically operate up to 600 ˚C (Romero, 2013) to achieve specific heat storage in the range of 630 kJ/kg for the brick only (500 kJ/kg for the unit), using masses of brick ranging from 40 kg to over 200 kg (Elnur, 2015; Dimplex, 2016). Due to the high operating temperatures for brick ETS needed to achieve the high specific heat storage, high levels of insulation are needed to combat uncontrolled heat losses (as high as 20 % of the stored heat (Romero, 2013)) and bulk mass is used to decrease the ratio of surface area to volume of heat storage to aid in this as well. As evidenced by the absence of small, portable brick ETS units, brick ETS units risk operating with unfavourable efficiency or require an excessive amount of insulation if designed with reduced mass of heat storage bricks. This fact limits brick ETS from being offered in formats more suitable for rental occupants, since their current size and storage mass offerings make it necessary to use high-power 208 V - 240 V electric heaters[10] (Dimplex, 2015; Elnur, 2015) rather than using low-power, conventional circuits (120 V in North America, maximum 1.5 kW). Furthermore, they require complete professional installation (electrical and assembly), eliminating the opportunity for portability. Conventional brick ETS units are intended to remain in one location as fixed indoor heating infrastructure rather than to offer the end-user the ability to reconfigure heater locations to better suite their needs.

1.1.4 PHASE CHANGE MATERIAL HEAT STORAGE

What can be done to remedy the inherent size and portability limitations of ETS units to make them better suited for use by rental tenants? The operating temperatures (including its effect on heat loss) could be reduced at no cost to energy storage capacity by using phase change materials (PCMs) for their high latent heats of transition (conventionally solid-solid or solid-liquid transitions) in addition to their sensible heat storage rather than relying exclusively on sensible heat storage of conventional materials (see Figure 1-2), e.g., brick (Wettermark et al., 1979; Abhat, 1983; Lane, 1983; Zalba et al., 2003; Mehling et al., 2008; Noël et al., 2016). Latent heat storage refers to the large

[10] Needed to complete charging the ETS units in the requisite time window imposed by regional TOD rate programs.

thermal energy associated with the phase transitions of pure substances and mixtures (e.g., melting and solidification) at their phase transition temperatures, a property that does not rely on generating large temperature differences. In fact, in-floor heating systems consisting of rectangular panels containing PCMs have been used in Japan to store heat supplied by off-peak electricity (Lane, 1985). This practice, however, does not appear to have been adopted widely in other countries in the intervening decades. The latter might be due to the uncontrolled heat release inherent to these designs, and therefore performance, comfort, and heat storage efficiency vary more widely than for active heat release from brick ETS units. Heat storage using PCMs, as for sensible heat storage using bricks, remains unfavourable for small, portable ETS units since heat storage efficiency is inversely proportional to the ratio of surface area to volume, despite the decreased rate of heat loss at lower operating temperatures.

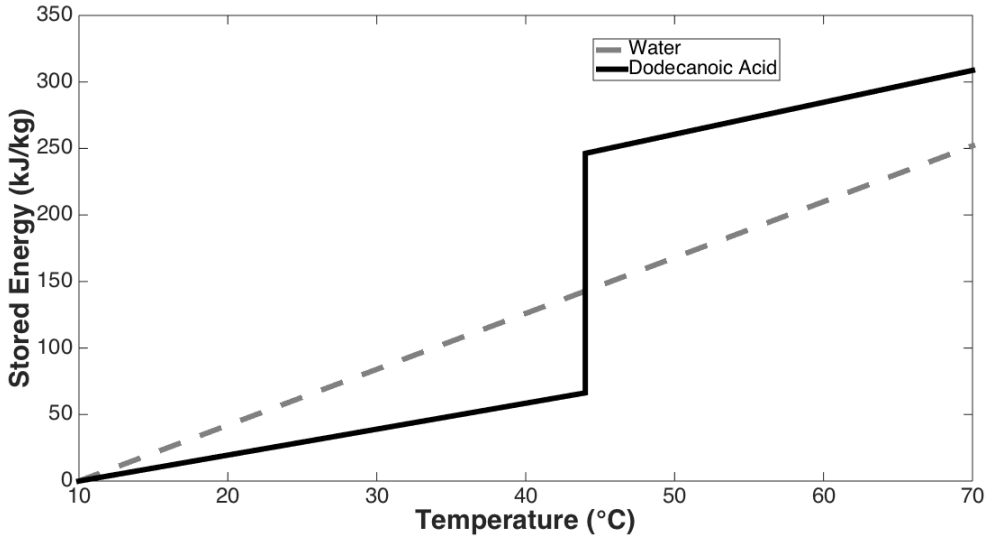

Figure 1-2: Comparison of sensible-only heat storage (water) vs. combined sensible and latent heat storage (dodecanoic acid). Water has a specific heat capacity of 4.2 kJ kg^{-1} K^{-1} (Felder et al., 2000) while dodecanoic acid has respective solid and liquid specific heat capacities of 1.95 kJ kg^{-1} K^{-1} and 2.4 kJ kg^{-1} K^{-1} and latent heat of transition of 180 kJ kg^{-1} at 44 ˚C (Desgrosseilliers et al., 2013c).

How can portable, efficient ETS be achieved? Figure 1-3 illustrates the effect of supercooling hysteresis on latent heat storage, an effect frequently observed for salt hydrate and sugar alcohol PCMs (Noël et al., 2016). Supercooling of these PCMs is manifested by the persistence of the higher-energy liquid metastable state at temperatures below the PCM's transition temperature (green line in Figure 1-3), capable of remaining

in thermal equilibrium with its surroundings for long durations (Sandnes, 2003). The stored energy in the supercooled state can be released on-demand by using proven solidification triggering techniques (blue line in Figure 1-3) (Sandnes, 2003). Supercooling behaviour can generate added utility to heat storage design by eliminating heat loss in the room-temperature supercooled state, resulting in improved heat storage efficiency, and providing the ability to selectively release the energy stored in the supercooled state, on-demand, in as few or as many heat storage volumes as desired. The latter gives rise to modularity of heat storage masses, benefiting both heat storage efficiency and dynamic heat transfer performance by preserving isolated, idle supercooled heat stores while releasing heat from others and selectively engaging individual, smaller heat storage masses in heat transfer operations, respectively.

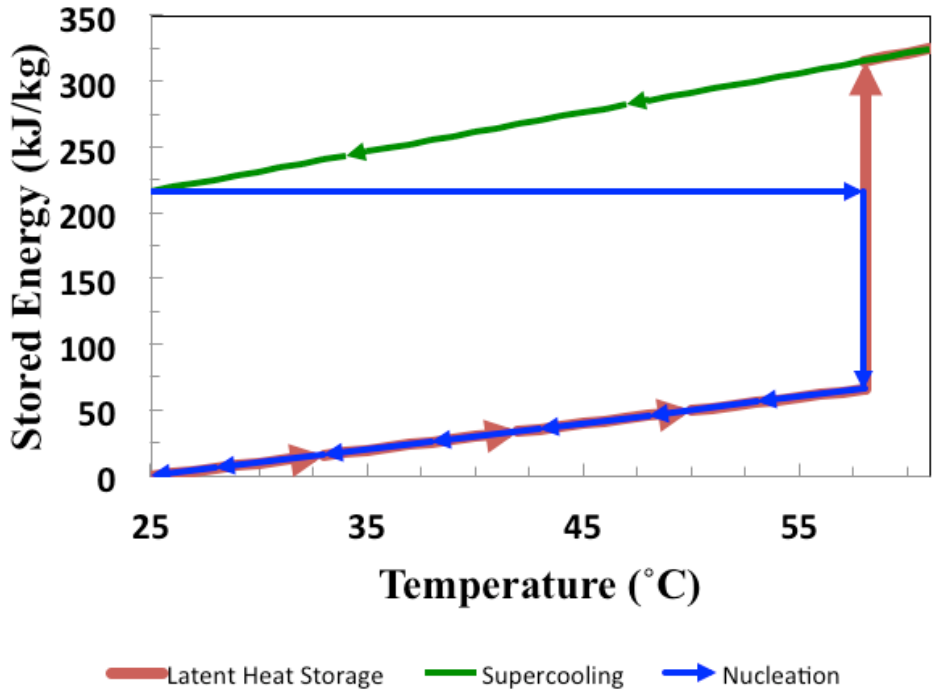

Figure 1-3: Example of supercooling hysteresis of sodium acetate trihydrate PCM. Reproduced from Desgrosseilliers (2012) with permission.

Although there is a substantial published knowledge base on the thermo-physical and chemical properties of supercooling PCMs, most notably salt hydrate PCMs (Green, 1908; Lane, 1983; Araki et al., 1995; Hirano et al., 2002b; Hirano et al., 2002a; Sandnes, 2003; Günther et al., 2007; Hirano et al., 2009; Desgrosseilliers et al., 2013a), integration of supercooling PCMs into practical heat storage devices is largely absent, or remain

unvalidated. The German company H.M. Heizkörper has had a cylindrical tank bulk heat storage product in development for seasonal heat storage in buildings since 2012 and another hybrid domestic hot water storage tank supplemented with supercooling PCM. Both products use supercooling sodium acetate trihydrate, and neither has shown signs of field validation success (H.M.Heizkorper, 2012). Otherwise, a limited number of laboratory designs have been developed (Schultz et al., 2005; Schultz et al., 2007; Hirano et al., 2009; Fan et al., 2012; Furbo et al., 2012; Dannemand et al., 2015a; Dannemand et al., 2015b), but none of these possesses the correct attributes for compact, modular supercooling heat storage in a portable ETS unit.

Salt hydrates are generally the supercooling PCM of choice over sugar alcohols due to their wide range of available transition temperatures (Zalba et al., 2003; Kenisarin et al., 2007) and natural abundance of many of their raw material precursors and simple chemical syntheses often resulting in low-cost of the PCMs (generally lower cost than organic PCMs, (Abhat, 1983; Kenisarin et al., 2007)). Sugar alcohols have similar attributes, but suffer from polymorphism (Fronczek et al., 2003) that affects phase transition cycle stability, and some organic PCMs, including sugar alcohols (Zhang et al., 2014), are more susceptible to thermal degradation than inorganic PCMs.

Modular, supercooling PCM heat storage, especially using salt hydrate PCMs, shows considerable promise for the development of a compact, portable ETS device. This research intends to explore this field of technology and address the gaps in knowledge for cycle reliability of supercooling PCMs, compact-modular heat transfer and enclosure designs, integration in a room ETS device, and internal phase transition process modelling.

1.2 TOPICAL REVIEW

1.2.1 SUPERCOOLING AND PROPERTIES OF SALT HYDRATE PCMS

1.2.1.1 SALT HYDRATE PCMS

Salt hydrate PCMs consist of an ionic salt that also contains water molecules in the crystal unit cell, forming a hydration compound. Their names begin with the ionic salt compound followed by the term ‘hydrate’ with a numerical prefix (e.g., ‘tri’ or ‘hexa’) designating the hydration stoichiometry. Salt hydrate PCMs generally undergo a phase

transition, whereby the crystalline solid decomposes into an aqueous solution of the water of hydration and the dissolved ionic salt (Green, 1908; Lane, 1983; Meisingset et al., 1984). Although the decomposition reactions of salt hydrates give the appearance of melting, they are usually two-step processes of sequential chemical reactions (decomposition + dissolution) (Green, 1908; Meisingset et al., 1984; Garg et al., 1985), but remain classified as phase change processes nonetheless. Their total enthalpies of transition are likened to those of physical phase change processes (i.e., melting/solidification and solid/solid transitions of pure substances), in the range of 100 kJ/kg to 300 kJ/kg, rather than with those of reversible chemical reactions commonly classified for heat storage applications, in the range of 1,000 kJ/kg to 2,000 kJ/kg (Wettermark et al., 1979).

Most salt hydrates undergo incongruent phase change processes, meaning that the composition of the aqueous solution differs from that of the solid and often gives rise to incomplete phase transition at the maximum equilibrium transition temperature (i.e., peritectic point on a binary phase diagram; see example binary phase equilibrium diagram in Figure 1-4), causing a portion of the anhydrous salt to risk being unrecovered in subsequent cycles (Green, 1908; Sidgwick et al., 1922; Abhat, 1983; Lane, 1983; Araki et al., 1995). On the other hand, pure eutectic salts and salt mixtures also risk deviating from the initial system composition after repeated cycling due to vapour loss.

A common practice that is used to overcome the tendency to produce unrecoverable anhydrous salt is to dilute the salt hydrate in excess water, resulting always in a decrease of the maximum transition temperature but allowing the salt to dissolve completely (Abhat, 1983; Araki et al., 1995; Sandnes, 2003; Farid et al., 2004; Sandnes et al., 2006). Unlike pure salt hydrate compounds, dilute salt hydrate mixtures produce incremental phase change in the entire range of solubility, up to the maximum transition temperature corresponding to the average system composition. Wettermark et al. (1979) classified this process as *heat-of-solution* storage, a subcategory of latent heat storage (e.g., PCMs).

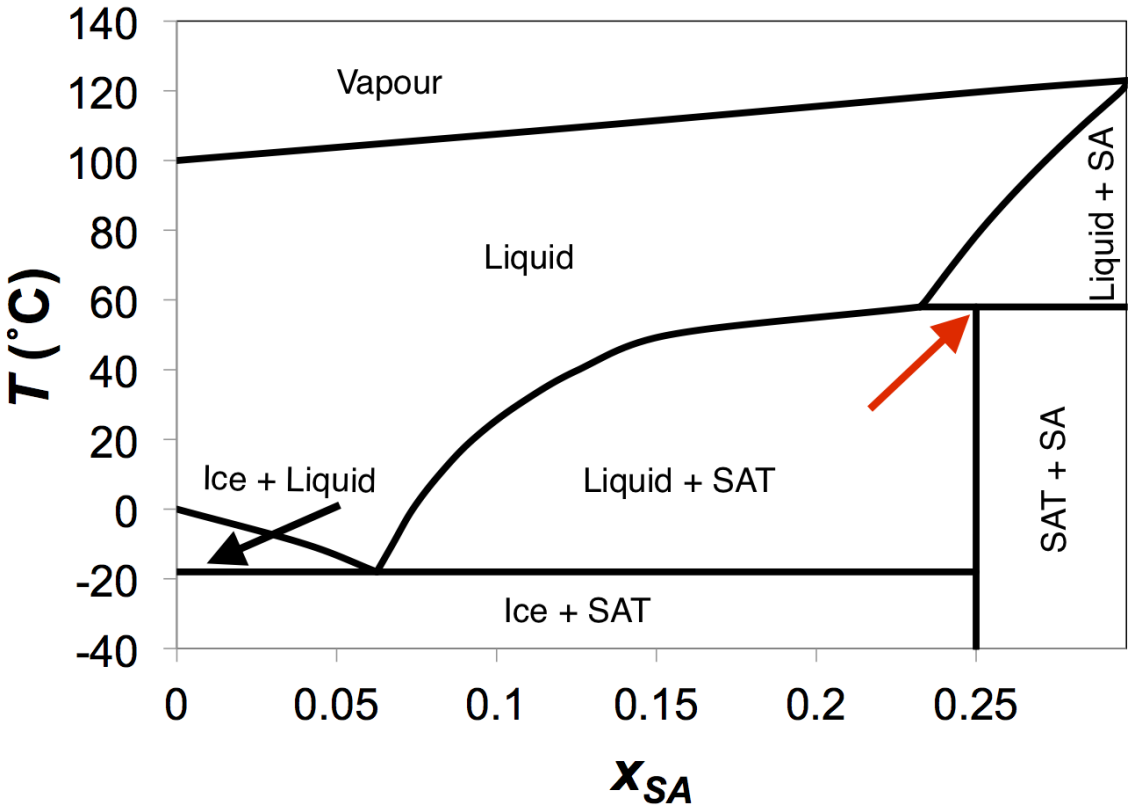

Figure 1-4: Binary phase diagram of sodium acetate ($NaCH_3CO_2$, denoted SA) and water, using data from Green (1908) in the SA mole fraction (x_{SA}) range $0 \leq x_{SA} \leq 0.298$. SAT denotes the hydrated compound sodium acetate trihydrate ($NaCH_3CO_2 \cdot 3H_2O$); the red arrow indicates its peritectic point at $x_{SA} = 0.250$ and $T_{trans} = 58$ ˚C.

During the solidification of dilute salt hydrates (mass sink), however, the remaining excess solution fraction can become segregated and thereby migrate to the top of the enclosure. Reheating will further accentuate this process during decomposition/dissolution of the solid salt hydrate due to the elevated buoyancy (i.e., lower density) of the dilute liquid fraction in comparison to the saturated solution that is produced from heating the solid salt hydrate (mass source) (Dannemand et al., 2015a; Dannemand et al., 2015b), which can still lead to anhydride formation under certain conditions. This process is akin to the stratification of bodies of water at rest (either natural or artificial (Pinel et al., 2011)), whereby thermal and salinity gradients develop and become stable (i.e., resist mixing, see Figure 1-5) unless a mixing event of sufficient intensity is induced (e.g., flow mixing, wind shear, strong circulation due to heating or cooling, or mechanical agitation) (Mays, 1999; Mays, 2000; Edzwald, 2011). The process

of solution stratification is also observed in electrochemical cells that contain active electrolytes (i.e., consumed and produced at the electrodes) (Pavlov, 2011). Of further concern to salt hydrate solutions is that salinity-based stratification is equally stable to uniform solutions (especially the case for fully miscible/ideal solutions) since diffusion transport in solutions occurs too slowly to affect stratification in practical timescales (Zimmerman, 1997). Also, salinity induced stratification causes greater barriers to mixing than does thermal stratification, so much so that stable salinity stratification can defeat the natural thermal gradient of buoyant fluids (i.e., temperature increases bottom-up) (Pinel et al., 2011), and be present in otherwise shallow reservoirs.

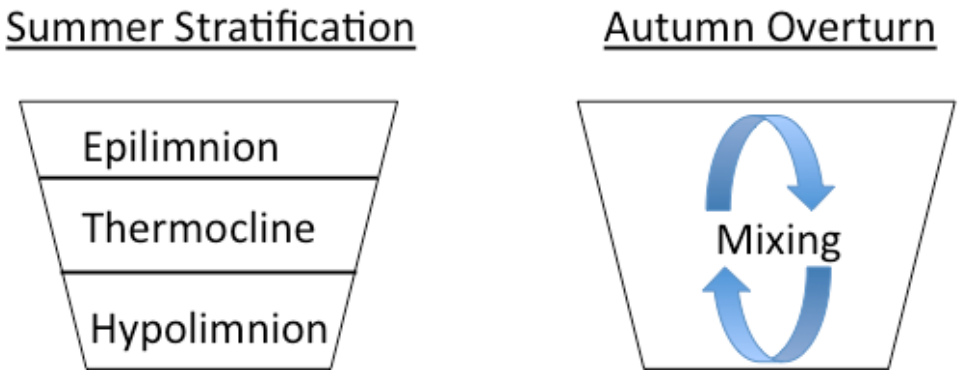

Figure 1-5: Illustration of thermal stratification and mixing in lakes. Epilimnion, thermocline, and hypolimnion refer to the top, uniformly mixed strata, region of steep temperature gradient, and bottom uniformly mixed strata in natural bodies of water (Edzwald, 2011). Salinity stratification can be structurally similar to this kind of thermal stratification.

Gelling or thickening of the solution can effectively 'freeze' the uniform composition in place, but hinders natural convection heat transfer in the dissolved PCM (Lane, 1985; Dannemand et al., 2015b); as well, mechanical agitation maintains solution uniformity, but adds risk of failure of moving parts and/or shaft seals in the enclosure (Lane, 1985). Natural convection during heating and cooling of the PCM contributes to 'soft' mixing of the solution (Dannemand et al., 2015a), capable of avoiding at least the condition generating anhydride, but unlikely to mix the solution thoroughly. However, the stratification performance of a salt hydrate solution can only be determined experimentally for the PCM composition, enclosure geometry, and heat exchange conditions in question. The effects of altering the degree of dilution in extra water,

enclosure depth and height (both affect buoyancy circulation in closed containers, whereas length does not (Welty et al., 2001)), supply temperature of the heat exchange fluid and fluid flow rate, and degree of PCM superheating/supercooling on diminishing the effect of solution stratification are remain unknown.

Salt hydrates can undergo various stages of decomposition (Lane, 1983) if there also exist other hydration compounds (i.e., different hydration stoichiometries). Consequently, the properties of salt hydrate solid/liquid mixtures are dependent on the system's relative enthalpy (denoted H), temperature (denoted T), and phase compositions (denoted x) – H-T-x – making transient determinations of their properties more complex than with conventional congruent[11]-melting PCMs that depend on enthalpy and temperature alone – H-T. However, with sufficient temperature-dependent thermodynamic knowledge of the individual dilute salt hydrate mixture chemical species, one can construct a mathematical model relating the H-T-x effects for salt hydrates, provided the salt hydrate chemical reaction kinetics are fast, i.e., dictated by equilibrium rather than kinetic effects. Desgrosseilliers et al. (2013) demonstrated the implementation of such a model to predict the liquidus line[12] of sodium acetate trihydrate (see Figure 1-6), $NaCH_3CO_2 \bullet 3H_2O$, from measured enthalpy data collected by Sandnes and Rekstad (2006) using the T-history method for sodium acetate trihydrate diluted in in 1:1 mole ratio extra water.

[11] Meaning PCMs for which the solid and melt have identical compositions.
[12] Refers to the equilibrium solution saturation curve (T-x) in a binary phase diagram.

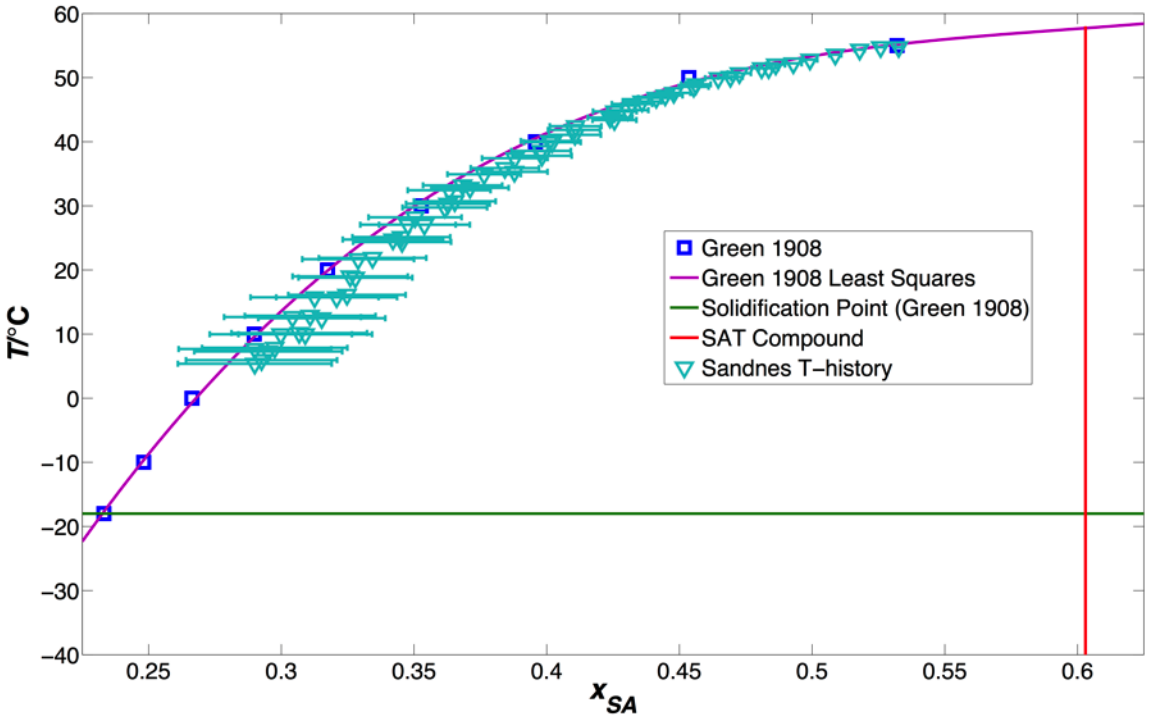

Figure 1-6: Liquidus line determination for $NaCH_3CO_2 \cdot 3H_2O$ by implementation of the thermodynamic *H-T-x* model (∇) in comparison to the liquidus line determined by Green (1908) using traditional cooling curves (□) (Desgrosseilliers et al., 2013a). Reproduced with permission from Elsevier ©.

The founders of PCM science studied many PCMs for heat storage and formulated the conditions for suitable PCM selection that are still presently used: good chemical stability, high latent heat of transition, suitable transition temperature, little or no supercooling, minimal volume change from phase transition, low toxicity, low cost, and high thermal conductivity (Wettermark et al., 1979; Abhat, 1983; Lane, 1983). The criterion of minimal supercooling was motivated by past failures whereby researchers neglected to account for incongruent melting and supercooling for salt hydrate phase change heat storage only to have their heat storage experiments lose capacity over time due to phase segregation and lose the ability to solidify and discharge heat altogether[13] (Lane, 1983). Insisting on minimal supercooling neglects the practical uses of

[13] The experimental solar house, *Dover* House, designed by Maria Telkes in 1948 using Glauber's salt, sodium sulfate decahydrate, as a latent heat storage PCM eventually failed to nucleate after repeated cycles (Lane, 1983).

supercooling that are explored in this thesis, therefore the condition for little or no supercooling is omitted in the present treatment (Desgrosseilliers, 2012).

1.2.1.2 SUPERCOOLING OF SALT HYDRATE PCMS

The ability for salt hydrate PCMs to substantially supercool is fundamental to their use in long-term heat storage. Nauman reported a solution of pure sodium acetate trihydrate (henceforth called SAT) to supercool as much as 108 ˚C below the peritectic phase transition temperature of 58 ˚C (Naumann et al., 1989). However, researchers studying the supercooling ability of another common salt hydrate, sodium hydrogen phosphate dodecahydrate, have found it to produce only moderate supercooling, less than 14 ˚C (Sandnes et al., 2006; Hirano et al., 2009), and is therefore not likely practicable for supercooling heat storage. The maximum degree of supercooling ($T_{trans} - T$, i.e., condition causing autonucleation of the supercooled PCM) for any salt hydrate compound can be estimated from the approximate relation found experimentally by Gopal for the latent heat of transition and the maximum transition temperature (Lane, 1983):

$$(T_{trans} - T)_{max} = \frac{\Omega}{\Delta \widehat{H}_{trans}}, \tag{1.1}$$

where T_{trans}, T, Ω, and $\Delta \widehat{H}_{trans}$ represent the equilibrium transition temperature, supercooled temperature, equation constant equal to 330 kJ/mol for most substances, and the molar latent heat of transition. However, Eq.(1.1) fails to account for volume effects, whereby the probability of nucleation increases at larger volumes due to the higher frequency of nuclei formation (Lane, 1983), and offers no means of correlating the maximum degree of supercooling to the duration of stable supercooling at higher temperatures. No current model is capable of resolving these issues.

Thermodynamic theory using Gibbs energy changes (ΔG) explains the supercooling phenomenon as a large activation potential-energy barrier that prevents the formation of solid by heterogeneous nucleation so long as $\Delta G > 0$ (see Figure 1-7). The Gibbs energy barrier can be only overcome ($\Delta G < 0$) at low-enough temperatures or if a sufficiently large seed crystal is present (seed crystal radius, r, exceeds critical radius, r_c) to promote further solidification (Lane, 1983) and overcome surface formation instabilities given by $r^2\sigma$, where σ is the surface tension of the solid surface immersed in solution, such that:

$$\Delta G = 4\pi \left(r^2 \sigma - \frac{T_{trans} - T}{T_{trans}} \frac{r^3}{3} \rho \, \Delta H_{trans} \right) \quad (1.2)$$

Furthermore, the Gibbs energy analogy correctly represents the supercooled state as a metastable solution (i.e., not at thermodynamic equilibrium), in which the system persists, but is inherently unstable and will spontaneously generate the equilibrium solid phase given sufficient time and opportunity (i.e., nucleation probability increases with solution mass and elapsed time) (Lane, 1983).

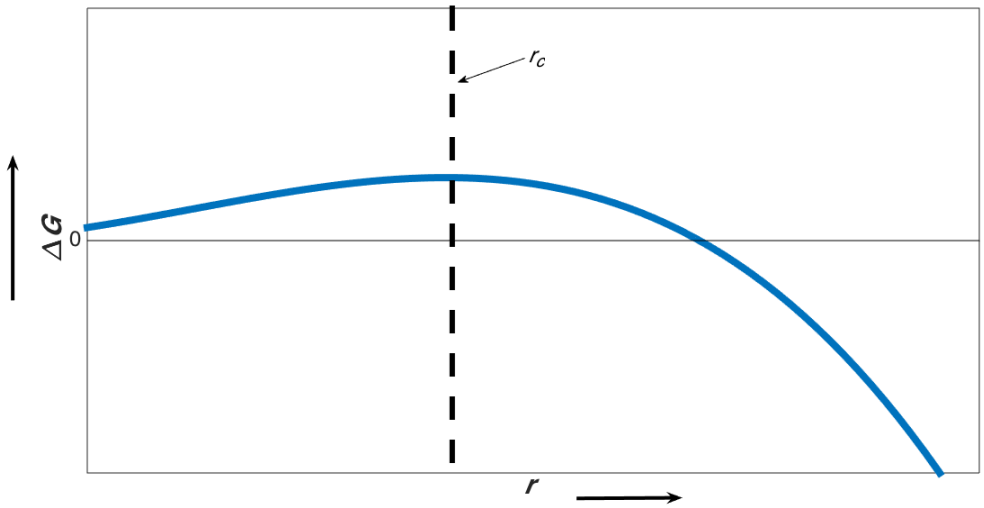

Figure 1-7: Gibbs energy change of a growing spherical solid of radius *r*. Particles with $r < r_c$ (critical crystal growth radius) cannot overcome the activation energy barrier ($d\Delta G/dr > 0$) and can only dissolve, while those with $r > r_c$ spontaneously grow ($d\Delta G/dr < 0$).

1.2.1.3 PROPERTIES OF SUPERCOOLING PCMS, NUCLEATION TRIGGERS, AND PRACTICAL EVALUATIONS

There are many salt hydrates reported in the literature (Lane, 1980; Abhat, 1983; Lane, 1983; Zalba et al., 2003; Farid et al., 2004; Sharma et al., 2005; Kenisarin et al., 2007; Verma et al., 2008; Sharma et al., 2009; Agyenim et al., 2010), but very few have complete and independently verified reports of their thermophysical properties. One particular salt hydrate has benefited from considerable scientific study and its thermal behaviour, phase transition, and supercooled properties are well characterized: $NaCH_3CO_2 \bullet 3H_2O$ (SAT). Unlike many of the PCMs for which reported properties in the reviews are incomplete, conflicting, and sometimes erroneously cited (as identified by

Desgrosseilliers et al. (2013c)), SAT has been reported in a vast scientific literature for over 100 years (Green, 1908; Sidgwick et al., 1922; Richards et al., 1929; Sturley, 1932; Franzosini et al., 1983; Meisingset et al., 1984; Naumann et al., 1989; Anthony et al., 1990; Araki et al., 1995; Rogerson et al., 2003c; Rogerson et al., 2003b; Rogerson et al., 2003a; Sandnes, 2003; Sandnes et al., 2006; Günther et al., 2007; Sandnes, 2008; Wei et al., 2010; Marcus, 2013) and used commercially in therapeutic heat packs for nearly as long (Rogerson et al., 2003c; Rogerson et al., 2003b; Rogerson et al., 2003a; Sandnes, 2003; Sandnes, 2008). Furthermore it is considered to be non-toxic and environmentally safe to use, and SAT is made from abundant and inexpensive feedstocks (e.g., acetic acid and sodium bicarbonate).

The binary phase diagram of sodium acetate anhydride (henceforth called SA) has been determined with sufficient detail first by Green (1908) then by Sidgwick et al. (1922), from which it is known that SAT is the only existing hydrated compound whose peritectic transition temperature is 58 ˚C (see Figs. 3 and 5). Sandnes studied the enthalpy-temperature (*H*-*T*) histories of supercooled SAT solutions in water to determine the nominal pure phase heat capacities as well as the approximate latent heat of transition using the *T*-history method (Sandnes et al., 2006). The *T*-history method is a simple laboratory calorimetry determination of PCM properties using common laboratory test tubes filled with PCM and temperature probes to record the sample and control's temperature history. The control is used to calibrate the calorimetric determination of the PCM properties (Yinping et al., 1999; Sandnes et al., 2006; Kravvaritis et al., 2010; Kravvaritis et al., 2011).

Sandnes also studied the nucleation phenomenon of supercooled SAT solutions in water either from submerged nucleation triggering devices or external seed crystal addition and contributed compelling evidence to support the theory championed by Barrett and colleagues that submerged nucleation triggering is achieved by retaining stable seed crystals in the high pressure contacts of the triggering device (usually opposed stainless steel surfaces under an applied pressure) (Anthony et al., 1990; Sandnes, 2003; Sandnes, 2008). Their findings suggest that seed crystal retention in supercooled salt hydrate solutions is primarily a function of the applied pressure (contact pressure) and the

phase transition properties, which can be estimated by the Clayperon equation over narrow ranges of temperature:

$$\frac{\Delta P}{\Delta T} \cong \frac{dP}{dT} = -\frac{\Delta \hat{H}_{trans}}{T_{trans}\Delta \hat{V}_{trans}} \tag{1.3}$$

where ΔP and ΔT refer to the pressure and temperature differences from the equilibrium transition state at 1 atm, $\Delta \hat{H}_{trans}$ and T_{trans} are the molar latent heat of transition and transition temperature at 1 atm, and $\Delta \hat{V}_{trans}$ refers to the molar volume difference between the aqueous and solid phases ($\Delta \hat{V}_{trans} > 0$) at the 1 atm transition point. Günther et al. (2007) reported solidification temperatures of SAT under high pressures and found good agreement with measurements of the 'melting' temperatures of SAT under the same high pressures. Consequently, the data reported by Günther et al. (2007) correspond well with estimates from Eq.(1.3) in the range of 331.15 K to 353.15 K, but fails to agree beyond 373.15 K (or $P > 0.2$ GPa) as demonstrated by Sandnes (Sandnes, 2003). The investigations of Sandnes and Barrett and colleagues contradict the theory proposed by Rogerson and Cardoso that seed crystal retention is caused by elevated capillary pressures in the small crevices of nucleation triggering devices (Anthony et al., 1990; Rogerson et al., 2003c; Sandnes, 2003; Sandnes, 2008).

Sandnes (2008) also explored the effectiveness of common hardware as solidification triggering devices, for which the general quality is to possess hard metal surfaces in direct contact with one another. The high-pressure contact formed between two opposing hard surfaces is generally sufficient to retain stable seed crystals in solution at temperatures exceeding the normal transition temperature, and releasing the contact exposes the crystals to the supercooled solution, spontaneously inducing isenthalpic solidification and generating a porous solid, afterwards proceeding at rate corresponding to the rate of heat transfer from the system and resulting in further densification of the solid (i.e., following the changes in equilibrium states (Sandnes, 2003; Sandnes, 2008)).

Triggering solidification by ultrasonic irradiation (Rogerson et al., 2003b; Sandnes, 2003; Wei et al., 2010) or applying electric fields using electrodes are largely ineffective or impractical (Sandnes, 2003). Nucleation can be reliably induced using the 'cold finger' method, whereby a section of the supercooled solution is subjected to significant chilling, generating local homogeneous nucleation that spreads throughout the remainder of the

PCM, requiring energy and/or material input consumption to achieve sufficient chilling (Sandnes, 2003; Fan et al., 2012; Furbo et al., 2012; Dannemand et al., 2015a; Dannemand et al., 2015b).

Fast nucleation kinetics are very important for the practical use of PCMs, in particular for supercooling PCMs. Rapid crystal growth rates confirm chemical kinetic control of the solidification process, meaning that solidification proceeds at a rate commensurate with the system-average reaction rate expression (ignoring mass transfer/local concentration effects) and remains mostly constant until quickly reaching the equilibrium state. Following the initial, isenthalpic solidification from the supercooled PCM, changes in equilibrium states occur more slowly, and therefore result in the apparent heat transfer control of the solidification reaction rate.

SAT crystal front expansion rates have been recorded in the range of 2 mm/s to 7.3 mm/s for varying dilutions of SAT in water (Ahmad, 2002; Wood et al., 2011), much faster than for pure sodium hydrogen phosphate dodecahydrate, $Na_2HPO_4 \cdot 12H_2O$, or sodium thiosulfate pentahydrate, $Na_2S_2O_3 \cdot 5H_2O$, recorded $\leq$ 1 mm/s and $\leq$ 0.3 mm/s, respectively (Hirano et al., 2002a; Wood et al., 2011). Ahmad (2002) and Wood *et al.* (2011) both found that SAT crystal front expansion rates depend strongly on the solution concentration, but are mostly invariant to the degree of supercooling, $T_{trans} - T$ (Ahmad, 2002). Ahmad (2002) measured crystal front expansion rates of solutions in the range of approximately 43 mass% SA to 50 mass% SA in water, while Wood *et al.* (2011) performed these measurements in two solutions: 33.6 mass% SA and 56 mass% SA in water.

Araki et al. (1995) studied the thermophysical properties of SAT at various compositions of SA in water below 60.3 mass% SA (Araki et al., 1995). They reported results for specific heat capacities and thermal conductivities of the individual states (solid, equilibrium liquid, and supercooled liquid) with varying temperatures and compositions and provided empirical functions representing all of their data as a function of composition and temperature for each phase. The composition dependence of the liquid-phase (equilibrium and supercooled) specific heat capacities by Araki et al. (1995) closely resemble those obtained using the rule of mixtures, therefore suggesting ideal solution behaviour in concentrated aqueous SAT solutions (Desgrosseilliers et al.,

2013a). Araki et al. (1995) also reported the latent heat of transition for SAT as a function of composition, however this data does not correspond to the report by Meisingset et al. (1984) that was validated with experimental data and a complete thermodynamic model by Desgrosseilliers et al. (2013a). Meisingset and Grønvold gave a detailed account of their determinations of the latent heat of transition of SAT using adiabatic calorimetry (Meisingset et al., 1984), and Marcus provided a review of density measurements of pure SAT solutions and those of other salt hydrate solutions over large temperature ranges found in the literature (Marcus, 2013). Richards and Gucker also reported on their calorimetric determinations of the heat of solution of SA in water as a function of concentration, for which there is only significant non-linearity observed in very dilute solutions (Richards et al., 1929). Ideal solution behaviour with respect to the solution specific heat capacity has been confirmed by Desgrosseilliers et al. (2013a) for concentrated solutions of SA in water.

Other reports on the thermodynamic properties of SAT have been found in the literature, but these are either not in the relevant ranges of conditions for heat storage, e.g., at temperatures between 10 K and 300 K (Franzosini et al., 1983), or the reported data are no longer considered valid either due to more recent or well-supported investigations, like those of Sturley and Wei (Sturley, 1932; Wei et al., 2010), or citing erroneous data, like those of Furbo (Schultz et al., 2005; Schultz et al., 2007; Fan et al., 2012; Furbo et al., 2012; Dannemand et al., 2015a; Dannemand et al., 2015b).

Beyond these physical property measurements and determinations of supercooling salt hydrate PCMs, very few reports are available on in-situ investigations of the phase change process in macro-scale heat storage devices (Schultz et al., 2005; Schultz et al., 2007; Hirano et al., 2009; Fan et al., 2012; Furbo et al., 2012; Dannemand et al., 2015a; Dannemand et al., 2015b), and only one such study has also proposed a numerical simulation of the phase change process coupled with internal and external heat transfer (Fan et al., 2012). H.M. Heizkörper, a company developing commercial SuperTESSs using supercooling SAT in water to store solar thermal energy for use in preheating domestic hot water and for indoor heating (H.M.Heizkorper, 2012) has not revealed any detailed evaluations of its prototypes or any scale-up validations. Investigations by Furbo and coworkers have been reported only for large-scale investigations, with masses of

sodium acetate mixtures ≥ 100 kg per storage unit, varying between pure SAT and 55 mass% to 58 mass% SA in water (Schultz et al., 2005; Schultz et al., 2007; Fan et al., 2012; Furbo et al., 2012; Dannemand et al., 2015a; Dannemand et al., 2015b). These experiments were not conducted with any means of internal visualization of the PCM phase change behaviour prior to integrating the storage with the means for heat exchange with a liquid heat exchange fluid (Schultz et al., 2005; Schultz et al., 2007; Fan et al., 2012; Furbo et al., 2012; Dannemand et al., 2015a; Dannemand et al., 2015b). Hirano et al. (2009) also did not include any means of internal visualization before implementing their storage and heat exchange design. The single numerical phase change and internal/external heat transfer simulation by Fan et al. (2012), although supposed to simulate the incongruent phase change behaviour of 58 % SA in water, modelled the thermodynamic behaviour incorrectly as only that of the pure PCM (60.3 % SA in water, *H-T* dependence only), ignoring solution concentration effects completely (*H-T-x* dependence), as well as producing very poor agreement of the predicted heat exchange capacity rate, *UA*, with that of the experimental device. Fan et al. (2012) also did not address the fundamental difficulty of numerically modelling phase change with heat transfer supplied from below, whereby the model unrealistically simulates total adhesion of the solid PCM to the container walls and suspended above the liquid PCM.

Although there is considerable knowledge available in the literature on the thermo-physical properties of SAT, including both equilibrium and supercooled properties, the knowledge of in-situ transient phase change coupled with transport processes (heat, mass, and momentum transport) is lacking both by observation and by computer simulation. These are required in the analyses of the heat exchange rates to and from SuperTESSs for detailed heat exchange design, incremental scale-up and validation of the desired behaviours, identification of mechanisms affecting the supercooling stability of PCMs (e.g., solution stratification), and transient integrated system modelling for space heating applications. The present research aims to conduct in-situ observations of the corresponding phase change process and solution stratification in the intended encapsulation device resulting from this research. The knowledge gained is used to guide the development and scale-up of the device from bench-top scale to commercial scale.

1.2.2 ENCAPSULATION AND HEAT EXCHANGE

With the additional requirements, specific only to supercooled salt hydrate PCMs, to house internal solidification triggering devices or to allow access to external nucleation sources as well as suppress unintended nucleation when supercooled, encapsulation criteria pioneered by Lane *et al.* (1978) encompass the essential requirements for successful PCM integration into heat storage systems. Lane's criteria are: mechanical durability and integrity, good heat transfer, chemical compatibility, and vapour impermeability (Lane et al., 1978; Lane, 1980), with added considerations to cost and ease of manufacture (Lane et al., 1978). Poor encapsulation selection results too easily in failure of PCM containment and it is emphasized by two of Lane's selection criteria. Secondary to sufficient PCM containment are the encapsulation's contributions to performance (i.e., heat transfer) and preservation of the PCM (e.g., vapour impermeability, nucleation suppression). The last of Lane's criteria cover practical considerations for fabrication and commercial viability.

With respect to chemical compatibility of the encapsulant and PCM, Lane previously identified thermoplastics as the most compatible with salt hydrates (Lane et al., 1978; Lane, 1980), although metals and their alloys can still be selected with proper attention to corrosion resistance (Lane, 1985). The German company H.M. Heizkörper uses cylindrical stainless steel containers with aluminum fins for increased heat transfer imbedded in the PCM for their prototype supercooling SAT heat storage product, *Thermobatterie* (H.M.Heizkorper, 2012), but there is no available scientific literature to support this encapsulation option. In particular, aluminum is typically a poor choice for concentrated salt solutions (Lane, 1985) and can be subject to aggressive corrosive attack if it is in electrical contact with the stainless steel, becoming the anode in a galvanic cell.

Of special interest are the encapsulation options provided by flexible, thin, metallized thermoplastic films. Lane reported on the mechanical and barrier properties of 0.18 mm thick, lightweight laminate films containing aluminum with layers of polyethylene and polyester for use with non-supercooled salt hydrate PCMs (Lane et al., 1978), while Furbo and Schultz used 0.118 mm thick pouches of a similar laminate film in their experiments using a supercooled SAT (Schultz et al., 2007). Aluminized films used in food, Li-ion pouch-cell, and electronics packaging can be bag-sealed to provide a close,

conforming fit to its contents (Lane et al., 1978; Lane, 1980; Targray, 2012), but these films can also be adhered to compatible thermoplastic substrates to construct semi-rigid encapsulation volumes.

In addition to providing reliable physical containment for salt hydrate PCMs with substantially reduced mass and volume and associated material costs compared to rigid thermoplastic or stainless steel constructions, aluminized films also provide integral heat transfer area improvements to nucleated supercooled salt hydrate PCMs by virtue of their layered construction (Desgrosseilliers, 2012; Desgrosseilliers et al., 2013b; Desgrosseilliers et al., 2014b). The latter inhibits simple planar heat conduction due to the poor thermal conductivity of the thermoplastic layers (i.e., series resistance heat conduction), but enables transverse heat conduction from a non-uniform heat source (e.g., salt hydrate solidification front) along the length of the highly thermally conductive layer of aluminum foil to be dissipated in areas with no direct contact with the non-uniform heat sources (Desgrosseilliers et al., 2013b). Improvements to the discharge heat transfer from freshly nucleated supercooled salt hydrate PCMs (as PCM solidification emanates from discrete nucleation sites) is essential to their use in SuperTESSs, since heat discharge is the most limiting heat transfer regime in all PCMs (unaided by natural convection), and the heat released from solidification can account for $\geq$ 49 % of the stored energy (Hirano et al., 2009; Desgrosseilliers et al., 2014c). A simple to use, explicit, one-dimensional, steady-state laminate heat conduction model called 'two-region fin model' has been formulated and validated to predict the heat spreading performance of thin aluminized thermoplastic films (Desgrosseilliers et al., 2013b; Desgrosseilliers et al., 2014a; Desgrosseilliers et al., 2014b; Desgrosseilliers et al., 2016).

Since the probability of heterogeneous nucleation of supercooled salt hydrate PCMs increases with PCM volume (Lane, 1983), salt hydrate PCM volumes are best kept in relatively small, isolated volumes, i.e., macro rather than bulk encapsulation. Modular heat exchanger design would best suit this requirement, and allows for flexible/adaptable sizing of both the individual heat exchange modules and overall SuperTESS. Of further benefit to modular heat exchanger design would be the ease of access to individual supercooling PCM volumes for servicing by simply disconnecting the desired module from the SuperTESS without affecting other modules operating in the system. Of further

concern to supporting PCM supercooling (i.e., suppressing autonucleation), care must be taken to ensure the PCM cavity is made smooth, to eliminate potential sites capable of trapping stable seed crystal under high contact pressure or capillary pressure. Variations in stress caused by both thermal expansions of the encapsulation and the PCM under thermal cycling risk inadvertently exposing the supercooled solution to seed crystals (Furbo et al., 2012; Dannemand et al., 2015a; Dannemand et al., 2015b).

Plate-and-frame type heat exchanger design, considered to have the largest heat exchange area (extended surfaces excluded) for the occupied floor area of any industrial liquid-to-liquid heat exchanger type (McCabe et al., 2005; Green et al., 2008), is the most likely adaptable type of heat exchanger to meet the requirements of modular construction and individual supercooling PCM volume isolation. These heat exchangers are composed of corrugated heat exchange plates and two end-plates supported by carrying bars and compressed by large bolts spanning its length. Two fluids flow between adjacent pairs of plates in a counter-current arrangement (see schematic representation in Figure 1-8), in thin, alternating channels enclosed by the adjacent plates (Green et al., 2008). Plate-and-frame type heat exchangers owe their elevated heat transfer coefficients and heat transfer efficiencies obtained at low Reynolds number (Re) (McCabe et al., 2005; Green et al., 2008) to the extended surfaces and vortex generation (Khoshvaght-Aliabadi, 2015) of the plate corrugations, and small characteristic length of heat diffusion in the fluid channels.

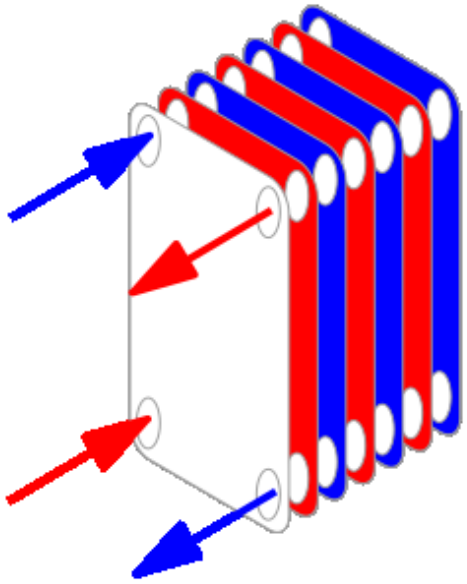

Figure 1-8: Schematic representation of counter-current flow arrangement in a plate-and-frame heat exchanger. The blue and red arrows represent the cool and warm fluid inlet and outlets, respectively. The red and blue alternating plates represent the adjacent warm and cool fluid heat exchange channels, in which their respective fluids flow counter-current to one-another. Reproduced with permission from ©Krzysztof Zajączkowski / CC-BY-SA-3.0.

Unlike traditional plate-and-frame heat exchangers in which there are two counter-current mobile phases on either side of the heat exchange plates, one used for PCM heat storage must consist of stationary cavities containing PCM, each equipped with heat exchange plates located on either side of the cavities and separating the cavities from one-another. The heat exchange plates separating neighbouring cavities can be either shared between them (in thermal contact with both cavities) or individual to each cavity (separate heat exchange plates abutting one-another, but thermally insulated from one-another and each in thermal contact with only one cavity). The mobile phase flowing through the heat exchange plates can flow in either a parallel or series arrangement to one another. Such a heat exchanger would resemble the design used for cooling individual, prismatic Li-ion cells in the Chevrolet Volt automotive T-Pack, wherein coolant flow is delivered to individual Li-ion pouch-cell pairs in a parallel flow arrangement and with the flow controlled from an external manifold (G.M., 2010). Of further benefit to supercooling salt hydrate PCM heat exchanger design using a plate-and-frame configuration is the inherent prismatic geometry of the individual heat exchanger

components, which typically reduces the heat diffusion path length when compared to other geometries.

There are few documented examples of either adapting or reconfiguring plate-and-frame heat exchange for use with PCM heat storage. Medrano and coworkers (2009) examined several conventional heat exchanger technologies (double-pipe, finned-tube bundle, and plate-and-frame) for use with PCM heat storage. All of the conventional heat exchangers examined were adapted for use with a commercial paraffin PCM simply by filling one side of the heat exchangers with PCM, with the other side remaining for use with a flowing heat exchange fluid (Medrano et al., 2009). However, their simple repurposing of a plate-and-frame heat exchanger for use with PCMs has proven fruitless in comparison to the other heat exchanger types (Medrano et al., 2009) since the heat exchange plate cavities are designed with small clearances (typically 2 mm - 10 mm, (Green et al., 2008)) with the aim of promoting high heat-transfer rates between adjacent flowing fluids, and not intended for the retention of a non-flowing heat sink/source.

Over the course of their iterations, Furbo and coworkers (Fan et al., 2012; Furbo et al., 2012; Dannemand et al., 2015a; Dannemand et al., 2015b) have reconfigured the traditional plate-and-frame heat exchanger design to suit the purposes of PCM heat storage. Their work began with PCM pouches constructed from metallized film submerged in a heat exchange fluid (Schultz et al., 2005; Schultz et al., 2007) and evolved to producing large plate-and-frame style PCM enclosure/heat exchangers (Schultz et al., 2005; Schultz et al., 2007; Fan et al., 2012; Furbo et al., 2012; Dannemand et al., 2015a; Dannemand et al., 2015b). The latter were constructed with sizeable PCM cavities to contain supercooling SAT (pure and mixtures), exchanging heat with two adjacent heat exchange plates (arranged for parallel flow) hosting an externally circulating fluid for heating and cooling (Fan et al., 2012; Furbo et al., 2012; Dannemand et al., 2015a; Dannemand et al., 2015b). These supercooling PCM enclosure/heat exchangers were made large (for example 3 m × 2 m × 0.05 m PCM cavity) and contained in excess of 100 kg, so they were configured to be rested horizontally, with one heat exchange plate above and one below the PCM cavity (Furbo et al., 2012). In this configuration, however, the influences of the respective heat exchange plates are strongly dissimilar due to their positions with respect to the internal circulation of the liquid PCM

in either heating or cooling, affecting heat exchange performance and PCM phase transition, further challenged by the varying levels of thermal contact between the PCM and the top plate due to thermal expansion and phase change. From this perspective, a vertical PCM enclosure with the two heat exchange plates located vertically on either side would be preferred since only in this configuration could both plates provide equal impact on the heat exchange and phase change processes and maintain thermal contact with the PCM equal to one-another.

Handbook relations for estimating Nusselt[14] numbers of mobile heat exchange fluid phases in plate-and-frame heat exchangers are readily available and proven adequate in industrial settings (McCabe et al., 2005; Green et al., 2008). This process is only feasible to determine the heat transfer coefficient of the mobile fluid phase and applicable only in estimating the rate of heat transfer assuming that the materials of construction do not act as significant heat sinks (e.g., steady-state assumption). PCM heat transfer in a closed volume is inherently transient, and therefore does not conform to steady-state heat transfer methodologies and requires rigorous analysis of the thermal history and transport processes. However, for a fixed enclosure and heat exchanger design, it might be possible to accumulate sufficient experimental data to propose and validate state and boundary condition based models (e.g., pseudo-steady state approaches) to predict PCM transient behaviour.

Kabbara (2015) has proposed one such model able to predict either gross discharge time or desired characteristic lengths for discharge heat transfer using a Fourier number analogy for PCM systems undergoing solidification. This method requires prior experimental characterization and can only be used in comparison to a system under similar heat exchange conditions (i.e., boundary heat flux or temperature) and using identical PCMs (Kabbara, 2015). Kabbara (2015) demonstrated preliminary experimental validation using a coil-in-tank encapsulation and heat exchange design, which possesses three independent characteristic lengths for heat transfer (planar, cylindrical, annular),

[14] The Nusselt number, Nu, expresses the ratio of a fluid's convection heat transfer coefficient to its representative conductance across the characteristic length of the flow channel. A high Nu indicates a system with a large value of convection heat transfer coefficient with respect to the fluid's representative conductance.

while plate-and-frame heat exchangers have the benefit of having only one characteristic length (planar).

In absence of empirical or theoretical overall heat exchange coefficient (U) calculation methodologies for PCM heat storage using supercooling salt hydrates, the experimental studies reported in the literature can at least be used as benchmarks for new designs. While industrial heat exchangers are designed to achieve overall heat transfer coefficients of 7,400 W/m^{2}K using water and 4,000 W/m^{2}K using glycol (Green et al., 2008), the plate-and-frame type enclosure/heat exchanger developed by Furbo and coworkers for seasonal solar heat storage has been reported[15] to achieve 29.2 W/m^{2}K to 64.9 W/m^{2}K for charging and 51.9 W/m^{2}K to 86.0 W/m^{2}K for discharging, each conducted with total water flow rate between 2 L/min and 7 L/min (Fan et al., 2012). Furbo and coworkers developed their design with the aim of nominally achieving a heat capacity rate (UA) of 500 W/K (corresponding to U = 81.1 W/m^{2}K for their heat exchanger design) in both charge and discharge modes, which they deemed satisfactory for seasonal heat storage for an efficiently designed home in Denmark (Fan et al., 2012; Furbo et al., 2012; Dannemand et al., 2015a). Note that Furbo and coworkers only used wall temperature measurements within the heat exchange plate channels as proxies for PCM storage temperatures (Fan et al., 2012), therefore underestimating the actual mean temperature difference of the overall heat exchange process, resulting in artificially high values of the reported overall heat transfer coefficients. Choi et al. (1996) investigated the heat exchange coefficients of finned and unfinned tube heat exchangers in a cylindrical SAT PCM vessel with heat transfer coefficients reported in the range of 45 W/m^{2}K to 250 W/m^{2}K.

Specially reconfigured plate-and-frame type heat exchangers show promise for modular, compact supercooling salt hydrate PCM heat storage systems. Appropriately sized PCM cavities are required to house a sufficient thermal mass for heat storage instead of the thin heat exchange channels used in conventional heat exchangers, but care must also be practiced in selecting the PCM enclosure thickness (i.e., characteristic length of heat transfer) to achieve desired discharge heat-transfer rates. Vertical enclosures, kept sufficiently small for handling, are preferred to horizontal enclosures for reasons of

[15] Reported heat capacity rates (UA) normalized to the approximate heat exchange area, 6.16 m^2.

improved thermal contact and uniformity of heat transfer of the heat exchange plates with the PCM. Also, parallel flow of the heat transfer fluid into the heat exchange plates of a PCM enclosure is preferred over a series arrangement. This research aims to explore these areas of development and thoroughly validate the reliability and performance of this type of heat exchanger for use with supercooling SAT diluted in excess water. Experimental evaluations of the discharge heat transfer will also be used to determine a suitable PCM enclosure thickness to obtain a desirable discharge time and time-weighted overall heat transfer coefficient using the Fourier number analogy method by Kabbara.

1.2.3 INDOOR HEATING

In choosing supercooled SAT as a heat storage PCM medium in a modular SuperTESS prototype, the compatibility with indoor heating systems is restricted primarily to convective air-heaters, for which the heat source temperature requirements are typically less elevated (40-60 ˚C) than those required for hydronic baseboard or in-floor heating (70-90 ˚C) (Lane et al., 1978). The conditions for heat exchange in particular indoor air-based heating systems can be more conducive still to heat exchange with a supercooled SAT SuperTESS than what is suggested above: for instance, efficient central air-heat exchangers used for whole home heating in the individual homes at DLSC need only a circulating liquid supply temperature ≥ 28 ˚C (minimum district-heating loop temperature), although the exact supply temperature varies as a function of outdoor air temperature (Sibbitt et al., 2011). Similarly, air-to-air heat pumps need only supply condenser temperatures around 30 ˚C to heat the indoor air via fan driven liquid-air, finned tube heat exchangers (LG, 2014).

Convective air heating can be accomplished either directly or indirectly, meaning that either air exchanges heat directly with the heat storage mass or a liquid is used as an intermediary to exchange heat between the heat storage masses and the indoor air. Conventional brick ETS units employ direct air heating, however, due to the bricks' poor heat exchange characteristics, high heat storage temperatures (nominally up to 600 ˚C) must always be maintained to provide adequate air heating (Romero, 2013). Direct-air heat exchange is also limited by air's own poor convective heat transfer characteristics in comparison to common liquids: e.g., Pr ~ 7 for water and Pr ~ 1 for air at room

temperature[16] (Green et al., 2008) giving rise to typical, turbulent (Re = 6,000) individual convective heat transfer coefficients in the range of 1,000 W/m^2K and 100 W/m^2K, respectively. Consequently, liquid heat exchange results in more efficient heat transfer in compact designs than does air heat exchange, and liquid-to-air heat exchange can be performed more efficiently and compactly than air-heat storage mass heat exchange. Therefore, rather than using direct air heating, heat exchange compactness and high efficiency can be achieved by employing indirect air heating via a single, efficient liquid-to-air heat exchanger and using distributed liquid heat exchangers among the heat storage masses. Although it is overcome by the benefits just listed, indirect air heating does inherently decrease the maximum possible heat exchange efficiency due to adding an intermediary heat exchange process not present in direct air heating.

Pertaining to liquid-to-air heat exchange, the use of multi-pass and extended surface (finned-tube) heat exchangers help reduce the occupied volume and improve heat-transfer rates, efficiencies and effectiveness. High-effectiveness heat transfer equipment (e.g., air-heating indoor heat pumps and home central air-heaters at DLSC (Sibbitt et al., 2011; LG, 2014)) lowers the heat source temperature and capacity rate requirements to achieve the desired heat-transfer rates and fluid outlet temperature (e.g., outlet indoor air temperature). With respect to PCM heat storage, the use of high-effectiveness heat transfer equipment results in deeper heat storage discharge, higher round-trip efficiencies, and reduced PCM mass required for heat storage.

Fundamentally, liquid-to-air heat exchangers (see example in Figure 1-9) are categorized as shell-and-tube heat exchangers, in which the air always occupies the single-pass only shell section with the liquid occupying the single or multi-pass tube section. Multi-pass tube sections in counter-current arrangements alone result in 5 % to 9 % increases in the mean temperature difference (MTD) correction factor (0.96-0.99 for two and three passes, respectively (Green et al., 2008)). Exercising diligent high-effectiveness design, liquid-to-air heat exchangers can achieve liquid outlet temperatures as low as 8 ˚C above the inlet air temperature (Green et al., 2008), equal to 28 ˚C to 33 ˚C in rooms with air between 20 ˚C and 25 ˚C. Evidence of this principle made practical is

[16] The Prandtl number, Pr, expresses the ratio of momentum diffusion to thermal diffusion, whereby, in convective heat transfer, a high Pr indicates increased effect of thermal advection to thermal diffusion.

found in the designs of modern air-heating heat pumps (LG, 2014) and low-temperature source central air heaters used at DLSC (developed by Nu-Air Ventilation Inc., (Sibbitt et al., 2011)).

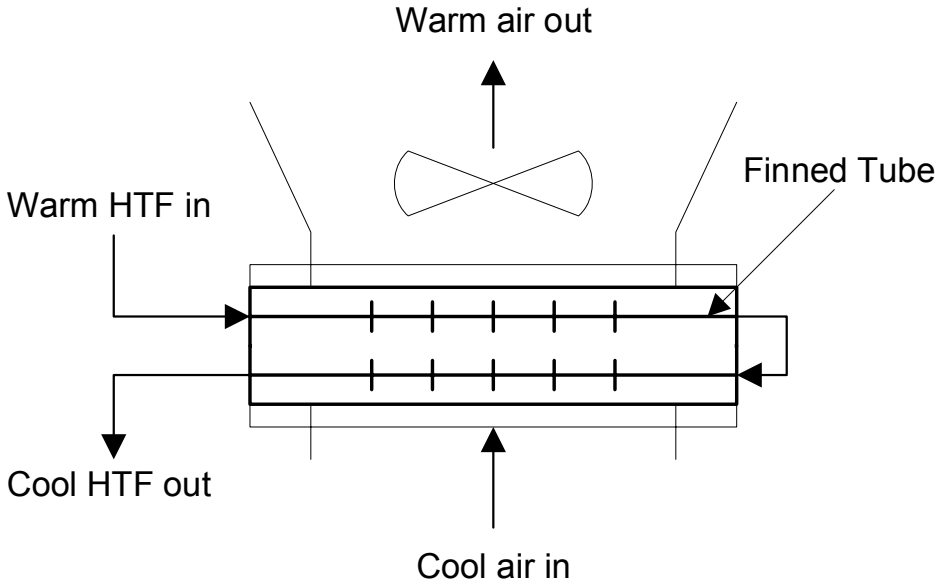

Figure 1-9: Schematic representation of a 1-2 liquid-air heat exchanger (one shell-pass, i.e., blown air, and two tube passes).

It is apparent that indirect-air heating is most suitable for the development of compact ETS technologies. Distributed liquid heat exchange among the heat storage masses is more practicable for compact and efficient heat exchange design than direct air-heating presently used for brick ETS units, albeit at a slight additional component cost and with increased control strategy complexity. High effectiveness, low source-temperature liquid-to-air heat exchangers needed to complete heat exchange to the indoor air are already commonplace and field proven, therefore the barrier for adoption into compact, portable ETS units is low. Therefore, the present research aims to address the integration of the closed-loop, distributed, liquid heat exchanger circuit, exchanging heat with the individual heat storage masses, with the liquid-to-air heat exchanger. Appropriate sizing of the liquid-to-air heat exchanger for individual room heating will be addressed as well.

1.3 RESEARCH STATEMENT

The opportunity and need for new portable, compact ETS units to deliver off-peak electricity indoor heating cost savings has been argued. Of particular importance is the

portability and compactness of such proposed ETS units, which would be uniquely disposed to fulfill the needs of rental tenants (both residential and commercial) that are otherwise unaddressed.

Elaborations on how ETS compactness and portability can be achieved have concluded that supercooling salt hydrate PCMs possess the necessary qualities and have been sufficiently well documented to pursue immediate research and development into early prototype development. Their supercooling ability yielding battery-like heat storage behaviour, although used for decades in therapeutic hand warming pouches, has lacked fundamental engineering development to become feasible for implementation into contemporary ETS units or other indoor heating systems. Furthermore, detailed, transient phase-change modelling to aid heat storage system design and investigate heat storage capacity loss mechanisms (e.g., vapour loss and solution stratification) as well as optimize external and internal heat transfer processes has so far been largely absent and poorly executed.

The present research has taken the aim to elevate the state of development and knowledge in several of these areas with the aim of generating a commercially exploitable early prototype supercooling ETS technology. The activities pursued to do so are supercooling salt hydrate PCM selection for indoor air-heating ETS, iterative detailed enclosure design and evaluation to ensure the support of supercooling PCM characteristics (e.g., supercooling, solidification triggering, phase change) and cycle reliability and detailed design and evaluation of external heat transfer integrated with the PCM enclosure and balance-of-system heat transfer design and evaluation for ETS operation. Following supercooling salt hydrate PCM selection, all of the other research activities were conducted largely in parallel to one another, utilizing each other's findings to inform decisions for each step's individual developments and evaluations. Also, each stage of development was advanced incrementally so as to best identify courses of action and independently validate design features and operating conditions from one-another as much as practicable.

CHAPTER 2: FUNDAMENTAL DESIGN

2.1 INTRODUCTION

The following sections outline the supercooling ETS unit design objectives as well as examine the design considerations needed to fulfill them. These include the selection of a supercooling salt hydrate PCM, a report of its properties, and examination of the chemical and mechanical features of the designs that were developed and evaluated as described in Chapters 3 and 4.

2.2 DESIGN OBJECTIVES

The designs for the supercooling salt hydrate PCM enclosures (i.e., heat storage cells) and the integrated ETS system were both driven by benchmarks and requirements established in Chapter 1 regarding the performance of similar PCM heat storage devices, conventional indoor room heating, thermo-physical and chemical properties of salt hydrate PCMs, and desired attributes for the identified customer segments. Additional requirements were also derived to address design codes and consumer product regulations.

The American Society of Mechanical Engineers (ASME) Boiler and Pressure Vessel (BPV) design code is stipulated in government regulations and requires third-party certification for proof of compliance; consumer appliance electrical design codes are also mandated by government regulations, requiring third-party product certification as well for proof of compliance. Electrical certification is necessary and cannot be dismissed due to the nature of the proposed ETS unit, however, the ASME BPV code has a provision for exclusions applying to the present technology proposal. Specifically, the BPV code provisions classifies boilers as devices generating hot vapours for processes or heating purposes and excludes pressure vessels operating below 2 atm from mandatory certification (ASME, 2013). The proposed ETS unit does not qualify as a boiler, and therefore would not require ASME BPV certification if operating below 2 atm.

With respect to the supercooling salt hydrate PCM enclosures and integrated heat-exchange plates, the design objectives are listed below:

1. Modularity of the individual enclosures (i.e., plate-and-frame style design);
2. Internal pressure < 2 atm (heat transfer fluid and PCM);

3. PCM must generate useful latent heat discharge above 28 ˚C (i.e., liquid-to-air heat exchange);
4. Select an abundant, low-cost, inherently safe supercooling salt hydrate PCM;
5. Heat storage fraction retained during supercooling[17] ≥ 40 %;
6. Ability to support supercooling at room temperature (~20 ˚C) for seasonal durations (i.e., one year);
7. Reliable nucleation triggering device to initiate latent heat discharge from a supercooled state for on-demand heating;
8. Total heat storage ≥ 400 kJ/kg (combined sensible and latent heats over range of operating temperatures);
9. Complete PCM heat charge achieved in << 7 hours per enclosure[18];
10. Nominal overall heat transfer coefficient > 30 $W\,m^{-2}\,K^{-1}$ (charge and discharge)[19];
11. Nominal heat discharge power ≥ 600 W[20];
12. ≥ 10 y design life for commercial units[21];
13. Enclosure structural materials to occupy ≤ 20 % of heat storage cell volume[22].

Specifically regarding ETS room heater systems, the additional design objectives are:

A. External surface temperatures < 40 ˚C for inherent safety regarding occasional physical contact with indoor occupants;
B. Internal pressure < 2 atm;
C. Total mass ≤ 30 kg for sufficient portability (i.e., can be easily carried by two adults);

[17] This criterion is not discussed in Chapter 2, however rationale is simply based on minimum utility of supercooled heat storage vs. non-supercooling latent and sensible heat storage.
[18] This is the minimum off-peak period offered by utilities and most common in the United Kingdom (Byrom, 2016).
[19] This criterion corresponds to the minimum reported overall heat transfer coefficient value reported by Fan et al. (2012).
[20] Heating power equal to that of typical portable electric heaters.
[21] This value is chosen to be competitive with conventional heat pumps, brick ETS units, and solar thermal installations.
[22] This criterion is not discussed in Chapter 2, and was chosen as reasonable goal for structural materials minimization on the bases of the cost of materials and promoting high heat storage density of the finished product (i.e., minimize volume of non-heat storage materials).

D. Noise ≤ 54 dB(A) during operation;
E. Nominal heat discharge power ≥ 600 W[18];
F. ≥ 10 y design life for commercial units[19];
G. Unit functions using 120 V and maximum 12.5 A electrical supply in North America;
H. Achieves full charge of all PCM modules in 7 h (i.e., minimum duration of off-peak periods).

2.3 PCM SELECTION

2.3.1 PCM SCREENING

Objectives 2-6, 8 (and B, partly) express the supercooling salt hydrate PCM attributes that are required to yield useful heat storage cells and a compelling supercooling ETS unit for supplemental indoor heating. These objectives capture the necessity for compactness of heat storage, utility of heat discharge via a liquid-to-air heat exchanger, reliability and utility of supercooling to improve heat storage efficiency, safety to indoor occupants, and affordability.

Affordability is simple to assess qualitatively via the availability of constituent atoms. As a rule of thumb, atoms of low period numbers (i.e., belonging to the top rows of the periodic table of elements) are typically abundant in the Earth's crust (Ashby, 2013). Considering its ubiquitous association with 'salts', sodium cations in ionic compounds (i.e., salts) bodes well for its natural abundance. Regarding anion availability, those containing oxygen, carbon, nitrogen, and hydrogen[23] (Ashby, 2013), individually or in combinations thereof (i.e., polyatomic anions) should be considered naturally abundant as well.

Three sodium-based salt hydrates with long-standing and notable histories in PCM science (Green, 1908; Hammick et al., 1920; Lane, 1983; Sandnes, 2008), and each paired with relatively abundant anion constituents were identified: a) sodium sulphate decahydrate (T_{trans} = 32 ˚C, ΔH_{tans} = 250 kJ/kg (Abhat, 1983; Zalba et al., 2003)), $Na_2SO_4 \bullet 10H_2O$, commonly known as Glauber's salt; b) sodium hydrogen phosphate dodecahydrate (SHPD; T_{trans} = 36 ˚C, ΔH_{tans} = 265 kJ/kg (Abhat, 1983; Hirano et al.,

[23] Halogens are excluded from consideration due to concern for aggressive metal corrosion (Garverick, 1994).

2002a)), $Na_2HPO_4 \bullet 12H_2O$; and, c) sodium acetate trihydrate (SAT; $T_{trans} = 58$ ˚C, $\Delta H_{tans} = 284$ kJ/kg (Green, 1908; Meisingset et al., 1984; Desgrosseilliers et al., 2013a)), $NaCH_3CO_2 \bullet 3H_2O$. Based only on their constituent atoms, SAT can be deemed slightly more abundant than either Glauber's salt or SHPD, which can be considered equally abundant. Furthermore, all three salt hydrate PCMs are equally safe to use; none pose any particular threat to human and animal health and the environment (AcrosOrganics, 2014; AlfaAesar, 2015a; AlfaAesar, 2015b).

Used undiluted, these salt hydrate PCM candidates would each provide similar heat storage capacities in the temperature range 28 ˚C to above 60 ˚C (i.e., sum of latent and sensible heats). However, since all three PCMs are peritectic compounds (i.e., each form a secondary solid phase at T_{trans} for the pure compound) they should instead be used with extra water of dilution to promote phase-change cycle-stability. In this case, the maximum heat storage capacity would be obtained using diluted SAT instead of Glauber's salt or SHPD (assuming comparable dilutions), owing to SAT's higher transition temperature[24] that results in a higher extent of phase-change above 28 ˚C. Figure 2-1 illustrates this principle, whereby a larger amount of solid salt hydrate is available for phase-change at temperature 'b', farther below T_{trans} (representing SAT), than there is at temperature 'a', nearer T_{trans} (representing Glauber's salt and SHPD). Therefore, the contribution of the latent heat storage fraction to the total heat storage (sensible + latent) from SAT is highest of all the candidate salt hydrate PCMs, allowing SAT to preserve more heat storage from supercooling than would Glauber's salt or SHPD. Due to SAT's higher T_{trans} than for Glauber's salt or SHPD, higher heat-transfer rates are expected during heat discharge (solidification) than would be generated from Glauber's salt or SHPD. All considered, SAT diluted in excess water was selected as the PCM with which to develop the proposed supercooling PCM ETS technology.

[24] The transition temperatures of Glauber's salt and SHPD are each very close to the minimum useful heat exchange temperature of 28 ˚C during heat discharge, therefore engaging in less overall phase-change than would SAT.

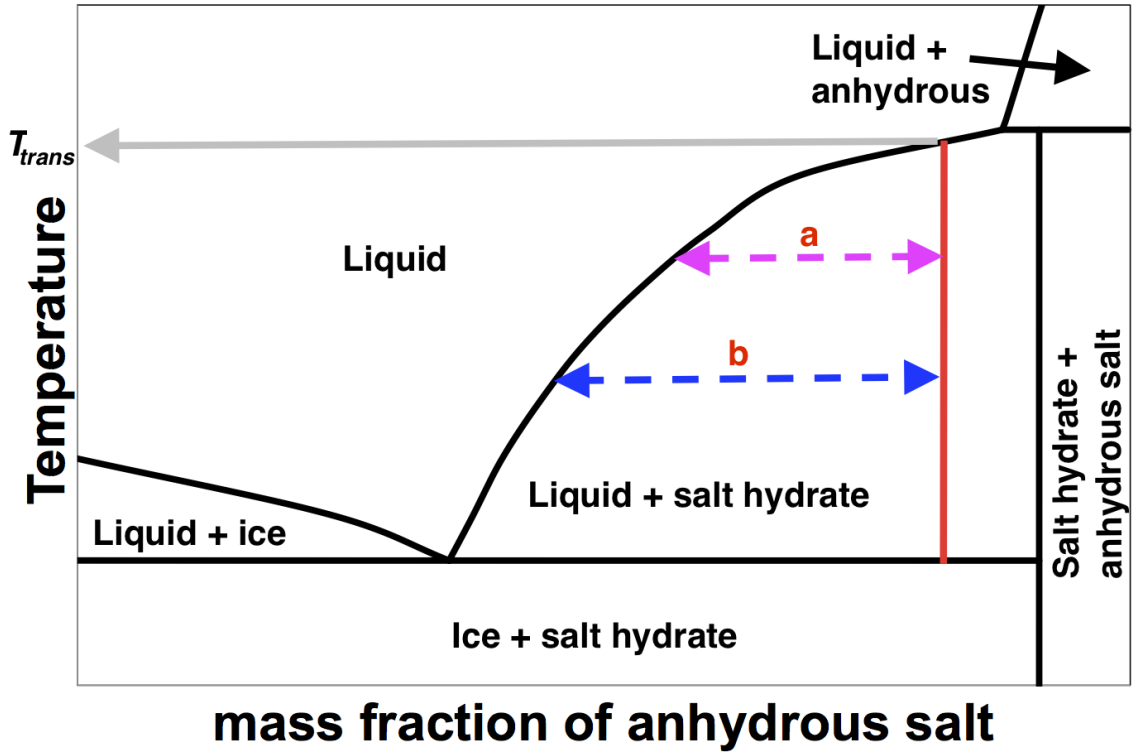

Figure 2-1: Representation of extent of phase-change of diluted salt hydrates. The vertical line abutting dashed arrows 'a' and 'b' represents the average composition of the salt hydrate PCM. At a temperature nearer T_{trans}, length 'a' is shorter than length 'b' at a temperature farther from T_{trans}. These lengths are directly proportional to mass of solid present for phase-change at either temperature.

It is interesting to note, as well, that diluted PCM's have the added capacity to improve heat-transfer rates during the charging process compared with the pure PCM. This is attributed to gradual phase-change occurring over the entire range of operation when the PCM is below T_{trans}, generating an effect of increased apparent heat capacity, capable of maintaining a larger temperature difference with respect to the heat source than would the pure PCMs (phase change occurs only at T_{trans}). However, the benefit to heat-transfer rates during the heat charging process of diluted PCMs is confined to weak dilutions since increased dilution has the effect of decreasing the amount of PCM for charging and also decreases T_{trans}.

2.3.2 PROPERTIES OF SELECTED PCM

2.3.2.1 BINARY PHASE EQUILIBRIUM

Benefiting from over 100 years of scientific study, SAT is among the most thoroughly characterized salt hydrate PCMs. For instance, SAT has been documented to

supercool to temperatures as low as -50 ˚C (Naumann et al., 1989) and to remain supercooled at room-temperature for several years (Sandnes, 2003), making SAT a very practical room-temperature supercooling medium (objective 6 in Section 2.2). SAT's thermodynamic, physical, and transport properties relevant to the development of a supercooling PCM ETS unit are documented in this section.

The binary phase equilibrium diagram for water and sodium acetate has been explored by Green (1908) and displayed in Section 1.2.1.1 Figure 1-4 on a mole-basis in the SA mole fraction range spanning $0 \leq x_{SA} \leq 0.250$. Due to the mass basis taken in the subsequent treatments of the binary phase equilibrium behaviour and thermodynamic modelling of SA in water, Figure 2-2 reproduces Figure 1-4 using a mass-basis in the SA mass fraction range $0 \leq w_{SA} \leq 0.658$, where $w_{SA} = x_{SA} \div \left(82\left(\frac{x_{SA}}{82} + \frac{1-x_{SA}}{18}\right)\right)$.

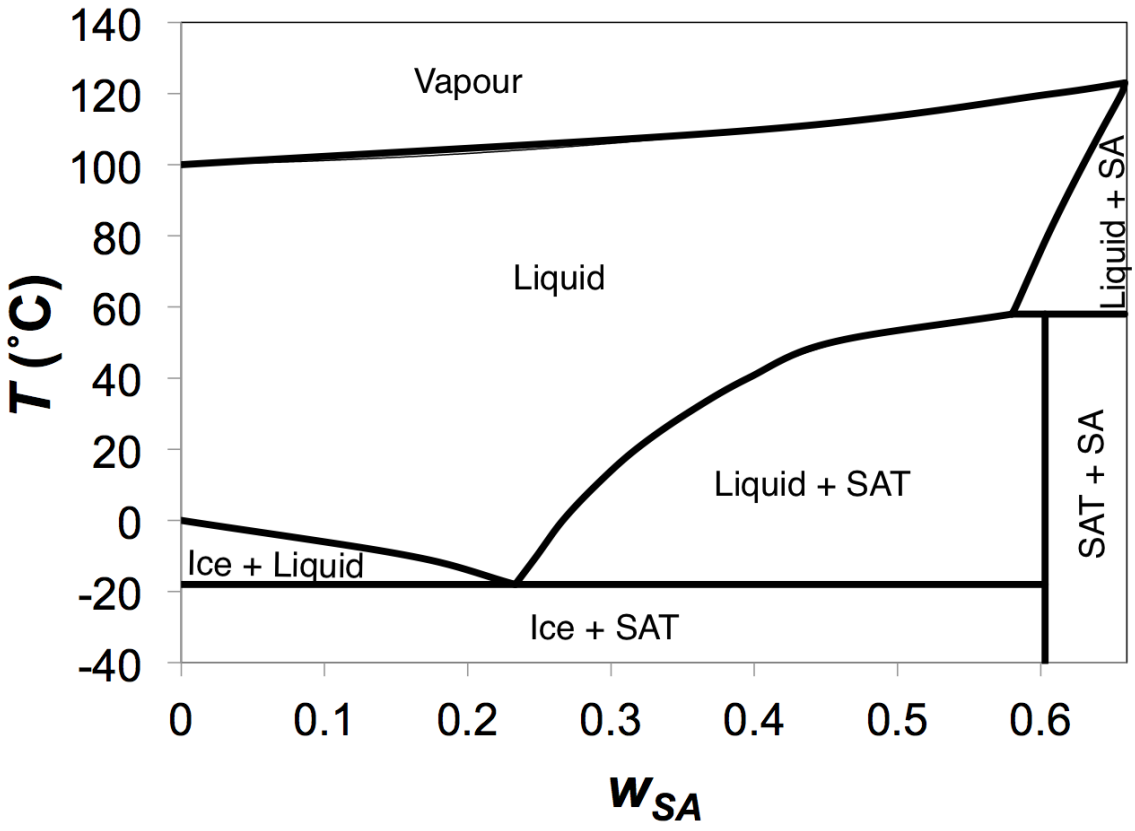

Figure 2-2: Binary phase diagram of anhydrous sodium acetate ($NaCH_3CO_2$) and water reproduced from Figure 1-4 on the basis of mass fraction ($0 \leq w_{SA} \leq 0.658$). SA mass fraction is denoted by w_{SA}.

The pure, peritectic SAT compound corresponds to $w_{SA} = 0.603$ ($x_{SA} = 0.250$, $T_{trans} = 58$ ˚C), therefore the range in Figure 2-2 is sufficiently inclusive of the binary phase equilibrium behaviour of SAT for the purposes of supercooling heat storage. Regarding the practice of PCM dilution used to promote phase-change cycle stability, discussed in Section 1.2.1.1, it has become commonplace for heat storage researchers and practitioners using SAT to prepare solutions of 1:1 molar ratio of water and SAT (henceforth called 1:1 SAT in water or SAT PCM). This corresponds to $w_{SA} = 0.532$ ($x_{SA} = 0.200$, i.e., 4:1 molar ratio of water and SA) in Figure 2-2, for which the maximum solid-liquid equilibrium temperature is 55 ˚C, slightly lower than T_{trans}, and sufficiently far away from the second liquidus region (beginning at $w_{SA} = 0.580$ in Figure 2-2, $x_{SA} = 0.233$ in Figure 1-4), liquid + SA, to avoid further complications, even with the effect of long-term vapour loss. In this secondary liquidus region, a fully dissolved equilibrium liquid at $w_{SA} = 0.603$ ($x_{SA} = 0.250$) exists only above 80 ˚C. Using a least-squares line of best fit, the two respective liquidus lines in Figure 2-2 for concentrated solutions of SA in water were represented by:

$$T_{liq} = 1368.4w_{SA}^3 - 2412w_{SA}^2 + 1459.9w_{SA} - 244.3, \quad (2.1)$$

and

$$T_{liq} = 815.63w_{SA} - 414.21, \quad (2.2)$$

where T_{liq} is the liquidus (i.e., saturated liquid) temperature for mixtures with SA concentration w_{SA}. Equation (2.1) is valid for $0.233 \leq w_{SA} \leq 0.580$, while Eq. (2.2) is valid for $0.580 \leq w_{SA} \leq 0.658$.

Regarding objective 2 in Section 2.2, the maximum operating temperature can be inferred from the binary equilibrium phase diagram in Figure 2-2 for 1:1 SAT in water, $w_{SA} = 0.532$ ($x_{SA} = 0.200$). Conservatively assuming that air occupies the vapour space in the PCM cavity of the heat storage cell, when first filled with fully dissolved PCM, at a pressure equal to 1 atm, the partial pressure of PCM vapour (mainly water vapour) must remain ≤ 1 atm (i.e., normal boiling point of the solution)[25]. The topmost curve in Figure 2-2 represents the normal boiling point (T_b) of solutions, for which $T_b = 116$ ˚C for 1:1

[25] Filling the PCM cavity with the solution added at the maximum operating temperature (with the heat storage cell also at this temperature) ensures that the internal pressure will not exceed the partial pressure generated by the solution, since these vapours will displace much of the air initially present.

SAT in water (T_b = 120 ˚C for pure SAT), constituting the derived maximum internal operating temperature for the proposed SAT supercooling heat storage cell. Practically speaking, however, it is advisable to operate below T_b, around 110 ˚C, henceforth chosen as the operating temperature limit for the development of the supercooling ETS unit and heat storage cells.

2.3.2.2 THERMODYNAMIC PROPERTIES

Desgrosseilliers et al. (2013a) validated an SAT-water thermodynamic model for concentrated solutions of SAT ($0.280 \leq w_{SA} \leq 0.532$; $0.079 \leq x_{SA} \leq 0.200$) with solid SAT, including phase-change in the temperature range 5 ˚C to 55 ˚C. This model was formulated using the specific heat capacity functions for pure SAT (w_{SA} = 0.603; x_{SA} = 0.250) dissolved in its own water of hydration (equilibrium and supercooled), between 30 ˚C and 80 ˚C, and pure solid SAT between 30 ˚C and 55 ˚C (Araki et al., 1995). The individual phase thermodynamic, phase change, and supercooling model equations are:

$$H_{SAT(aq)}(T) = 1.56\left(T - T_{ref}\right)\frac{\text{kJ}}{\text{kg K}} + \frac{4.27}{2} \times 10^{-3}\left(T^2 - T_{ref}^2\right)\frac{\text{kJ}}{\text{kg K}^2} + 284\,\frac{\text{kJ}}{\text{kg}}, \tag{2.3}$$

where $H_{SAT(aq)}$ represents the relative enthalpy of pure dissolved and supercooled liquid SAT,

$$H_{SAT(s)}(T) = 0.811\left(T - T_{ref}\right)\frac{\text{kJ}}{\text{kg K}} + \frac{4.06}{2} \times 10^{-3}\left(T^2 - T_{ref}^2\right)\frac{\text{kJ}}{\text{kg K}^2}, \tag{2.4}$$

where $H_{SAT(s)}$ represents the relative enthalpy of solid SAT,

$$H_w(T) = 4.18\,\frac{\text{kJ}}{\text{kg K}}\left(T - T_{ref}\right), \tag{2.5}$$

where H_w represents the relative enthalpy of extra water of dilution (not belonging to SAT's water of hydration) from 0 ˚C to 100 ˚C. All three, component relative enthalpy equations (Eqs. (2.3)-(2.5)) are calculated in reference to the reference temperature, T_{ref}, conveniently selected as T_{trans} = 58 ˚C for pure SAT. Combined, Eqs.(2.3)-(2.5) represent the total mixture relative enthalpy, H:

$$H(T) = w_w H_w(T) + (1 - w_w - w_s)H_{SAT(aq)}(T) + w_s H_{SAT(s)}(T), \tag{2.6}$$

where, w_w and w_s represent the mass fraction of extra water and mass fraction of solid SAT, respectively. At temperatures below the liquidus line (w_s = 0 above the liquidus

line), w_s can be determined using the lever rule for the average system mass fraction of 1:1 SAT in water, $w_{SA} = 0.532$ ($x_{SA} = 0.200$), needing only to know the saturated solution SA mass fraction at $T_{liq} = T_{syst}$ from either Eqs. (2.1) or (2.2), $w_{SA,liq}$:

$$w_s = \frac{0.532 - w_{SA,liq}}{0.603 - w_{SA,liq}}. \tag{2.7}$$

Regarding objective 8 in Section 2.2, Eq. (2.6) can be used to determine the heat storage capacities obtainable using 1:1 SAT in water. Using the chosen upper temperature limit for the supercooling heat storage cell of 110 ˚C ($w_w = 0.117$ and $w_s = 0$) and an initial temperature of 20 ˚C ($w_w = 0.117$ and $w_s = 0.751$), the resulting heat storage capacity of 1:1 SAT in water is 475 kJ/kg[26] for the charging process. However, since heat discharge is only useful above 28 ˚C, the maximum possible discharge capacity from a charged state at 110 ˚C to a discharged state at 28 ˚C ($w_w = 0.117$ and $w_s = 0.727$), regardless of the path taken (meaning with or without supercooling before triggering solidification), is 449 kJ/kg with round-trip efficiency of 94.5 %.

Regarding the thermodynamic cycle, two cycles result in the heat charge and discharge capacities just discussed: discharge without supercooling (solidification triggered at 55 ˚C upon cooling, Cycle 1) and with supercooling (solidification triggered at 28 ˚C, Cycle 2). Alternatively (Cycle 3), if heat is discharged from the charged state at 110 ˚C, and discharged to 28 ˚C in a supercooled state ($w_w = 0.117$ and $w_s = 0$), then allowed to supercool to room temperature at 20 ˚C ($w_w = 0.117$ and $w_s = 0$) and solidified at any later time on-demand, reheating to 53 ˚C ($w_w = 0.117$ and $w_s = 0.358$) and then discharged at equilibrium to the ground state of 20 ˚C ($w_w = 0.117$ and $w_s = 0.751$), the cycle provides only slightly less available heat for discharge, equal to 425 kJ/kg (89.5 % round-trip efficiency). Figure 2-3 illustrates differences in the paths taken in Cycles 1-3, with detailed information listed in Table 2-1.

[26] This value is calculated outside the validated temperature limits for Eq. (2.6). However, the extrapolated result remains valid for capacity sizing calculations since the extrapolated range accounts for only 21 % of the total calculated heat storage capacity and that individual heat capacities of the aqueous phase species do not exceed theoretical limits.

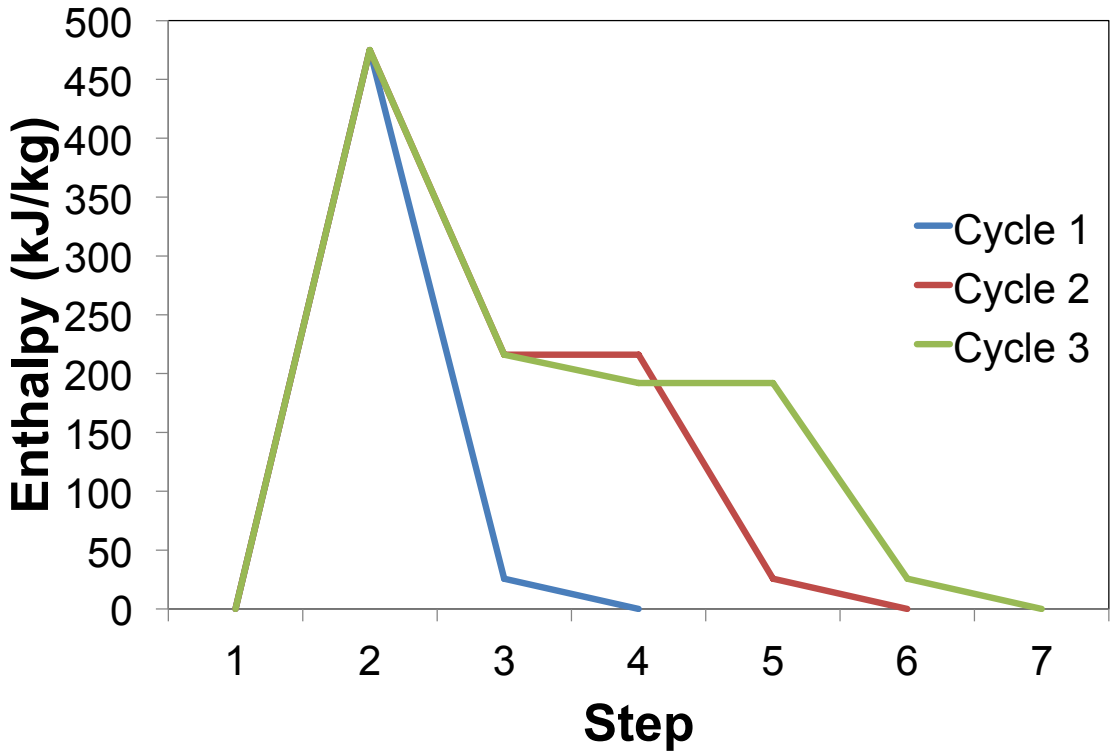

Figure 2-3: Illustration of the 1:1 SAT in water thermodynamic cycles for heat storage cell charge-discharge. Cycle 1 does not include supercooling; Cycle 2 includes supercooling that is triggered at 28 ˚C; Cycle 3 includes supercooling that is triggered at 20 ˚C.

Table 2-1: Thermodynamic cycle information for the data shown in Figure 2-3. The relative enthalpies are calculated from Eq. (2.6) with a basis of 20 ˚C, w_w = 0.117, and w_s = 0.751.

Step	Cycle 1		Cycle 2		Cycle 3	
	Enthalpy (kJ/kg)	Temperature (˚C)	Enthalpy (kJ/kg)	Temperature (˚C)	Enthalpy (kJ/kg)	Temperature (˚C)
1	0	20	0	20	0	20
2	475	110	475	110	475	110
3	26	28	216	28	216	28
4	0	20	216	54	192	20
5			26	28	192	53
6		-	0	20	26	28
7				-	0	20
Net heat discharge capacity	449 kJ/kg		449 kJ/kg		425 kJ/kg	
Round-trip efficiency	94.5 %		94.5 %		89.5 %	

As can be seen in Figure 2-3 and Table 2-1, Cycles 1 and 2 demonstrate that there is no difference in the net heat discharge available from SAT PCM heat storage cells if supercooling is confined to temperatures ≥ 28 ˚C. Note, however, that although some heat storage capacity is lost from supercooling to 20 ˚C before triggering solidification for final heat discharge, remaining supercooled at 20 ˚C eliminates long-term heat losses and retains 40 % of the initial heat stored nearly indefinitely (see Cycle 3 in Table 2-1). The latter can generate practical value when the ETS system heat discharge demands do not exceed the 259 kJ/kg available sensible heat stored in the supercooled SAT PCM, therefore allowing the stored latent heat from supercooling to remain untapped until it is needed next. Note, however, that supercooled long-term heat storage retention decreases as a function of supercooling temperatures, becoming only 34 % of the initial stored heat at 10 ˚C, 28 % at 0 ˚C and 22 % at -10 ˚C, so care must be exercised in designing for anticipated supercooled idle states. For typical indoor heating, air temperatures are kept nominally above 20 ˚C (i.e., similar to basis for heating degree days, see Section 1.1.3), therefore it is safely assumed that supercooling in a heated indoor space would occur only as low as 20 ˚C, capable of preserving a larger amount of the initial heat storage capacity and fulfilling objective 5 Section 2.2.

Consequently, Cycle 3 illustrates how a supercooling ETS unit can reliably maintain round-trip efficiencies above 89.5 % without complicated weather-predictive control algorithms, while conventional brick ETS units are generally limited to round-trip efficiencies ≤ 80 % (Romero, 2013).

Cycles 1-3 each demonstrably satisfy objectives 5 and 8 in Section 2.2, therefore fulfilling that element of the heat storage cell design. Reports of properties relevant to mechanical design and thermal design remain.

2.3.2.3 PHYSICAL AND TRANSPORT PROPERTIES

The volumetric expansion of the room temperature equilibrium SAT-water mixture to its fully dissolved state above $T_{liq} = 55$ ˚C and further expansion to the maximum operating temperature of 110 ˚C are essential to inform heat storage cell mechanical design, heat transfer design, and PCM filling protocol. Assuming ideal mixture/solution behaviour (i.e., additive property of pure species volumetric properties), the mixture density of SAT(s)-SAT(aq)-water is:

$$\rho_{mix}(T) = \left(\frac{w_s}{\rho_s(T)} + \frac{w_w}{\rho_w(T)} + \frac{1-w_w-w_s}{\rho_l(T)}\right)^{-1}, \quad (2.8)$$

where ρ_{mix}, ρ_s, ρ_w, ρ_l correspond to the mixture average, solid SAT, liquid water, and aqueous pure SAT densities at temperature T, respectively, and $w_w = 0.117$ for the SAT solution in question. Only nominal data are available for solid SAT, for which ρ_s =1450 kg/m^3 (Green et al., 2008). Liquid water is characterized in the temperature range 290 K to 647.13 K by Yaws (2010):

$$\rho_w(T) = 325 \times 0.27^{-\left(1-\frac{\left(\frac{T}{\mathrm{K}}-273.15\right)}{647.13}\right)^{0.23}} \mathrm{kg/m^3}, \quad (2.9)$$

and pure aqueous SAT (w_{SA} = 0.603) by (Marcus, 2013):

$$\rho_l(T) = 1565.3\,\frac{\mathrm{kg}}{\mathrm{m^3}} - 0.888T\,\frac{\mathrm{kg}}{\mathrm{m^3 K}}. \quad (2.10)$$

The results of Eqs. (2.8)-(2.10) are shown in Table 2-2 for the three volumetric states of interest to mechanical design. The 10.5 % change in volume generated at the 55 ˚C fully dissolved state is nominal for typical PCMs, while the 14.9 % change at the 110 ˚C fully charged state warrants specific attention.

Regarding objective 2 in Section 2.2, the 14.9 % volume change at 110 ˚C suggests that the PCM should be initially loaded into the heat storage cell and sealed at or near this temperature. This strategy ensures that only a maximum of 1 atm internal pressure is achieved at 110 ˚C and that aqueous PCM does not exceed the initial fill level and risk overflowing from the heat storage cell during operation. Rather than operating at a net positive gauge pressure, the room temperature discharged state of the SAT PCM would likely reside in a net negative gauge pressure, generating a vacuum due to the expansion of the vapour space and due to low vapour pressure at that condition. As a by-product of the volume changes described in Table 2-2, the exposed area for heat transfer would be greatest at 110 ˚C and lowest at 20 ˚C, which would be manifested as an artificially reduced value of the overall heat exchange coefficient, U, evaluated at 20 ˚C using the nominal heat transfer area of the heat storage cell heat exchange plates.

Table 2-2: Component and mixture-average temperature dependent densities of supercooling diluted SAT PCM (w_{SA} = 0.532).

T	w_s	ρ_w	ρ_l	ρ_{mix}	Volume %-difference from 20 ˚C
20 ˚C	0.751	1016 kg/m^3	1300.5 kg/m^3	1361 kg/m^3	-
55 ˚C	0	988.9 kg/m^3	1273.9 kg/m^3	1232 kg/m^3	10.5 %
110 ˚C	0	943.1 kg/m^3	1225.0 kg/m^3	1184 kg/m^3	14.9 %

Regarding the transport properties of SAT, important to internal heat transfer and natural convection of the aqueous phase, the reported thermal conductivities and viscosity are not fully characterized for their dependence on mixture composition and temperature. Of the limited data available, nominal values for pure SAT are extracted since the pure species (water and SAT) values are not drastically dissimilar from one-another, suggesting they should be generally representative of their mixtures. Thermal conductivity data reported by Araki et al. (1995) suggest a nominal value of 0.4 W m^{-1} K^{-1} to be taken, while a nominal viscosity of 19 cP should be taken (Yoon et al., 2000).

2.4 HEAT EXCHANGE FLUID SELECTION

The heat exchange fluid, circulating externally to the supercooling salt hydrate PCM heat storage enclosures, exchanges heat with the enclosed PCM, inline electric heater, and liquid-to-air heat exchanger. At its highest temperature, the heat exchange fluid is used to heat the salt hydrate PCM during charging and bring the PCM to thermal equilibrium with the heat exchange fluid at the PCMs maximum charge temperature. Due to dynamic electric heater controls (typically utilizing dead-band limits around the setpoint temperature) needed to heat the heat exchange fluid temperature during PCM charging, the heat exchange fluid's maximum operating temperature can be assumed to be equal to 2 ˚C above the PCM's maximum charge temperature, therefore 112 ˚C.

In consideration of the maximum design pressure limit established in Section 2.2 (objective 2) to avoid the ASME BPV code invocation, the heat transfer fluid must only be allowed to generate vapour pressures < 1 atm (assuming an initial reservoir air pressure of 1 atm, use of a pressure equalizing expansion tank, and negligible hydrostatic pressure in the system). Furthermore, a desirable heat exchange fluid should be only weakly corrosive to most common heat exchanger metals and alloys (e.g., aluminum, copper, brass, stainless steel, steel), have low flammability risk under the operating conditions, and be inherently safe for human exposure and environmental release in the event of a leak.

Since the vapour pressure of water exceeds 1 atm above 100 ˚C, a different heat transfer fluid must be used to remain below the maximum operating pressure at temperatures up to 112 ˚C. Propylene glycol (PG) is frequently used for this type of service as it is a safe, non-toxic fluid with very little odour (Dow, 2003), and has very low vapour pressure in comparison to water (see vapour pressure of aqueous PG solutions in Figure 2-4) and is only weakly acidic ($K_a = 10^{-14.8}$ at 25 ˚C (Riddick et al., 1985)). However, PG has significantly higher viscosity (up to 60 cP at 20 ˚C, see Figure 2-5) and lower specific heat capacity than water (2.51 kJ kg^{-1} K^{-1} for PG vs. 4.18 kJ kg^{-1} K^{-1} for liquid water, both at 25 ˚C (Felder et al., 2000; Dow, 2003)), therefore PG is usually mixed with water (PG is completely miscible in water) to produce a solution of lower vapour pressure and acceptable viscosity and heat capacity for adequate convective heat transfer.

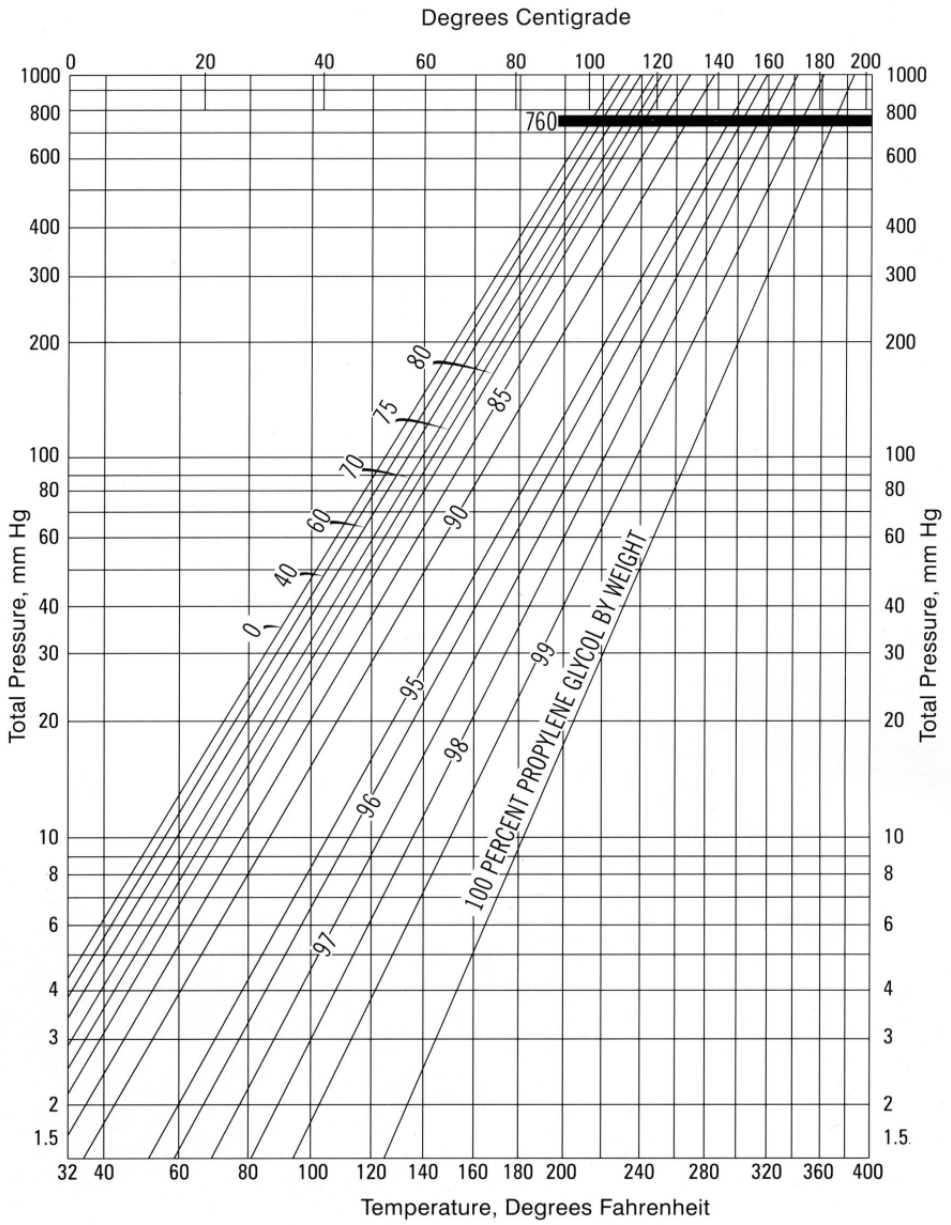

Figure 2-4: Vapour pressure of aqueous propylene glycol by mass percent of propylene glycol (Dow, 2003). Provided courtesy of The Dow Chemical Company.

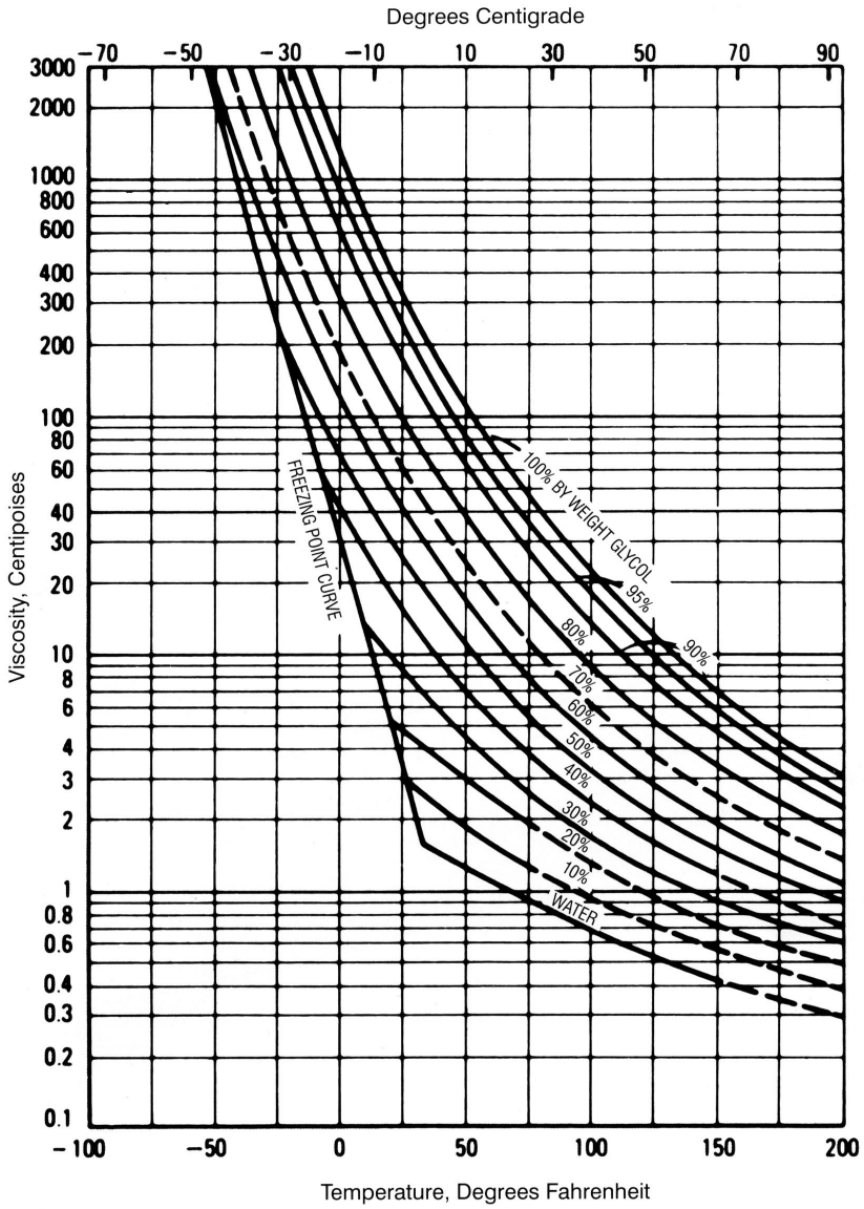

Figure 2-5: Viscosity of aqueous propylene glycol by mass percent of propylene glycol (Dow, 2003). Provided courtesy of The Dow Chemical Company.

As can be inferred from Figure 2-4, mixtures of PG and water with vapour pressures less than 1 atm can be prepared with ≥ 80 mass% PG for use up to 118 ˚C, while solutions with ≥ 70 mass% PG can be used to 110 ˚C. Solutions prepared with 40 vol% PG (~ 43 mass% PG, see Figure 2-6) are typical in residential solar thermal installations, mainly for cold climate anti-freeze performance and can be purchased pre-mixed from solar thermal system vendors, but should not be used above 105 ˚C to limit the solution vapour pressure to 1 atm (Figure 2-4). The high PG mass% required to decrease the

solution vapour pressure is attributed to the high molecular weight of PG in comparison to water, resulting in lower corresponding mole-fractions of PG than mass-fractions (see Figure 2-6). In a solution, the total vapour pressure is the sum of the individual species partial vapour pressures, equal to the products of the individual saturated vapour pressures and their liquid mole-fractions in ideal solutions (Raoult's law):

$$P_{vap} = \sum P_{vap,i} = \sum x_i P_{sat,i}, \tag{2.11}$$

where P_{vap} is the solution vapour pressure, $P_{vap,i}$ is the partial pressure of species i in the solution, $P_{sat,i}$ is the saturated vapour pressure of pure species i, and x_i is the species i liquid mole-fraction.

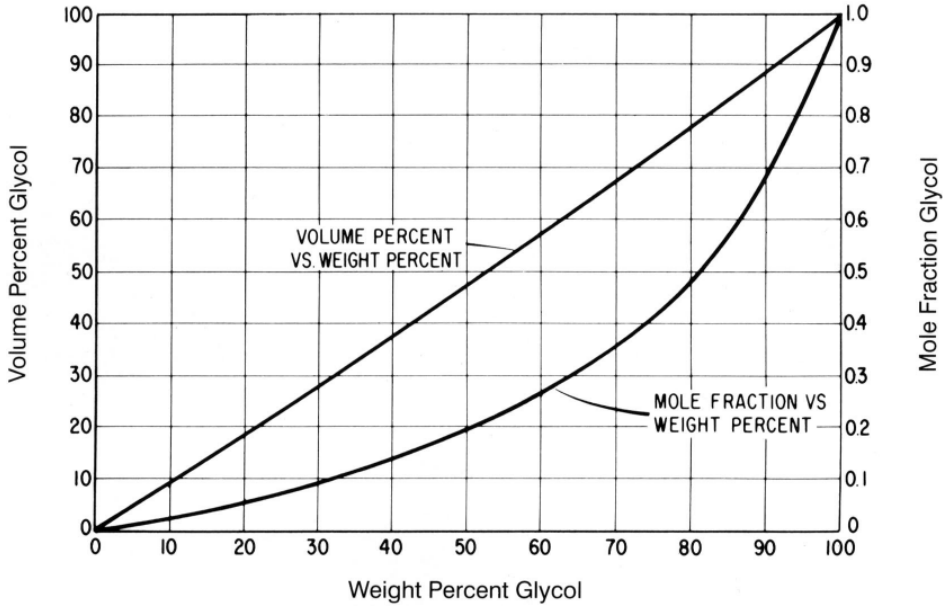

Figure 2-6: Volume percent, mass percent, and mole-fraction conversions for aqueous PG (Dow, 2003). Provided courtesy of The Dow Chemical Company.

Of consequence to solution selection for low vapour pressure is the effect on the solution flash point. Since water is non-flammable and PG produces flammable organic vapours, PG solutions should be prepared with the minimum PG content to achieve the desired vapour pressure at the desired operating temperature limits, but minimizing PG partial vapour pressure. The flash point for PG (minimum temperature at which flammable vapours are present) is 104 ˚C (Dow, 2003), corresponding to a saturated vapour pressure (P_{sat}) of pure PG equal to 3.8 kPa, calculated using Antoine's equation for PG (T = 377 K (NIST, 2016)):

$$P_{sat}(T/\mathrm{K}) = 10^{6.07936-\frac{2692.187}{T-17.94}}\ \mathrm{bar}\ . \qquad (2.12)$$

At the maximum operating temperature limit equal to 112 ˚C, the saturated vapour pressure of PG, using Eq. (2.12), is equal to 5.60 kPa. Assuming that the partial vapour pressure of PG at the solution flash point is the same as for pure PG[27] (3.8 kPa) and using the calculation of component partial pressures used in Raoult's law (Eq. (2.11)), the mole-fraction of PG must be kept below 0.68 for vapours to remain non-flammable, corresponding to solutions with ≤ 90 mass% and ≤ 89 vol% PG (see Figure 2-6).

Therefore, given these precautions to avoid flammability of the PG vapours in indoor environments, a suitable heat transfer fluid for use in the proposed supercooling PCM ETS unit should be prepared with at least 75 mass% PG in water (~ 73 vol% PG) and no more than 90 mass% PG in water (89 vol% PG). The use of this range of fluids will permit operations to temperatures ≤ 117 ˚C (Figure 2-4) in order to ensure that solution vapour pressure remains below 1 atm, suggesting that components and structural materials should be designed for an operating temperature limit of 120 ˚C.

2.5 CHEMICAL CONSIDERATIONS

Chemical design of systems and components is aimed at ensuring their reliabilities and longevities (objectives 12 and F in Section 2.2) by using either passive or active elements and strategies to combat their susceptibilities to chemical media to which they are exposed and the conditions in which they must persist.

Of principal concern to the development of a supercooling ETS unit are the PCM, both in its liquid and solid states, as well as the circulating heat transfer fluid exchanging in the closed-loop heat exchange circuit. The PCM and heat exchange fluids must remain chemically stable at all operating states (charge, discharge, supercooling, idle) to ensure long-term cycle stability of the heat storage and heat withdrawal processes as well as both must be safeguarded against loss-of containment and diffusive and evaporative mass losses across system boundaries.

The respective PCM and heat exchange fluid thermal stabilities in the imposed operating conditions have already been addressed in Sections 2.3 and 2.4. However, these each constitute the chemical media to which the structural materials must resist chemical

[27]Flammability of PG vapours over an aqueous solution is assumed to be more difficult due to the displacement of oxygen in air by elevated amounts of water vapour.

degradation (e.g., solvent and corrosive attacks). These same materials are also responsible for preventing material losses (diffusive and evaporative) from both chemical media with which they are charged to contain and isolate, henceforth called barrier materials.

The following sections detail the material selection and design strategies that have been employed to support chemical stability and integrity of the barrier and structural materials. Note, however, that passive elements and strategies are exclusively chosen for the development of the supercooling ETS unit reported herein. This has been adopted to limit design complexity with respect to electrical and mechanical controls and avoid unnecessary material, mechanical and electrical exchanges within the fluid system (PCM and heat exchange fluid).

2.5.1 CHEMICAL COMPATIBILITY

2.5.1.1 SALT HYDRATE PCM EXPOSURE

Regarding material selection for the supercooling salt hydrate heat storage enclosures, the structural materials must contain and isolate the water-SAT mixture without intervention for several years and resist chemical attack for the design life of the components.

The SAT water mixture, when fully dissolved above the phase transition temperature and when this solution is supercooled, constitutes a concentrated aqueous solution of a weak base (acetate anion is the conjugate base of acetic acid) and poses a corrosive threat to some metals. In the absence of organic solvents, the aqueous SAT solution is compatible with thermoplastics, most notably with polyolefins such as polypropylene, and poses no threat of chemical attack.

With respect to the corrosion resistance of metals and their alloys, the caustic strength of the solution, pOH, must be determined for the most concentrated solution obtainable in supercooling SAT heat storage enclosure. Equation (2.13) shows the hydrolysis reaction of the acetate anion:

$$CH_3COO^-_{(aq)} + H_2O_{(l)} \leftrightharpoons CH_3COOH_{(aq)} + OH^-_{(aq)}, \quad (2.13)$$

occurring simultaneously with the inherent hydrolysis of water,

$$2H_2O_{(l)} \leftrightharpoons H_3O^+_{(aq)} + OH^-_{(aq)}, \quad (2.14)$$

for which, the equilibrium constant, K_w, is equal to 10^{-14} at room-temperature. The equilibrium constant, K_a, for the hydrolysis reaction of acetic acid, CH_3COOH, at 25 ˚C is equal to 1.76×10^{-5} (Oxtoby et al., 2002), thereby resulting in the equilibrium constant, K_b, for the hydrolysis reaction in Eq. (2.13) at 25 ˚C from:

$$K_b = \frac{K_w}{K_a} = 5.68 \times 10^{-10}. \tag{2.15}$$

Assuming that chemical activities of the individual, aqueous chemical species represented in Eqs. (2.13) and (2.14) are approximately equal to their respective molar concentrations (i.e., ideal solution assumption, previously confirmed for aqueous SAT in the concentration range of interest (Desgrosseilliers et al., 2013a)), the reaction quotients for Eqs. (2.13) and (2.14) are expressed as:

$$K_b = \frac{[CH_3COOH][OH^-]}{[CH_3COO^-]}, \tag{2.16}$$

and

$$K_w = [H_3O^+][OH^-], \tag{2.17}$$

where [] denotes molar concentrations of the chemical species identified within. While $[OH^-]$ is present in both Eqs. (2.16) and (2.17) and both chemical equilibria must be satisfied, some of their constituent terms can be neglected due to scale differences in their values. These values are represented by their respective mass balance equations:

$$[CH_3COO^-] = [CH_3COO^-]_i - a, \tag{2.18}$$

$$[CH_3COOH] = a, \tag{2.19}$$

$$[OH^-] = [OH^{-1}]_i + a - b, \tag{2.20}$$

$$[H_3O^+] = [H_3O^+]_i - b, \tag{2.21}$$

where a and b denote the respective extents of reaction for Eqs. (2.13) and (2.14) with signs selected on the anticipated reaction outcomes using LeChâtelier's principle, and concentrations denoted with the subscript i denote initial system values prior to the hydrolysis reactions.

The SAT water mixture is prepared using distilled, or de-ionized water with neutral pH (pH = pOH = 7), so prior to the hydrolyses generated by Eq. (2.13), $[OH^{-1}]_i = [H_3O^+]_i = 10^{-7}$M. Since material selection for corrosion resistance is based on the most challenging condition (i.e., largest value of pOH), the initial concentration of the acetate

anion is calculated based on assuming a heat storage system using pure, undiluted SAT, for which the initial concentration is:

$$[CH_3COO^-]_i = [NaCH_3CO_2 \cdot 3H_2O]_i = \frac{\rho_{SAT}}{M_{w,SAT}} = \frac{1.3050}{136.08\times10^{-3}}\text{M} = 9.59\text{ M}, \quad (2.22)$$

where $M_{w,SAT}$ and ρ_{SAT} refer to the molar mass and supercooled liquid phase density of SAT at 293.15 K (room temperature) as calculated from Eq. (2.10), with the latter chosen for the maximum value of $[CH_3COO^-]_i$.

By examining the scales of the respective terms in Eqs. (2.18)-(2.20), Eq. (2.16) can be simplified to:

$$K_b = \frac{a^2\ M}{9.59\ M-a}, \quad (2.23)$$

assuming that $a >> 10^{-7}$ M, since $[H_3O^+]_i = 10^{-7}$ M and $b \leq [H_3O^+]_i$. Calculating a from Eq. (2.23) results in $a = 7.38 \times 10^{-5}$ M, satisfying this criterion, and yielding pOH = 4.13 and corresponding to pH = 9.87. In comparison to a strong base, the latter pOH corresponds to less than 1 mass% of NaOH in water. Therefore, the solution is only mildly caustic at its highest concentration, and approaches pH neutrality when the mixture contains mainly solid and only a small amount of dilute solution in its room temperature discharged state (for mixtures of SAT and water only, since only solid is present below 58 ˚C for pure SAT). However, at high temperatures, it is unclear how the equilibrium of Eq. (2.13) is affected. Therefore, pH ~ 10 is cautiously assumed, since pH ≥ 7 for Eqs. (2.13) and (2.14). Acetate anion, CH_3COO^-, is a weaker base than its conjugate acid, CH_3COOH, as evidenced by $K_a >> K_b$ at 25 ˚C, therefore assumed always to favour the stability of CH_3COO^- and the reactivity of CH_3COOH at other temperatures.

Under such caustic conditions and an oxygen rich environment (air is present in the PCM enclosure), the general corrosion of most metals is limited due to oxide stabilization (i.e., metal oxide corrosion products have poor solubility in caustic solutions due to poor ion dissociation in water); however, aggressive corrosion mechanisms (e.g., pitting, stress-corrosion cracking, grain boundary attack) are not so easily abated.

Aluminum and its common alloys (e.g., alloy 6061), although highly desired for excellent heat transfer properties and lower density than other metals, risk succumbing to aggressive corrosion when exposed to concentrated salt solutions (Abhat, 1983). Ferrer et al. (2014) documented pitting corrosion for aluminum exposed to the commercial

inorganic PCM SP21E from Rubitherm after only 12 weeks at 38 ˚C. Metal selection handbooks by Garverick (1994) and Davis (1997) also caution against using aluminum in caustic environments, as well as for magnesium, tin, chromium, zinc, and zinc containing brass and bronze. When using these metals for caustic service, they must be paired with an isolating layer, such as polymeric film or coating.

Steel, cast iron, copper, and aluminum-bronze show only moderate resistance to caustic solutions and typically only at moderate temperature (Garverick, 1994; Davis, 1997), so these are also not recommended unless a polymer lining is employed to isolate the metal from the solution. Metals that are recommended for use in caustic solutions above 100 ˚C are limited only to type 300 series stainless steels (austenitic), zirconium, and nickel alloys (Garverick, 1994; Davis, 1997), of which type 304 stainless steel is the most economical and possesses good thermal diffusivity in comparison to the other corrosion resistant metals.

From this analysis, two suitable metal selections arise: type 300 series stainless steels (preferably type 304) are recommended for wetted contact with the caustic salt hydrate solution, while conventional aluminum alloys (e.g., alloy 6061) can be used for non-submerged components (i.e., wetted on one side only) and must be isolated from the solution by a polymeric film or coating. The concentrated salt hydrate solution PCM constitutes a strong electrolyte, so use of dissimilar metals (including dissimilar alloys) in the solution is discouraged as it might result in accelerated corrosion from galvanic attack.

2.5.1.2 HEAT TRANSFER FLUID EXPOSURE

As identified in Section 2.4, aqueous solutions of PG in water have been selected for use in the proposed supercooling PCM ETS unit. Fortunately, PG is a very weak acid, and is therefore compatible with common flow network and heat exchanger metals and alloys (e.g., aluminum, copper, brass, steel, stainless steel). However, as an organic compound, PG does pose a risk of solvent attack to some polymers, used for tubing, fittings, vessels, and gaskets.

Polymers that resist non-polar and polar organic solvent attacks are generally suitable for use with PG. Polyolefins (polypropylene and polyethylene) resist all solvent attacks, but these are limited in their operating temperature limits. Fluoropolymers, such as

polytetrafluoroethylene (PTFE, aka Teflon ™) and perfluoroalkoxy alkane (PFA) are highly chemically resistant and have high operating temperatures, and therefore deemed suitable for all applications in flow networks using aqueous PG solutions. Silicone elastomer gaskets are high-temperature and solvent resistant, and therefore recommended for use with aqueous PG solutions.

2.5.2 NUCLEATION TRIGGERING

In Section 2.3.2, latent heat storage during extended periods of supercooling in diluted SAT is anticipated to retain 40 % of the thermal energy stored from charging nearly indefinitely. However, supercooled heat storage only realizes its benefit to the user by releasing the stored thermal energy on-demand when warranted by ETS system indoor heating demands.

Controlled, on-demand, heat release from supercooled SAT PCM (objective 7) can be reliably achieved by introducing a nucleation promoter into the supercooled PCM, the most suitable of which is the stable, crystalline solid of same PCM (Lane, 1983). These can be introduced into the supercooled PCM either from an external source (dropped-in directly or cascading from a neighbouring container via interconnecting capillary (Sandnes, 2003)) or internal source (submerged mechanical contact devices (Sandnes, 2008)). Only internal sources provide the benefit of self-contained operation (i.e., operation without intervention), and therefore they were chosen at the exclusion of external sources for the development of the proposed supercooling PCM heat storage cell.

Sandnes (2003, 2008) characterized internal sources (i.e., nucleation triggering devices) as having, above all, the capacity to retain stable seed crystals in isolation from the surrounding, bulk PCM and apply a suitable contact pressure over the seed crystals for them to remain stably in the solid phase when heated above the normal[28] T_{trans} (recall discussion in Section 1.2.1.3). Since elevated contact pressures are needed to reliably retain stable seed crystals above their normal T_{trans}, metal nucleation triggering devices are preferred nearly exclusively over plastic devices.

Controlled exposure of the retained seed crystals is also necessary, so these devices must have the capacity for repeated mechanical deformation, meaning they should be

[28] Meaning occurring normally at 1 atm.

flexible (elastic deformation only) but also provide a threshold resistance to deformation when at rest. This translates to meaning devices must be pre-strained or pre-loaded at rest, whereby mechanical action induces a relaxation of the contact regions and separation of their interfaces to expose the seed crystals. Consequently, preference is given to devices with greater pre-loading at rest, resulting in greater contact pressure. There is no guarantee of a seed crystal at every contact junction; therefore devices containing high populations of contact junctions are preferred over those with fewer.

Ascribing to the internal nucleation triggering theory championed by Anthony et al. (1990) and independently supported by the experiments of Sandnes (2008) and Günther et al. (2007), the function of an internal triggering device also depends on the initial loading of seed crystals. Seed crystal formation from a supercooled liquid under extended, localized pressurization is not a reliable method of generating seed crystals due to the over reliance on the probability of autonucleation only, which is inherently poor in a practical supercooling PCM medium. Prior to loading the PCM into the finished heat storage cell, Sandnes (2008) recommends conditioning or 'activating' nucleation-triggering devices as a method to pre-load them with a sufficient supply of seed crystals. Simply put, this process requires only that the contact regions of the nucleation triggers be separated and exposed to the stable solid PCM in question, then permitted to clamp the solid particles in their contact regions. This can either be accomplished externally by exposing the triggers to a container of solid salt hydrate or by exposing the triggers to a solution that is permitted to evaporate and coat their open contacts, or internally to the heat storage cell by triggering nucleation of the PCM by externally inserting a piece of solid salt hydrate and opening and closing the trigger contacts to the solid PCM generated around them.

Since the flexure of triggering devices necessitates either complex internal actuation or external actuation needing to manipulate the PCM enclosure materials both to locate and flex the triggering device, triggering devices requiring only linear motion actuation were selected. A linear tension can be provided using just a simple actuator (e.g., linear solenoid) capable of imparting the load externally to the PCM heat storage cell via a sealed rod in connection with a spring. The other end of the spring need only be anchored

to the base of the PCM heat storage cell to succumb to extension and subsequent release of entrapped SAT seed crystals into the surrounding supercooled SAT PCM.

Simple, pre-loaded, extension springs have been identified from these criteria and were chosen for implementation into the proposed supercooled SAT PCM heat storage cell designs. Selected springs were chosen for their combinations of pre-loading as well as lengths, coil diameters and wire diameters, affecting the amount of contact junction area. The spring nucleation triggers must remain in perpetual submerged contact with the SAT PCM, therefore springs were exclusively chosen from type 300 series stainless steel extension springs for their corrosion resistance to the chemical environment discussed in Section 2.5.1.1. Spring nucleation trigger 'activation' must always be observed prior to putting the heat storage cells into service.

2.6 MECHANICAL CONSIDERATIONS

The following sections are aimed at addressing the preliminary mechanical considerations prior to fabricating prototype heat storage cells and an integrated ETS system prototype. Mechanical considerations encompass structural design, external heat exchange and heat exchange fluid network, fabrication, assembly, moving parts, and leak-tightness.

2.6.1 SERVICE TEMPERATURE/PRESSURE

All structural materials used in the fabrication and assembly of the supercooling salt hydrate PCM ETS unit, including tubing, instruments, and fittings, must be rated for safe use and maintain integrity within the operating temperatures and pressures imposed in Sections 2.2, 2.3, and 2.4. Component and material failures risk the release of hot fluids under moderate pressure, posing a burn danger to persons situated near the ETS unit. In case of inabilities to source materials, components, or instruments of sufficient robustness, operating condition limits for the system must be reduced to those of the least robust material, component, or instrument to ensure safe operation in occupied indoor environments.

With respect to risk of combustion of indoor materials, the unit's operating temperature limit specified in Section 2.3 falls far below the auto-ignition temperatures of common household solid combustibles (e.g., 330 ˚C for polyethylene (InChem, 2004)),

and therefore does not pose a significant threat of fire for use indoors. This aspect is considered an inherent safety feature of the proposed supercooling salt hydrate PCM ETS unit.

Lastly, sufficient thermal isolation must be employed to maintain external surface temperatures of a commercial ETS unit below 40 ˚C to ensure occupant safety (objective A in Section 2.2), comfort, and adequate thermal efficiency of the system. Ethylene propylene diene monomer (EPDM) elastomer foams are compatible and practicable within this range and widely available. EPDM foams can be used in direct contact up to 149 ˚C with hot flow network components, individual heat storage cells, as well as for lining the inside faces of cabinet panels exposed to indoor occupants (AeroflexUSA, 2016).

2.6.2 EXTERNAL HEAT EXCHANGE

Two separate external heat exchanges must be facilitated within the proposed ETS system: heat exchange between the circulated heat exchange fluid and the PCM enclosed in the individual heat storage cells via two heat exchange plates supplied per cell, and between the heat exchange fluid and the indoor air via a liquid-to-air heat exchanger. Due to the unique function and construction of the heat exchange plate pairs for each PCM heat storage cell, it is unlikely that commercial plate-and-frame heat exchange plates can be appropriated for this purpose, so a custom design should be explored. Off-the-shelf or modestly customized liquid-to-air heat exchangers, on the other hand, can be easily found and selected to suite the application well.

The heat exchange plate pairs used with each PCM heat storage cell fulfill objectives 9-11 and objectives E and H, either independently from other cells or in cooperation with them. Although industrial plate-and-frame designs are generated using complex, hybrids of flow directing patterns (i.e., generate turbulence at low Re) and proprietary computer-assisted design processes (Green et al., 2008), they are nonetheless founded in conventional heat exchange science and long-standing best practices. For instance, flow patterns in heat exchange plates fulfill any of three functions: generate local turbulence, distribute the flow evenly throughout the flow plate, and/or provide surface area enhancement.

Flow patterns providing a significant obstacle to unidirectional flow (short-circuited flow between inlet and outlets) generate local turbulence (i.e., vortex-generating) that results in increasing the fluid's convective heat transfer coefficient (Khoshvaght-Aliabadi, 2015). In this view, designing for tortuous flow should lead to optimal heat transfer design, but can be detracted by generating excessive pressure drop that leads to fluid channelling preferentially along the perimeter of the flow plate[29]. This type of channelling causes fluid flow to avoid accessing the bulk of the available surface area for heat transfer, reducing the overall heat-transfer rate. On the other hand, these same patterns, when situated on the heat exchange surface, also provide enhanced surface area benefits in the way of fin heat transfer. In this view, a greater population of small geometric fin entities would provide more benefit from fin heat transfer enhancements than would the same occupied volume of larger geometric fin entities.

Geometric entity shape, size, population, and distribution must all be coordinated to maximize the benefit to heat transfer from all three functions; parametric studies are therefore required and could result in many iterations. In an effort to reduce material prototyping, finite element method (FEM) computational tools were used to examine a set of potential heat-exchange plate designs and select the most promising design to implement in a prototype for experimental evaluation, as discussed in Section 4.5.

Regarding the design and selection of a suitable liquid-to-air heat exchanger, some parameters such as air flow rate, number of tubing passes (1 to 3 passes, Section 1.2.3), tubing size, and fin size and distribution are fixed for available designs and their effects are generally already characterized for the consideration of the purchaser over pre-defined ranges of heat exchange output and efficiencies. However, these heat exchangers can be found in two principal classes: axial or tangential fans.

Generally speaking, tangential fans (cross-flow fans) are the preferred embodiment for ETS technologies (including brick) due to their low-noise operation, uniform airflow distribution in comparison to axial fans (propeller fans), and unsurpassed compactness (sized radially and longitudinally instead of radially-only for axial fans). For selection in commercially sold ETS units, tangential fan liquid-to-air heat exchangers are

[29] Suppression of fluid flow channelling is likely the primary reason for the use of hybrid-patterns in industrial heat exchange plates.

recommended, however, axial fans can also be selected for reasons of availability or price in early prototype development since room heating performance and compactness need not be refined for use by customers.

2.6.3 HEAT EXCHANGE FLUID NETWORK

In the proposed ETS system, the heat exchange fluid network supports charging the PCM heat storage cells using a submerged electric heating element, discharging heat from the PCM heat storage cells, and supplying heat to the indoor environment via a liquid-to-air heat exchanger. In a fully functional ETS unit, the heat exchange fluid network would have the capacity to conduct PCM charging in parallel to direct air-heating (using supplied electric heat during off-peak periods) as well as conducting either of these functions separately, as demanded by the ETS unit's user and the current system conditions.

To do so in a controlled and reliable manner and to minimize complexity, the system must be closed-loop, and should consist of at least these components:

- Small sealed reservoir;
- Pump (preferably centrifugal for low noise and pressure, compact size, and simple, proportional motor control);
- Manual ball valves for isolation (maintenance and installation);
- Submerged electric heating element (preferably installed inline for optimum compactness);
- Actuated ball valves for function selection (e.g., PCM charging vs. direct air-heating)[30];
- Liquid-to-air heat exchanger combined with a compact and low-noise fan;
- Expansion tank;
- Thermocouples in the fluid streams (minimum three for function analysis in prototypes and minimum one for commercial products);
- Heater shut-off mechanism to prevent overheating (either due to low-flow or loss-of-fluid);

[30] These need only be for open-close service; proportionally actuated valves increase item cost, bulk, and control complexity.

- Pressure relief device downstream of pump and heater (objectives 2 and B, e.g., burst disc).

Note, however, that the pressure relief device can be omitted when using an open reservoir in ETS system prototype development. That configuration is not recommended for commercial ETS systems since open reservoirs risk leaking in transportation and suffer continual vapour losses, requiring regular intervention to operate the system.

As for the in-stream thermocouples, a minimum of one could be used in a commercial device since only the fluid supply temperature is required for operation (either to charge the PCM heat storage cells or for liquid-to-air heat exchange). Three or four could be used for detailed prototype performance evaluations in order to determine individual rates of heat transfer in the system at upstream and downstream positions in the fluid network. A flow meter is also necessary in the determination of heat-transfer rates in the heat transfer fluid network, but is not required in commercially ready devices.

2.6.4 MACHINABILITY/PROCESSABILITY

With the aim of producing a commercially viable supercooling PCM ETS technology, consideration must be given in the early stages of development to matters of mass-production. Highly specialized and complex parts as well as those made of material composites, tend to increase the cost and reduce the throughput of production in comparison with simple parts made of a single raw material.

The plastic structural components used in the fabrication of the PCM heat storage cells should be adaptable to high-volume moulding processes (injection or compression moulding), both the thermoplastic selection and overall shape and shape of its features. Regarding metallic components, emphasis is placed on reducing the amount of processing (resulting in material loss and consumption of labour and energy) needed to generate a part from bulk stock material (e.g., sheet or bar stock) and use of rapid and reliable processing methods (e.g., sawing and milling). Attempts must be made to minimize features generated from parts exclusively by milling, since milling has a tendency to produce high volumes of unusable scraps.

2.6.5 HEAT STORAGE CELL ASSEMBLY

As discussed in Section 2.6.4, simple, homogeneous raw materials are preferred in the construction of the structural components used to assemble the PCM heat storage cells on the basis of cost and throughputs. Additionally, regarding the heat storage cells only, welded, soldered, or brazed unions of metallic components in wetted contact with the SAT PCM are discouraged. All of these methods for joining metal parts to one-another cause inhomogeneities in the local metallurgy (whether by heat treatment, e.g., welding, or the introduction of a dissimilar filler material, e.g., solder), putting either the base material or the material joining the parts at risk of accelerated corrosion due to electrical contact of dissimilar metals in a concentrated electrolyte. However, with careful selection of the method and materials as well as conducting experimental validations of corrosion resistance, the risks associated with these methods can be mitigated and therefore employed in the manufacture of PCM heat storage cells.

Regarding the remainder of the PCM heat storage cell components, whether metallic or plastic/elastomeric, parts must be made smooth where wetted SAT PCM contact is expected. Polishing or filing might be necessary to eliminate any sources of surface irregularities. Surface irregularities, either crevices or protrusions, can risk trapping stable SAT seed crystals and exposing them to the bulk, supercooled PCM to cause accidental solidification and loss of the supercooled heat storage (objective 6).

Likewise, the means of joining all of the parts together that form the PCM heat storage cell must be robust under repeated heating and cooling cycles (thermal expansion) and maintain liquid and vapour tightness as well as maintaining stable contact junctions in order to prevent the retention of stable SAT seed crystals, risking release into the bulk PCM. Joining these parts using uniformly distributed compression is recommended as well as using polymeric/elastomeric gasket seals between wetted, dissimilar structural components. If installed with sufficient strain under compression, compressible gasket seals add margin to help resist leaks and excessive relaxation of contact areas during frequent thermal expansion/contraction.

2.6.6 MOVING PARTS

In general, moving parts should be minimized throughout the entire proposed ETS system in an effort to reduce the risk of active component failures and ensure lengthy

product service life without intervention (objective F in Section 2.2). Only active components essential to ETS system operation (including fluid network components listed in Section 2.6.3) and selected for their long service lives should be selected for use in the development of commercially viable ETS systems.

With the exception of the nucleation triggering devices integrated into the PCM heat storage cell design that are essential to generate the solidification reaction for heat discharge from the supercooled SAT PCM, moving parts in contact with the SAT PCM are strictly prohibited. As discussed in Section 2.5.2, straining and relaxation of rigid surfaces in wetted contact with the SAT PCM can inadvertently trap stable seed crystals and release them into the supercooled SAT solution and triggering solidification at undesirable times, defeating the function of the purpose-selected nucleation triggering devices. Therefore, to support their intended function (objective 6), all other cyclically varying mechanical contacts (especially from moving parts) must be eliminated.

2.6.7 MODULARITY

The desire for PCM heat storage cell modularity is expressed in objective 1 in Section 2.2, but how does it translate to improved design and performance of the heat storage cells? Bulk heat storage encapsulation tends often to be the default (Lane, 1985), and was subsequently chosen for implementation for supercooling heat storage using diluted SAT by H.M. Heizkörper (H.M.Heizkorper, 2012), but what is gained in low-cost of encapsulation[31] is lost in excessive complexity of heat exchange design (Lane, 1985). In the analysis of seasonal heat storage design for the Drake Landing Solar Community, Desgrosseilliers et al. (2014c) demonstrated there are significant advantages to modular, isolated heat storage masses, namely that they can result in improved heat storage charging dynamics, improved availability of readily usable heat storage, and preservation of heat storage during discharge (especially in regard to supercooling).

Charging dynamics and usable heat storage availability are equally affected by modularization: limiting the number of modules being actively charged with heat decreases their combined thermal mass in comparison to the whole system, therefore

[31] Bulk, cylindrical encapsulation has the lowest ratio of encapsulation area (directly proportional to the mass of structural materials) to internal volume of conventional bulk storage encapsulants, excluding bulk, spherical encapsulation due to impracticality and complexity of construction.

resulting in more rapid heating of the masses and making this energy input available at a higher temperature for useful heat transfer than would be achieved using the whole system. With respect to the preservation of heat storage during discharge operations, isolation of heat storage modules protects them from cascading solidification either due to intended or unintended nucleation triggering. Limiting the volumes of individual supercooling PCM heat storage cells by modularization also improves their resistances to spontaneous autonucleation of the supercooled PCM[32] as well as mitigates the risk of oversizing the heat storage capacities for the application. In the latter case, conservative undersizing increases the probability of complete, useful heat discharge after inducing solidification from nucleation triggering during typical operation of an ETS unit, since solidification forces the release of the chemically stored thermal energy (latent heat) whereby any remaining thermal energy becomes subject to idle heat loss.

Lastly, rectangular geometries are generally more apt for modularization than are other geometries. Rectangular prisms are the best geometries to stack well alongside one-another and be placed flush against flat surfaces without leaving any voids. Thin rectangular prisms also inherently provide larger ratios of heat transfer area to volume than do other geometries of equal volume and possess only one principal direction of heat diffusion, therefore benefiting heat transfer operations and simplifying heat transfer design of the heat storage cells. Consequently, small, thin rectangular prism PCM heat storage modules were chosen exclusively for the development of the proposed supercooling ETS system.

2.6.8 VAPOUR AND LIQUID SEALS

Objectives 12 and E in Section 2.2 make reference to the desire to operate commercially sold supercooling ETS units without significant intervention for the duration of the design life (≥ 10 y). To aid in doing so, the proposed design must safeguard against SAT PCM degradation and loss of heat transfer fluid. SAT is an inorganic PCM, therefore is generally not susceptible to thermal degradation, but it is however sensitive to changes in local and mean compositions. The aqueous PG heat transfer fluid, although susceptible to mild thermal degradation (Dow, 2003), would

[32] Autonucleation, as discussed in Section 1.2.1.2, is a function of volume, supercooling duration, and degree of supercooling, the limits of which can only be determined experimentally at present.

require mandatory intervention in the event of a sufficient loss of inventory[33] as this would result in a complete disablement of the ETS unit's heat transfer functions.

Mean composition stability of the supercooling SAT PCM is contingent on halting water vapour and liquid losses, both affecting the SAT mixture's maximum phase transition temperature and risk of anhydrous formation at high concentrations of SAT (approaching 58.0 mass% SA in water (Green, 1908)).

Vapour and liquid seals must be employed in the construction of the heat storage cells to ensure minimal water loss. Gaskets and films can be easily employed at static interfaces between components to prevent liquid and vapour losses, and can be further assisted using chemically inert and high-temperature resistant silicone rubber adhesive sealants. Chemically inert Teflon™ tape can be used to seal around threaded fitting junctions interfacing with the heat storage cells. For moving parts that engage with the SAT PCM mixture contained in the enclosure, elastomeric bellows seals should be employed.

To maintain adequate aqueous PG inventory during the ETS unit's design life, it is essential to employ the proper means of fluid network liquid and vapour sealing. Leak-tight fittings, either inherent to their design (e.g., gasketted or compression style fittings), or assisted by thread sealing using sealing pastes and Teflon™ thread tape are essential and must be verified during system commissioning.

Since compressed air can be used as a proxy for liquid vapours generated during use of supercooling PCM-based ETS units and because it is more challenging to ensure air-tightness vs. liquid-tightness[34], adequate air-tightness (measured as rate of depressurization) measured within the anticipated operating pressure range[35] will signal both adequate vapour and liquid tightness (e.g., < 10 kPa/d).

[33] Best practice for closed-circuit heat exchange fluids dictates using the minimum possible inventory in order to generate rapid thermal response to its heat sinks and sources.
[34] Liquid leaks are inhibited by capillary pressure resistance in small channels, whereby air and vapours are not.
[35] Excessive pressurization during air-tightness testing can risk damaging components, therefore care must be exercised to limit the extent of pressurization.

2.7 CONCLUSION

Chapter 2 has presented detailed elaborations of the supercooling heat storage cell and supercooling ETS system design criteria, as well as the selection and characterization of the supercooling diluted SAT PCM, and selection of the PG-water based closed-loop heat transfer fluid (HTF), as summarized in Table 2-3.

Material compatibility examinations stemming from the PCM and heat transfer fluid selections, further constrained by the detailed design criteria have generated lists of suitable material candidates. Type 300 stainless steels and high-temperature thermoplastics as well as high-temperature silicone rubber gasket seals are universally suitable for use in the proposed heat storage cell and ETS system designs, while aluminum, copper and brass can only be used with care to isolate them from the supercooling SAT PCM contained within the cells as well as avoiding any dissimilar metal junctions in wetted systems (either heat transfer fluid or PCM).

The operating temperature limit was established from the heat transfer fluid selection in Section 2.4 as being the limiting factor affecting the ability to fulfill design objective 2, needed to avoid mandatory ASME BPV code certification in most jurisdictions. Additional safety margin was nonetheless desired for all structural and fluid network components, therefore requiring that only robust components be selected.

Design philosophies regarding component manufacturing, modularity, external heat transfer, reductions of complexity and moving parts, and nucleation triggering mechanisms were also established to guide the detailed designs put forward in Chapters 3 and 4 in order to mitigate risks in developing supercooling PCM heat storage technology that is useful for indoor heating integration.

Table 2-3: Summary of design strategies required to address the design objectives in Section 2.2.

Objective(s)	Description	Strategy
1	Heat storage cell modularity	Rectangular prism geometry chosen
2/B	Internal pressure < 2 atm (PCM and HTF)	-PCM: 1:1 SAT in water maintained ≤ 110 ˚C -HTF: 75 mass% PG in water maintained ≤ 112 ˚C and protected by burst disc
3	Useful heat discharge from PCM ≥ 28 ˚C	-SAT selected as salt hydrate PCM. Made of abundant constituent atoms, safe, and supercools to as low as -50 ˚C. -Phase change occurs to a maximum of 58 ˚C (55 ˚C for 1:1 SAT in water). Retains 40 % of heat when supercooled to 20 ˚C -Heat storage cells assembled without crevices or cyclically strained contacts capable of retaining SAT seed crystals
4	Abundant, low-cost, and safe supercooling salt hydrate PCM	
5	Supercooling retains ≥ 40 % of stored heat	
6	PCM reliably supercools to 20 ˚C for seasonal durations	
7	Reliable on-demand heat release from supercooled state	Internal, linearly actuated, ‘activated’, metal extension spring nucleation trigger selected.
8	Total PCM heat storage ≥ 400 kJ/kg	Net heat storage between 425 kJ/kg and 449 kJ/kg for 1:1 SAT in water from 20 ˚C to 110 ˚C
9/H	Heat storage cells achieve full charge << 7 h	Heat storage cells include two integrated heat-exchange plates sized for their PCM capacities
10	Nominal heat transfer coefficient > 30 W m^{-2} K^{-1} (charge/discharge)	Use raised geometric entities in the design of the heat exchange plate HTF flow channel
11/E	Nominal heat discharge power ≥ 600 W	Balance cell heat transfer area, number of cells operating in parallel and liquid-to-air heat exchanger to deliver heat load
12/F	Design life ≥ 10 y for commercial units	-Dilute SAT 1:1 in excess water -Vapour and liquid-sealed heat storage cells and flow network -Use type 300 series stainless steels to mitigate corrosion from PCM or use film-protected aluminum -Use only silicone rubber gaskets throughout
13	Heat storage cell structural materials occupy ≤ 20 vol%	Discussed in Chapter 3
A	External surface temperature of ETS units ≤ 40 ˚C	EPDM foam insulation used on all hot components
C	Total mass ≤ 30 kg	Discussed in Chapters 3 & 4
D	ETS unit generates noise ≤ 54 dB(A)	Use tangential fan for liquid-to-air heat exchanger
G	ETS unit functions using 120 V and max 12.5 A for use in North America	Discussed in Chapter 4

CHAPTER 3: ENCLOSURE DESIGN

3.1 INTRODUCTION

This chapter elaborates on the incremental design and evaluation of the heat storage cells used in the course of the project to achieve the remaining design objectives stated in Section 2.2. Namely, these designs were intended to address aspects of objectives 1, 6, 7, 9, 13, C, and H, with C and H also addressed further in Chapter 4.

3.2 ENCLOSURE VERSIONS

During the course of the project, three incremental designs were developed, each intended to independently validate essential features, leading from a rudimentary design (Mark I) to subsequent heat storage cells integrated with their heat-exchange plates (Marks II and III) and the balance-of-system to form together a component integration prototype ETS. The stages of development and design features are detailed in the following sections, each design designated by its sequential 'Mark' name. The respective technical drawings can all be found in Appendices A to C. Furthermore, since all heat storage cell iterations and their respective components were custom-made in small quantities only, all components developed for this project were fabricated by means of conventional machining as well as computerized numerical control (CNC) milling where appropriate.

3.2.1 MARK I

3.2.1.1 BASE CONSTRUCTION

Mark I, the first embodiment of the design principles devised in this project and discussed in Chapter 2, had to be executed cautiously and made purposefully incomplete, since heat exchange plates were excluded at this stage of development. Instead, the Mark I design included a sight-glass (in place of one of the heat exchange plates) through which to conduct internal visual observations of the phase-change processes, supercooling, and nucleation triggering. Additionally, visual observations conducted through the sight-glass served to further assess the chemical compatibilities of the materials of construction with the enclosed SAT PCM.

Consequently, the Mark I heat storage cell could not facilitate heat exchange with externally circulated liquid heat-transfer fluids (HTF), and therefore could only function

to produce phase-change in a temperature-controlled air-environment, namely using a thermally controlled environmental chamber capable of both heating and cooling.

The Mark I heat storage cell embodied the fundamental design features selected to produce a compact, modular, plate-and-frame type heat storage cell. Figure 3-1 depicts the underlying structure ('base') to the heat storage cell design, shared also with Marks II and III. The heat storage cell base was constructed of polypropylene (PP) to resist chemical degradation from SAT PCM exposure, resist excessive softening at moderately high temperatures, and also selected for suitability for high-volume thermoplastic production methods (e.g., injection and compression moulding) as well as for its relatively low cost[36].

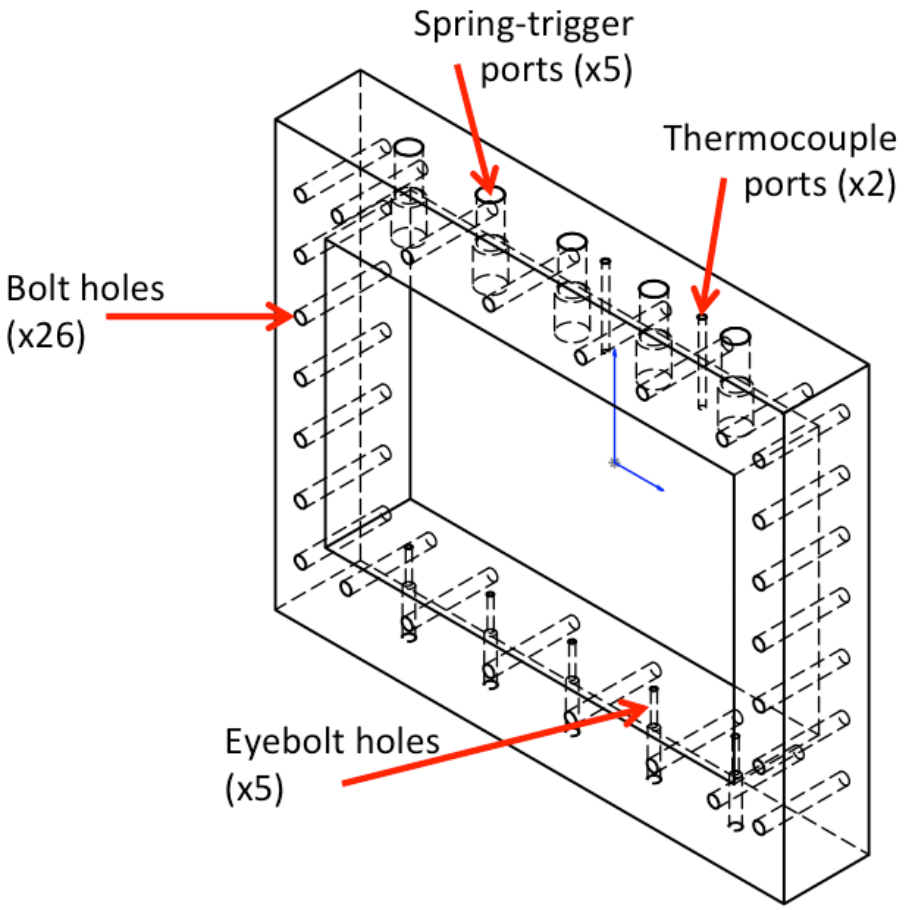

Figure 3-1: Mark I heat storage cell base perspective and transparent wire-frame view.

[36] Polyolefins (most commonly polyethylene and polypropylene) are simple and common commodity polymers, used widely in bottle and film packaging (Ashby, 2013).

The heat storage cell base size was kept consistent throughout all iterations, nominally measuring 254 mm × 304.8 mm × 50.8 mm (height×width×depth) externally, with internal dimensions of 160 mm × 244.8 mm × 50.8 mm yielding a volume of 1.99 L. These dimensions were selected on the basis of occupying a small module area (~ 1 ft^2 per lateral face) combined with > 1 kg of PCM capacity, and raw material availability[37] from which to fabricate the base. The detailed dimensions can be found in Appendix A.

With consistent internal volumes, Marks I-III heat storage cells contained approximately 2.4 kg of SAT PCM, capable of storing 1.1 MJ (0.31 kWh) between 20 ˚C and 110 ˚C. Respecting objective 13 in Section 2.2, the SAT PCM cavity in all of the heat storage cell bases developed for this project (i.e., Marks I to III) occupied 51 % of the total enclosure volume (excluding heat-exchange plate assemblies). This corresponded to a heat storage cell void fraction (non-SAT PCM volume fraction, excluding the heat-exchange plate assemblies) of 49 % for Marks I to III, exceeding the desired ≤ 20 vol% occupied by heat storage cell base structural materials stated in objective 13. However, since the structural material fraction used in the heat storage cell bases depends on the rectangular base aspect ratio (i.e., width to height), heat storage cell capacity and heat exchange design must precede structural material optimization. For example, a heat storage cell double the width of Mark I and preserving the wall thicknesses used in Mark I would result in a base structural material fraction of 42 %. Therefore, structural material optimization (i.e., minimization) was not prioritized in this project.

The design of the heat storage cell base shown in Figure 3-1 was rectangular for modularity, but consisted only of the perimeter walls for structure, resembling an ‘open picture-frame’. While thermoplastics are preferred for chemical resistance to the SAT PCM, the two largest faces of the base were left unobstructed by the base (‘open picture-frame’) to facilitate the placement of metal or thin film heat-exchange surfaces in intimate contact with the PCM in order to minimize resistance to heat transfer due to structural materials. However, aside from these heat exchange surfaces, increased resistance to heat transfer is desired to reduce external heat losses, for which thermoplastics are preferred to metals, therefore defining the ‘open picture-frame’

[37] PP sheet-stock was ordered from McMaster.com, from which orders could only be placed in increments of 12” per side (excluding thickness).

geometry of base. The 'open picture-frame' base design was also necessary for the fabrication of the interior details of the Mark I base and its subsequent iterations.

3.2.1.2 HEAT STORAGE CELL ASSEMBLY

In all of the subsequent iterations, the base was designed to unite and align the heat-exchange plates and their gasket-seals to collectively define the heat storage cell module assembly as well as the internal cavity (i.e., rectangular void space inside the base) to house the SAT PCM. However, in the case of Mark I, the base was instead used to unite a 1/2" (12.7 mm) thick polycarbonate (PC) sight-glass to cover one open face and a laminated polyethylene/aluminum/nylon ($35/40/29 \times 10^{-6}$ m thick layers, respectively (Targray, 2012), henceforth called 'aluminized film') barrier-film[38] supported by a rigid aluminum perimeter plate to cover the remaining face and enclose the SAT PCM within the assembly, shown in Figure 3-2 and Figure 3-3. The PC sight-glass was sealed against the base using a 1/16" (1.6 mm) thick compressible silicone rubber gasket (hand-cut using a carpet knife), whereas the aluminized film was used to seal the opposite face as well as contain the PCM. The aluminized film used in the Mark I heat storage cell design was intended to be used as the sole heat transfer surface in direct contact with flowing HTF, due to its chemical inertness to the SAT PCM and HTF as well as its very thin construction (i.e., low thermal resistance) and heat-spreading abilities (Desgrosseilliers et al., 2013b; Desgrosseilliers et al., 2014a; Desgrosseilliers et al., 2014b; Desgrosseilliers et al., 2016). This proved useful for the operation of Mark I inside a temperature-controlled chamber, but was substituted in the subsequent designs with a rigid metal plate for improved structural integrity and dimensional stability.

[38] The aluminized film used in this project is commonly sold as Li-ion pouch cell, heat sealable film (Targray, 2012).

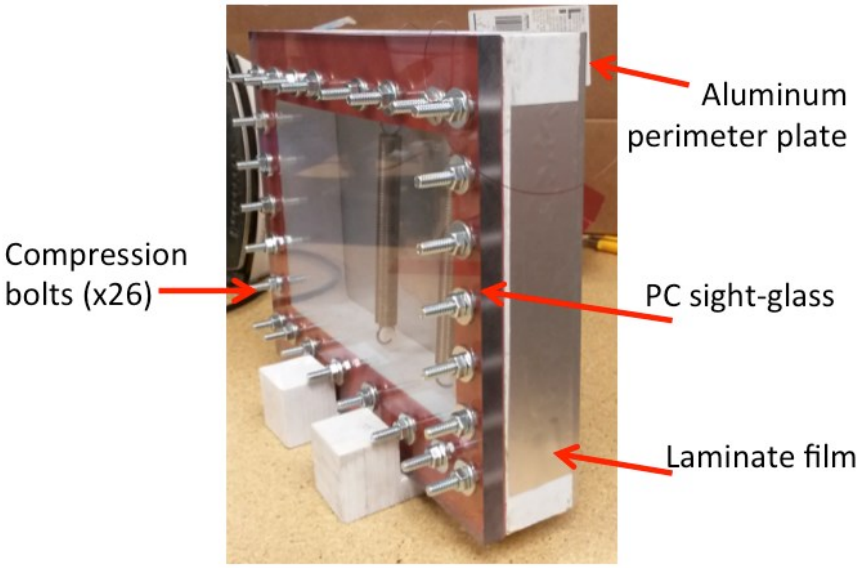

Figure 3-2: Mark I heat storage cell assembly showing the end-plate features and bolt compression.

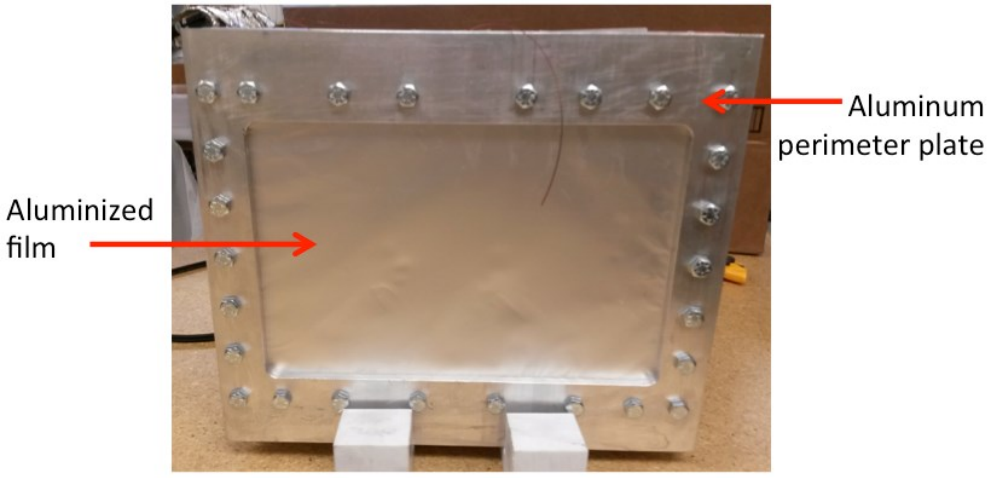

Figure 3-3: Mark I heat storage cell design showing the aluminized film supported by the aluminum perimeter plate.

As was shown in Figure 3-1, the Mark I base was equipped with bolt-holes distributed throughout the entire perimeter, thermocouple and spring-nucleation trigger ports passing through the top of the base, as well as tapped holes at the bottom in which to secure eyebolts. The bolt holes were distributed along the perimeter and bolts (shown in Figure 3-2 and Figure 3-3) were used to apply a uniform compression force to combine the heat storage cell components together in a liquid and vapour-tight seal. Note that the bolt holes were located in such a way to isolate the bolts from the PCM contained within the heat storage cell, and therefore did not require selection for corrosion resistance. The

thermocouple ports consisted of tapped holes to accommodate compression fittings used to support the thermocouple probes (T-type, 316 stainless steel sheathed model TMTSS-062U-12 probes from Omega Engineering Inc.) suspended in the PCM cavity. Spring-nucleation trigger ports were also located at the top of the base to accommodate the passage of linear actuators used to exert tension on the spring-nucleation triggers submerged in the SAT PCM. The tapped holes at the bottom of the base, centered with the spring-nucleation trigger ports above, were used to secure nylon eyebolts to the bottom of the base (item 9686T71 on McMaster.com), selected to form a soft seal against the PP base and to chemically resist the SAT PCM.

The base was designed to operate in the upright orientation shown in Figure 3-1. With the exception of the eyebolts threaded into its bottom, the base was kept free of perforations through its perimeter on all three sides that would be permanently wetted by the SAT PCM in order to minimize opportunity for leaks. The surfaces on all faces forming the PCM cavity were also made smooth to minimize opportunity to trap SAT PCM seed crystals that would risk inadvertently triggering nucleation. On the top side of the Mark I base, however, the spring-nucleation trigger ports were left unsealed.

Figure 3-4 shows the assembled Mark I heat storage cell left empty of PCM. Consistent throughout all iterations, the nucleation-triggering mechanism visible in Figure 3-4 consisted of type 302 stainless steel extension springs positioned vertically inside the PCM cavity and actuated from overhead by pull-action, direct-current (DC) solenoids, while remaining anchored to the bottom of the base. Furthermore, all designs used in this research employed machined PP cylinders (called pegs, see Figure A- 7 in Appendix A) to assist solenoid actuation by coupling their actuator shafts to the upper ends of the springs, extending into the PCM cavity where the actuators could not.

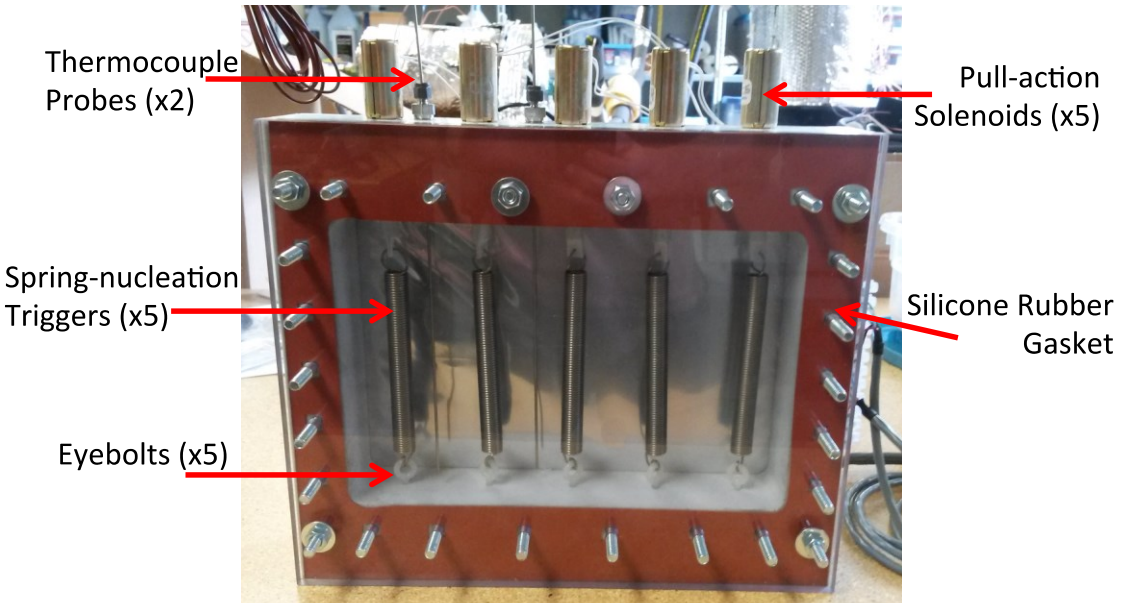

Figure 3-4: Mark I heat storage cell component assembly showing thermocouple probes, pull-action solenoids connected to spring-nucleation triggers via their respective pegs, and red silicone rubber gasket seal.

The particular spring-nucleation trigger arrangement used in Mark I relied on the bottom-secured nylon eyebolts to provide vertical support to the extension springs as well as to constrain the lower ends of the springs in order to generate displacement from the tension applied by the solenoids overhead. The pegs extending from the top of the springs and through the top of the base loosely constrained the spring movement laterally so that they would remain aligned with the solenoid actuators. The bottom spring-ends were connected to the eyebolts by crimping the spring wire end around the eyebolt, while their top ends were joined to the pegs by simply passing the wire loop end through a small hole. The solenoid actuator shafts were connected to the top ends of the pegs via plastic dowel pins passing through their mutually aligned holes.

Five equidistant nucleation-spring triggers were used in the Mark I design to evaluate the triggering dynamics of the SAT PCM using varied arrangements (one, two, three, or five) of simultaneously actuated spring-triggers to inform better selection of spring-trigger distribution in the subsequent designs. To do so, each solenoid actuator was wired independently for the Mark I design. Due to the special constraints generated by housing five spring-triggers in the Mark I base, only compact, tubular pull-action solenoids could be used (12 V DC, model LT6x 12-I-12 by Guardian Electric Manufacturing Co.).

Type 302 stainless steel spring-triggers, 5” long, with an outside diameter of 0.5” OD, and 0.055” wire diameter (item 9065K435 on McMaster.com), were used in the Mark I design due to their suitable length and lower threshold load (4.63 N (McMasterCarr, 2016b)) for displacement for actuation by the tubular solenoids. Note that due to the fixed positions of the springs and their respective solenoids, their respective PP pegs were individually custom-made to provide adequate insertion of the actuator shafts into the solenoids at rest.

Prior to complete assembly and filling the heat storage cell with fully dissolved SAT PCM, the spring-triggers were ‘activated’ (recall Section 2.5.2) by repeatedly extending and returning the springs to their rest positions against a bed of pure, solid SAT. This activation procedure was also used for the spring-triggers in Marks II and III.

3.2.2 MARK II

The Mark II heat storage cell, although similar to the Mark I design, adopted a few improvements identified from the evaluations of Mark I (revealed in detail in Section 3.3) and incorporated heat exchange plates into the heat storage cell design in order to be operated within a simulated ETS system. The Mark II heat storage cell base is shown in Figure 3-5.

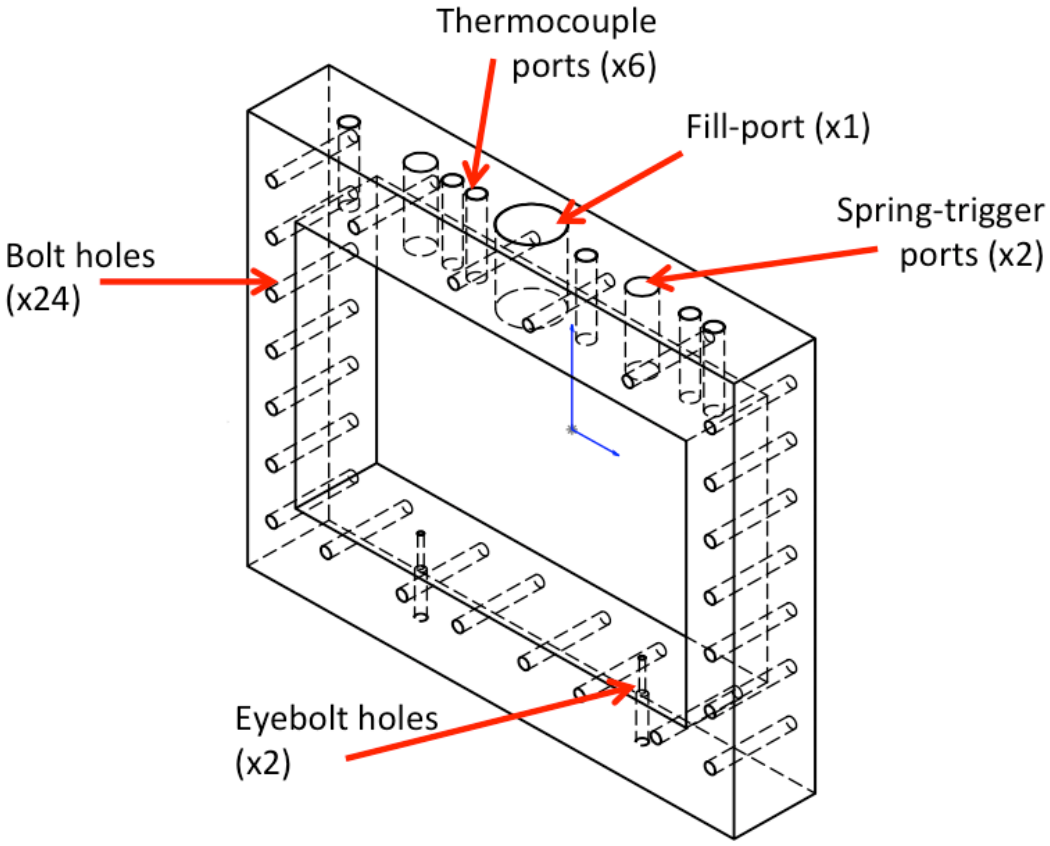

Figure 3-5: Mark II heat storage cell base perspective and transparent wire-frame view.

Of note to Mark II, the base shown in Figure 3-5 accommodated only two spring-nucleation triggers while increasing the thermocouple probe count from two in Mark I to six and adding a separate fill-port through which to load the fully dissolved SAT PCM into the heat storage cell cavity[39]. After loading the PCM, the fill port was sealed using a plastic, threaded cap-plug. The additional thermocouples used in Mark II were arranged inside the PCM cavity to examine the SAT PCM's horizontal and vertical temperature distributions during operation, by distributing pairs of lower-level ('bottom'), mid-height ('middle'), and upper-level ('top') thermocouple probes throughout the length of the cavity (Figure 3-6).

[39] PCM filling in Mark I was conducted through the thermocouple ports with one removed during the filling process.

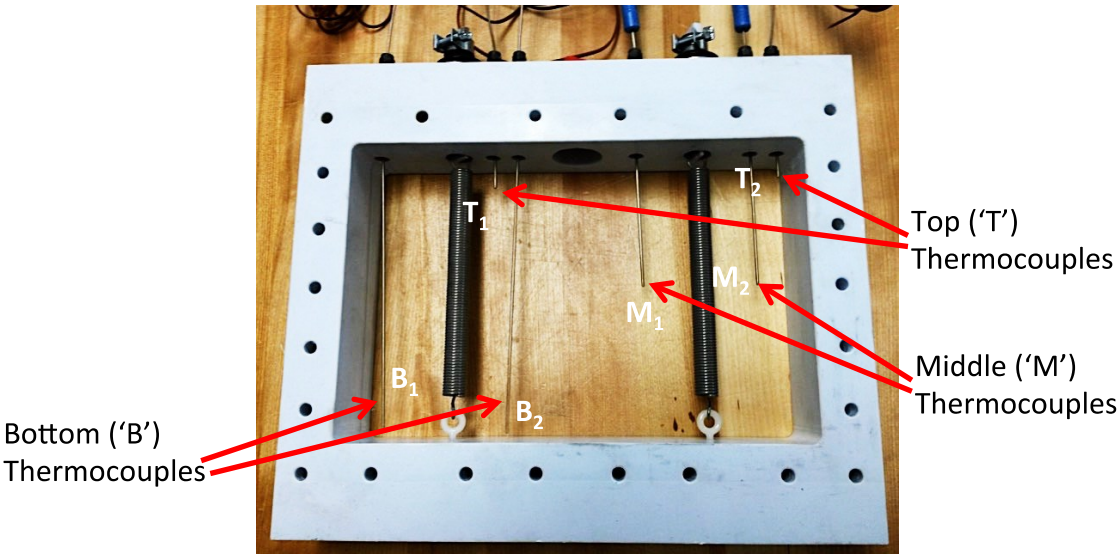

Figure 3-6: Mark II base showing thermocouple pair locations.

Regarding the two spring-nucleation triggers that remained in the Mark II base, improvements were also made to the assembly of the PP peg union with the solenoid actuator shafts and the tops of the spring-nucleation triggers. Figure 3-7 shows the details of the sealing mechanism used with the PP peg union assembly, whereby the PP peg was permitted to extend beyond the top of the base in order to seal it using a flexible neoprene bellows (item on 5298K79 McMaster.com) in an effort to prevent vapour loss from the PCM cavity and to isolate the solenoid actuators from the PCM liquid and vapours. The seal is maintained around the PP peg using a bolt-clamp to compress the bellows collar to the PP peg, while sealing the bellows' flange-end to the base using an aluminum compression ring and machine screws.

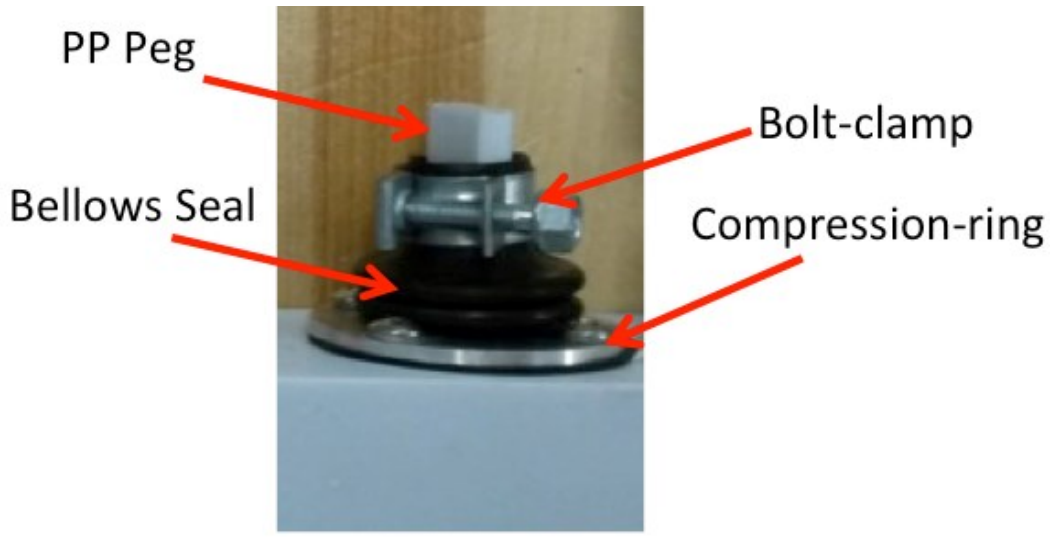

Figure 3-7: Detail of the bellows seal around the PP Peg in Mark II.

The solenoid actuators, made larger and more powerful due to the improved spacing on the Mark II base, were linked to the tops of the PP pegs using clevis pins restrained by cotter pins to connect to their actuator shafts. In order to alleviate the problem of individual length tolerances on each custom PP peg used in Mark I, Mark II instead uses height adjustable stands (pictured in Figure 3-8) attached to the solenoid bodies to suspend them over top their respective PP pegs (Figure B- 8 in Appendix B). The selected pull-action solenoids were 24 V DC box-solenoids by Magnet-Schultz of America Inc. (item 70155K5 on McMaster.com).

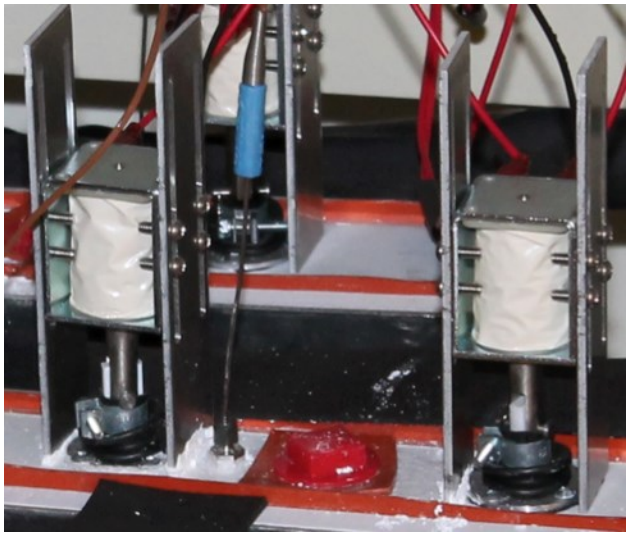

Figure 3-8: Solenoid actuators suspended over their respective bellows sealed PP pegs. The solenoids were vertically positioned along slotted aluminum plates on either side and affixed using machine screws.

The selected extension springs were also stronger (item 94135K36 on McMaster.com) in Mark II than they were in Mark I, requiring a minimum load of 17.1 N to begin displacement (McMasterCarr, 2016a) instead of only 4.63 N (McMasterCarr, 2016b). The selected extension springs were 6” long, had an outside diameter of 0.5”, and had a wire diameter of 0.068”. Springs with high pre-loading (i.e., minimum load to generate displacement) are generally preferred since they can better assure seed crystal retention by generating higher contact pressures, and springs with high spring constants provide resistance to lateral flexure (risking the exposure of seed crystals in the supercooled PCM) caused by impacts to the ETS device experienced during normal operation. The bottom spring-ends in Mark II were linked to the supporting eyebolts in the same manner as they were done in Mark I, shown in Figure 3-9.

Figure 3-9: Close-up view of the crimped spring-wire attachment used to secure spring-bottoms to the eyebolts in Marks I and II.

The Mark II heat storage cell assembly incorporated two flow-plate assemblies on either side of the open picture-frame faces of the base. The flow-plate assemblies (one pair shown in Figure 3-10) consisted of an outer, thermally insulating PP plate and an inner, thermally conductive aluminum plate. The two plates cooperatively formed an HTF channel, contained between the flat inner face of the PP plate and the embossed and patterned face of the aluminum flow-plate. HTF was introduced into this channel via the inlet port on the lower corner of the PP plate and exiting (after once diagonally traversing

the patterned flow channel) via the outlet port on the upper corner of the PP plate (illustrated in Figure 3-10). The pair not shown in Figure 3-10 was located on the opposite side of the base, but with the flow ports in the PP plate identically oriented towards the front and rear of the base to promote uniform heat transfer inside the PCM cavity (i.e., heat transfer symmetry). Out of concern for the structural integrity of the PP plate at elevated temperature, a thin aluminum plate was also added to the outer face of the PP plate to increase stiffness during operation (Figure B- 7 in Appendix B).

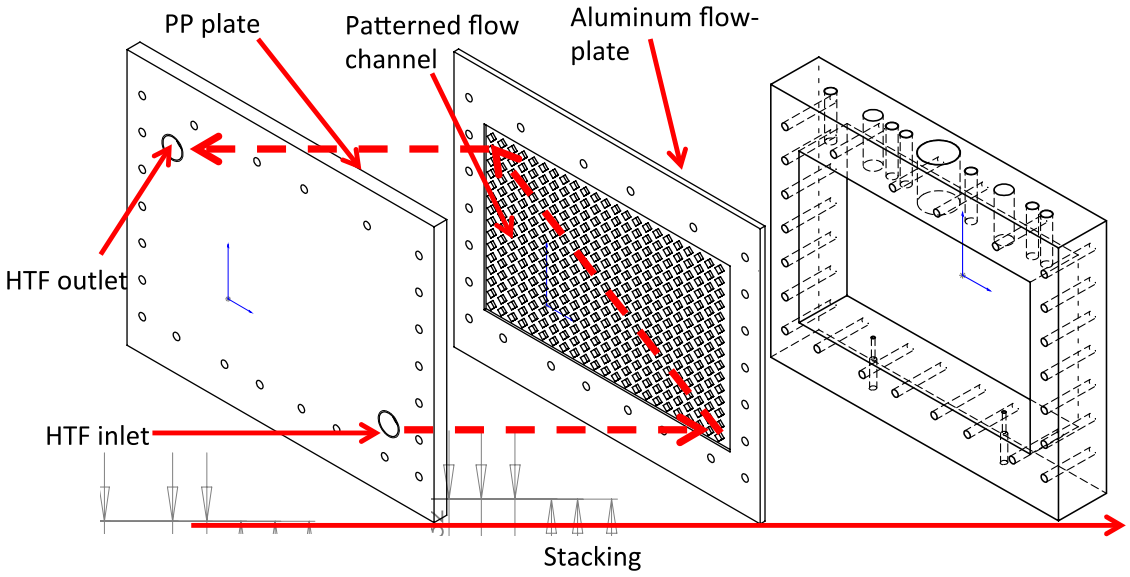

Figure 3-10: View of Mark II heat-exchange plate stacking order on one side of the base. The dashed lines are added to illustrate the direction of HTF flow.

Not shown in Figure 3-10, but shown later for Mark III in Section 3.2.3, are the gasket seal and the aluminized film seal. The two flow plates were sealed together to form the flow channel using a compressible, 1/16" (1.6 mm) thick silicone rubber gasket, hand-cut to form a perimeter-seal around the embossed patterned area of the aluminum flow-plate. Since the aluminum plate was chemically incompatible, but still a low-cost and highly thermally conductive alternative to stainless steel, the thin aluminized barrier-film was used to cover the exposed surface area on the PCM-side of the aluminum flow-plate to isolate the aluminum from the corrosive SAT PCM and seal the assembly to the base. However, a suitable method for adhering the aluminized film to the aluminum flow-

plate could not be identified or demonstrated[40], therefore the two components could not be assembled in a way such that optimum thermal contact could be ensured. Only a flush placement during assembly and the hydrostatic fluid pressure from the PCM inside the heat storage cell could contribute to the improvement of thermal contact between the aluminized film and the aluminum flow plate, albeit non-systematically.

3.2.3 MARK III

The Mark III heat storage cell design shown in Figure 3-11 only improved slightly on the design of Mark II (with everything else remaining the same) and was intended to be the first design step towards developing commercially ready heat storage cells. The principal improvements incorporated into the base were the spring-tabs integrated into the bottom of the base and the two side-entering HTF inlets with respective flow channels traversing the base, each one to supply the heat exchange plates located on either side of the base. The spring-tabs (Figure 3-12) were developed to improve the leak-tightness of the Mark III base with respect to the SAT PCM by removing the only perforations through the base below the top-level. HTF inlets in the Mark III base as well as the respective channels traversing the length of the base below the PCM cavity (then turning 90 ° to supply HTF flow to the respective heat exchange plates) were incorporated into the Mark III design to alleviate poor heat transfer otherwise associated with the PCM usually remaining at the bottom of the heat storage cell during the charging process. A moderate, but precisely directed heat supply to the bottom of the base should accelerate the overall phase-change process during charging and hasten the transition of the last remnants of solid SAT PCM sinking to the bottom of the cavity. Dual-channels were chosen simply to improve heat transfer uniformity at the bottom of the base, closest to the mid-line, while taking advantage of heat transfer symmetry.

[40] Heat sealing the polyethylene layer of the film to the aluminum plate was attempted using a hot, electric clothes iron but did not produce adequate adhesion of the film to the plate.

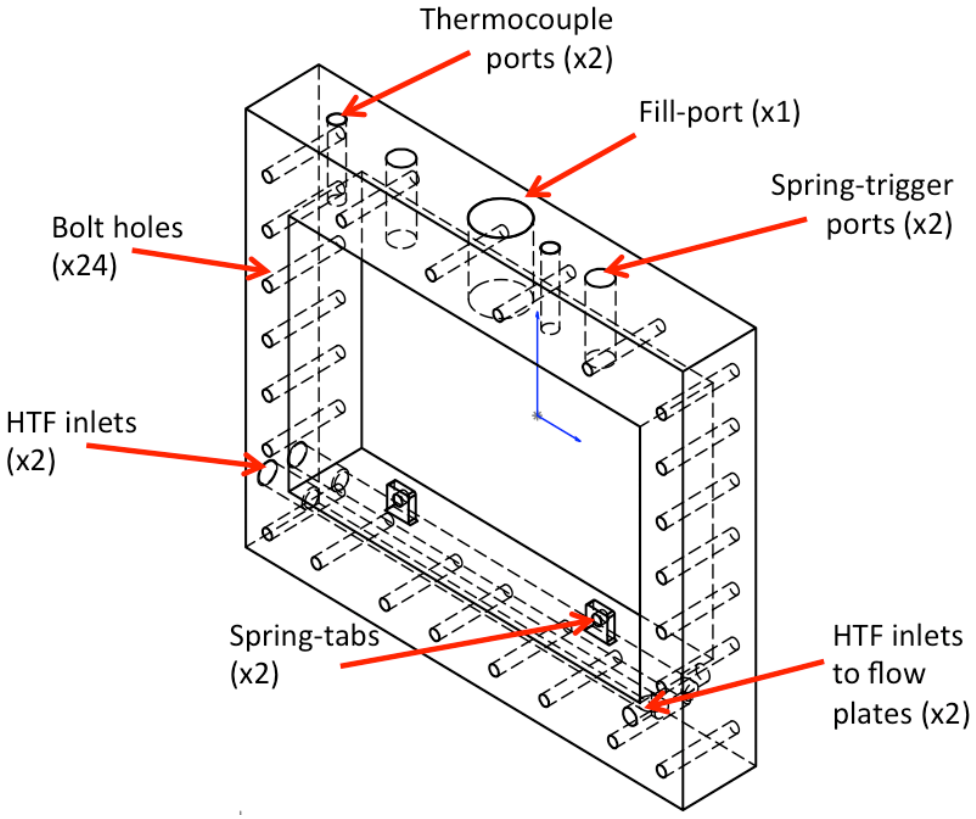

Figure 3-11: Mark III heat storage cell base perspective and transparent wire-frame view.

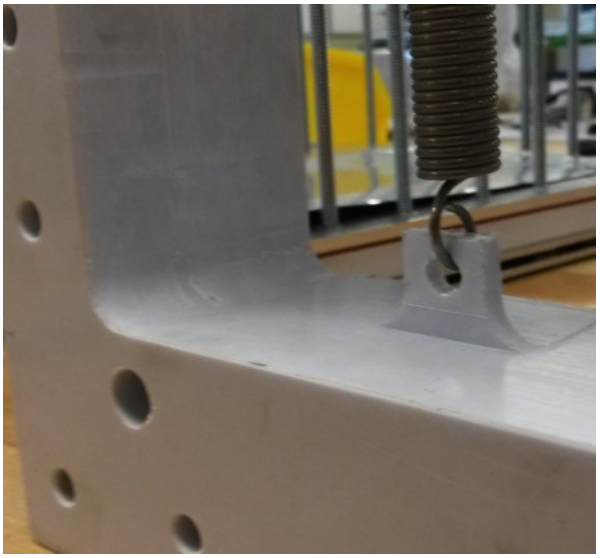

Figure 3-12: Close-up of one of Mark III's base-integrated spring-tab and crimped spring bottom-wire.

Only two thermocouples were employed in the Mark III heat storage cell in an effort to begin minimizing components and monitoring devices. Figure 3-13 shows the locations of the two thermocouples inside the Mark III base. However, at least two

Mark III bases were fabricated with the bottom HTF channel orientation opposite the one shown in Figure 3-13 and their top thermocouples ('T') were later substituted with middle ('M') thermocouples.

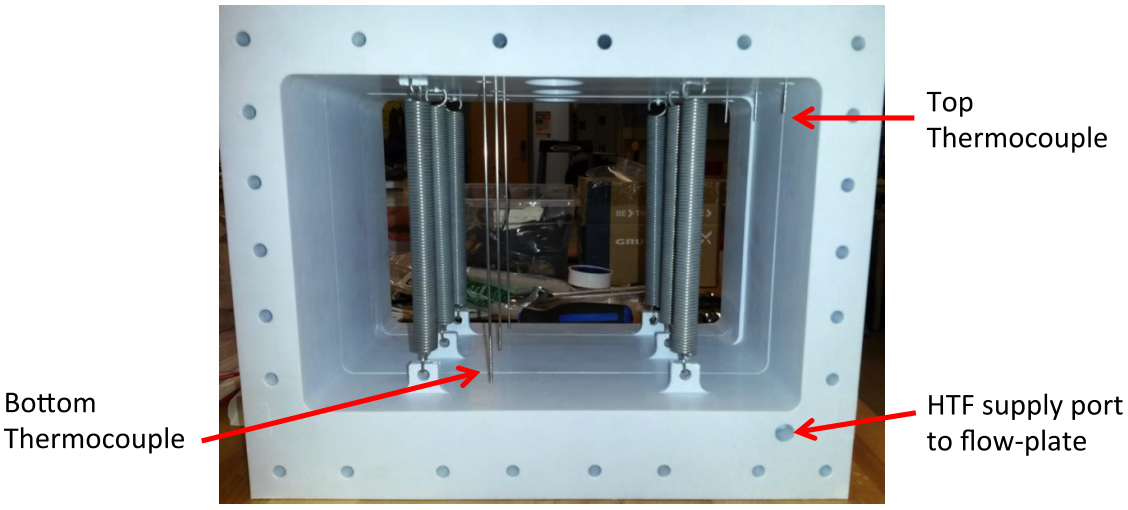

Figure 3-13: View of the thermocouple locations inside the Mark III PCM cavity (3 bases shown in series).

Regarding heat storage cell assembly, the arrangement was equivalent to that of the Mark II, but with PP plates, gaskets, and aluminum flow-plates designed to integrate with the internal HTF flow channels of the Mark III base. Figure 3-14 illustrates their stacking arrangement (excluding the silicone rubber gasket and aluminized barrier film) and also shows the direction of HTF flow from inlet in the base to outlet in the PP plate.

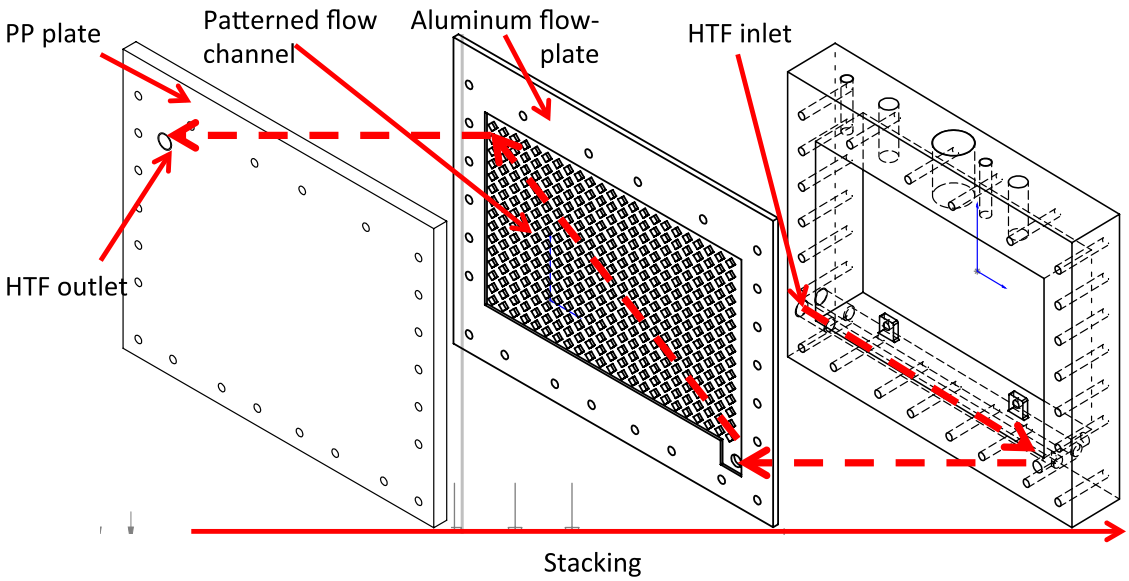

Figure 3-14: View of Mark III heat-exchange plate stacking order on one side of the base. The dashed lines are added to illustrate the direction of HTF flow.

The silicone rubber gaskets and aluminized barrier films used to isolate the aluminum flow-plates from the SAT PCM are shown in detail in Figure 3-15 and Figure 3-16. Note the necessity for each one to permit the passage of HTF from the Mark III base to the adjacent heat exchange plate assemblies, but remain sealed and isolated from the PCM contained in the heat storage cell cavity.

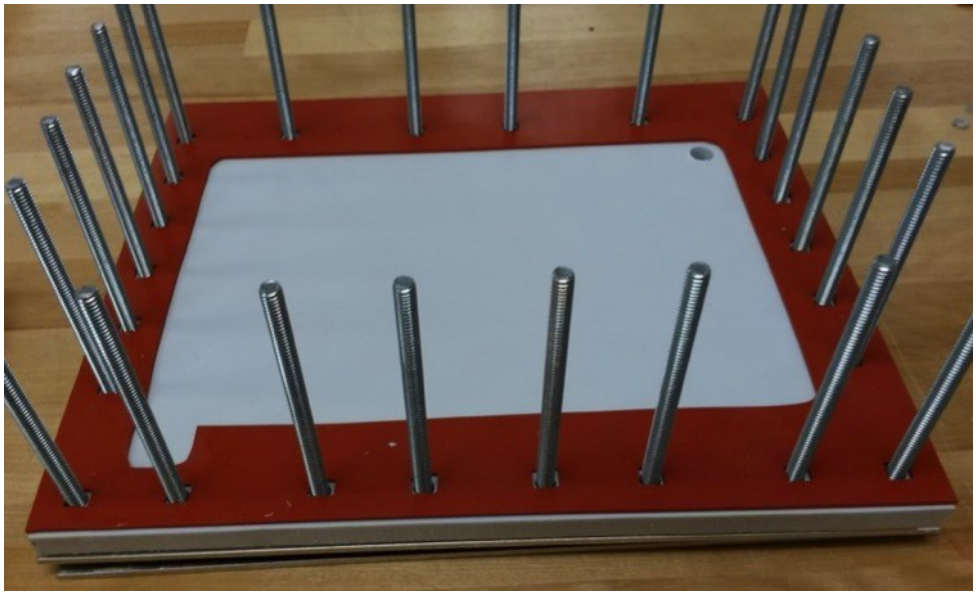

Figure 3-15: Inside-facing view of the PP plate assembled with the silicone rubber gasket.

Figure 3-16: Inside-facing view of the complete heat exchange plate assembly for Mark III, showing the aluminized barrier film used to isolate the aluminum flow plate from the SAT PCM.

Just as for the Mark II heat storage cell assemblies, the Mark III assemblies also included additional aluminum end-plates for added stiffness to the PP plate during operation at elevated temperature. This is shown in the profile view of the heat exchange assembly in Figure 3-17.

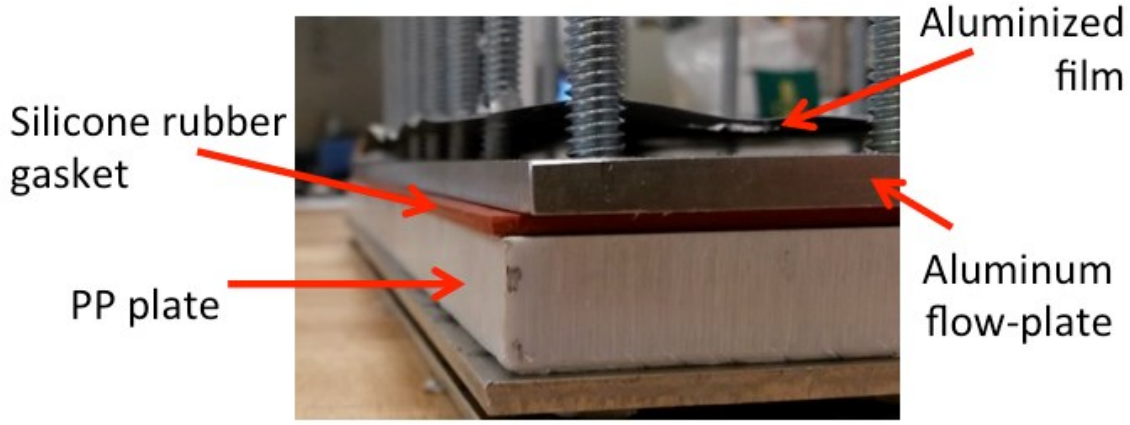

Figure 3-17: Profile-view of the stacked heat exchange assembly shown in Figure 3-16.

3.3 ENCLOSURE EVALUATIONS

Experiments were devised to characterize and evaluate the internal phase-change process, supercooling, and reliable nucleation triggering. The design features incorporated into the individual heat storage cell designs (Marks I to III) were also

assessed for their success to support their function for housing the SAT PCM and facilitating the exchange of heat.

3.3.1 EXPERIMENTAL METHODS

Details of the experimental designs, procedures, and their constituent instruments, components, and equipment are found in these next sections.

3.3.1.1 MARK I PHASE-CHANGE EVALUATIONS

Just one Mark I heat storage cell was produced, however, an incomplete assembly was briefly used for set-up purposes (having only two springs instead of five and not having the tubular solenoids installed). Mark I was fabricated for the purposes of observing the internal phase-change process, confirm the ability to supercool the SAT PCM inside the heat storage cell, and to test whether nucleation could be triggered successfully, as well as explore varied arrangements of the spring-nucleation triggers.

Phase-change experiments were conducted inside an Associated Environmental Systems model ZBHD-205 temperature-controlled environmental chamber, capable of both heating and cooling between -65 ˚C and 200 ˚C. The Mark I heat storage cell was placed inside the environmental chamber on machined PP supports to maintain it upright and was positioned to have the PC sight-glass facing the windowed door of the chamber (Figure 3-18). The heat storage cell's thermocouple wires were passed through the chamber's built-in cable port, through which a third thermocouple wire was also passed to introduce a bare T-type thermocouple into the chamber to sample the air temperature during operation. Outside the environmental chamber, the three thermocouple wires were each connected to a National Instruments (NI) model 9211 4-channel thermocouple module installed in a model 9174 compact DAQ 4-slot chassis for data logging in LabView 2015. During chamber operation, the solenoid cables remained disconnected from the controller and power supply and stowed inside the thermal chamber.

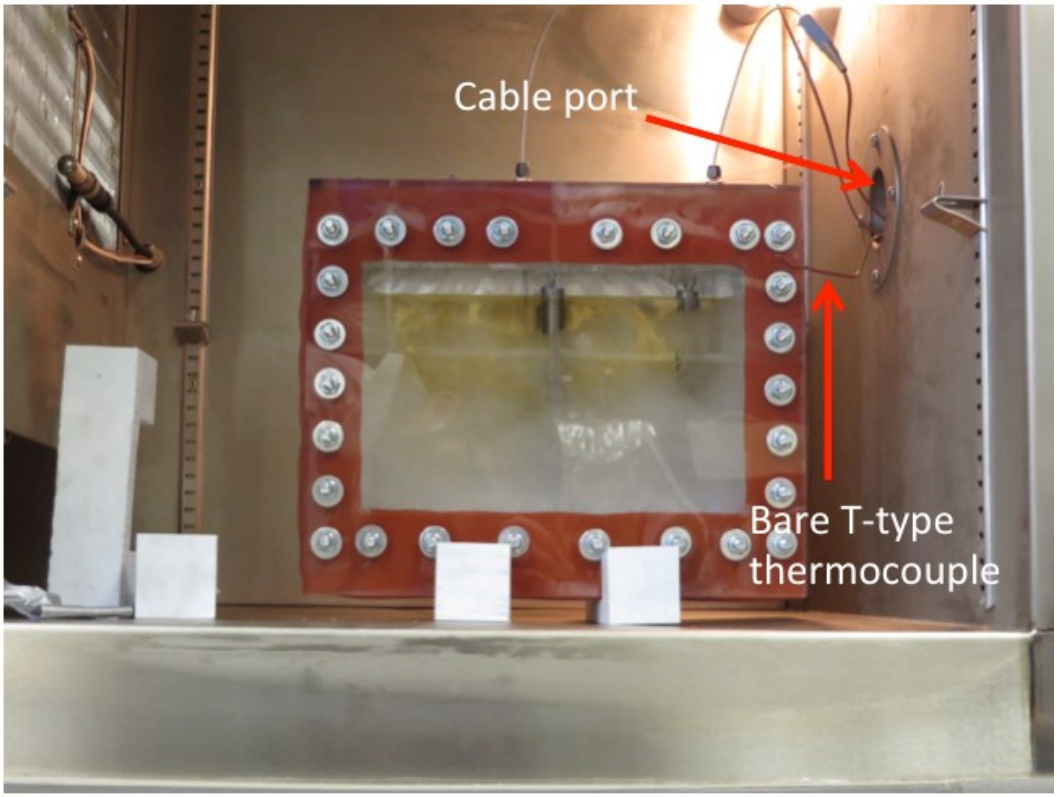

Figure 3-18: Incomplete Mark I heat storage cell in the environmental chamber, showing thermocouple wires traversing the chamber's cable port and the exposed thermocouple wire added to log the chamber's air-temperature.

The operation of the environmental chamber was controlled via the built-in micro-controller, through which ramp-soak profiles could be programmed. The programming varied little, with exceptions noted with their observations in Section 3.3.3.1, and mostly followed the profile illustrated in Figure 3-19. As these experiments were the inaugural phase change experiments conducted in the project, a cautious approach was adopted to heat the Mark I heat storage cell, not exceeding 95 ˚C in the environmental chamber. These evaluations centred principally around observations of the complete phase change processes rather than to achieve the maximum charged state of 110 ˚C.

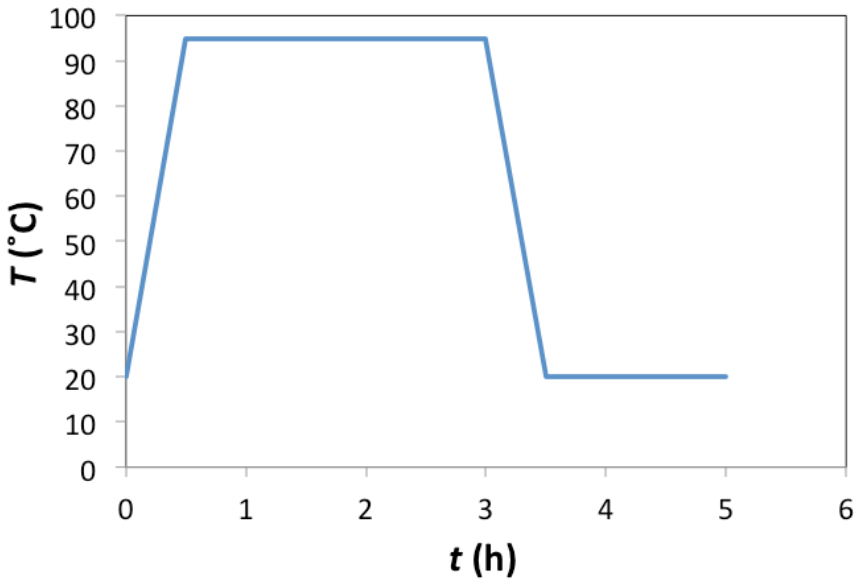

Figure 3-19: Sample heating and cooling profile program used to operate the environmental chamber to conduct Mark I experiments.

While the environmental chamber was used to charge and supercool the Mark I heat storage cell, nucleation experiments were conducted outside the environmental chamber on a lab bench in order to facilitate observation and measurements. While resting the heat storage cell on the lab bench, the solenoid cables were connected to individual channels on an NI 9472 digital sourcing module, supplied power at 12 V DC from an Extech model 382275 600 Watt Switching Mode DC Power Supply. A LabView virtual interface (VI) was used to control the relay action of the individual NI 9472 channels, whereby solenoids could be either activated individually or in groups.

During nucleation experiments, the Mark I internal temperature measurements were acquired via the imbedded thermocouples and the compact DAQ/LabView. Visual records of the solidification process were also acquired in high-definition, 30 frames-per-second video using a Canon PowerShot SX280HS digital camera, positioned in front of the PC sight-glass during nucleation experiments. Likewise, infrared (IR) thermographic images were also captured in series during some of these experiments using an Infrared Cameras Inc. ICI 7320 S (±1 K or 1 %) with a 25 mm lens and recorded using the IR Flash software provided by the manufacturer. This camera was tripod-mounted in front of the aluminized film side of the Mark I heat storage cell to take measurements of the surface temperature distribution on the outside surface of the aluminized film, as

performed in prior laminate film heat transfer experiments by Desgrosseilliers et al. (2016). Attempts were made to capture thermographic images facing the PC sight-glass, but these proved ineffective since the IR images could not reveal internal temperatures behind the PC sight-glass, which presumably caused either problematic refraction of the internal IR emissions or too much absorption of these emissions to allow for useful measurements to be conducted.

3.3.1.2 MARK II PRESSURE RELEASE TESTS

Motivated by concern for uncontrolled vapour loss from the SAT PCM in the Mark I heat storage cell, made noticeable by decreasing PCM liquid level when fully dissolved and by apparent corrosion of the tubular solenoid casings (Figure 3-20), efforts were made to improve the vapour leak-tightness of the Mark II and III heat storage cells (e.g., bellows seals around the PP pegs).

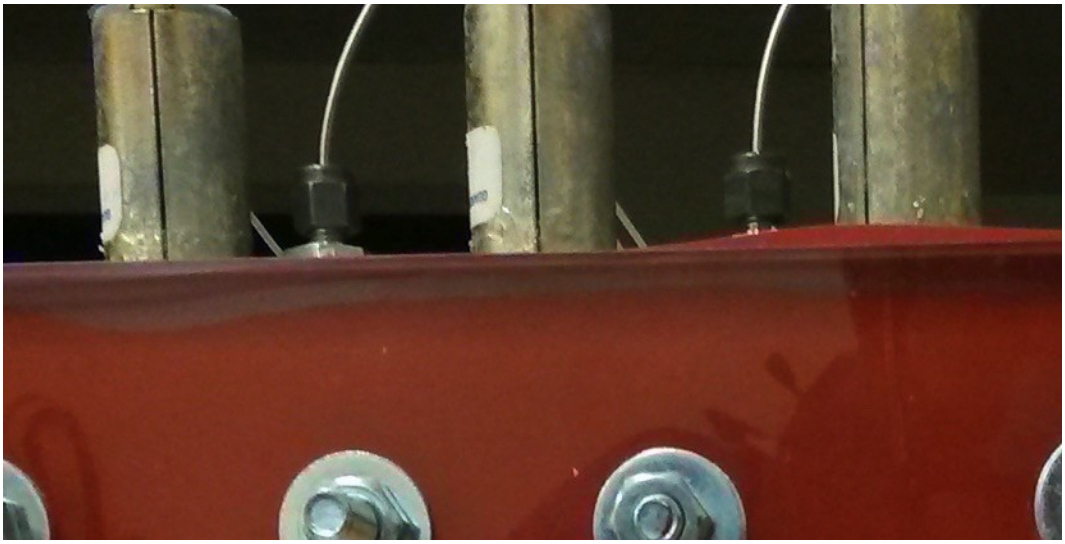

Figure 3-20: Photograph showing apparent corrosion of the tubular solenoid casings on the Mark I heat storage cell.

An evaluation of the effectiveness of these measures was also determined. Pressure release tests were conducted using only the Mark II heat storage cell (preceded the development of Mark III) under both positive and negative internal gauge pressures. Figure 3-21 illustrates the process diagram of the experiments used to produce these tests.

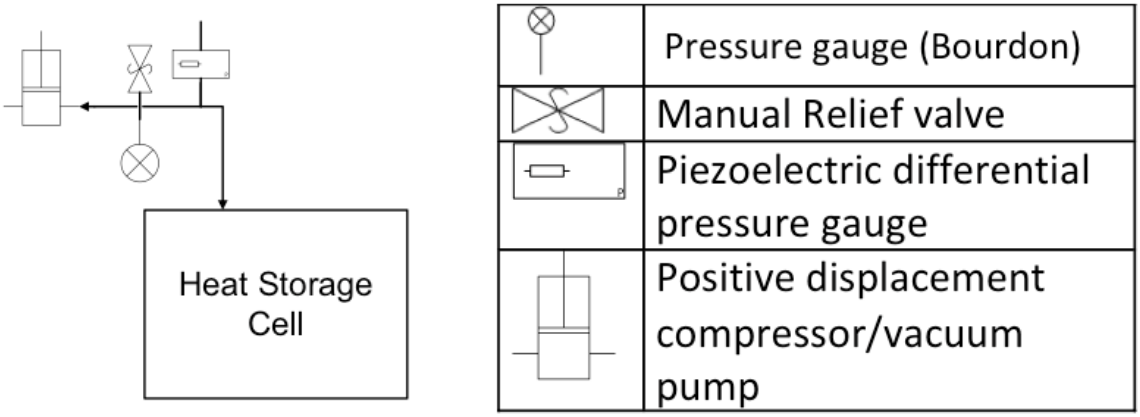

Figure 3-21: Schematic representation of the Mark II pressure release experiments.

The positive displacement compressor/vacuum pump, relief valve, and bourdon pressure gauge were supplied by using a fully integrated, manually operated pump (item 9963K21 on McMaster.com). The piezoelectric differential pressure gauge, model PX26-005DV by Omega Engineering Inc. (0 psid to 5 psid, ±1 %), used in the experiment enabled logging pressure data via an NI 9201 ± 10 V analogue input module and compact DAQ/LabView. An excitation voltage was supplied via the Extech model 382275 600 Watt Switching Mode DC Power Supply. All components were connected using flexible polyvinyl chloride tubing and barbed fittings. The pressure sampling tubing was ring-clamp sealed to one port of the differential pressure gauge, while the other remained exposed to the ambient environment (i.e., psid became psig).

Post-processing of the pressure data logged via LabView was conducted in Matlab, using the user function called *Orifice_dia*, described in Appendix D. The function was used to estimate the equivalent sharp-edged orifice diameter that corresponded to the measured rates of pressure change. Since the locations of all leaks are difficult to ascertain, calculating the diameter of the equivalent sharp-edged orifice yielding the same leakage rate was used to gauge the approximate scale of the leaks that remained and to compare leak rate measurements. McCabe et al. (2005) lists the steady-state equation for compressible fluids as:

$$S = \dot{m}\left(C_d Y \sqrt{2\Delta P \rho}\right)^{-1}, \tag{3.1}$$

$$D = 2\sqrt{S/\pi}, \tag{3.2}$$

where S, $\dot{m}$, C_d, Y, ΔP, ρ, and D correspond to the orifice cross-section area, mass flow rate, sharp-edged orifice discharge coefficient (0.61), compressibility parameter,

differential pressure, fluid (air) density, and orifice diameter, respectively. Since the fluid in question is air, the following equations substitute the corresponded property values for air.

The compressibility parameter, Y, in Eq. (3.1) was calculated from (McCabe et al., 2005):

$$Y = 1 - 0.41\left(1 - \frac{P_2}{P_1}\right)1.4^{-1}, \tag{3.3}$$

where P_1 and P_2 were the internal and external pressure (the latter assumed 1 atm throughout), respectively. The mass flow rate and density in Eq. (3.1) were calculated from the ideal gas equation (assuming T = 298.15 K), where:

$$\dot{m} = \frac{29\times10^{-3}\ \frac{\text{kg}}{\text{mol}}\ 1.9\ \text{L}}{8.31451\ \frac{\text{kPa·L}}{\text{mol·K}}\ 298.15\ \text{K}}\frac{P_i - P_{i-1}}{1\text{s}}, \tag{3.4}$$

and

$$\rho = \frac{29\times10^{-3}\ \frac{\text{kg}}{\text{mol}}\ P_i}{8.31451\ \frac{\text{kPa·L}}{\text{mol·K}}\ 298.15\ \text{K}}, \tag{3.5}$$

where P_i and P_{i-1} are the current time step recorded pressure and previous time step recorded pressure (recorded at 1 Hz), respectively.

Although pressure release tests are inherently transient, it is assumed that the model would still apply to yield a relative measure of the equivalent orifice diameter, especially for well-sealed systems that should behave in a pseudo steady-state manner.

3.3.1.3 MARK II AND III PHASE-CHANGE EVALUATIONS

Controlled charge/discharge experiments for Mark II (x1) and Mark III (x3) heat storage cells were conducted using the autonomous system depicted in Figure 3-22. The right-side portion of the system (fan-heater-pump loop, henceforth called 'ETS loop') was developed to simulate ETS functions (charging, discharging, supercooling, room-heating, closed-loop liquid heat transfer, and liquid-to-air heat transfer) by integrating the heat storage cells with the typical balance of components. The left side (henceforth called 'heater-chiller loop') was developed to charge, supercool, and discharge the heat storage cells under strictly controlled conditions. Both systems could be executed simultaneously or individually. In the latter case, one of the two systems would be deactivated while the

remaining system would be used to conduct experiments with all of the heat storage cells (or subset thereof by shutting-off flow to some) by opening the ball valves linking the two systems and closing the ball valves isolating the heat sink/source and fluid reservoir of the deactivated system. Note that although Figure 3-22 shows a capacity for six heat storage cells, only four were used during the project (one in the ETS loop and the other three in the heater-chiller loop).

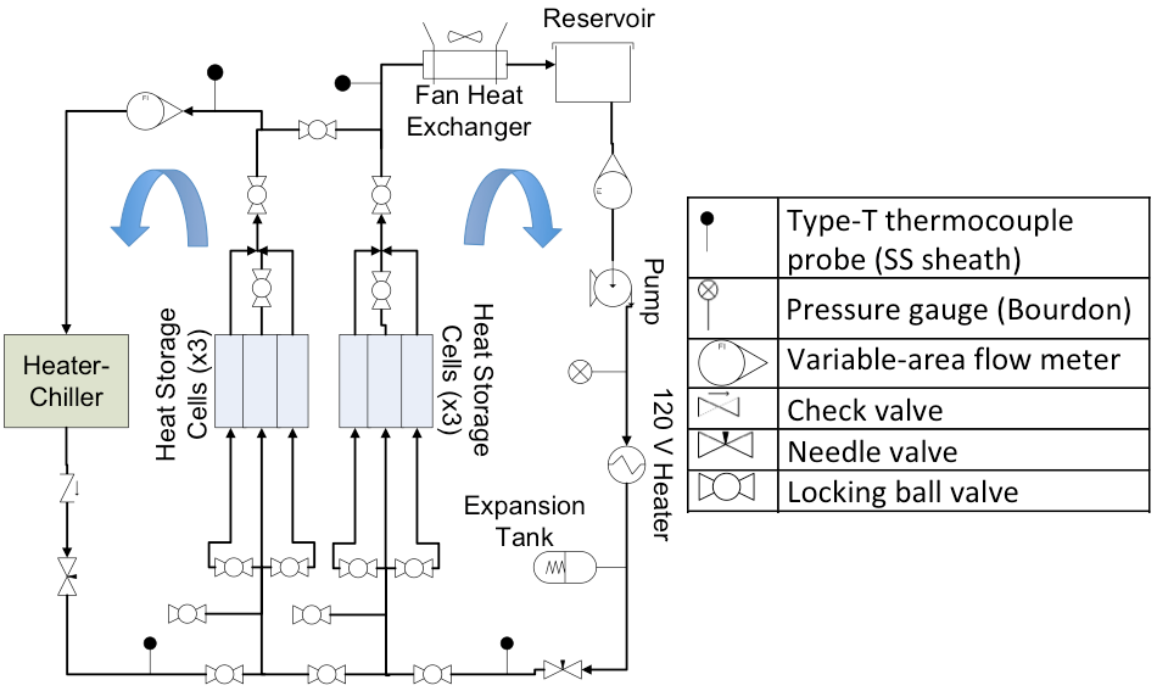

Figure 3-22: Process and instrumentation diagram of the simulated ETS testing loop (right-side, using the fan, pump, and heater) and the cyclic testing loop (left-side, using the heater-chiller). With respect to the diagram, the simulated ETS loop drives HTF flow in a clockwise direction, while the cyclic testing loop drives HTF flow in a counter-clockwise direction.

While Figure 3-22 depicts the relative layout of the process elements of the closed loop HTF system and heat exchange equipment, auxiliary elements to the operation of the system are not shown. Figure 3-23 Figure 3-24 show the physical layout of the process systems, their components (labelled), their electronic controls/monitoring systems and power supplies, and computer for data collection. Generally, 1/2" OD tubing (0.436" ID) copper tubing with double-ferrule brass compression fittings were used throughout the flow network, with the exception only of interfaces with stainless steel components (heater-chiller, expansion tank, and 120 V heater), wherein high-temperature, PFA plastic compression fittings were used between the dissimilar metals. For convenience, the flow

network was filled with pre-mixed 40 vol% PG in water, and therefore operation was restricted to < 105 ˚C (recall Section 2.4). Both the ETS loop reservoir and the integral heater-chiller reservoir were open to atmosphere, but loosely covered by their respective lids. Only one Bourdon gauge (Figure 3-23) was installed in the system, selected to be placed downstream of the pump discharge in the ETS loop to serve only as a simple indication of the system pressure achieved in the ETS loop to ensure that objective B was satisfied in the integrated prototype system.

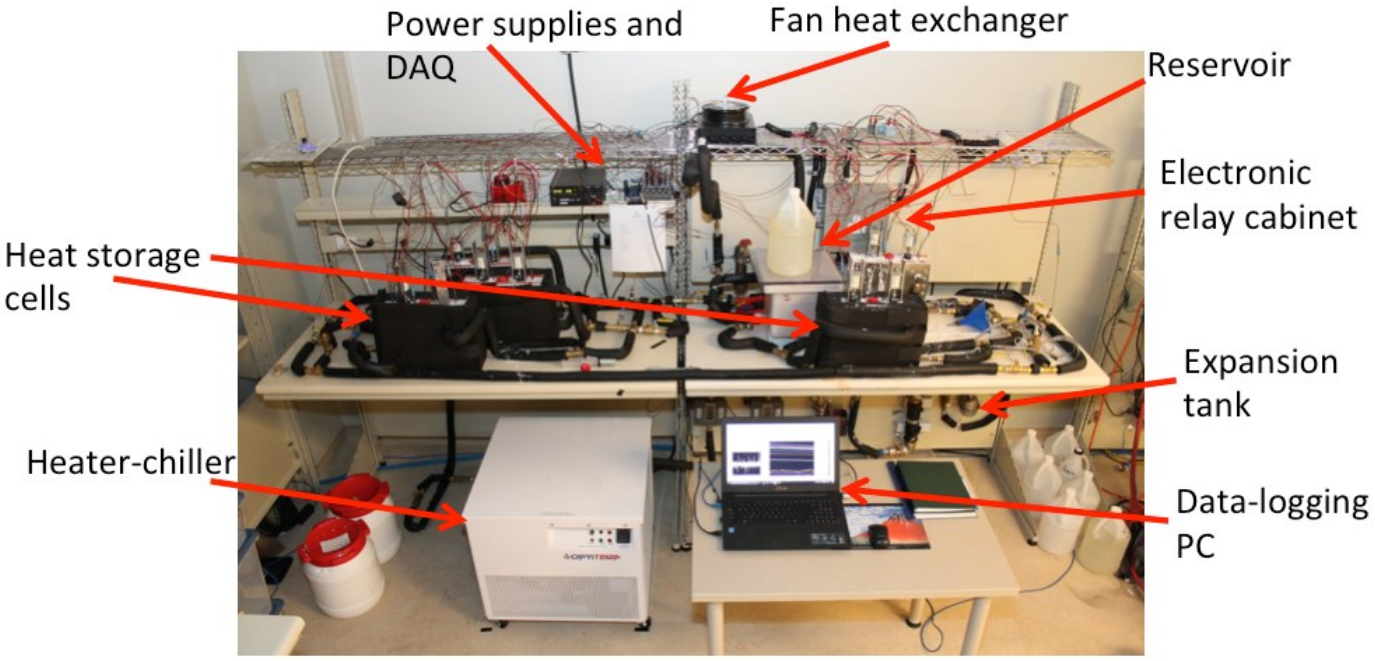

Figure 3-23 Experimental installation of the process illustrated in Figure 3-22.

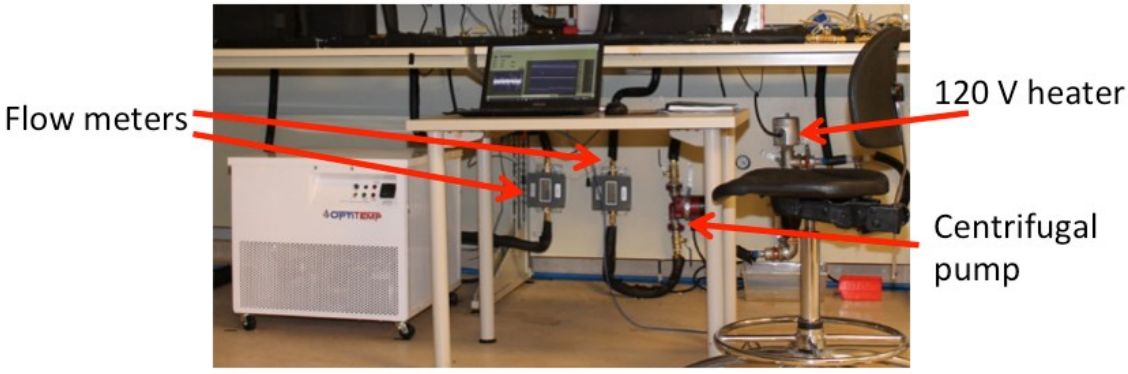

Figure 3-24: View of instruments and components beneath the tables in Figure 3-23.

EPDM foam insulation (black insulation shown in Figure 3-23 and Figure 3-24), both tube insulation and flat sheet insulation, were used throughout both systems. Tube insulation (Tundra Seal, 1/2" ID and 3/8" wall thickness) was fit to the tubing using the integral taped seam, whereas sheet insulation (1" thick Armaflex sheet) was hand-cut to size and placed on all lateral sides of the heat storage cells using EPDM tape (Armaflex tape) to keep them in place. Fittings remained without thermal insulation.

Electronic control and monitoring of both systems were accomplished via LabView 2015 and an NI model 9174 compact DAQ 4-slot chassis equipped with a 4-channel NI 9211 thermocouple module, 16-channel NI 9213 thermocouple module, 8-channel NI 9201 analogue input (voltage) module, and 8-channel NI 9472 digital sourcing module. The analogue input module recorded calibrated flow-rate measurements generated by both Omega Engineering Inc. 0.2 GPM to 2.0 GPM (water, ± 2% full scale) digital variable-area flow meters (model FLR63O2D), both powered simultaneously by a 12 V DC wall adapter (item 76000735-ND on Digikey.ca).

The digital sourcing module was used to generate relay switching signals (0 V to 5 V DC, supplied by a 5 V DC wall adapter, item 993-1236-ND on Digikey.ca) to a SainSmart 16-channel high-power relay module (10 A per channel) and an Omega Engineering Inc. model SSR330DC50 50 A solid-state relay, both powered simultaneously by an Extech model 382275 600 Watt Switching Mode DC Power Supply at 24 V DC to activate the relay channels. Both heat storage cell's (both Mark II and III) 24 V DC solenoids pairs, used to actuate the spring-nucleation triggers, were wired in parallel to a single relay channel supplying their power from the Extech DC power supply. One more 10 A channel was used to activate the fan motor in the fan-cooled liquid-to-air heat exchanger (item 35145K74 on McMaster.com) and the 50 A solid-state relay was used to activate the thermostatically controlled 120 V AC, 1.5 kW electric immersion heater (item 3656K132 on McMaster.com, shown below the table in Figure 3-24), used as a flow-through heater in the ETS loop. Note that a 3 A variable AC transformer (item B00DDFGQZ2 on Amazon.ca, 0 V to 130 V AC, ± 5 V) was used to modulate the voltage supplied to the fan motor for the liquid-to-air heat exchanger. The dedicated pump (Grundfos Alpha centrifugal pump with 3-speed motor, 120 V AC) for the ETS loop and the heater-chiller (OptiTemp model OTC-.75A, 208 V AC) were each

supplied by their own power supplies, separate from the relay controlled devices. Regarding the ETS development objectives, the Grundfos Alpha pump operated quietly (≤ 43 dB(A) (Grundfos, 2014), fan-cooled liquid-to-air heat exchanger excluded) in all flow conditions, thus partly fulfilling objective D. The absolute pump discharge pressure, measured by the Bourdon gauge, was also noted to remain below 1.3 atm in all flow conditions, thus fulfilling objective B.

In-flow thermocouples (type-T 316 stainless steel sheathed probes, Omega model TMTSS-062U-12, ± 0.5 ˚C) were used to monitor temperatures in the circulated PG solution in both loops upstream and downstream of the heat storage cells, and two additional thermocouples were later added to the flow network, but not shown in Figure 3-22, since these were not in-flow probes. Rather, they were adhesively mounted surface type-T thermocouples from Omega (model SA1-T, ± 0.5 ˚C), used to better gauge the circulating PG solution temperatures at the liquid-to-air heat exchanger liquid outlet and at the inlet to the variable-area flow meter used in the ETS loop. Also, two more bare lead type-T thermocouples (model 5TC-TT-T-24-36, ± 0.5 ˚C) were used to measure the air inlet and outlet temperatures of the liquid-to-air heat exchanger.

The OptiTemp model OTC-.75A heater-chiller included a built-in reservoir, positive displacement pump (nominal 4 GPM water flow rate), 3 kW electric heater, 2.3 kW refrigeration cycle for recirculated chilling, and a built-in microcontroller with programmable ramp-soak automation and PID temperature set-point control. Therefore, the function of the pump, heater, and chiller were automated by the built-in microcontroller rather than through LabView, but the function of the solenoids remained in LabView control.

Regarding system control, the solenoids, for both loops, and the heater and fan in the ETS loop were controlled via LabView, and the temperature and solenoid activation histories of the heat storage cells were monitored and recorded by the virtual interface (VI) at every data acquisition interval. A charge-discharge hysteresis algorithm (Figure 3-25) was implemented into the LabView VI developed to automate the experiments, whereby its logical outputs at each interval controlled heating, cooling, and solenoid activation processes. The logical outputs refer to the state variables, N_i and S_i, that were used in the VI to record the SAT PCM's charge status ($N_i = 1$, fully dissolved; $N_i = 0$,

solidified) in the heat storage cells and the nucleation trigger status ($S_i = 1$, nucleation-trigger actuation; $S_i = 0$, nucleation-triggers at rest), were determined according to the heat storage cell temperature history and the state-threshold temperatures, T_h (for charging) and T_l (for supercooling). For instance, a status of $S_i = 1$ would signal the VI to activate a software relay, signalling through the digital sourcing module to the corresponding hardware relay channel. Generally, heating was activated for instances of $N_i = 0$, and the fan motor was activated for instances of $N_i = 1$[41].

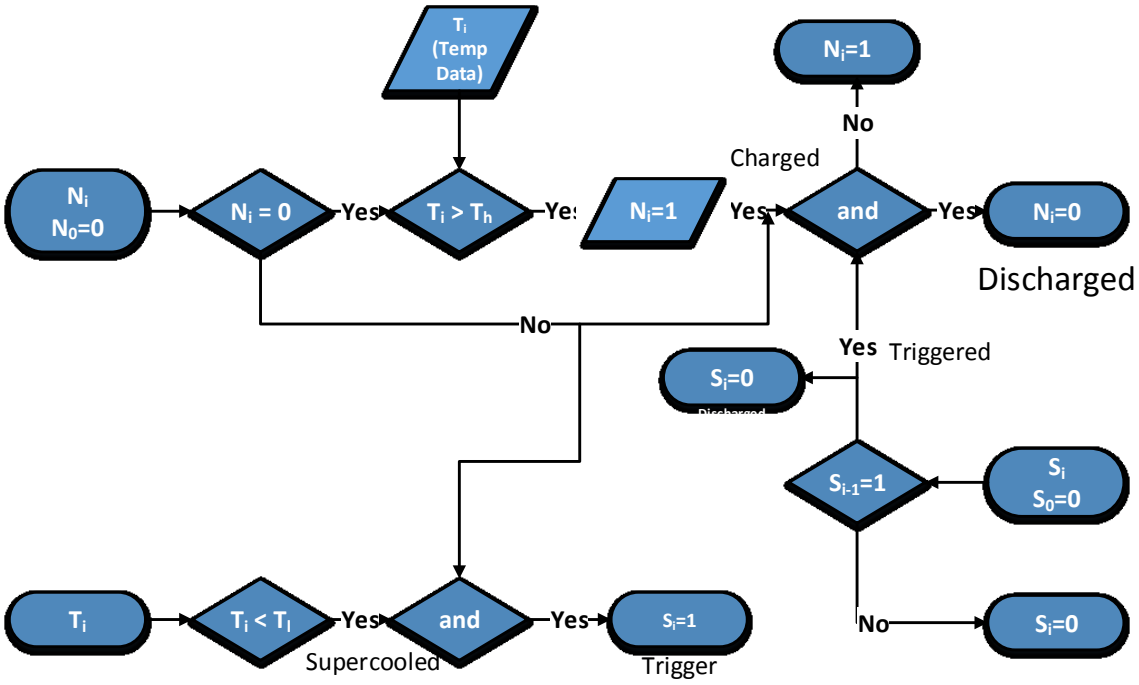

Figure 3-25: Flow-chart representation of the charge-supercooling-discharge hysteresis algorithm. The algorithm is used to monitor current heat storage cell temperatures (T_i) and perform operations on the status variables, N_i and S_i, used to monitor PCM charge ($N_i = 1$, charged) and nucleation triggering ($S_i = 1$, activate triggers) at every data capture interval, i. The variables T_h and T_l correspond to the charged state temperature threshold and the supercooled state temperature threshold, respectively.

Due to the method of implementing the algorithm in Figure 3-25 into the LabView VI, a value of $N_i = 0$ would not be assigned until returning to the triggering condition in Figure 3-25 a second time, causing the spring-nucleation triggers to extend a second time, albeit in the freshly solidified SAT PCM rather than supercooled SAT solution. Although

[41] Additional temperature hysteresis control was used in the VI to control these respective operational states.

this was not intended in the design of the VI, it was generally considered beneficial to their nucleation efficacies, as it would give a second opportunity during which to capture and withhold SAT seed crystals for the subsequent cycle. Consequently, this has been adopted in the general practice of this project and recommended for heat storage cell ETS development in order to achieve objective 7 in Section 2.2.

3.3.2 CONTAINMENT INTEGRITY

Of singular importance regarding enclosure evaluations is the ability to reliably store their contents without breaches to their integrity. Evaluations of this criterion are reported in the following sections.

3.3.2.1 PRESSURE RELEASE TESTS

The inherent propensity to leak either vapour or liquid can be evaluated from the unfilled heat storage cells via pressure release tests. As Mark I was not designed to resist vapour leaks from the top of the base, only Mark II was pressure tested (described in Section 3.3.1.2) for leakage determinations. It was assumed that Mark III either matched or exceeded the leak-tightness of Mark II due to their similarities.

Positive pressure tests were conducted on the Mark II heat storage cell both before and after addressing leaks that could be detected using water around sealed joints. Following these evaluations, a vacuum test was also conducted on the Mark II heat storage cell. Figure 3-26 summarizes their results from Eqs. (3.1) to (3.5), using the Matlab user function *Orifice_dia* found in Appendix D. Note the error bars shown in Figure 3-26 reflect only the variability of the respective datasets corresponding to each test. Also note that the error was largest for the tests in which leak rates were largest (MII and MII (sealed vac)), incidentally, corresponding to the tests in which the leakage rates deviated most strongly from the pseudo steady-state assumption used in the model.

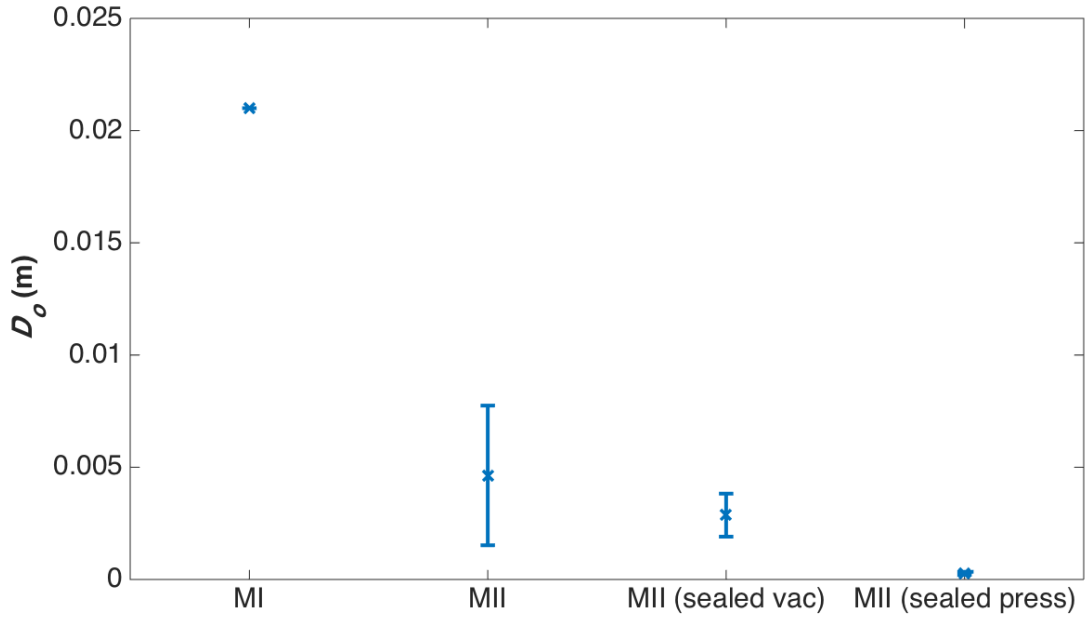

Figure 3-26: Calculated sharp-edged orifice diameters, D_o, for the Mark II (denoted MII) heat storage cell under pressure and vacuum. The estimated orifice diameter for Mark I (denoted MI), based on the approximate open area remaining around the solenoid actuator shafts in the base, was added for comparison. The designation of 'sealed' for MII results signifies those results that were obtained after addressing leaks identified after the first pressure test (denoted simply 'MII').

Although Mark I was never evaluated in a pressure release test, the value assigned for Mark I in Figure 3-26 corresponds to the approximate total open-area that was present around the solenoid actuator shafts since they remained vented to the outside. Using this as a basis for comparison, Figure 3-26 shows that efforts, both in design and in careful leak detection, have resulted in a substantially more leak-resistant Mark II heat storage cell. Leakage sites that were identified and corrected in this evaluation consisted of the eyebolts at the bottom of the base and the plastic cap-plug used to seal the filling port. It was noted that these areas would warrant further consideration during thermal operation of the heat storage cell (excluding the eyebolts for Mark III).

The difference between the vacuum test and the sealed positive pressure test (results in Figure 3-26) was not considered of great importance since the test conditions neglected the differential thermal expansion of the materials of construction and other temperature-related effects that will certainly impact the leak-tightness of the Mark II and III heat storage cells during their intended operation. Nevertheless, gains in the leak-tightness were noted from the pressure release tests for Mark II, and by extension Mark III.

3.3.2.2 REPEATED THERMAL CYCLING

Evidence of the challenges faced for maintaining leak-tightness during thermal exercising of the heat storage cells was found after repeated thermal cycling. Figure 3-27 shows the appearance of a solid sodium acetate deposit (unknown if anhydrous or hydrate, henceforth referred as 'salt deposit') directly underneath an eyebolt hole in the Mark I heat storage cell. This observation was made after the heat storage cell was kept idly supercooled at room temperature until it spontaneously autonucleated after 167 days (longest supercooling duration recorded in this project). The location of the salt deposit coincided with the apparent location of the source of the autonucleation, shown in Figure 3-28. Soon after, this was confirmed by the duplication of the solidification pattern in Figure 3-28, resulting again from autonucleation, after the SAT PCM in Mark I was fully dissolved and supercooled for 20 days. It was noted also that traces of supercooled dissolved SAT would sometimes be found underneath the Mark I enclosure when charged and supercooled in the environmental chamber used to thermally exercise the Mark I heat storage cell.

Figure 3-27: A deposit of solid SAT found directly underneath an eyebolt port underneath the Mark I heat storage cell at the end of a 167 day long-term supercooling experiment.

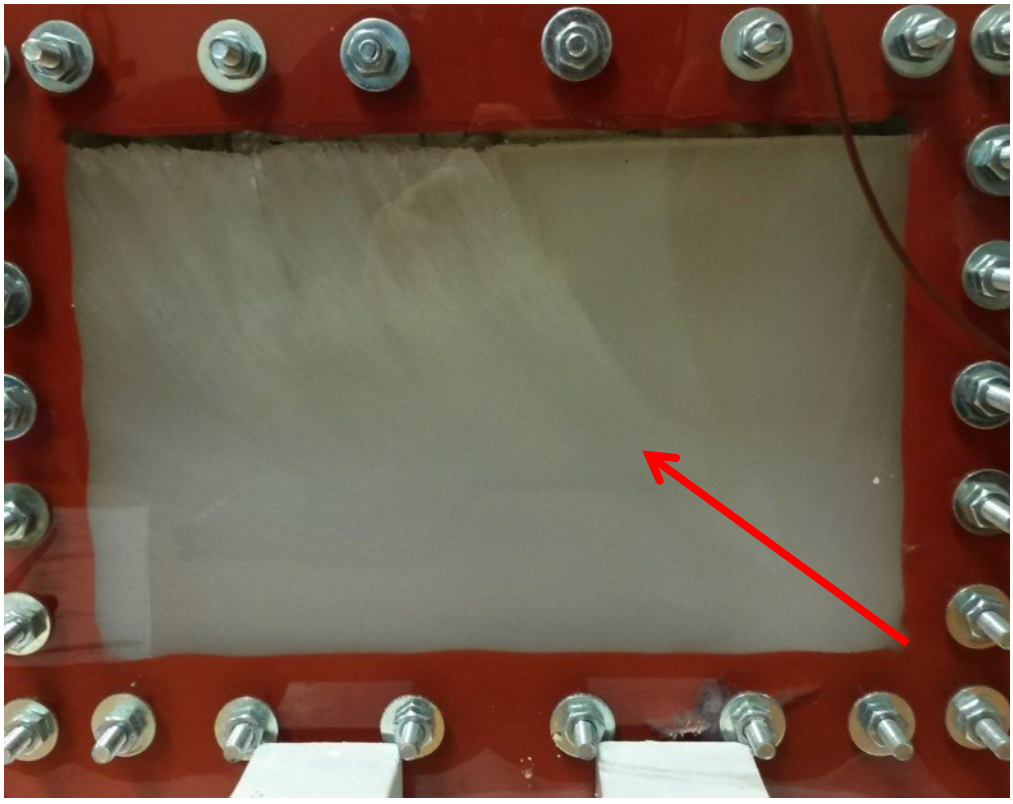

Figure 3-28: End of 167 day long-term supercooling of Mark I at room-temperature, resulting in autonucleation. The arrow traces the progression of solidification front expansion, appearing to have originated from the lower-right corner, confirmed by a subsequent supercooling experiment that lasted 20 days until autonucleating, also displaying the same crystal growth pattern. This area sat overtop the solid deposit shown in Figure 3-27.

Due to their locations, these observations of salt deposits underneath the Mark I eyebolt holes gave apparent validation to the suspicion that differential thermal expansion caused transient breaches to occur in sealed ports. Unlike the flat surfaces that were sealed using compressed rubber gaskets, the threaded ports did not have compressible seals on which to rely for maintaining adequate contact during occasions of excessive differential thermal expansion. Incidentally, the gasket seals (silicone rubber and aluminized film) of the Mark I heat storage cell neither showed evidence of harbouring residual solid SAT in crevices inside the PCM cavity nor the appearance of salt deposits along their exterior contact junctions. The eyebolt hole breach persisted and could not be corrected with thermal treatments alone, therefore the long-term supercooling ability of the Mark I heat storage cell would remain compromised.

Solid salt deposits were also found underneath the EPDM sheet insulation covering one of the two heat exchange assemblies on the Mark II heat storage cell following 37 controlled cycles (discarded runs not counted) in the circulated HTF system (Figure 3-29 and Figure 3-30). It was noted that no such evidence could be found underneath the insulation covering the other heat exchange assembly on the Mark II heat storage cell, and that salt deposits shown in Figure 3-29 also revealed no apparent origin to the leak on that side. However, the salt deposits shown in Figure 3-30 suggested the leak originated along the two salt encrusted compression bolts seen in the photo.

Figure 3-29: Traces of sodium acetate, either anhydrous or trihydrate, found at the bottom edge of the Mark II heat storage cell after 37 repeated charge-supercooling-discharge cycles in the circulated HTF experiments shown in Figure 3-23.

Figure 3-30: Evidence of an SAT leakage source along a compression bolt in the Mark II heat storage cell, shown encrusted with sodium acetate solid (either anhydrous or trihydrate). The appearance of this containment breach corresponds with the appearance of trace solid in Figure 3-29.

The evidence of salt deposits seemingly originating along compression bolts in the Mark II heat storage cell suggested that perhaps the aluminized barrier film seal between the aluminum flow plate and the base became compromised. Evidence of a PG solution leak could not be found, therefore the silicone gasket seal used to seal the components of the heat exchange assembly was assumed to have remained functioning properly. Since the aluminized film could not strain significantly under the compression of the bolt assembly, its failure to adjust to changes in the compression force (caused by differential thermal expansion and/or net HTF/PCM internal pressure variations) was suspected to be the root cause. Consequently, the use of compressible gasket seals throughout the heat storage cells should be considered in future revisions, while eyebolts were already eliminated in the Mark III heat storage cell design.

3.3.3 PHASE CHANGE

Complete charge, supercooling, and discharge cycles were conducted using all of the heat storage cell designs developed for this project (Marks I, II, III), each loaded with the selected SAT PCM mixture composition described in Section 2.3.1. These evaluations were performed with the goals of inducing complete phase-change (decomposition/dissolution and solidification) in order to test the intended phase-change process (i.e., matching the phase-change properties of 1:1 SAT in water), test that stable

supercooling was supported by the respective heat storage cell designs, evaluate the prospects of long-term supercooling at room-temperature, and identifying irregularities in these operations. The results of these evaluations were used to judge the success of the respective heat storage cell designs with respect to the PCM behaviour as well as determine suitable operating conditions to reliably yield the desired PCM heat storage behaviour.

Cumulative heat transfer analyses were not performed for any of these experiments. As has been amply demonstrated by Kabbara (2015) and Murray (2012), calculating the cumulative heat transfer from integrated dynamic heat exchange data for previously uncharacterised heat storage devices risks generating results with excessively high cumulative uncertainties. These uncertainties would be too large to yield any useful determinations or comparisons of energy storage amounts or round-trip efficiencies. For this reason, this research has forgone cumulative heat transfer determinations and opted only for detailed phase-change process evaluations and instantaneous heat exchange rate determinations (Chapter 4) instead.

3.3.3.1 THERMAL CHAMBER EVALUATIONS (MARK I)

The earliest evaluations were conducted using the Mark I heat storage cell, performed within a temperature-controlled environmental chamber as described in Section 3.3.1.1. This constituted a first-of-its-kind experiment; therefore, no comparisons were available from which to establish nominal operating parameters to generate a complete charge-supercooling-discharge cycles. Consequently, exploratory exercises were undertaken with respect to establishing useful operating parameters inside the temperature-controlled chamber and later for the circulated HTF experiments of Marks II and III. Note, that although the Mark I temperature probes were both shown to be positioned at the bottom of the PCM cavity in Figure 3-4, the thermocouple nearest the wall was later substituted with a top-located probe. The probe names listed in the figures (Middle-bottom and Edge-top, Figure 3-31) identify their positions within the Mark I heat storage cell.

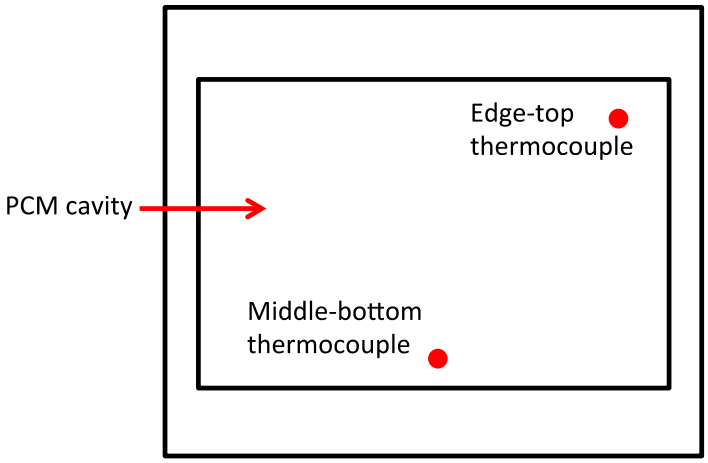

Figure 3-31: Mark I schematic diagram showing the approximate locations of thermocouples (red circles) in the PCM cavity.

Figure 3-32 shows the consequence of insufficient extent of charging. Despite the PCM temperature probes inside Mark I having recorded temperatures exceeding T_{trans} for 1:1 SAT in water (55 ˚C), autonucleation (t = 350 min in Figure 3-32) was observed during the period intended to induce supercooling. Not much could be ascertained from the PCM thermocouple probes (middle-bottom and edge-top) during the charging process from t = 0 min to t = 240 min nor during the apparent supercooling process from t = 240 min to t = 350 min that would suggest a cause for the autonucleation.

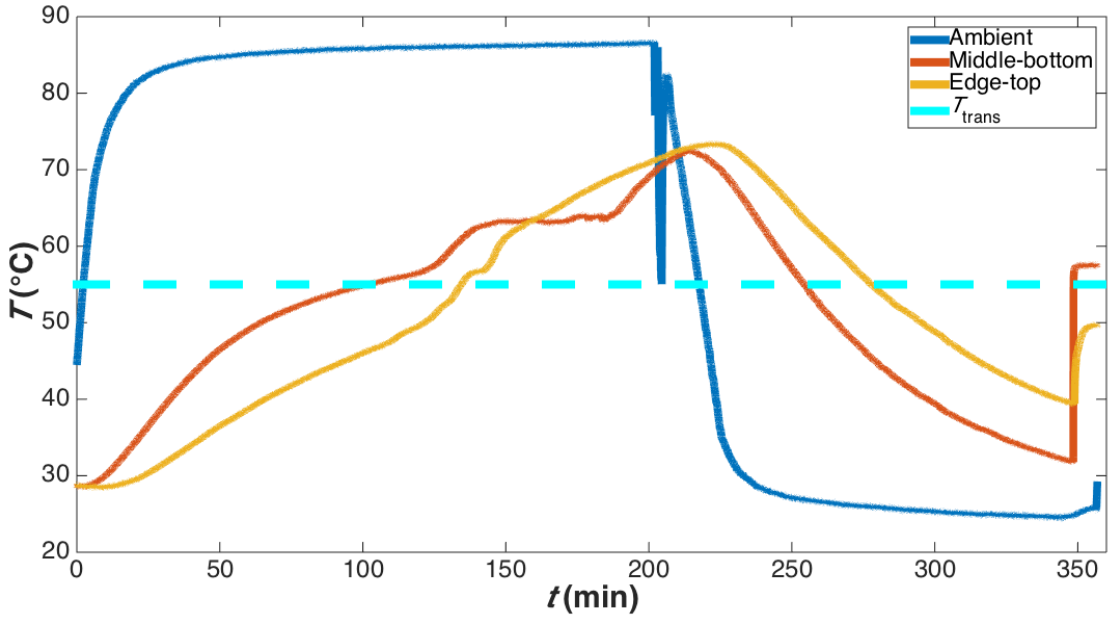

Figure 3-32: Incomplete charging (PCM < 75 ˚C) of Mark I resulting in autonucleation. The dashed line corresponding to the average SAT PCM composition T_{trans} = 55 ˚C (Sandnes et al., 2006) has been added for reference. The vastly different autonucleation curves suggest solution stratification was in effect.

Note the absence of a melting plateau typical for pure, congruent PCMs, which is instead substituted with the smoothly decreasing slope of the temperature profile of the SAT PCM below T_{trans}, caused by incremental phase-change intensifying up to T_{trans}. The middle-bottom probe did, however, show a plateau-like feature above 60 ˚C around t = 150 min. Visual observations conducted at the time confirmed this was caused by solid PCM near the middle-bottom of the PC-sight-glass[42] (for example, see Figure 3-33) collapsing toward the bottom of the cavity toward the side with aluminized film due to the inherent porosity[43] and resulting poor integrity of the diluted SAT PCM system. The observed erratic temperature profile and significant temperature suppression was likely caused by the collapsing solid, still below T_{trans}, falling into a superheated liquid region, undergoing phase-change too quickly (surrounded by superheated liquid) and with too

[42] Phase-change occurred more slowly near the PC sight-glass due to its inferior capacity for heat conduction heat transfer compared with the aluminized film.

[43] Nucleation of a supercooled concentrated SAT PCM generates a uniformly porous solid (corresponding to the equilibrium phase-fractions of solid and liquid), trapping the remaining equilibrium liquid inside the pores. The pores grow larger when heated again to T_{trans}, while the remaining solid becomes more fragile.

little thermal mass to cause the local temperature measurement to return to T_{trans} during this process.

Figure 3-33: Solid SAT PCM remaining near the bottom of Mark I (early model with only two springs) while charging in the environmental chamber. The reflection of the solid PCM produced on the aluminized film shows that more solid SAT remains near the PC sight-glass than toward the aluminized film.

The apparent supercooling region in Figure 3-32 depicted smooth cooling curves, showing no features relating to solidification (e.g., halts or breaks in the curves) until the autonucleation was detected. However, upon examination of the autonucleation temperature curves, it was noted that both thermocouples recorded vastly different temperatures post-nucleation. In a uniformly mixed supercooled, incongruent PCM, the warmest supercooled area of the PCM (edge-top) would normally exceed or match the temperature of the corresponding cooler area (middle-bottom) after nucleation due to the relative proximity of its equilibrium enthalpy to that of the fully dissolved PCM at T_{trans}. Therefore, solution stratification was confirmed, meaning that the resulting solution from the phase-change process became separated into a more dilute solution at the top (i.e., lower post-nucleation temperature recorded by edge-top) and a more concentrated solution at the bottom, the full extent of which could not be determined with only two thermocouple probes. This process, as outlined in Section 1.2.1.1, is generated by the vast buoyancy difference between the solid (heavy) and liquid (light), and perhaps further

accentuated by the collapse of solid PCM toward the bottom during the charging process. As outlined in Section 2.3.2.1, a PCM concentrated beyond $w_{SA} = 0.58$, approaching pure SAT at $w_{SA} = 0.603$, becomes bound between a second liquidus line in which solid anhydrous sodium acetate remains until $T \geq 78$ ˚C (T_{liq} from Eq. (2.2) at $w_{SA} = 0.603$).

Therefore, a minute amount of solid anhydrous SA (although not observable through the sight-glass) was suspected to remain at the bottom of the PCM cavity during the experiment recorded in Figure 3-32, allowing the solution to moderately supercool until the SA could hydrate again and generate spontaneous solidification of the surrounding supercooled SAT PCM. Consequently, the subsequent reheating (Figure 3-34) of the autonucleated PCM in Mark I from the events of Figure 3-32 confirmed the ability to supercool successfully after heating the PCM up to 86 ˚C, therefore giving credence to the hypothesis of the generation of solid SA for 58 ˚C $\leq T \leq$ 78 ˚C. Figure 3-35 further confirms the absence of unusual or erratic features in the PCM cooling curves after complete dissolution of the PCM up to 86 ˚C in Figure 3-34. Note that this process required 5 hours to achieve complete dissolution of the SAT PCM with the chamber temperature setpoint at 85 ˚C, despite beginning in the warm, freshly nucleated state.

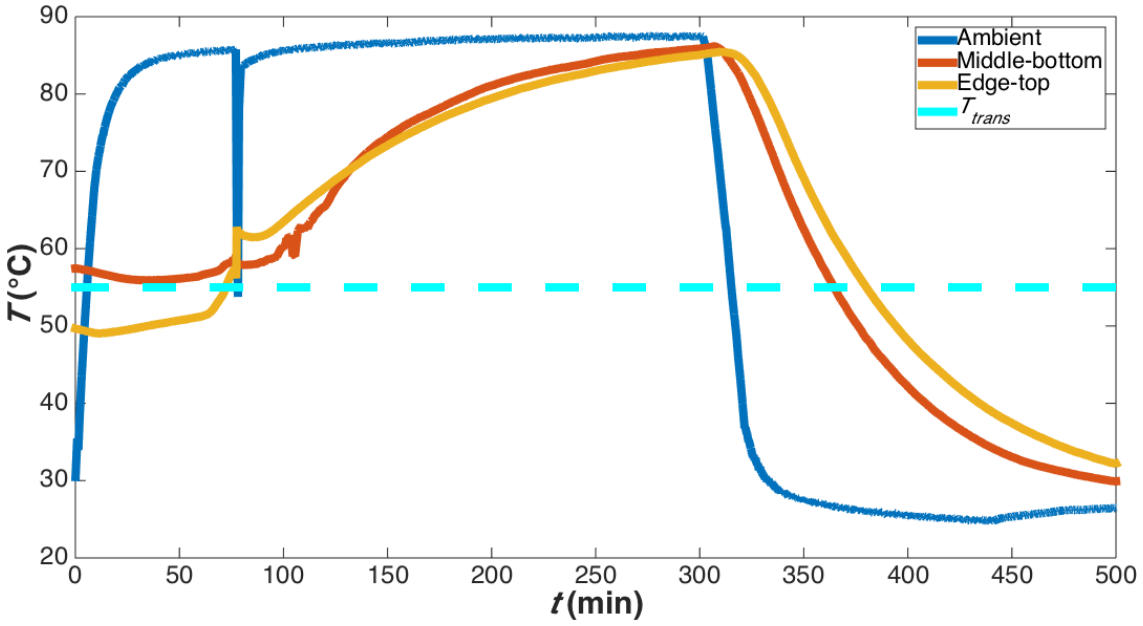

Figure 3-34: Complete charging (up to 86 ˚C) of Mark I, resulting in complete supercooling. The charge-cycle began immediately after triggering nucleation from supercooling at room-temperature. The dashed line corresponds to the average SAT PCM composition T_{trans} = 55 ˚C.

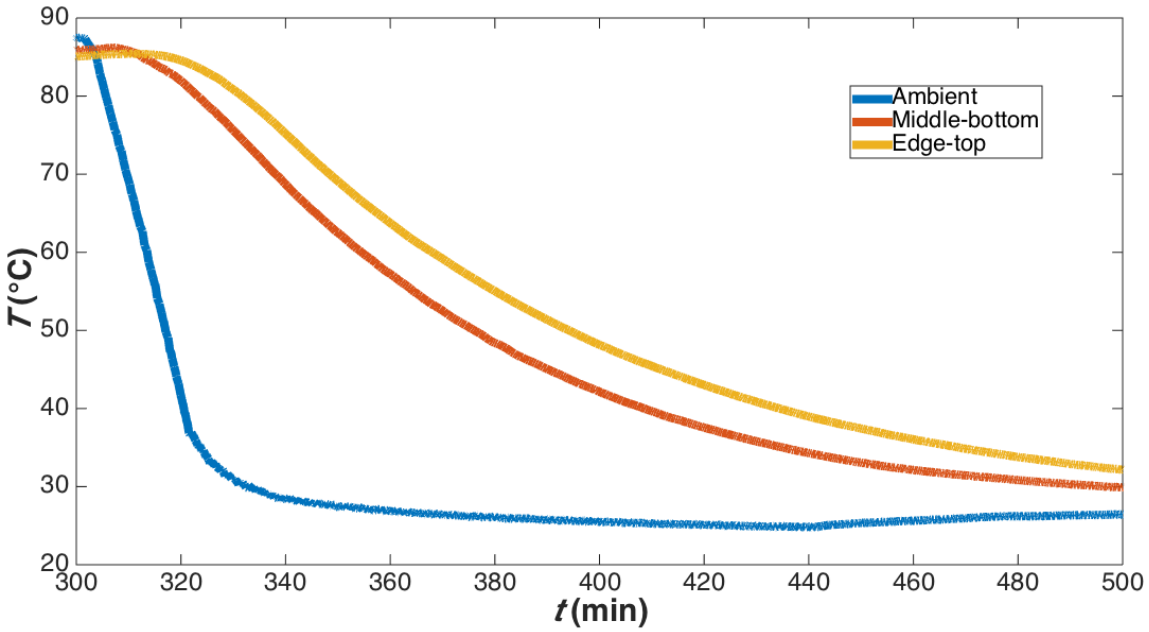

Figure 3-35: Close-up of complete supercooling shown in Figure 3-34. Cooling curves (middle-bottom and edge-top probes) remained monotonically smooth, corresponding to single-phase cooling only (i.e., no halts or breaks).

Regarding evidence of the presence of anhydrous SA in the Mark I heat storage cells during phase-change cycles, Figure 3-36 shows residual crystalline solid material (somewhat transparent) at the bottom of the PCM cavity after repeated cycles for which $T \leq 80$ ˚C during charging. Full dissolution and successful supercooling was eventually recovered as evidenced in Figure 3-37 by introducing fresh water in the PCM, consistently charging the PCM above 80 ˚C, and inducing mixing by manual agitation at elevated temperatures.

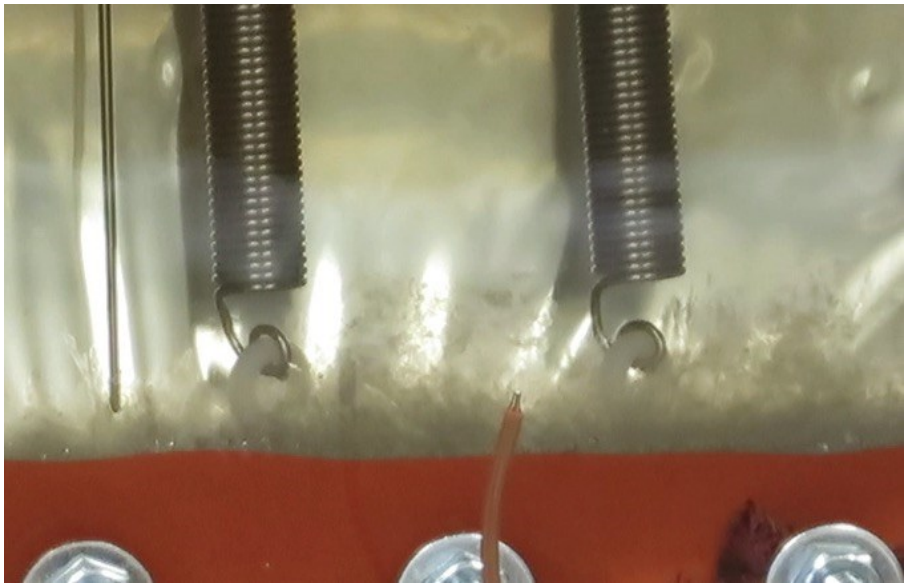

Figure 3-36: Suspected anhydrous SA at the bottom of Mark I following repeated cycles with failure to supercool and $T < 80$ ˚C during charging. The surrounding liquid in this image was supercooled for one day.

Figure 3-37: Image capture from HD video taken at the beginning of a nucleation triggering experiment using Mark I. The SAT PCM was fully dissolved and supercooled to 22 ˚C with no signs of anhydrous SA present. The spring-nucleation triggers shown here correspond to those shown in Figure 3-36.

3.3.3.2 REPEATED THERMAL CYCLING

As was noted from the Mark I experiments, full dissolution would only occur reliably when the temperature measured at the bottom of the heat storage cell would exceed 80 ˚C, suggesting that the SAT PCM became stratified following a few cycles. Despite

stratification, the function of the SAT PCM remained the same, and would supercool reliably following complete dissolution. Failure to do so resulted in suspected anhydrous SA formation at the bottom of the heat storage cell that would compromise the ability to supercool successfully, often resulting in uncontrolled autonucleation of the surrounding supercooled PCM. Using air as a heat transfer medium, which is generally a poor choice with respect to convective heat transfer at solid interfaces, caused charging times to nominally exceed five hours (if initiated from the room temperature discharged state).

The lessons learned regarding operating parameter selection for reliable phase change cycling from the Mark I experiments were applied to Marks II and III experiments, operated in either of the two autonomous circulating HTF systems (ETS and heater-chiller loops). Since heat exchange was supplied to the heat storage cells via their respective heat exchange plate pairs, with the heat storage cells and their respective heat exchange plates plumbed for parallel HTF flow, higher heat-transfer rates to the SAT PCM were anticipated for both Marks II and III, also resulting in substantially shorter anticipated charge durations than observed for Mark I. Furthermore, the Mark III heat storage cells were the first to be equipped with HTF heat exchange inlet channels traversing the bottoms of their bases, providing additional heat transfer area directed where the solid SAT PCM would reside during charging. Consequently, an accelerated charging process for Mark III was anticipated in comparison to Mark II. Recall that only one Mark II heat storage cell was fabricated for these experiments while there were three Mark III heat storage cells.

Since the ETS loop consolidated all operating function control to the user-programmed LabView VI (unlike with the heater-chiller loop), charge-control could be implemented on the basis of the internal temperatures of the heat storage cells, rather than exclusively controlled by timed steps. As such, the ETS loop was used to evaluate state-based charging durations in order to evaluate the ability to achieve objectives 9 and H in Section 2.2. Although the programming of the ETS loop charge-control could be further refined to reflect the inherent charge duration to the individual heat storage cells, it was programmed conservatively to ensure complete charging/dissolution of the SAT PCM. Specifically, the VI included a one hour hold initiated after the minimum of the real-time internal temperature readings exceeded 80 ˚C to ensure complete dissolution of the PCM

prior to concluding the charging operation and initiating supercooling. Charged only to 80 ˚C, the calculated heat storage capacity of SAT PCM in the heat storage cells using Eqs. (2.3) to (2.6) in Section 2.3.2.2 was at least 377 kJ/kg instead of 475 kJ/kg at 110 ˚C; 51 % would also remain stored if supercooled to 20 ˚C instead of 40 % for SAT PCM initially charged to 110 ˚C.

The discharge processes generated by the ETS and heater/chiller loops, although not charging the cells up to 110 ˚C, were programmed to resemble the profile of Cycle 2 in Section 2.3.2.2. Initially, the sensible heat-only discharge would generate a supercooled SAT PCM < 28 ˚C, causing the nucleation triggers to activate and produce latent-only discharge until discharged < 26 ˚C, re-initiating the charge control algorithm.

Note that the thermocouple probes belonging to the individual heat storage cells of Mark II (x1) or Mark III (x3) were named according to their heat storage cells' respective locations in the closed-loop circulating HTF system. The sole Mark II heat storage cell was installed in position '5' (see Figure 3-38), therefore its respective thermocouple probes were named $X5_p$, where 'X' denoted the vertical position ('B', 'M', or 'T'), and the subscript 'p' ('1' or '2') denoted the individual thermocouples shown in Figure 3-6 in Section 3.2.2. The Mark III heat storage cells were installed in positions '1', '3', and '4' (see Figure 3-38), for which their respective thermocouples were named XN, where 'X' denoted the vertical position ('B', 'M', or 'T', but only two present per cell, recall Figure 3-13) and 'N' denoted the heat storage cell position ('1', '3', or '4'). Positions '1' and '2' (unoccupied) belonged to the ETS loop side of the system, while '3', '4', and '5' belonged to the heater-chiller loop side (see Figure 3-22).

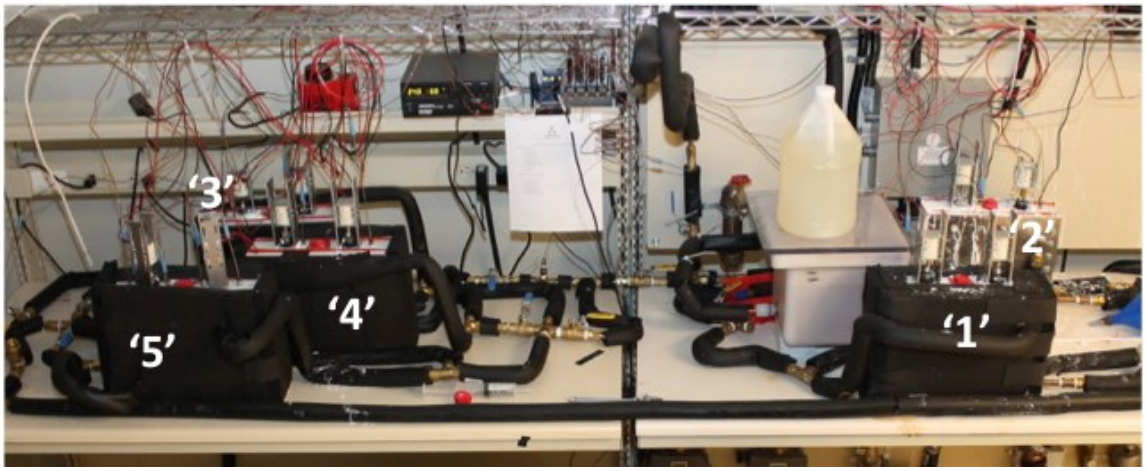

Figure 3-38: Marks II and III circulating HTF experiment table-top view showing locations of heat storage cells '1' to '5'.

3.3.3.2.1 MARK II

Figure 3-39 shows the result of repeated thermal cycling of Mark II in the ETS loop with an HTF flow rate of 3 L/min combined flow to both the heat storage cell heat transfer plates, and an HTF maximum temperature setting of 90 ˚C used for the 120 V heater's thermostat. The power supplied to the fan for HTF cooling was set to 100 V with air inlet temperatures varying between 20 ˚C and 22 ˚C throughout all experiments. Note that temperature profiles within the respective bottom ('B'), middle ('M'), and top ('T') thermocouple pairs (representative locations shown in Figure 3-40) were closely overlapped in Figure 3-39. They are more easily distinguished in all of the subsequent figures in this section that have shorter timescales.

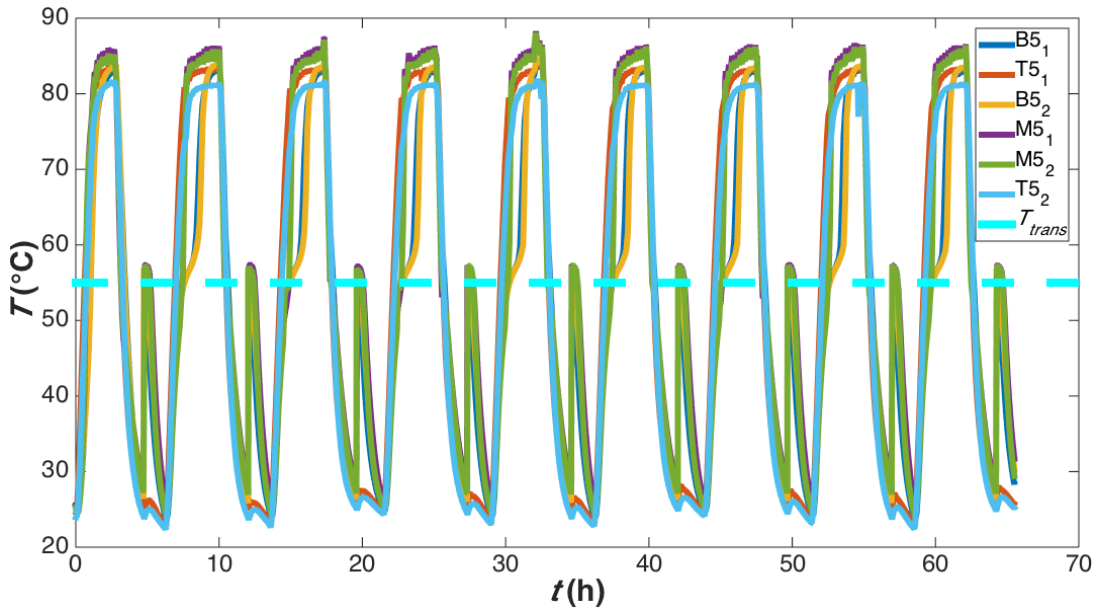

Figure 3-39: Mark II repeated cycling in ETS loop at 3 L/min HTF flow rate and with the fan voltage set to 100 V AC. The dashed line corresponds to the average SAT PCM composition T_{trans} = 55 ˚C.

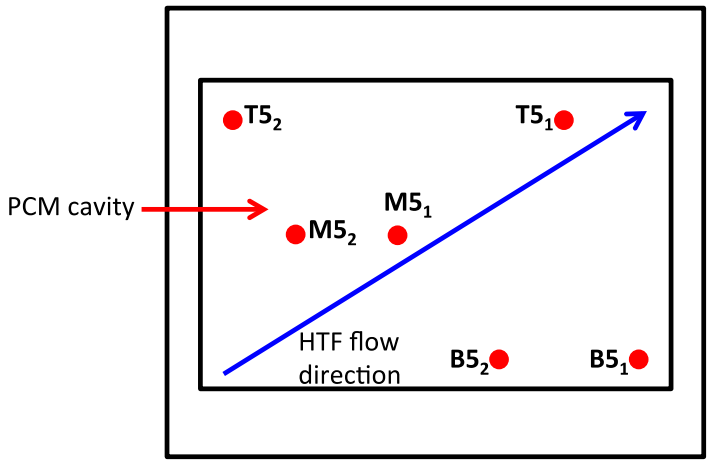

Figure 3-40: Mark II schematic diagram showing the approximate locations of thermocouples (red circles) in the PCM cavity as well as the relative direction of HTF flow (blue arrow).

The charge-supercooling-discharge behaviour was well maintained throughout, exhibiting charge durations of 3.8 h and discharge durations (supercooling included) of 3.6 h. When the HTF flow rate was changed to 1.5 L/min, these durations became 4.8 h and 3.7 h, respectively; the discharge duration remained mostly unchanged due primarily to the fact that solidification was the heat transfer limiting process (not assisted by internal natural convection of the PCM) and only weakly affected by the HTF flow rate,

as was similarly observed by Liu et al. (2014) for PCM heat storage using dodecanoic acid.

Figure 3-41 shows the closely replicated phase-change processes as recorded by all six thermocouples located in the Mark II PCM cavity (recall Figure 3-6) during subsequent cycles spanning 24 h. Note that phase change is absent during the charging process of the first cycle as it was initiated from a supercooled room-temperature state rather than the corresponding equilibrium state.

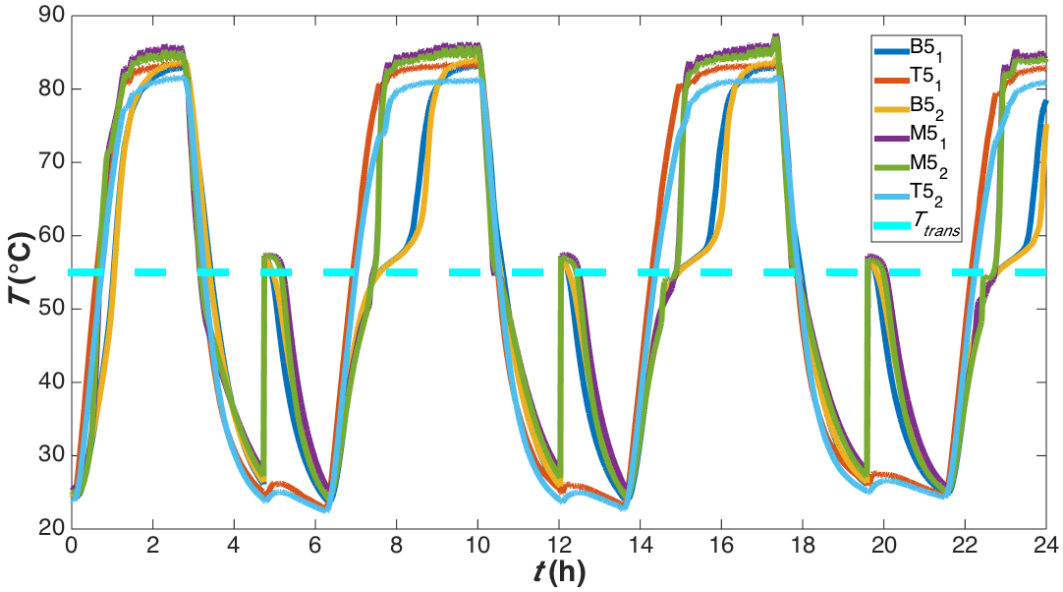

Figure 3-41: 24 hour close-up of the Mark II experiment shown in Figure 3-39. The dashed line corresponds to the average SAT PCM composition T_{trans} = 55 ˚C.

In a detailed look at one of the complete cycles shown in Figure 3-41, Figure 3-42 shows the Mark II phase-change processes in comparison to T_{trans} = 55 ˚C for the uniformly mixed SAT PCM, also showing the HTF inlet and outlet temperatures used to generate heat transfer with the PCM. Of note to the recorded internal temperature profiles for Mark II in comparison to each other and to T_{trans} were:

1. The SAT PCM became stratified with respect to salt concentration, as evidenced by the absence of solidification-heating in the profiles of $T5_1$ and $T5_2$, as well as the nucleation temperatures recorded by $B5_1$, $B5_2$, $M5_1$, and $M5_2 \geq T_{trans}$;
2. Relating to 1, the top thermocouples revealed the presence of a dilute local SAT solution ($0.32 \leq w_{SA} \leq 0.35$, locally, i.e., saturated liquid between 20 ˚C

and 30 ˚C), since no phase-change was detected at those location during charging as well;

3. Extended duration of the phase change process was observed for probes $B5_1$ and $B5_2$, exclusively, without the appearance of erratic temperature behaviour associated with solid SAT PCM collapsing toward the bottom;
4. Only very weak horizontal temperature gradients were recorded between thermocouples of similar vertical position;
5. Vertical temperature gradients (isolated for comparison in Figure 3-43) revealed unusual thermal stratifications, both during charging and supercooling;
6. And, temperature profile anomalies during supercooling, occurring around the approach to 55 ˚C, were recorded by both $M5_1$ and $M5_2$ (neither halt nor breaks).

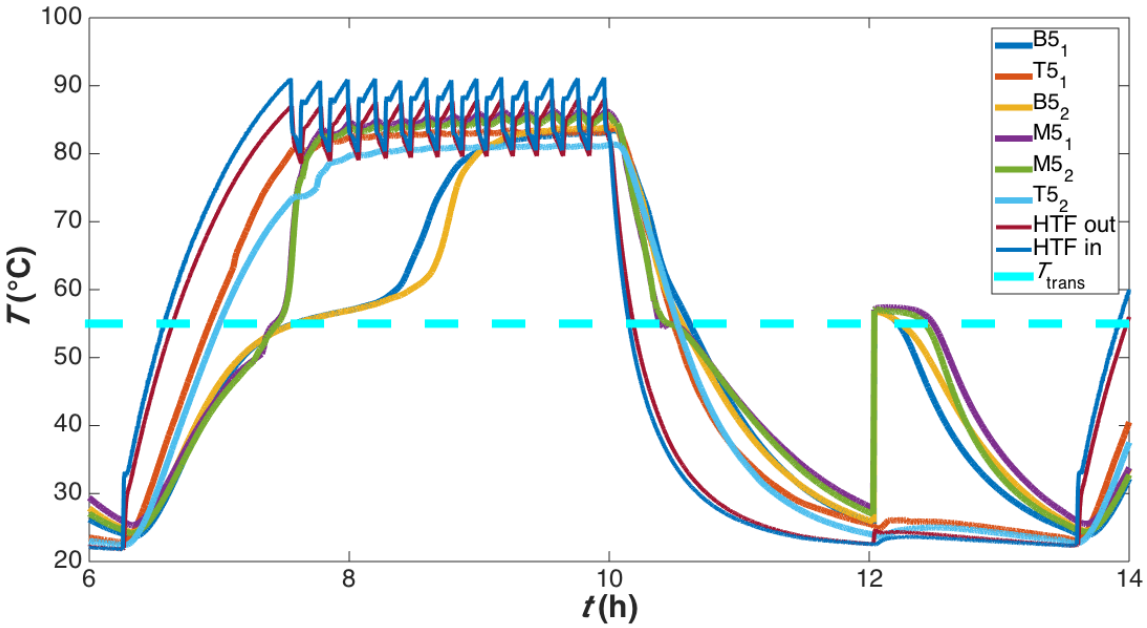

Figure 3-42: Close-up of first complete Mark II cycle shown in Figure 3-39 and Figure 3-41 also showing HTF temperatures in the ETS loop. The dashed line corresponds to the average SAT PCM composition T_{trans} = 55 ˚C.

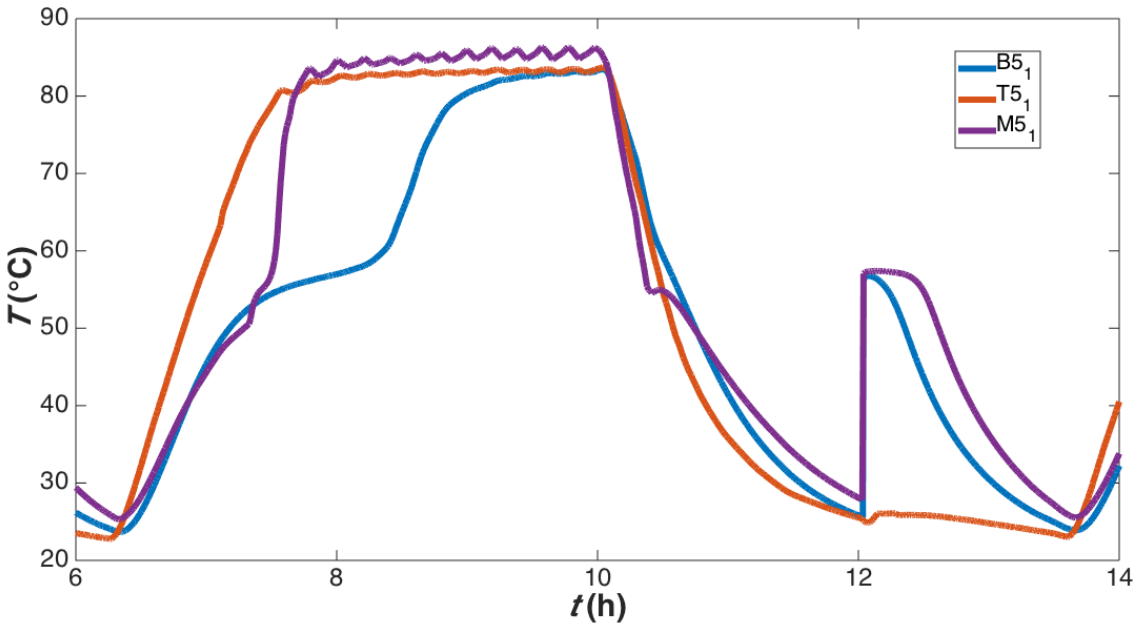

Figure 3-43: Temperature profiles shown in Figure 3-42, omitting HTF temperatures and duplicate bottom, middle, and top thermocouples, thereby revealing only the vertical temperature gradients.

There were no unusual revelations in items 1, 2, and 4 as relating to the experience gained from Mark I. Item 3, although constituting a deviation from Mark I, was attributable to the fact that phase-change occurs more stably (no collapse of the solid PCM) in Mark II than in Mark I due to the symmetry of heat transfer plates with respect to the base and PCM within it.

Regarding item 5, however, the middle thermocouples in Mark II were revealed to exceed the top thermocouples, for which normal thermal stratification would dictate the top to be warmer than at depths beneath it. As discussed in Section 1.2.1.1, the effect of solution stratification can overcome normal thermal stratification, sometimes causing the temperature at the top of the denser, concentrated solution residing underneath the lighter, dilute solution, to exceed its top-most temperature. The facts that temperatures recorded by $M5_1$ and $M5_2$ remained consistently higher than those from $B5_1$ and $B5_2$ and that they also shared similar post-nucleation temperatures suggest that the SAT PCM was separated into just two strata: one dilute strata resting overtop the other, concentrated strata.

The temperature anomalies noted in item 6, were observed to occur consistently between consecutive cycles (for example, see Figure 3-41). They also did not correspond

to the recorded phase-change conditions of the stratified SAT PCM (T_{trans} > 55 ˚C) nor did they affect the ability to successfully supercool Mark II, and therefore were not attributed to incomplete phase change[44], as was observed for Mark I. Instead, the anomalies were most likely attributable to the effects that solution stratification had on the vertical temperature gradient, such that the middle thermocouples might have been located near the re-establishment of the solution's thermocline, wherein a sharp temperature gradient would be found.

At the onset of heat transfer (e.g., cooling), natural convection patterns are initiated and disrupt the existing thermocline prior to stabilizing it anew, corresponding closely to seasonal overturn in lakes, also referred to as 'soft' mixing by Dannemand et al. (2015a). The temperatures surrounding the previously stable thermocline would become temporarily uniform due to local mixing until such time that a stable thermocline can be re-established. Support of this hypothesis was also found in the fact that location of the anomalies also corresponded to the times at which the middle probes re-established the thermal stratification pattern observed in their stratum with the bottom probes during charging and deviated strongly from the temperatures of the top probes (i.e., re-establishment of the thermocline).

Regarding the stability of solution stratification, repeated cycles of the Mark II enclosure did not reveal evidence of stratification intensification nor abatement; it remaining stable and repeatable throughout the experiments (discussed further in Section 3.3.5). However, as noted in Section 3.3.2.2, Mark II did eventually succumb to a breach of integrity to the PCM cavity, causing an irreparable failure to supercool after 37 cycles. This is shown in Figure 3-44 whereby the 'B' and 'M' thermocouples recorded autonucleation of the SAT PCM during heat discharge in the second cycle and for all subsequent cycles as well. As noted above Figure 3-42, the SAT PCM surrounding the 'T' thermocouple probes in Mark II did not respond to solidification due to solution stratification.

[44] Incomplete phase change would not likely occur exclusively in the middle of the PCM, since remaining solid SAT would normally be found at the bottom.

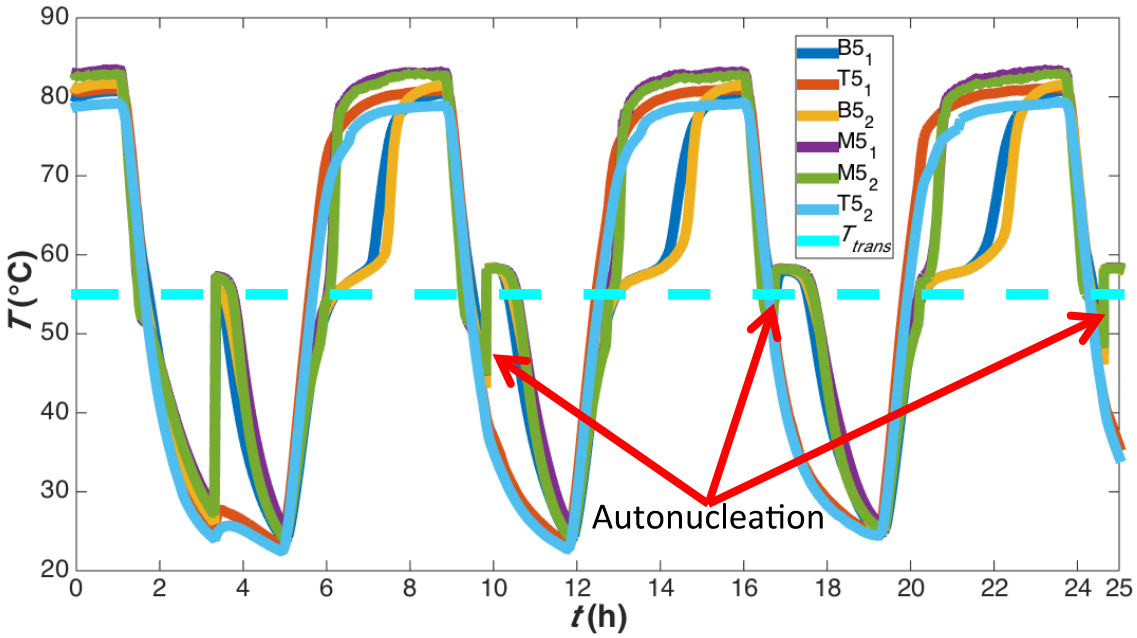

Figure 3-44: Development of permanent failure to supercool (i.e., autonucleation) in Mark II over repeated thermal cycling operated in the ETS loop with 2 L/min HTF flow rate and fan operated at 100 V AC. The dashed line corresponds to the average SAT PCM composition T_{trans} = 55 ˚C.

3.3.3.2.2 MARK III

Mark III heat storage cells, installed in positions '1', '3', and '4' of the circulated HTF system, were exercised in repeated thermal cycling experiments in order to evaluate their behaviour vis-à-vis Mark II, as discussed in Section 3.3.3.2.1. Of interest to these evaluations were thermal cycling stability (i.e., phase-change behaviour and both thermal and solution stratifications), supercooling reliability, and charge and discharge durations. Note that the Mark III heat storage cell in position '1' performed reliably until suffering from aluminized film seal integrity leaks (as were observed for Mark II), after which supercooling became compromised and could not be recovered. However, Mark III heat storage cells in positions '3' and '4' were able to cycle consistently and supercool reliably for all 65 and 66 recorded cycles, respectively, with neither exhibiting signs of PCM degradation or compromised seal integrity. Mark III '1' (equipped only with bottom and top thermocouples; B1 and T1 in Figure 3-45) was operated always individually. Mark III '3' (bottom and middle thermocouples; B3 and M3 in Figure 3-45) and '4' (bottom and top thermocouples; B4 and T4 in Figure 3-45) were always operated

simultaneously so as to each act as proxy to one another with respect to their combined thermocouple distributions.

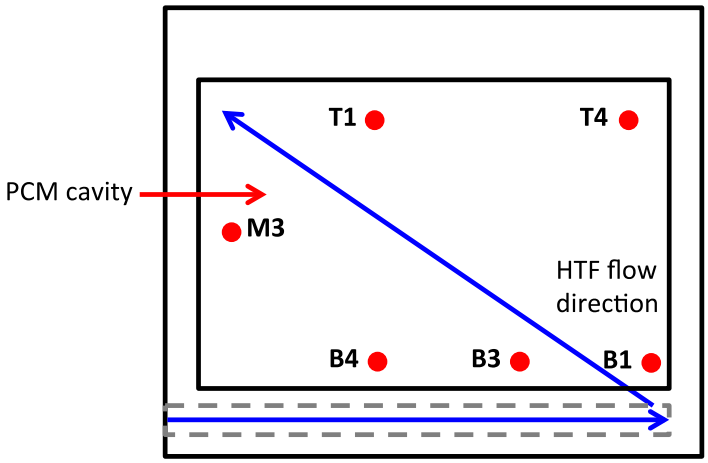

Figure 3-45: Mark III schematic diagram showing the approximate locations of thermocouples pairs (red circles) in the PCM cavity belonging to '1', '3', and '4', respectively. The relative direction of HTF flow (blue arrow) is also shown.

As had been observed for Marks I and II, Figure 3-46 illustrates the development of stable solution stratification in Mark III '1' during the course of the first 24 h of an ETS loop experiment. The established stratification became unchanged and stable in the period following, as was seen throughout the remaining repeated cycles of the experiment, shown in Figure 3-47.

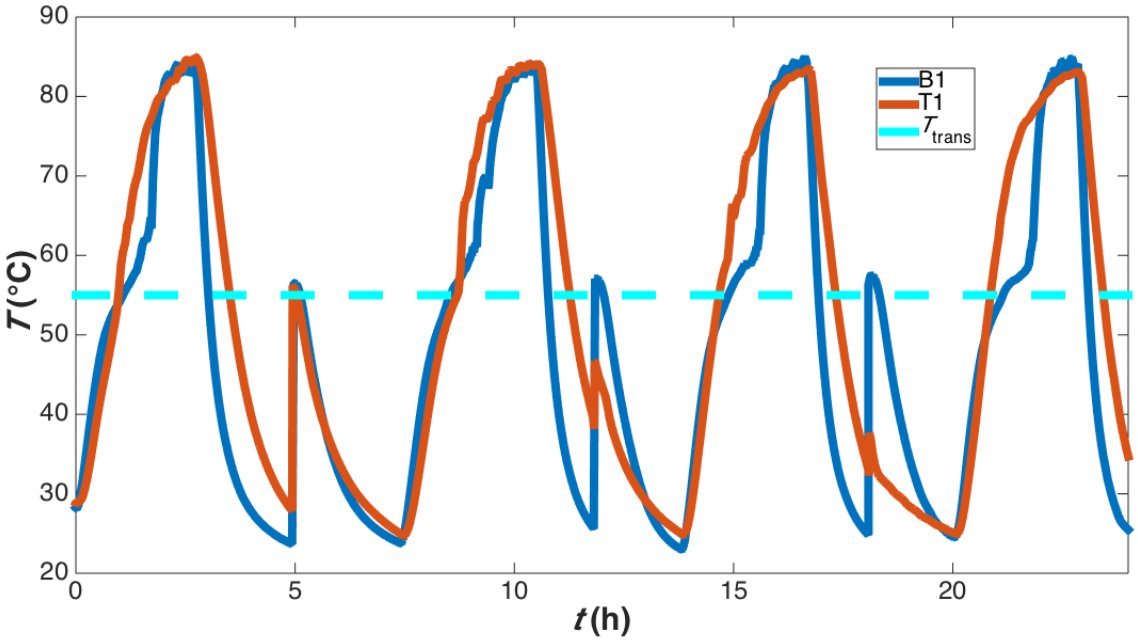

Figure 3-46: Mark III ('1') repeated thermal cycling in ETS loop at 3.2 L/min HTF flow rate and with the fan voltage set to 120 VAC, showing the experiment's first 24 hour interval. The temperature profiles of B1 and T1 showed the gradual development of solution stratification, whereby only the SAT PCM around B1 would remain responsive to solidification. The dashed line corresponds to the average SAT PCM composition T_{trans} = 55 ˚C.

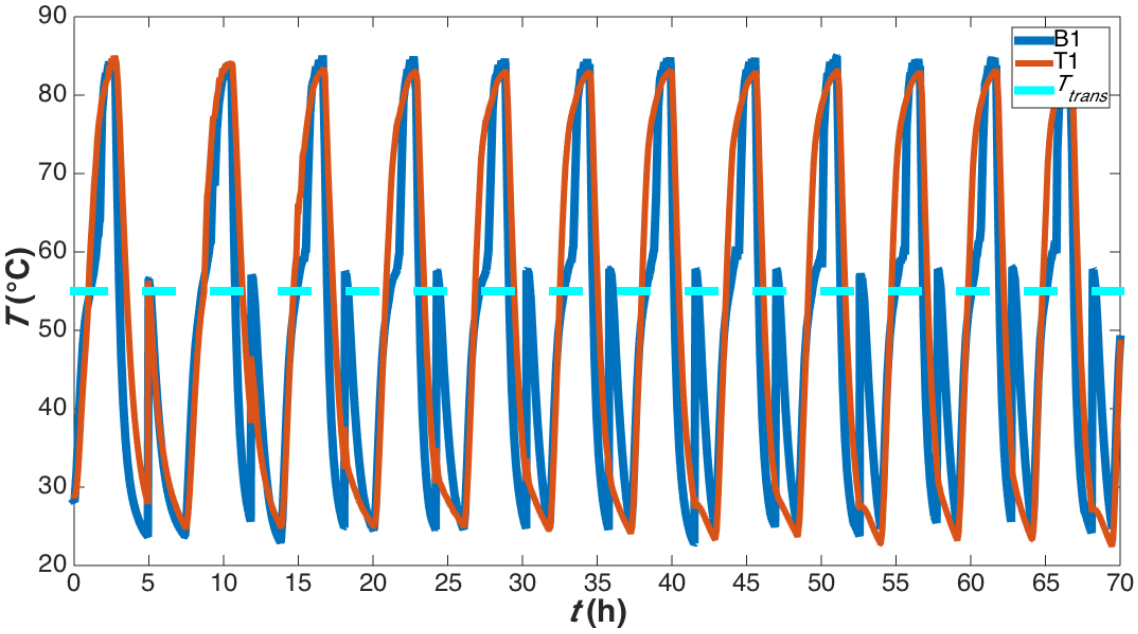

Figure 3-47: Complete Mark III ('1') repeated thermal cycling experiment in ETS loop at 3.2 L/min HTF flow rate and with the fan voltage set to 120 VAC, of which the first 24 hours were shown in Figure 3-46. The temperature profiles of B1 and T1 showed the stabilization of solution stratification after 35 hours. The dashed line corresponds to the average SAT PCM composition T_{trans} = 55 ˚C.

Operated in the ETS loop simultaneously (Figure 3-48), both Mark III '3' and '4' exhibited solution stratification corresponding to that which was observed for Mark III '1', also remaining stable for the remainder of the experiments. Supplied with an average HTF flow rate of 3.2 L/min (Figure 3-46 and Figure 3-47), the charge and discharge durations for Mark III '1' were found to be 2.9 h and 3.3 h (although the cooling fan was supplied power at 120 V, not 100 V), both significant improvements compared to Mark II under similar conditions. With average individual HTF flow rates of 1.8 L/min (Figure 3-48), Mark III '3' and '4' also displayed significantly improved charge durations compared to Mark II, equal to 4.1 h, while showing comparable discharge durations of 3.8 h. Although little impact was realized during discharge[45], the addition of HTF flow channels traversing the bottom of the Mark III base generated significant benefit to heat-transfer rates during charging, as intended in its design.

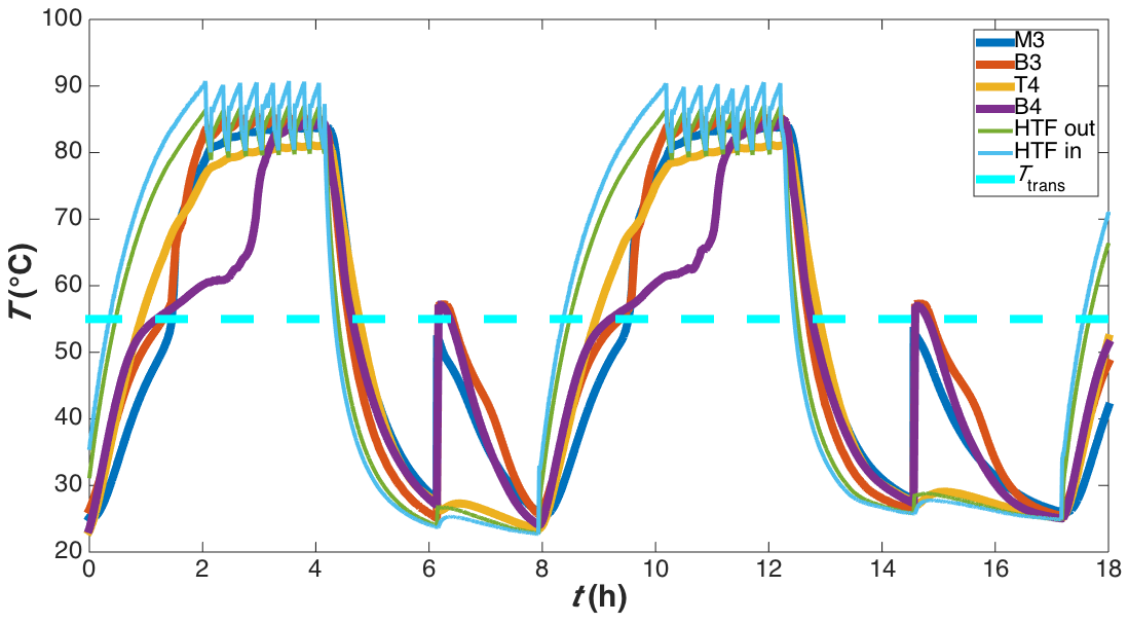

Figure 3-48: Mark III ('3' and '4') ETS loop experiment at 3.6 L/min combined HTF flow rate and with the fan voltage set to 100 VAC, also showing HTF temperatures in the ETS loop. The dashed line corresponds to the average SAT PCM composition T_{trans} = 55 ˚C.

Respecting thermal gradients in Mark III, Figure 3-49 illustrates the relationships between bottom, middle, and top thermocouples during a complete charge-supercooling-

[45] During solidification, heat discharge from the heat storage cells is dominated by the rate-limiting resistance to heat transfer generated by the stationary solid SAT.

discharge cycle for ‘3’ and ‘4’. Vertical thermal gradients during charging differed from the gradients observed for Mark II, whereby the natural thermal gradient within the lower, concentrated stratum was not observed due to the localized heat supply directed to the bottom of the Mark III bases, wherein the bottom probes (B3 and B4) exceeded the temperature of the middle probe (M3). During discharge, however, the natural thermal gradient was quickly established, also likely due to the localized heat transfer at the bottom of the Mark III bases. Similar to Mark II, the temperature of the upper, dilute stratum in ‘4’ (T4) was less than that measured in the lower stratum (B4).

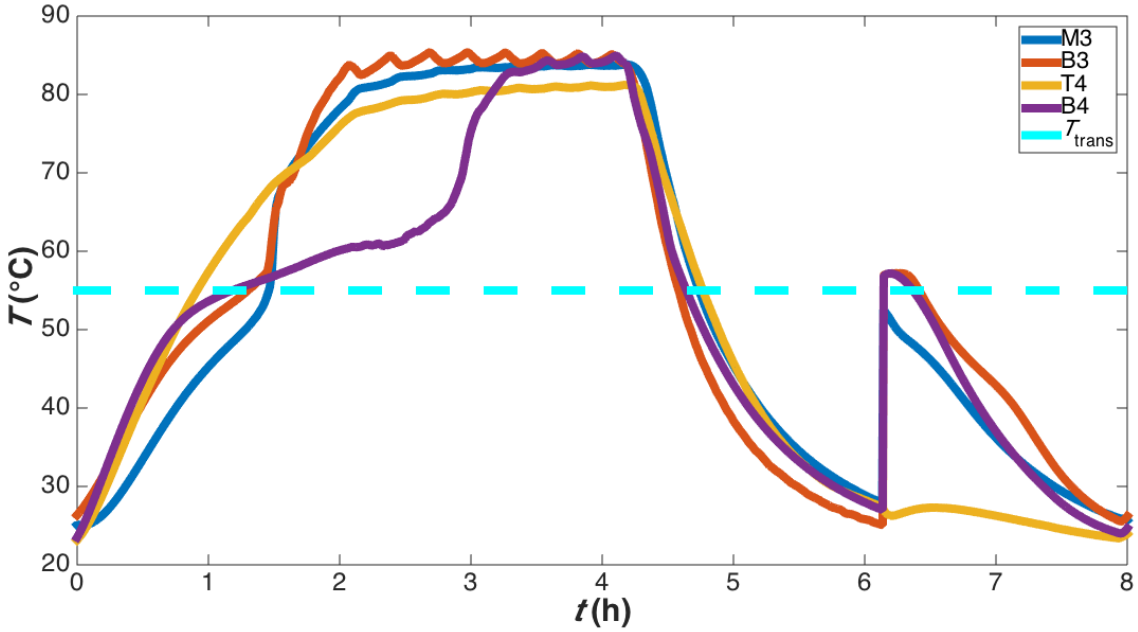

Figure 3-49: Close-up of the first cycle for both Mark III heat storage cells shown in Figure 3-48 (excluding HTF temperatures). The dashed line corresponds to the average SAT PCM composition T_{trans} = 55 ˚C.

Unique to the Mark IIIs, however, was the presence of a horizontal temperature gradient, as observed between B3 and B4 in Figure 3-49. Recall from Section 3.2.3 that the horizontal positions of the bottom probes varied with respect to the location of the HTF connection between the base and the adjacent heat exchange plate assemblies in at least one base. Note that the location of B4 corresponded to the depiction in Figure 3-13, B3 was located in the same horizontal location in ‘3’ as was T4 in ‘4’. Effectively, B4 was located farther from the base’s HTF connection to the heat exchange plate assemblies than was B3, and B4 shows a longer duration for complete phase-change and to achieve

the maximum charged state than at B3 (Figure 3-49). The latter illustrated that locations farther away from the HTF connections (i.e., inlet to the heat exchange plates) experienced lower rates of heat transfer than those nearer to the HTF connections. This was likely due to the non-uniform distribution of the HTF flow traversing the heat exchange plates diagonally toward the outlets and the decreasing HTF temperature towards the outlet resulting from heat transfer to the SAT PCM.

Erratic temperature variations observed for B4 during charging in both Figure 3-48 and Figure 3-49 correspond to those previously observed for Mark I, but absent in Mark II. This suggested that collapsing solid SAT PCM towards the bottom occurred regularly in Mark III, likely due to the base HTF channels directing heat at the bottom of the solid SAT PCM, effectively eroding the ability for the solid SAT to support itself within the heat storage cell during charging.

The nucleation temperatures recorded by M3 (~ 52.5 ˚C) in Figure 3-48 and Figure 3-49 were observed below $T_{trans} = 55$ ˚C, which was also unique to Mark III. This indicated that the local composition around M3 still remained close to $w_{SA} = 0.532$ (average composition of the SAT PCM), despite establishing stable solution stratification. Since M3 was used to substitute T3 and positioned only after the complete assembly of the Mark III '3' heat storage cell, its vertical position within the heat storage cell could not be determined with certainty. Therefore, it was noted that the position of M3 might have been more elevated than for the middle thermocouples in Mark II, which could have placed the probe higher in the thermocline (region of sharp gradients between strata) than in Mark II. When heated using an HTF flow with the maximum supply temperature set to 95 ˚C, as shown in Figure 3-51, the nucleation temperature recorded at M3 resembled that at B3 and B4 and it remained in normal thermal stratification with respect to B3 and B4 when the SAT PCM at all locations was fully dissolved, a pattern that remained consistently repeated at those conditions (Figure 3-51). This indicated a local solution concentration $w_{SA} > 0.532$, coinciding with the locations of B3 and B4, meaning that M3 then appeared to be located below the thermocline. Since the thermocline would be anticipated to rise in elevation when subjected to higher temperature HTF supply due to the thermal expansion of dissolved PCM as well as improved mixing caused by

intensifying natural convection, the hypothesis regarding the vertical position of M3 seemed to be confirmed.

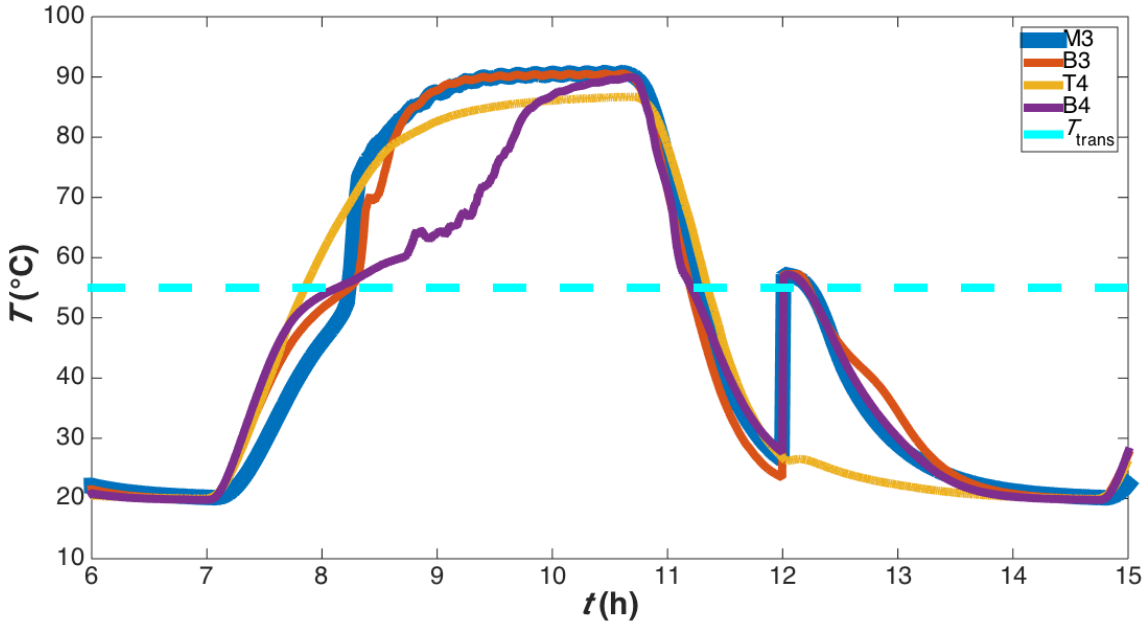

Figure 3-50: Complete cycle using Mark III ('3' and '4') heat storage cells in the heater-chiller loop at nominally 2 L/min HTF flow rate each. HTF heating and cooling temperatures were set to 95 ˚C and 20 ˚C, respectively, but not shown. The dashed line corresponds to the average SAT PCM composition T_{trans} = 55 ˚C.

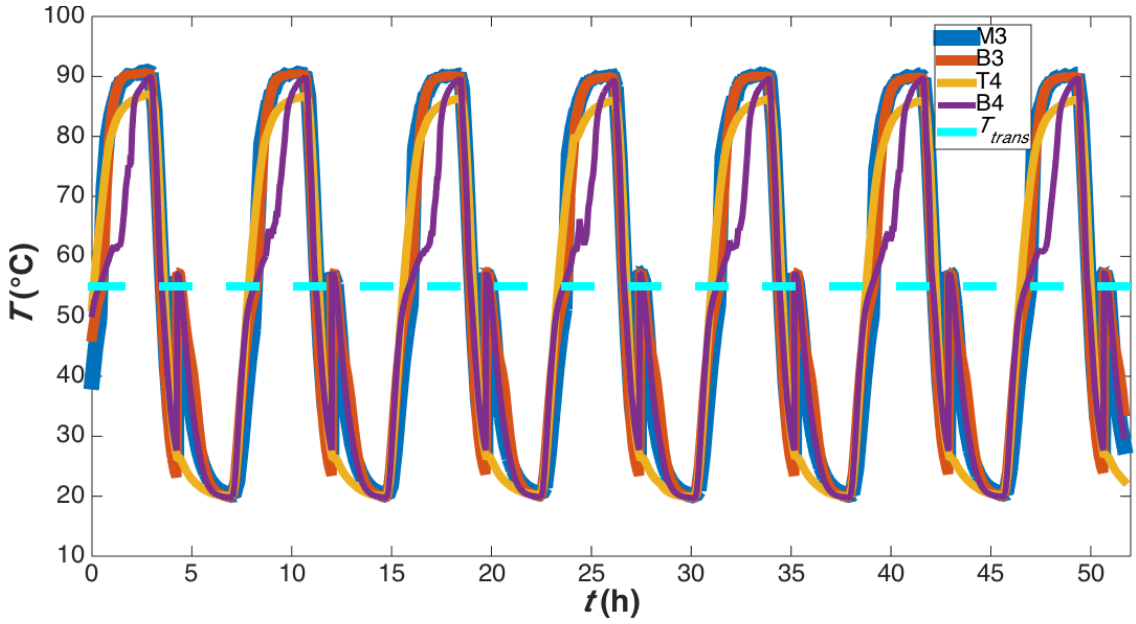

Figure 3-51: Repeated cycling of Mark III ('3' and '4') heat storage cells in the heater-chiller loop at nominally 2 L/min HTF flow rate each, corresponding to the single cycle shown in Figure 3-50. The dashed line corresponds to the average SAT PCM composition T_{trans} = 55 ˚C.

The instantaneous heat transfer rates notwithstanding (deferred to Chapter 4), the Mark III heat storage cells charged in the ETS loop up to 80 ˚C have exhibited charge-cycle average heat transfer rates of 0.24 kWh/cell ÷ 2.9 h = 0.083 kW/cell. As such, it is conceivable that an ETS system equipped with a 1.2 kW to 1.5 kW electric heater and capable of supplying HTF flow rate at a combined flow rate of ≥ 3 L/min could achieve simultaneous (i.e., parallel flow) full system charge up to 110 ˚C (0.3 kWh/cell) of at least fourteen Mark III heat storage cells in 7 h (14 cells × 2.3 kg/cell = 32 kg, equal to 4.2 kWh at 110 ˚C), and possibly capable of charging still more cells in succession to these.

Discharging these packs in successive groups of seven Mark III cells at low HTF flow rate (~ 1.5 L/min per cell, generating higher-temperature HTF supply to the fan heat exchanger), should suffice to deliver intermittent heat discharge at an average of 510 W, instantaneous discharge heat exchange rate notwithstanding (deferred to Chapter 4). Intermittently releasing the stored heat from an ETS system at controlled intervals to maintain thermostatic room temperature control could suffice to span the entire combined 17 h combined mid-peak and on-peak periods of TOD rate programs imposed in some jurisdictions (e.g., United Kingdom (Byrom, 2016)), at least during periods of mild outdoor weather.

3.3.4 NUCLEATION TRIGGERING

Information was sought from the Mark I heat storage cell thermal cycling experiments in the areas of nucleation triggering reliability, solidification front expansion rate (i.e., rate of self-heating after nucleation), and overall nucleation triggering strategy. The Mark I heat storage cell was equipped with five spring-nucleation triggers, capable of being individually or simultaneously actuated by their respective solenoids. These were selected to be triggered in symmetric and mostly equidistant scenarios of one trigger (middle-only), three (middle and both exterior triggers), or all five.

Figure 3-52 highlights the success with which the spring-nucleation triggers generated solidification within the supercooled SAT PCM. Not evidenced in the single video frame captured in Figure 3-52, spring-triggers subjected to greater extension generally produced a greater population of active solidification sites, which is preferred to reliably produce nucleation.

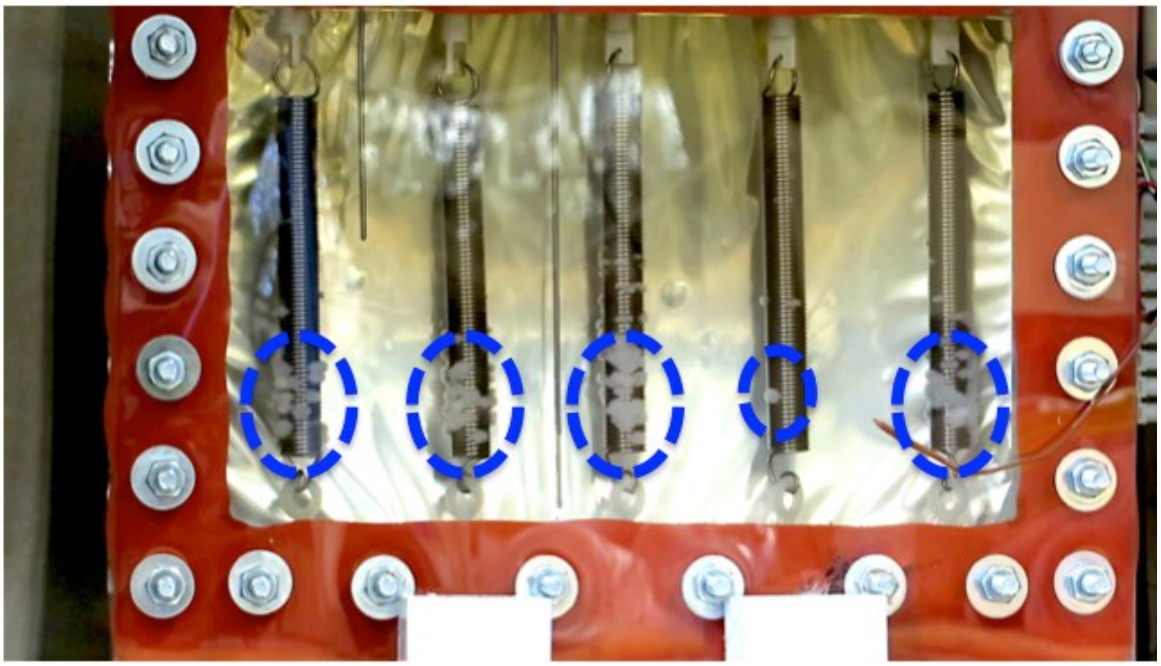

Figure 3-52: HD video frame capture of the onset of solidification (i.e., nucleation triggering) using all five spring-nucleation triggers in the Mark I heat storage cell. Nucleation triggering occurred after supercooling to 23 ˚C for > 12 h. Hashed ellipses have been added to highlight the main active nucleation sites.

The spring-solenoid pair located second from the right in Figure 3-52 consistently generated the least extension, and therefore typically fewer active nucleation sites. Since the pulling force generated by solenoids is a function of the shaft insertion depth at rest, whereby deeper insertions generate stronger forces, greater extension could not be generated from that spring-solenoid pair used in Mark I due to the fixed positioning. Marks II and III have addressed this failure by supporting the solenoids on adjustable stands and extending the PP pegs outside the base. However, improved actuation could also be achieved by using push-action solenoids, pushing in such a way as to exert an extension of the spring (e.g., assisted by pulleys or pointed upward from the PP peg). The latter would always result in the maximum displacement possible since the actuator shaft would remain at the maximum insertion depth while at rest, resulting in the maximum push force generated. Other linear electromechanical actuators, such as motor-driven screw drives, could also be used to generate displacement of the springs in a manner that is independent from their position with respect to the springs. Solenoids remain favourable nonetheless due to their compactness and simple, reliable operation.

Although just one active site would be needed to generate a solidification chain-reaction, the minimum is not preferred. From the perspective of reliability alone, even just to combat the risk of insufficient nucleation site exposure from one spring or solenoid failure, it is recommended to always use at least two spring-nucleation triggers, whatever the heat storage cell design.

As illustrated throughout Section 3.3.3, the spring-nucleation triggers shared amongst all heat storage cell designs developed in this project, Marks I to III, performed consistently as intended in > 200 complete charge-supercooling-discharge cycles cumulatively evaluated. Only the Mark I spring-triggers differed from those used in the Marks II and III heat storage cells by their coil dimensions and lower pre-loading force, 3.7 times lower than for Marks II and III. The risk associated with lower pre-loading force is primarily lower contact pressure between coils which is believed to be responsible for retaining SAT seed crystals at elevated temperatures, as the upper temperature limit for seed crystal retention is proportional to the contact pressure. Despite lower pre-loading force, the Mark I spring-triggers were nonetheless adequate to function reliably at PCM temperatures ≤ 85 ˚C. Mark III heat storage cells, exercised up to an internal temperature of 90 ˚C (Figure 3-51), with each cell just using two spring-nucleation triggers with higher pre-loading force than for Mark I, retained reliable nucleation triggering under repeated cycling.

Despite the success shared by the Mark I spring-nucleation triggers and those shared in the Marks II and III heat storage cell designs, given the intended heat storage cell operation up to 110 ˚C (objective 8 in Section 2.2), evaluations should be conducted using the extension springs selected for Marks II and III (rather than for Mark I) due to their anticipated higher operating temperature limit at which they would reliably retain seed crystal between their spring coils. Otherwise, spring-nucleation triggers with even higher pre-loading forces should be selected to ensure reliable function at elevated temperature. Higher spring pre-loading would also benefit from resistance to unintended flexure from minor shocks in use of an ETS system, which should be later evaluated to identify thresholds for normal operation. Note, however, that Mark I[46] frequently

[46] The Mark I heat storage cell was transported in its supercooled state approximately 100 m on a wheeled cart between rooms in adjacent buildings (also on different floors) without triggering

displayed adequate resistance to unintended nucleation triggering during manual shaking aimed at causing internal PCM agitation, suggesting that an evaluation of the presently selected springs should prove promising.

Regarding the particular impact of nucleation triggering strategy on the rate of SAT PCM self-heating (i.e., return to its corresponding equilibrium state), measurements of the solidification front expansion rate were conducted using optical analysis of HD video as seen through the PC sight-glass and infrared (IR) thermography. Due to the inability to view the internal solidification process of the SAT PCM through the sight-glass using IR, IR measurements were conducted using the IR thermography of the surface temperature evolution on the aluminized film side of the heat storage cell.

3.3.4.1 OPTICAL IMAGE PROCESSING

A correlation between optical images captured at 30 frames/s by individual HD video frames and the amount of solid SAT PCM present was required for the analysis of solidification front expansion rates. The video frames originated in full colour, RGB format, for which a correlation to solid SAT PCM would require a multivariable approach. Therefore, the image analysis was conducted using the video frames converted to grayscale, for which individual pixels are described only by their intensity value from light to dark.

Analyses were conducted entirely in Matlab R2014b, facilitated by the features in its Image Processing Toolbox. The algorithm used to import, convert, and process the image data can be found in Appendix D. The process consisted of identifying only the range of video frames in which solidification expansion occurred, in order to improve batch data processing speeds. Throughout this series of video frames, a horizontal cut-line was applied uniformly, from which grayscale pixel data was extracted and stored, as shown in Figure 3-53 and Figure 3-54. This approach was adopted instead of analysing the entire PCM portion of the frame, because only the solidification expansion from surfaces normal to the cut line could yield an accurate linear front expansion rate. Physical dimensions were ascertained for every video, since the exact camera perspective could not be reliably duplicated between tests. This was accomplished by examining objects in

---

nucleation from mechanical shock. Once delivered to the destination room, it rested on a desk in a high-traffic office for 167 days prior to autonucleation.

the frame (and close to the sight-glass frame-of-reference) of known dimension and comparing that to the number of pixels occupied in the span. Nominally, the video frames were recorded with a pixel resolution of approximately 0.2 mm/pixel in the sight-glass's frame-of-reference.

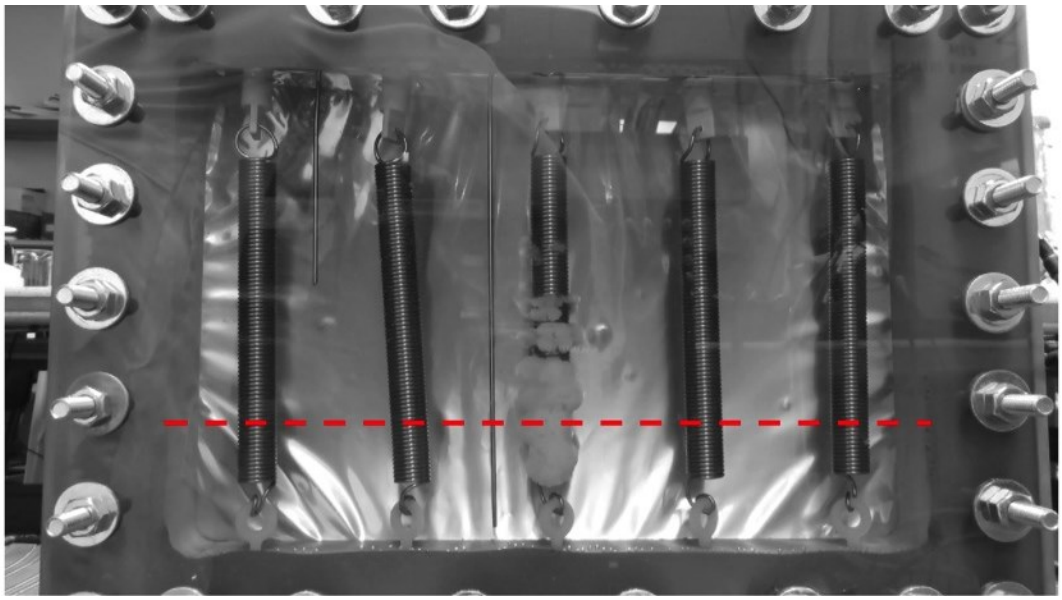

Figure 3-53: HD video frame capture imported in Matlab showing an image converted to grayscale. This image was taken at the beginning of the solidification process after supercooling to 25 ˚C. The dashed line illustrates the path through which the analysis of solidification was conducted.

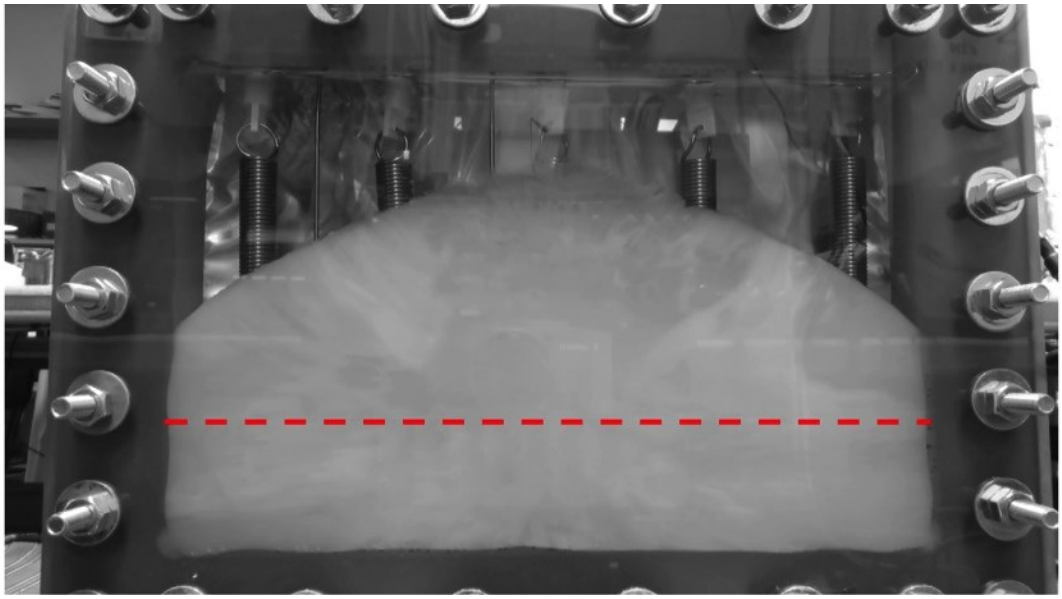

Figure 3-54: HD video frame converted to grayscale in Matlab corresponding to the end of solidification along the dashed cut-line from the experiment shown in Figure 3-53.

Extracting the data along the cut-line in Figure 3-54 revealed the distribution of pixel intensities corresponding to solid SAT shown in the histogram in Figure 3-55. A clear demarcation was determined in the region of grayscale pixel intensity ≥ 130 in Figure 3-55, chosen to represent pixels occupied by solid SAT in all of the optical analyses conducted hereafter.

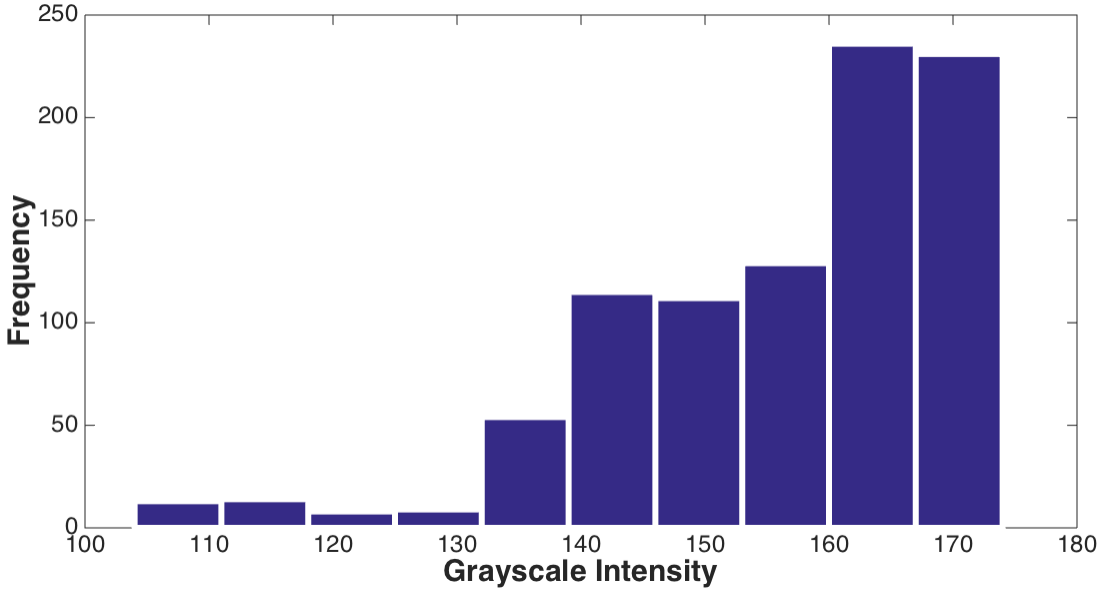

Figure 3-55: Histogram of grayscale pixel intensity along the cut-line in Figure 3-54.

Implementation of the grayscale intensity filter used to identify PCM generated binary images, such as the one shown in Figure 3-56, a method used previously by Kamkari and coworkers to analyze the melt fraction of dodecanoic acid in a transparent container (Shokouhmand et al., 2013; Kamkari et al., 2014). However, since only the pixels not previously recorded in that range could be treated as solid SAT with any certainty, subtraction of the binary image data from the first analysis frame was required (i.e., background subtraction).

Figure 3-56: Binary image conversion from the grayscale image in Figure 3-54 for pixel intensity ≥ 130.

Figure 3-57 shows the net result of this process, through which regions previously showing glare (i.e., high intensity) on the reflective aluminum film seen in the background of the PCM cavity were subtracted from the subsequent images. Despite the significant reduction in available pixels, the resulting image still showed a mostly uniform distribution of the solid SAT pixels on either side of the active spring trigger.

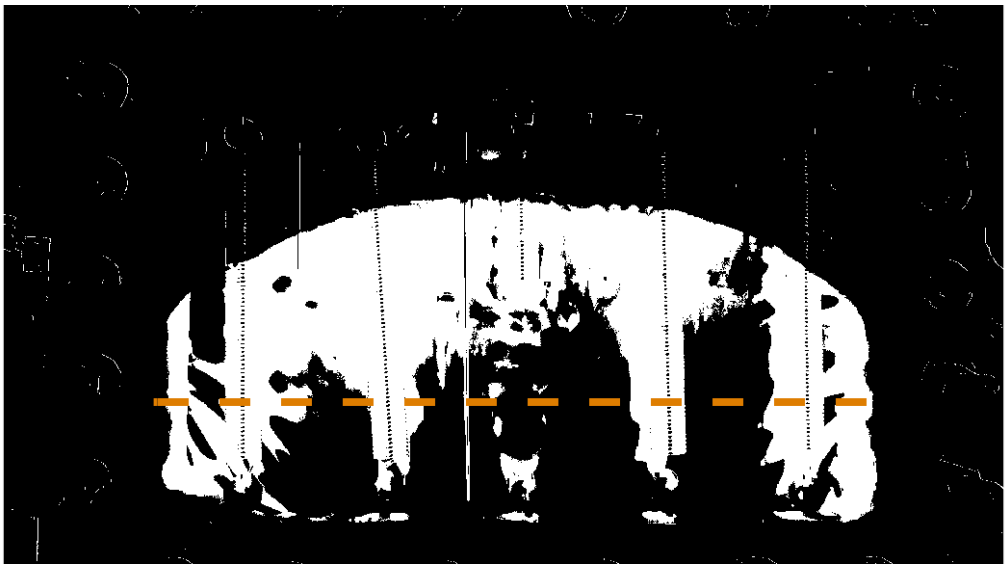

Figure 3-57: Net-binary image from Figure 3-56 after background subtraction (binary conversion of the frame in Figure 3-53).

However, as is shown in Figure 3-58, uniform distribution of white pixels representing solid SAT on either side of the active spring-triggers was not always observed. Such images as these made it difficult to confidently measure the solidification front progression from both sides of all active spring-nucleation triggers. Consequently, such datasets could not yield accurate solidification front expansion rate data, and only five datasets (inclusive of Figure 3-57) with qualities similar to those shown in Figure 3-57 were used to determine solidification front expansion rates for the SAT PCM in Mark I.

Figure 3-58: Net-binary image of solidification after triggering all five spring-nucleation triggers. Too many data absences were present along possible cut-lines to measure solidification emanating from all five sources.

Through this process, the total solid SAT pixel occupations along the cut-lines were recorded for several experiments. The data were further processed to reveal only the instances of positive solid SAT pixel occupation growth as well as dividing the data by the number of interfaces tracked by the cut-lines in order to determine the average frontal expansion profiles. The analyses yielded time-lapsed data of the crystal front expansion, as shown in Figure 3-59. From these figures, linear least-squares regressions were obtained with very good fit, with the slopes of these lines corresponding to each experiments' respective solidification front expansion rates. Uncertainty analyses were neither evaluated for the raw data nor the linear fit parameters since the optical data spacial and temporal resolutions (~ 0.2 mm and 0.03 s) fell below the thresholds for the observed solidification process (~ 7 mm/s) and the respective linear least-squares fits

were deemed excellent ($R^2 \geq 0.95$). Data following a significant linear trend indicated good symmetry of the individual solidification interface front expansion rates, and therefore high confidence in their determinations. Additional figures for experiments not shown here are found in Appendix E.

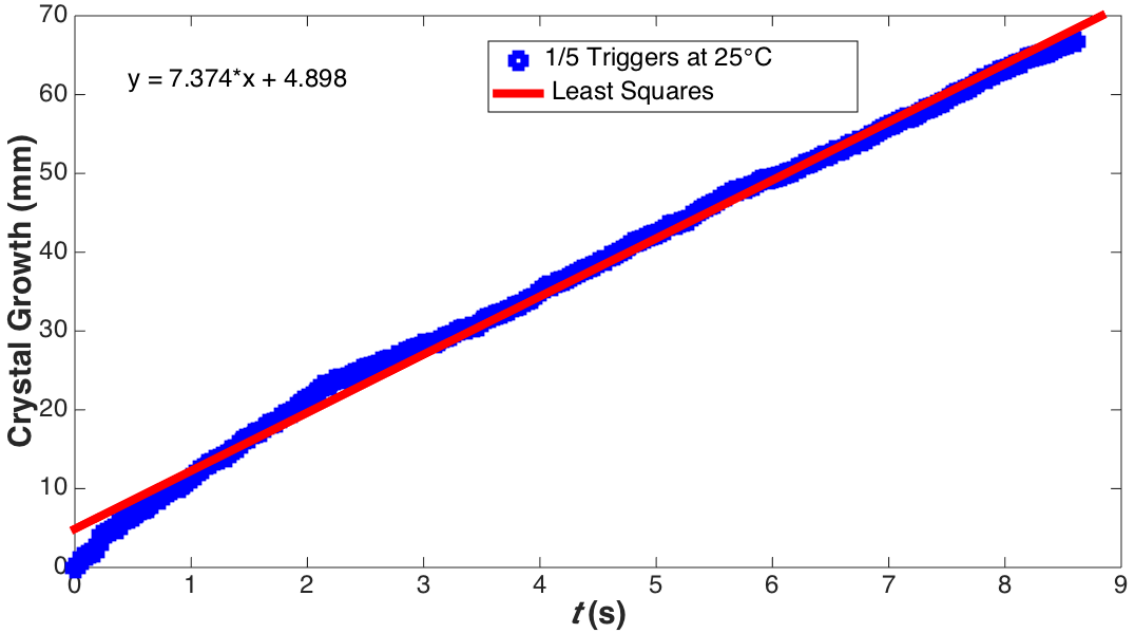

Figure 3-59: Optically measured SAT solidification front expansion corresponding to the experiment in Figure 3-57. R^2 = 0.954.

Conducting optical solidification front measurements proved generally more difficult when using more than one spring-nucleation trigger, so useful data from these were obtained only from select experiments. Only data from experiments for which the net-binary images uniformly captured solidification around all of the tracked spring-nucleation triggers were reported. Figure 3-60 and Figure 3-62 show the resulting linear plots obtained from an experiment using five and three spring-triggers, respectively. Their corresponding final, net-binary images are shown in Figure 3-61 and Figure 3-63, respectively.

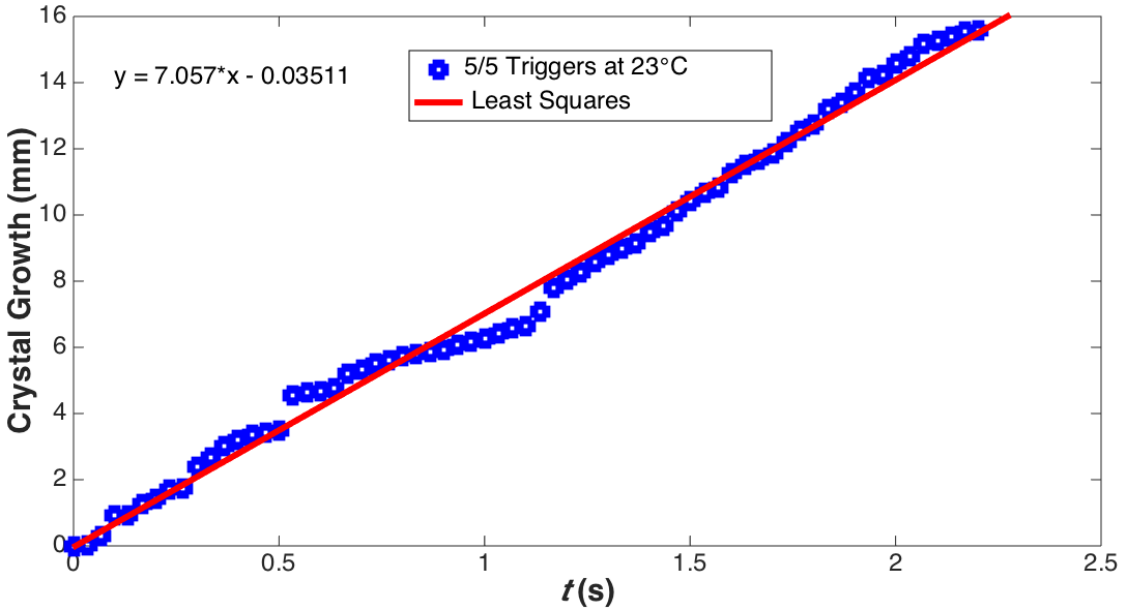

Figure 3-60: Optically measured SAT solidification front expansion corresponding to the experiment in Figure 3-61. R^2 = 0.986.

Figure 3-61: Net-binary image of solidification after triggering all five spring-nucleation triggers during a second experiment. Sufficient data could be extracted along a cut-line to analyze and report the solidification front expansion rate.

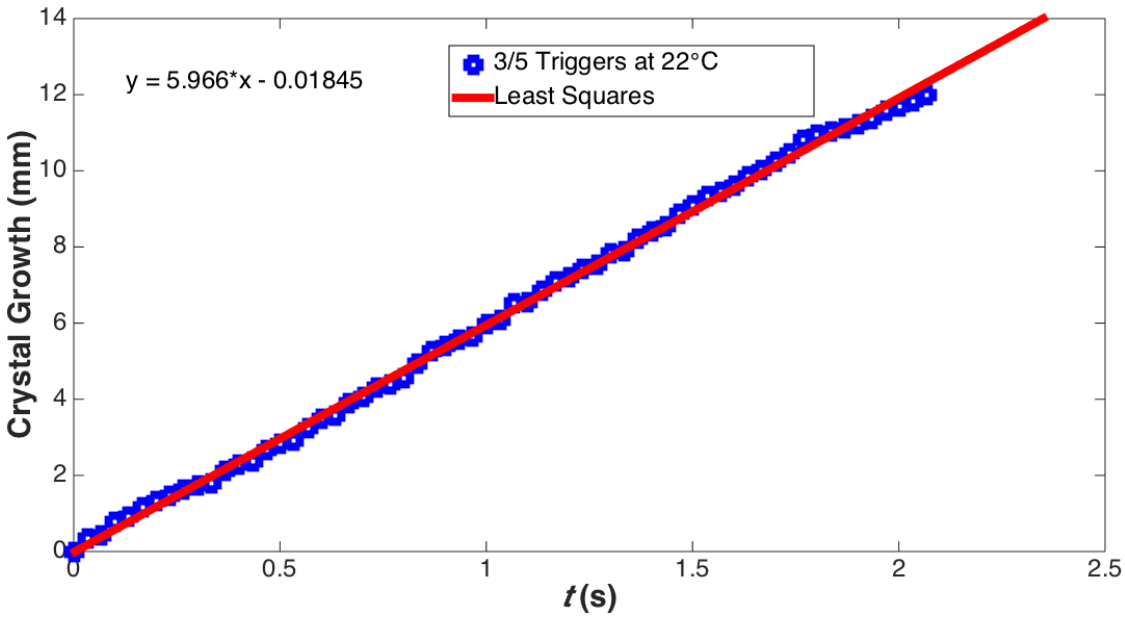

Figure 3-62: Optically measured SAT solidification front expansion corresponding to the experiment in Figure 3-63. R^2 = 0.999.

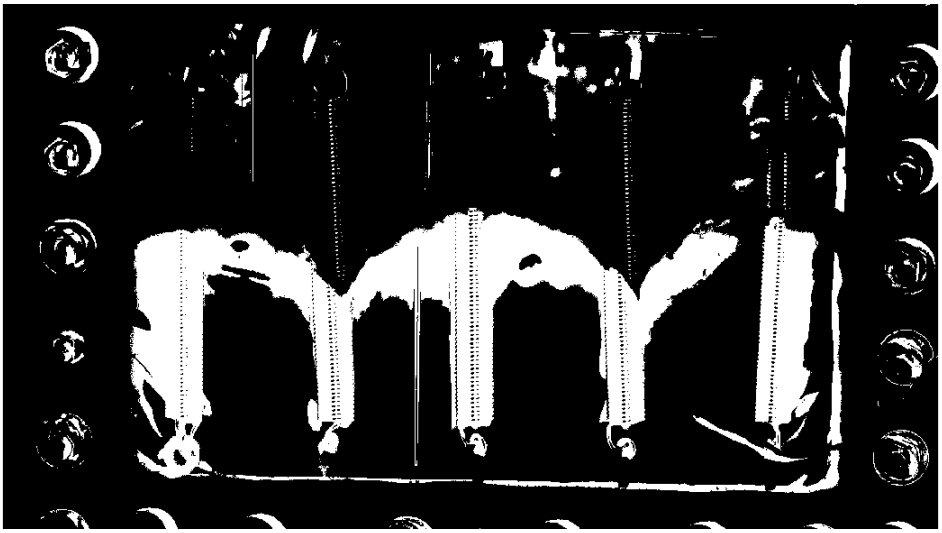

Figure 3-63: Net-binary image of solidification after triggering three spring-nucleation triggers. Despite large gaps, sufficient data could be extracted along a cut-line to analyze and report the solidification front expansion rate.

The results from all the optically measured solidification front expansion experiments are summarized in Section 3.3.4.3 along with the results obtained from infrared measurements, discussed below.

3.3.4.2 IR IMAGE PROCESSING

A similar process was undertaken to analyze the solidification front expansion rate as measured from the surface temperature IR thermography measurements of the Mark I heat storage cell's aluminum film (detailed in Appendix D). Only a few analyses were conducted this way due to the uncertainty in determining the extent of the solidification front, as it was somewhat obscured by the aluminized film's heat spreading ability (Desgrosseilliers et al., 2013b; Desgrosseilliers et al., 2014b). Because of this, only experiments using just one active spring-trigger were analyzed (heat spreading is further accentuated between adjacent sources).

In an effort to improve the quality of the data, the heat-spreading domain interface temperature (where heat spreading begins to extend beyond the heat source) was estimated from the Cartesian form of the two-region fin model equations with infinite boundary condition developed by Desgrosseilliers et al. (2013b). Assuming a nominal convective heat transfer coefficient in air of 40 $W\,m^{-2}\,K^{-1}$ (vertical heated surface (Desgrosseilliers et al., 2014a)), nominal plastic layer thermal conductivities of 0.4 $W\,m^{-1}\,K^{-1}$ (Desgrosseilliers et al., 2014a; Desgrosseilliers et al., 2016), an ambient temperature of 20 ˚C, and a heat source temperature of 55 ˚C, the interface temperature was determined to be around 53 ˚C for a wide range of heated lengths. For this reason, the argument used to identify solid SAT PCM from the IR thermographic images was established at 50 ˚C to account for IR measurement uncertainty.

Images obtained from IR thermography have the benefit of generating a very high contrast between the heat source and the cooler materials that surrounds it, since IR cameras generate pixel colour maps (including grayscale) in direct correlation to their calibrated surface temperatures measurements. The images shown in Figure 3-64 and Figure 3-65 illustrate the high contrast that was obtained using IR thermography, while Figure 3-66 shows the ease with which IR image grayscale intensities are correlated with the calibrated surface temperature measurments. Note that the nominal pixel resolutions in the images were approximately 0.26 mm/pixel, determined in the same manner as for the optical measurements in Section 3.3.4.1.

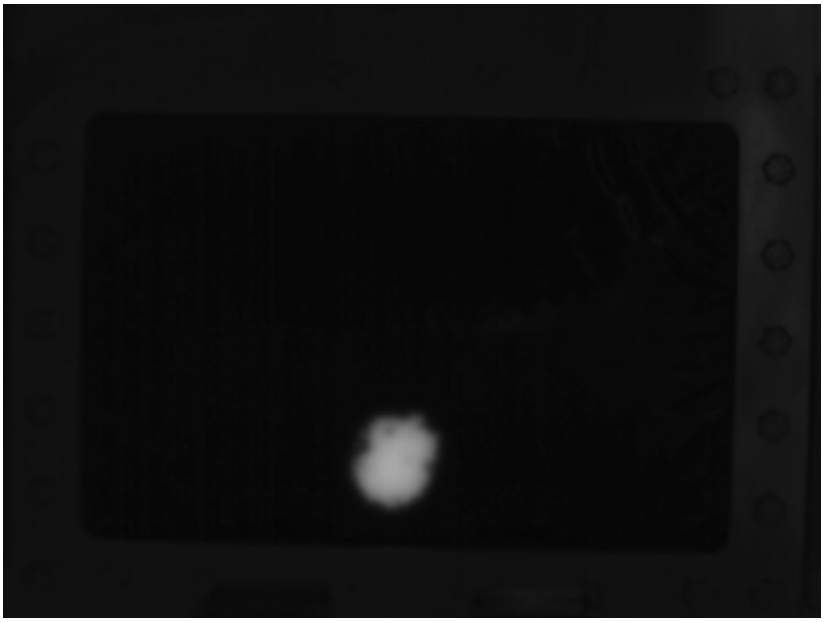

Figure 3-64: IR thermographic image of the beginning of solidification after activating only one spring-trigger. The thermographic basis of the image provides reliable contrast between solid SAT and the surrounding supercooled SAT regions behind the aluminized film.

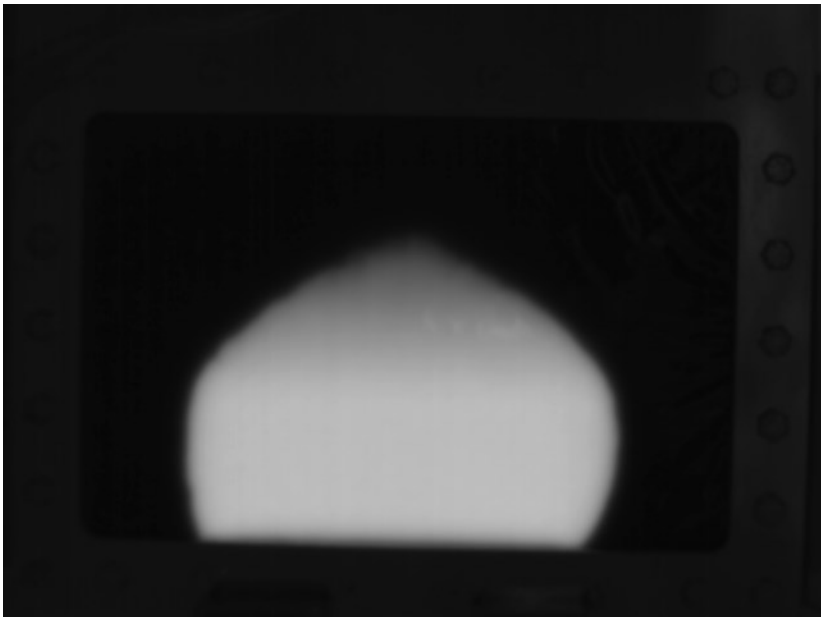

Figure 3-65: Expansion of the solidification front shown in Figure 3-64.

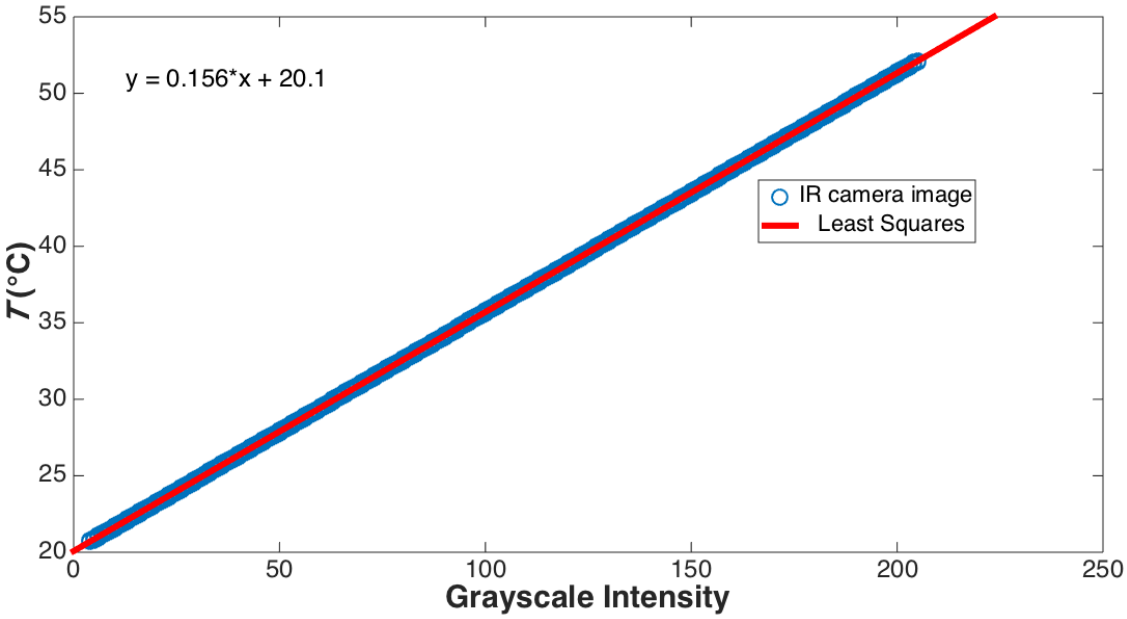

Figure 3-66: IR camera calibration curve inferred from IR temperature field data and corresponding grayscale image for fixed image colour map. $R^2 = 1$.

The IR images were captured in a continuous series, capable of constituting a video, however, each frame was not time-stamped with sub-second precision and the IR capture rate did not also remain constant throughout. To overcome this problem and permit the determinations of the elapsed time at every interval, the algorithm detailed in Appendix D assumed the camera's rated frame rate of 9 frames/s for only the initial interval, until reaching an image file possessing a sufficiently accurate timestamp, from which others were also identified, using the frame intervals formed between them to establish corrected frame rates. Note that due to this uncertainty, solidification front expansion rates determined from IR measured data were used only to support the optically determined solidification front expansion rates in Section 3.3.4.1 and Appendix E.

Employing the same data processing techniques as used for the optical image processing, linear curves describing the solidification front progressions were obtained. Figure 3-67 shows the result obtained from a solidification experiment conducted after supercooling to 20 ˚C. The slope from the linear regression, 7.6 mm/s, representing the average solidification front expansion rate, was similar to those determined from the optical measurements in Section 3.3.4.1 and shown in Appendix E, ranging from 6 mm/s to 9 mm/s. The figure for one other IR experiment is shown in Appendix E.

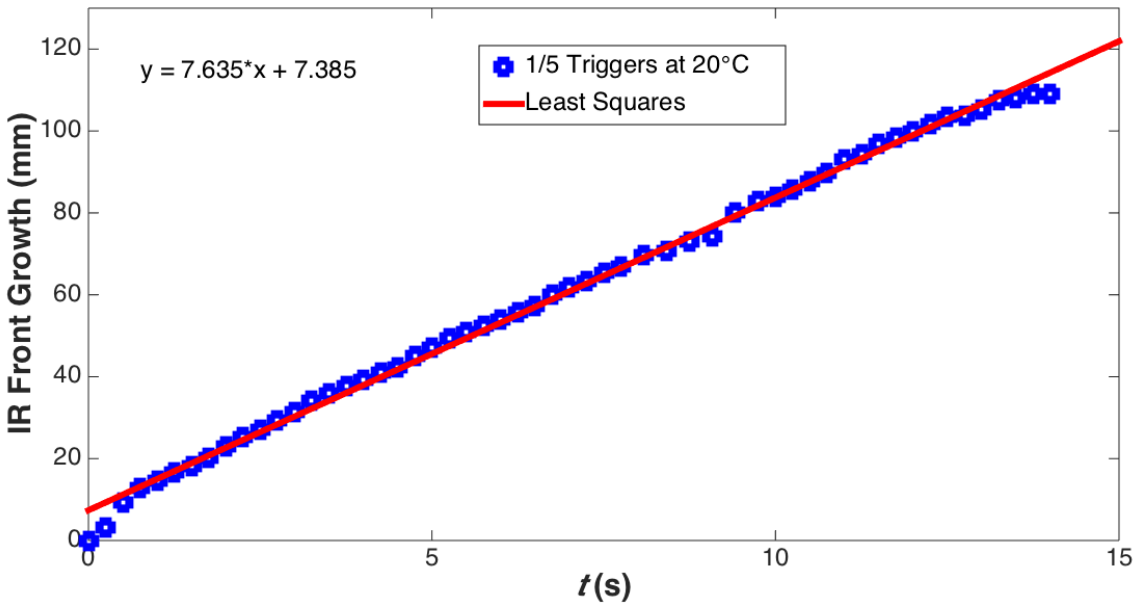

Figure 3-67: IR thermographically measured solidification front expansion from a single actuated spring-trigger. R^2 = 0.997.

3.3.4.3 RESULTS

Figure 3-68 summarizes the findings of the SAT solidification front expansion rates measured both optically and using IR thermography from nucleation experiments performed using the Mark I heat storage cell. Throughout the experiments, the number of activated spring-triggers was varied and so was the supercooling temperature prior to nucleation triggering. The findings from these measurements independently verified those reported by Ahmad (2002) and Wood et al. (2011), discussed in Section 1.2.1.3, that concentrated solutions ($w_{SA} \geq 0.5$) of SAT exhibit rapid crystallization kinetics with solidification front expansion rates ~ 7 mm/s. Due to solution stratification that has been prevalent throughout the experiments conducted for this project (detailed in Section 3.3.5), the average solidification rate from Figure 3-68, equal to 7.2 mm/s ± 2.2 mm/s (95 % confidence interval, 2σ), corresponds to solution concentrations varying between 53 mass% SA and 58 mass% SA in water, inclusively. As also reported by Ahmad (2002), the solidification front expansion rate remained independent of the supercooling temperature.

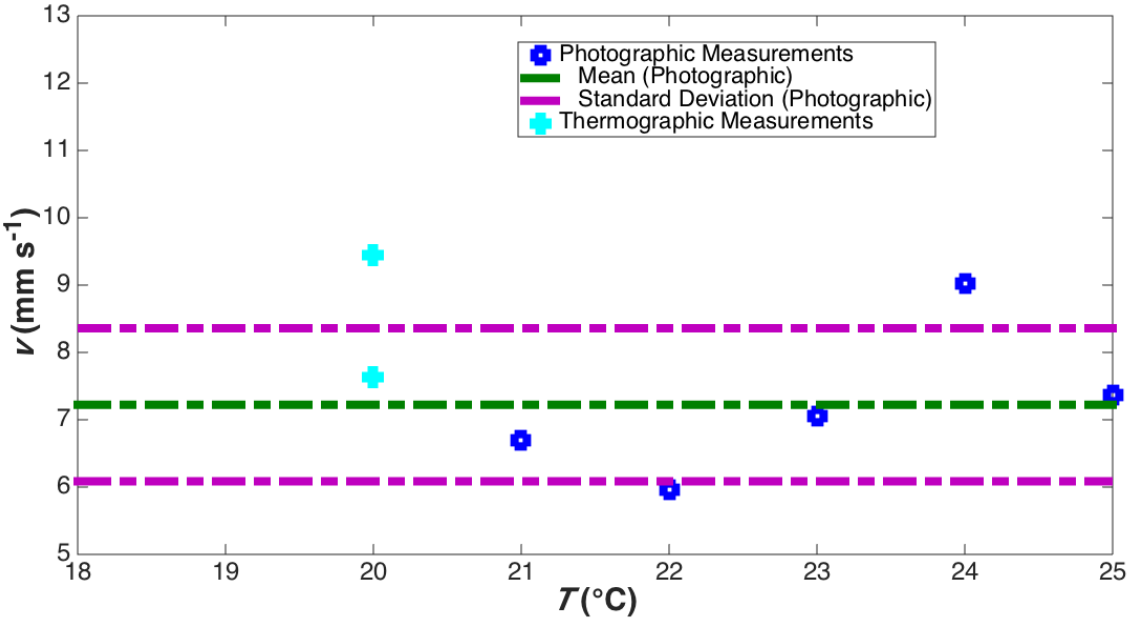

Figure 3-68: Summary of the SAT solidification front expansion rates both from optical and IR measurements in relation to their respective supercooled temperatures.

The number of solidification fronts spreading laterally throughout a heat storage cell is equal to double the number of activated spring-triggers. As few as two spring-triggers are recommended to be used in heat storage cells for which the PCM cavity width is as large as 600 mm in order to achieve a fully self-heated SAT PCM within 30 s of triggering nucleation. For the Mark I, II, and III designs, this corresponds to a self-heating time of around 10 s.

However, regardless the number of spring-triggers used in a heat storage cell, the rate of vertical solidification remains affected only by the random distributions of nucleation sites along the lengths of the individual spring-triggers, rather than by the locations or number of spring-triggers used. Consequently, initial vertical solidification might take longer to achieve completion than in the horizontal direction, and can only be aided by greater spring extension in an effort to more thoroughly expose potential nucleation sites, thus improving the vertical distribution of nucleation sites.

3.3.5 SOLUTION STRATIFICATION

Solution stratification, although remaining generally stable throughout the phase-change cycling evaluations of Marks I, II, and III when complete dissolution was achieved, diminishes the effective heat exchange plate area occupied by SAT solution undergoing phase change. As has been consistently observed for Marks I, II, and III, the

PCM could become separated into two concentration zones (strata) as the result of repeated charge-discharge cycles, shown for Mark I in Figure 3-69. The concentrated, lower stratum ($0.532 \leq w_{SA} \leq 0.603$) would occupy the majority of the heat storage cell, while the dilute, upper stratum ($w_{SA} \leq 0.35$) would occupy the remaining upper portion, effectively reducing the heat exchange plate assembly area exposed to SAT PCM undergoing phase change.

Figure 3-69: Mark I heat storage cell exhibiting solution stratification after repeated charge-discharge cycles with full dissolution. The solidified room-temperature state is shown for ease of visualization. The solution was separated into a smaller, upper stratum containing only dilute solution ($w_{SA} \leq 0.32$) and a larger, lower stratum containing a concentrated mixture of SAT and water ($0.532 \leq w_{SA} \leq 0.603$).

The dilute upper stratum would also occupy the only vapour-liquid interface present in the heat storage cell, therefore governing the ensuing vapour-liquid equilibrium. Due to its inferior sodium acetate concentration to the solution-average concentration, this interface would generate higher than desired vapour pressures, causing the normal boiling point to reduce from 117 ˚C to 107 ˚C $\leq T_b \leq$ 108 ˚C for a concentration ranging from $0.32 \leq w_{SA} \leq 0.35$ (saturated liquid between 20 ˚C and 30 ˚C). Heating the solution up to

110 ˚C in a vented heat storage cell would result in boiling and significant water vapour loss, but would result only in a slightly elevated pressure if heated in a sealed heat storage cell, with or without an external expansion tank. Regarding objective 2 in Section 2.2, sufficiently low internal heat storage cell pressures can still be achieved using either the PCM filling procedure described in Section 2.3.2.3 (slightly exceeding 1 atm after stratification is established) or by using an external expansion tank to attenuate the internal pressure rises.

Aside from the reduction in heat transfer area exposure to regions containing PCM capable of undergoing phase-change and the increase in solution vapour pressure, does stratification also alter the system's distribution of thermodynamic states? For instance, consider an upper stratum consisting of solution with w_{SA} = 0.32 (i.e., saturated solution at 20 ˚C), and a lower stratum consisting of a mixture with w_{SA} = 0.58 (i.e., lowest concentration with a saturated liquid at 58 ˚C), their mass distribution would correspond to 18 mass% and 82 mass%, respectively. Calculating their respective enthalpies changes between 20 ˚C and 110 ˚C using Eqs. (2.3) to (2.6) in Section 2.3.2.2, the system's total heat storage capacity at 110 ˚C would become 476 kJ/kg instead of 475 kJ/kg for the uniformly concentrated SAT PCM. For the complete thermodynamic cycles (Cycles 1-3) shown in Figure 2-3 and Table 2-1, the net heat discharge capacities for the stratified solution are 455 kJ/kg instead of 449 kJ/kg for Cycles 1 and 2 and 431 kJ/kg instead of 425 kJ/kg for Cycle 3. Therefore, despite causing a redistribution of the SAT in the heat storage cell, the heat storage capacities of stratified solutions remain largely unchanged from their mixed system average concentration of w_{SA} = 0.532, but do suffer from diminished heat transfer area exposure to the active SAT PCM and increased vapour pressure.

In an effort to explore solution stratification mitigation techniques available to implement for the Mark III heat storage cells[47] ('3' and '4' only) that required only operational changes, controlled experiments were conducted with the aim to explore the effects of charging and supercooling heat-transfer rates on internal natural convection-mixing. Cyclic testing using the ETS loop and varying the HTF flow rate were conducted

[47] Mark II and Mark III '1' were excluded due to each having suffered irreversible breaches of PCM containment, as discussed in Sections 3.3.2.2 and 3.3.3.2.2.

in the experiments already described in Section 3.3.3.2.2, affecting both the charge and discharge heat-transfer rates, while an additional experiment varying only the cooling ramp rate was conducted using the heater-chiller loop. The latter cooling rate experiment served to isolate the effects of the heating and cooling-induced internal natural convection mixing on solution stratification. In cooling rate-controlled experiments, the heater-chiller microcontroller was programmed with the varying cooling ramp-rates shown in Figure 3-70. These programed cycles were executed sequentially in ascending order of cooling ramp-rate durations, with each complete programmed heating-cooling cycle repeated five times before proceeding to the next program.

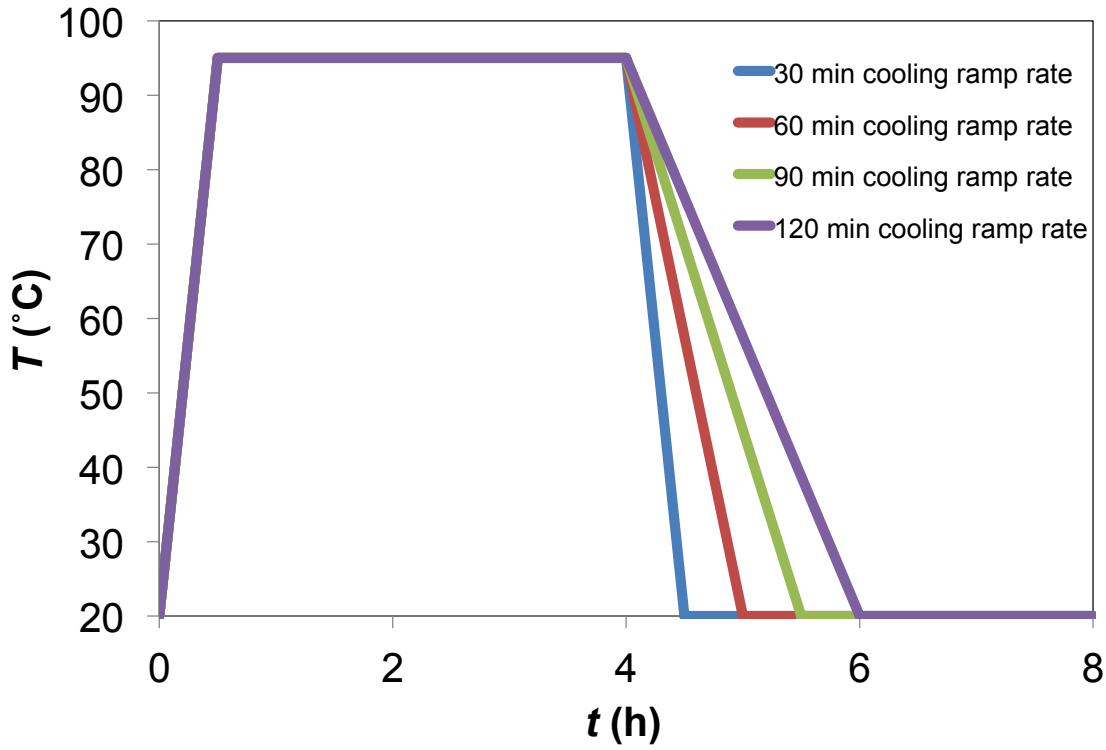

Figure 3-70: Heater-chiller HTF supply-temperature set-point programs with varying cooling ramp-rate only.

Figure 3-71 depicts the B3 temperature profiles resulting from the heater-chiller HTF supply-temperature programs illustrated in Figure 3-70, each curve belonging to the fifth cycle in each series. Although both Mark III '3' and '4' were evaluated in parallel, only the results from probe B3 are shown since the results from B4 duplicated those of B3 during the supercooling and solification phases, and did not yield any additional information.

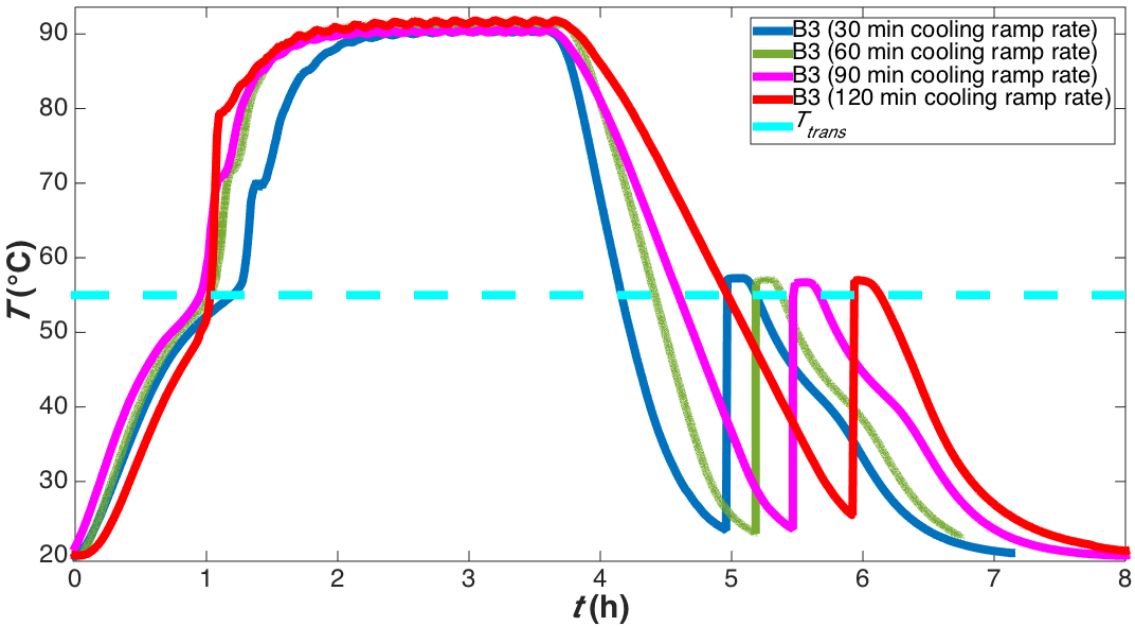

Figure 3-71: Comparison of the effect of cooling rates on solution stratification as observed from the B3 (Mark III '3') temperature profiles. HTF flow rate was supplied from the heater-chiller at an average of 2.5 L/min, exclusive of Mark III '4'. The dashed line corresponds to the average SAT PCM composition T_{trans} = 55 ˚C.

Based only on the observations of their respective nucleation temperatures in Figure 3-71, the variations in the cooling rates did not generate a significant impact on the local solution composition near B3. However, since nucleation from a supercooled state constitutes an isenthalpic process ($\Delta H = 0$), the pre- and post-nucleation B3 temperature data corresponding to each experiment in Figure 3-71 can be used to infer the local composition, respectively, from non-linear, constrained optimization:

$$\min((\Delta H_1 - \Delta H_2)^2) \text{ for } [w_w, w_{s2}] \tag{3.6}$$

$$s.t. \begin{cases} \Delta H_1(w_w, w_{s1}, B3_1) \\ \Delta H_1(w_w, w_{s2}, B3_2) \\ w_{s1} = 0 \\ T_{liq}\left(0.603\,\frac{1-w_w-w_{s2}}{1-w_{s2}}\right) = B3_2 \end{cases},$$

where ΔH_1, ΔH_2, w_w, w_{s1}, w_{s2}, $B3_1$, $B3_2$, and T_{liq} refer to the total enthalpy changes for states 1 (pre-nucleation, i.e., supercooled) and 2 (post-nucleation), each calculated from Eq. (2.6), system mass fraction of extra water (not originating from the decomposition of SAT), individual solid SAT fractions for states 1 and 2, pre-nucleation B3 temperature, post-nucleation B3 temperature, and the liquidus line temperature for the saturated liquid

in state 2, calculated from Eq. (2.1), respectively. The overall local concentration, w_{SA} is calculated from (3.6) using:

$$w_{SA} = (1 - w_w)0.603. \quad (3.7)$$

Using B3 data from Figure 3-71 and from Figure 3-48, Table 3-1 lists the calculated local SAT PCM concentrations (w_{SA}) from Eqs. (3.6) and (3.7). From the distribution of the data in Table 3-1 and the conditions under which the experiments were conducted, there does not appear to be a strong correlation between any of the operating conditions (HTF flow rate, HTF temperature, and cooling ramp-rate) and solution stratification mitigation via internal natural convection induced mixing. The only results of note appeared to be that the HTF flow rates of the heater-chiller experiments programmed with cooling ramp-rates of 60 min, 90 min, and 120 min were higher than the experiment with the cooling ramp-rate of 30 min, resulting in marginally improved mixing (lower w_{SA}) due to increased heat-transfer rates during charging. Furthermore, this result suggests that the effect is apparently stronger during heating than cooling, since the effect caused by the cooling ramp-rates were inversely proportional to the cooling heat-transfer rates (proportional to the intensities of internal natural convection mixing). The higher HTF flow rates were directly proportional to the heat-transfer rates during heating, therefore corresponding to the observed positive correlation.

Table 3-1: Local SAT PCM concentration determinations for Mark III around thermocouple B3 from nucleation temperatures in Figure 3-71 and Figure 3-48. Concentrations were determined using Eq. (3.6) and Excel's ® Solver.

Average HTF flow rate (L/min)	Max HTF charge temperature (˚C)	Cooling ramp-rate (min)	$B3_1$ (˚C)	$B3_2$ (˚C)	w_{SA}
1.8	90	n/a (ETS)	26.31	57.25	0.593
2.1	95	30	23.49	57.23	0.593
2.9	95	60	23.05	56.95	0.587
2.6	95	90	23.66	56.63	0.580
2.5	95	120	25.47	56.97	0.587

3.4 CONCLUSION

In an effort to achieve design objectives 1, 6, 7, 9, 13, C, and H in Section 2.2, three incrementally improved heat storage cell designs, designated as Marks I, II, and III were developed, fabricated, loaded with SAT PCM, and operated in combined heating and cooling experiments. Since the Mark III design improved on the previous versions, it alone was able to fulfill most of the design objectives and was deemed the only one suitable, with minor improvements, to integrate into early ETS prototypes for evaluation. However, regarding objective 13, Marks I to III remained unchanged in their respective base structural material volume fractions, all of them exceeding the stated 20 vol% objective by 29 vol%. Since heat exchange and heat storage capacity designs precede the heat storage cell structural design optimization, achieving objective 13 was deferred to subsequent improvements of the heat storage cell design, outside the scope of this project.

With the knowledge acquired from their evaluations, findings and recommendations for heat storage cell design and ETS operating conditions were established in the areas of containment integrity (objectives 6 and 12), complete phase-change cycles (charge-supercooling-discharge, objectives 6 and 9), nucleation triggering strategy (objective 7), stratification (objectives 8 and 12), and ETS operation best practices affecting heat storage cell performance (objectives G and H) and general ETS system operational and design constraints (objectives B-D):

1. Containment integrity:
    a. Use compressible gasket seals between wetted components to resist thermal expansion effects well, since aluminized films do not;
    b. Threaded perforations are at risk of leaking due to differential thermal expansion. Apply compressible gasket seals wherever possible (e.g., under fill-port cap-plug);
    c. Eliminate eyebolts at bottom of base and replace with integral spring-tabs (i.e., Mark III);
2. Phase-change:
    a. Internal PCM temperatures must exceed 80 ˚C to ensure full SAT dissolution and subsequent supercooling;

b. Relating to a., if using only one probe, it should be located at the bottom of the base and at the opposite end of the PCM cavity to the HTF inlets from the base to the adjacent heat exchange plates, where phase-change and full dissolution (≥ 80 ˚C) occurs last;
c. Faster charging dynamics are achieved using Mark III, attributed to its HTF channels traversing the bottom of the base;
d. Vertical thermal gradients were consistently observed, while horizontal gradients were only observed for Mark III (see b);
e. Internal observations using the built-in sight glass in Mark I did not suggest any evidence of the thermocouple probes affecting the local phase-change processes;

3. Nucleation
    a. Spring-nucleation triggers activated by flexing in a container filled with solid SAT yield reliable nucleation trigger function once submerged in SAT PCM;
    b. Repeating the activation procedure following significant SAT PCM solidification during operation is also recommended during every cycle with the aim to maximize the seed crystal population contained in the spring-nucleation triggers for subsequent cycles;
    c. Heat storage cells should be equipped with a minimum of two spring-nucleation triggers;
    d. Actuators capable of generating strong pull forces on the spring-nucleation triggers are preferred in order to generate greater spring extension. This can be achieved by using pull-solenoids with adjustable supports or using re-directed push-solenoids;
    e. Spring extension durations of 15 s produce reliable nucleation in supercooled SAT PCM;
    f. Extension springs with pre-loading of 17 N or higher are recommended for operation up to 110 ˚C;

g. Results independently confirmed literature reports of the solidification front expansion rate around 7 mm/s for concentrated SAT solutions ($0.532 \leq w_{SA} \leq 0.603$);
h. Two springs should adequately trigger a cavity measuring up to 600 mm wide in 30 s, while stronger spring extension is recommended to improve the rate of vertical solidification;
i. There was minor resistance to spring-triggering from mechanical shock noted from transportation and manipulation of Mark I, and therefore springs with stronger pre-loading should show promise for resistance to unintended triggering either during transportation or from minor shocks during stationary indoor operation;

4. Solution stratification:
    a. Solution stratification remained largely stable for fully dissolved SAT PCM for all heat storage cell designs under repeated charge-supercooling-discharge cycling;
    b. Solution stratification diminished access of SAT PCM capable of undergoing phase-change to heat transfer plate area;
    c. Due to top stratum dilution, higher vapour pressures are generated than at the solution-average concentration of sodium acetate;
    d. Increased vapour pressure can still be managed using the filling protocol described in Section 2.3.2.3 or by using an external expansion tank to attenuate the increased vapour pressure;
    e. Despite redistributing SAT in the SAT water mixture, solution stratification does not diminish its total heat storage capacity;
    f. Heat-transfer rates imposed during charging appear to have only a modest impact on abating solution stratification due to intensified natural convection mixing;
    g. Solution stratification remained unchanged with varying HTF cooling ramp-rates (0.58 ˚C/min to 2.5 ˚C/min) imposed during supercooling;

5. ETS operation/design:
    a. Grundfos Alpha circulating pump generated sufficient HTF flow rate (< 4 L/min) at low HTF pressure (≤ 1.3 atm) and with low noise (≤ 43 dB(A));
    b. Adequate charging dynamics (within 7 h) could be achieved in an ETS equipped with fourteen Mark III heat storage cells (32 kg of SAT PCM combined with a total heat storage capacity of 4.2 kWh), a 1.2 kW to 1.5 kW electric heater, and an HTF pump capable of generating flow rates ≥ 3 L/min, and completing their charges at 110 ˚C;
    c. Intermittent discharge from this ETS is anticipated to achieve thermostatic room temperature control in mild weather for the 17 h period required to avoid consuming mid-peak and on-peak electricity for indoor heating, otherwise consuming the stored energy in less time during colder days.

CHAPTER 4: HEAT EXCHANGE DESIGN

4.1 INTRODUCTION

This chapter details the development, selection, and evaluations of the heat transfer equipment integrated with the heat storage cell bases from Marks II and III as described in Chapter 3 that were used to facilitate heat exchange between a flowing HTF and the SAT PCM contained within the heat storage cells. An evaluation of the heat transfer integration of the heat storage cells with the liquid-to-air heat exchanger via the circulated HTF for ETS system development was also performed. An additional discussion is also provided concerning improvements to internal heat transfer to overcome heat discharge limitations (i.e., conduction heat transfer only) from the PCM during solidification, although such improvements were not executed in either the Mark II or Mark III heat storage cells. The heat transfer design activities described herein were aimed at addressing the remaining design objectives listed in Section 2.2, namely, objectives 10, 11, and E.

4.2 GOVERNING EQUATIONS

The governing equations for convective heat transfer used throughout this chapter are summarized herein.

Elemental to convective heat transfer study is the thermodynamic equation for the rate of heat transfer (Q):

$$Q = \dot{m} \int_{T_1}^{T_2} H dT = \dot{m} \Delta H \cong C_p \dot{m} (T_2 - T_1), \tag{4.1}$$

where $\dot{m}$, H, T_1, T_2, and C_p refer to the mass flow rate of HTF, HTF relative enthalpy, HTF inlet temperature, HTF outlet temperature, and HTF specific heat capacity. For 40 vol% PG in water HTF, the integrated HTF enthalpy in Eq. (4.1) is:

$$\Delta H = [0.00165(T_2^2 - T_1^2) + 3.6357(T_2 - T_1)] \text{ kJ kg}^{-1}, \tag{4.2}$$

where all temperatures are in ˚C (ASHRAE, 2013). Regarding the HTF mass flow rate in Eq. (4.1), volumetric flow rates were measured in the ETS and heater-chiller loops used to evaluate Marks II and III heat storage cells in repeated thermal cycling, from which $\dot{m}$ was calculated using

$$\dot{m} = \dot{V} \rho, \tag{4.3}$$

where $\dot{V}$ is the HTF volumetric flow rate, and the HTF density of 40 vol% PG in water, ρ, is:

$$\rho = [-0.0026T^2 - 0.3946T + 1046.3]\ \text{kg m}^{-3}, \tag{4.4}$$

where the HTF temperature is in ˚C (ASHRAE, 2013).

Respecting the interfacial transport processes of heat transfer, the rate of heat exchanged between a fluid medium and a heat sink or source (either fluid, solid or boundary only) is expressed with:

$$Q = UA(LMTD)\Gamma, \tag{4.5}$$

where *U*, *A*, *LMTD*, and *Γ* refer to the overall heat exchange coefficient, heat exchange surface area corresponding to *U*, log-mean temperature difference, and *LMTD* correction factor for non-counter current flow, respectively. With respect to the liquid-to-air heat exchanger used in the ETS loop, *Γ* = 0.96 (two-pass counter-current design, recall Figure 1-9), while *Γ* = 1 was assumed for the heat storage cell heat exchange assemblies due to the excess degrees of freedom otherwise incurred to determine *UA* from Eq. (4.5). The *LMTD* in Eq. (4.5) is determined using:

$$LMTD = \left((T_1 - T_2') - (T_2 - T_1')\right) / \ln\left(\frac{(T_1 - T_2')}{(T_2 - T_1')}\right), \tag{4.6}$$

where *T* and *T'* each refer to the respective hot HTF (heat source) temperatures and cold HTF (heat sink) temperatures.

Regarding the evaluation of heat transfer efficiency (η), Fakheri (2007) introduced:

$$0 \leq \eta = Q\left(UA(AMTD)\right)^{-1} \leq 1, \tag{4.7}$$

where *AMTD* refers to the arithmetic-mean temperature difference

$$AMTD = \hat{T} - \hat{T}', \tag{4.8}$$

for which $\hat{T}$ and $\hat{T}'$ refer to the hot HTF fluid and cold HTF average temperatures, respectively. Fakheri (2007) demonstrated that Eq. (4.7) results in the ratio of the actual heat-transfer rate to the optimum heat-transfer rate obtained for an equivalent, balanced heat exchanger of the same *UA* and operated with inlet and outlet temperatures corresponding to the least entropy generation (least irreversible). The condition for a balanced heat exchanger corresponds to equal HTF capacity rates, C_r = 1, where C_r is defined as:

$$C_r = C_{min}/C_{max}, \tag{4.9}$$

for which C refers to the HTF heat capacity rates calculated from

$$C = C_p \dot{m}. \tag{4.10}$$

With respect to counter-current heat exchangers, η approaches 1 as C_r also approaches 1, and, $\eta = f(C_r, UA)$ for all heat exchangers (Fakheri, 2007).

Lastly, due to the inherently transient nature of heat storage processes, experimentally derived results from Eqs. (4.1), (4.3), (4.5), (4.7), (4.9), and (4.10) were all obtained using time-averaged quantities of V, $LMTD$, and $AMTD$, averaged over the experimentally measured HTF residence time of individual experiments. Likewise, the HTF inlet and outlet temperatures used in Eq. (4.1) were adjusted for the residence time delay of the individual experiments and respective heat transfer processes (i.e., heat storage cell heat exchange or liquid-to-air heat exchange).

4.3 HEAT EXCHANGE RESISTANCE NETWORK

Represented as a series resistance network, the thermal resistances are shown in Fig. 4-1 in the order as they are situated in the ETS and heater/chiller loops between the temperature boundary conditions, T_{PCM} and T_{HTF} for the heat storage cells (Marks II and III) and between T_{HTF} and T_{air} for the liquid-to-air heat exchanger (ETS loop only). The boundary condition temperatures T_{HTF}, T_{PCM}, and T_{air} refer to the nominal circulating HTF temperature, nominal heat storage cell SAT PCM temperature, and indoor-air temperature in the heated space.

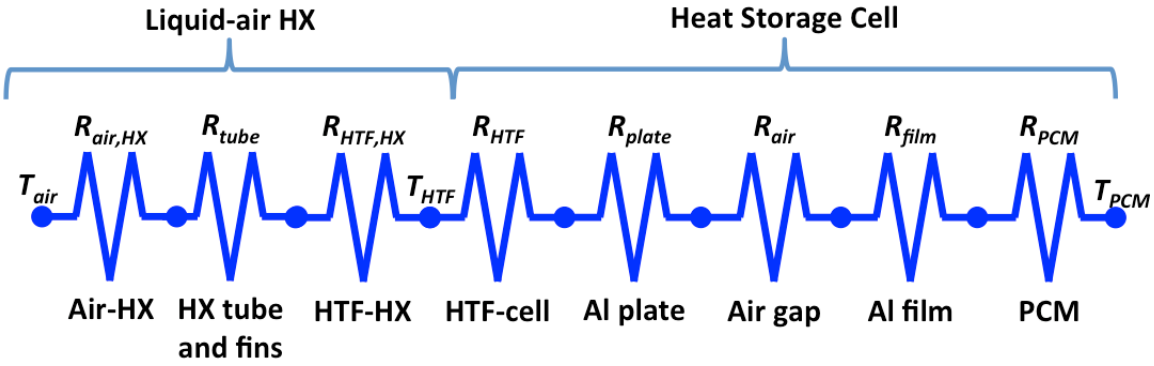

Figure 4-1: Heat exchange resistance network diagram depicting the thermal resistances in series for heat exchange between the circulating HTF and the SAT PCM contained within the heat storage cells and between the HTF and ambient air in the liquid-to-air heat exchanger.

In Fig. 4-1, $R_{air,HX}$, R_{tube}, and $R_{HTF,HX}$ represent to the convective heat transfer resistance for the air flowing through the liquid-to-air heat exchanger, conduction heat

transfer resistance for the tube walls and fins of the heat exchanger, and the convective heat transfer resistance for the glycol solution flowing through the tube-side of the heat exchanger, respectively. Likewise, R_{HTF}, R_{plate}, R_{air}, R_{film}, and R_{PCM} respectively represent the convective heat transfer resistance for the glycol solution flowing through the heat storage cell heat exchange plates, the conduction thermal resistance of the plates themselves, the conduction thermal resistance of the unsealed contact region between the aluminized films and the aluminum heat exchange plates, the conduction thermal resistance of the aluminized films, and the internal heat transfer resistance of the PCM, in whatever thermodynamic state it may be. Conduction thermal resistance is defined by:

$$R = L/k, \tag{4.11}$$

where L and k are the characteristic length of heat conduction and the material's thermal conductivity. Convection thermal resistance is defined by:

$$R = 1/h, \tag{4.12}$$

where h is the corresponding convection heat transfer coefficient.

Respecting the overall heat exchange processes represented by Eq. (4.5), resulting from either the heat storage cells (Marks II and III) or the liquid-to-air heat exchanger, their respective overall heat transfer coefficients, U, are determined from the individual component thermal resistances (denoted by R in Fig. 4-1). Since the thermal resistances depicted in Fig. 4-1 are in series, the resulting value of U for the heat storage cell is

$$U_{cell} = \left(R_{HTF} + R_{plate} + R_{air} + R_{film} + R_{PCM}\right)^{-1}, \tag{4.13}$$

and for the liquid-to-air heat exchanger,

$$U_{HX} = \left(R_{air,HX} + R_{tube} + R_{HTF,HX}\right)^{-1}. \tag{4.14}$$

As is seen in Eqs. (4.13) and (4.14), either values of U will approach the reciprocal values of their largest thermal resistances in series, or simply a nominal value if all thermal resistances are of the same order of magnitude. Therefore, a cursory examination of the component thermal resistances reveals which of those thermal resistances the values of U will approach, and therefore require detailed consideration.

Respecting Eq. (4.13), R_{plate} (2 mm, 260 W m^{-1} K^{-1} (Smith, 1998)), and R_{film} (0.104 mm, 0.49 W m^{-1} K^{-1} (Desgrosseilliers et al., 2016)) are readily quantifiable using design data and material properties in Eq. (4.11), while R_{HTF}, R_{air}, and R_{PCM}, require detailed evaluations, either by experiment or by numerical simulation to determine their

characteristic length (i.e., R_{air}) or values of h (i.e., R_{HTF} and R_{PCM}). However, R_{PCM} does at least have a lower bound to which it can be measured, equal to the conduction heat transfer of the completely densified solid (25.4 mm, 0.4 W m^{-1} K^{-1}), therefore $R_{PCM} > 0.06$ m^2 K/W for both Marks II and III. Nonetheless, assuming only a very thin layer of air between the aluminized film and the aluminum heat exchange plate, the respective values of thermal resistance can be ranked in their anticipated, approximate descending order: R_{PCM}, R_{air}, R_{HTF}, R_{film}, and R_{plate}. Since all three unknown thermal resistances, R_{PCM}, R_{air}, and R_{HTF}, are of close importance to the determination of U_{cell}, neither one of them can be neglected from evaluation with respect to the designs of Marks II and III.

Respecting Eq. (4.14), only R_{tube} (copper tube, ~2 mm, 390 W m^{-1} K^{-1} (McCabe et al., 2005)) can be readily estimated using design data and material properties in Eq. (4.11), while $R_{air,HX}$, and $R_{HTF,HX}$, require detailed evaluations. Nonetheless, based on the design principles of liquid-to-air heat exchange, whereby extended heat exchange surface area (i.e., fins) are used to aid the heat exchange process on the air-side rather than on the liquid side, the respective values of thermal resistance can be ranked in their anticipated, approximate descending order: $R_{air,HX}$, $R_{HTF,HX}$, and R_{tube}. Since both $R_{air,HX}$ and $R_{HTF,HX}$ are of close importance to the determination of U_{HX}, neither one of them can be neglected from evaluation.

4.4 INTERNAL HEAT TRANSFER DESIGN

Respecting internal heat transfer within the heat storage cell PCM cavity of either Marks II or III, several fundamental characteristics arise, owing primarily to their rectangular geometries:

1. Heat transfer symmetry would be achieved along the mid-depth planes of the bases, parallel to the heat exchange plates pairs located on either side of the bases, regardless of the dominant heat transfer mechanism (i.e., heat conduction and/or internal natural convection);
2. Two principal internal natural convection cells would be generated on either side of the symmetry plane during phase-change to the dissolved liquid, for which their convective intensities would be geometrically affected by the

depth from the heat exchange plate surfaces to the symmetry plane as well as the height of the heat exchange surfaces (McCabe et al., 2005);

3. Convective heat transfer during charging would transport heat in the dissolved liquid from the bottom of the PCM cavity to the top, along the heat transfer plate surface, due to the respective buoyancies of the dissolved liquid and solid SAT PCM, and re-circulated either due to interfacial phase-change heat transfer with solid SAT residing at the bottom of the cavity or to residual liquid temperature differences;
4. The interfacial surface area between the solid SAT PCM and the dissolved liquid would diminish as the phase change progresses from the heat transfer supplied via the heat-transfer plates, changing from a large, predominantly vertical surface to a smaller and increasingly horizontal surface (see Figure 4-2 for a general representation). Consequently, the rates of heat transfer and phase change would diminish in response;
5. Convective heat transfer would dominate when cooling from the equilibrium dissolved liquid to the supercooled state;
6. Heat transfer would occur only by conduction during SAT PCM solidification due to complete occupation of the porous nucleated SAT PCM from a supercooled state;
7. Heat transfer during heat discharge after nucleation would generate increased densification of the solid SAT PCM, corresponding to the local saturation of the remaining solution;
8. And, heat conduction during solidification would be directed into the solid SAT PCM predominantly normal to the heat transfer plate surface, up to the symmetry plane.

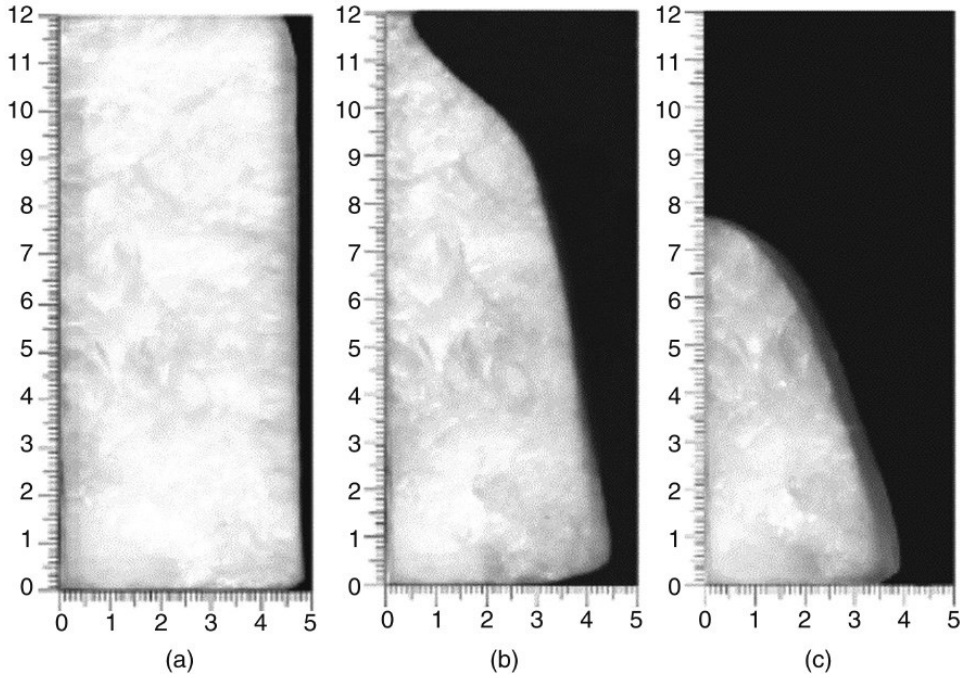

Figure 4-2: Melting of dodecanoic acid in a vertical rectangular cavity with the right wall temperature at 60 °C. Photographed with high contrast in which light areas are solid and dark areas are liquid. The frames depict elapsed times: (a) After 10 min of heating, (b) 90 min, and (c) 170 min. Reproduced from Shokouhmand et al. (2013) with permission from Elsevier ©.

Concerning these characteristics, items 4 and 8 warrant the most attention in internal heat transfer design. The heat-transfer deficiency identified in item 4 has been addressed in Mark III with respect to the HTF channels traversing the bottom of the base. The cyclic phase-change experiments reported in Section 3.3.3.2 have already demonstrated the success with which this feature increased heat-transfer rates during charging for Mark III in comparison to Mark II, although not appearing to provide such a marked benefit during heat discharge (i.e., supercooling and solidification).

Heat conduction in PCMs, owing to their typically low thermal conductivities (Zalba et al., 2003), represents the greatest challenge to internal heat transfer design with PCMs, thus making their heat transfer designs in large part discharge-motivated (Noël et al., 2016).

4.4.1 INTERNAL FIN HEAT-TRANSFER ENHANCEMENTS

Regarding improvements to the discharge heat-transfer rate during PCM solidification, the depth of the heat storage cells can be reduced, or internal fins, in

thermal contact with the individual heat transfer plates, can be introduced into the PCM cavity, both of which are intended to reduce R_{PCM}.

Transient, conductive heat transfer, regardless of phase change, constitutes a thermal diffusion process. As proposed and demonstrated by Kabbara (2015), thermal diffusion during solidification in PCMs can be qualitatively represented by their Fourier number (Fo):

$$\mathrm{Fo} = \alpha t L^{-2}, \tag{4.15}$$

where α, t, and L represent the PCMs solid-phase thermal diffusivity, elapsed time, and characteristic length of the thermal diffusion process, respectively. Since the Fo of solidifying PCMs are used only to correlate similar states in PCM heat-exchange systems using the same PCM and external heat transfer conditions, the value of the thermal diffusivity and the resulting Fo have limited relevance outside of comparisons between related systems (often times proportionately to one-another), and therefore the selection of α is of little importance. However, t and L reflect the specific operation of the PCM heat exchange system in question, and therefore care must be taken in their selections and subsequent analyses.

Respecting design, L is the only portion of Fo that can be altered with the aim of improving heat transfer performance during PCM solidification, defined for thermal diffusion processes as:

$$L = \frac{\text{volume}}{\text{heat transfer area}}, \tag{4.16}$$

for which vertically independent processes reduce to

$$L = \frac{A}{I}, \tag{4.17}$$

where A and I represent the surface area of the PCM in the horizontal plane affected by the heat transfer equipment and the perimeter of the heat transfer equipment in the horizontal plane responsible for generating heat transfer with the PCM, respectively. For the rectangular heat storage cell geometries of Marks II and III, this is simply $L = E$, where E represents the heat storage cell mid-depth normal to the heat transfer plate surfaces (E = 25.4 mm here). Therefore, halving E for Marks II and III in a hypothetical heat storage cell design (L = 12.7 mm), the estimated discharge duration required to achieve the same discharge state (equal values of Fo) would result in approximately 1/4

of the time elapsed for Marks II and III. However, in order to maintain the same heat storage capacities as Marks II or III, the hypothetical heat storage cell would require either double the length or height of the heat storage cell, therefore occupying a larger surface area in an ETS system and consuming more materials of construction for the heat exchange plate assemblies than would Marks II or III.

Alternatively, internal fin heat transfer enhancements could be used to yield a similar improvement without modification to the heat storage cell base. However, with respect to supercooling PCM heat storage cell design, a few restrictions apply: fully penetrating fins must be avoided to allow nucleation to spread throughout all the PCM, and fins must not encroach severely on the locations of spring-nucleation triggers as that could restrict their proper function. Only vertically oriented fins should be used as these would not interfere with the internal natural convection of the liquid SAT solution during charging or supercooling; in fact, vertical fins would likely also improve the rate of natural convection heat transfer. Unoccupied space should remain at the tops and bottoms of the fins in order to supply a path through which to propagate solidification after nucleation as as well as to avoid physical contact of the fins and base that could risk causing autonucleation by trapping seed crystals in a thermally exercised contact region. Furthermore, fin volume with respect to the internal PCM cavity volume must be minimized, as it displaces the PCM and reduces the heat storage cell's heat storage capacity. Note that due to the poor heat transfer characteristics of solid PCMs, the efficiency of internal fins[48] is anticipated to be maintained rather high with long fin penetration.

The principal function of vertical internal fins would be to enhance conduction heat transfer during heat discharge from the solidified SAT PCM to the heat transfer plate pairs by reducing the characteristic lengths of thermal diffusion within the PCM cavity in comparison to the heat storage cell without fins. Due to their intimate thermal contacts to the individual heat transfer plates, attached fins extend and distribute their influence (i.e., heat transfer area) into the bulk of the PCM. However, it is their distribution within the PCM that affects thermal diffusion improvements most importantly.

[48] Fin efficiency is defined as the ratio of a fin's rate of heat transfer to that of the fin if the temperature throughout was equal to the temperature at the base of the fin (McCabe et al., 2005).

Figure 4-3 demonstrates one possible distribution of fins within the PCM cavity. In this conformation, the fins maintain equal spacing between each other (called inter-fin distance, 2*z*) and are symmetrically arranged on opposite sides.

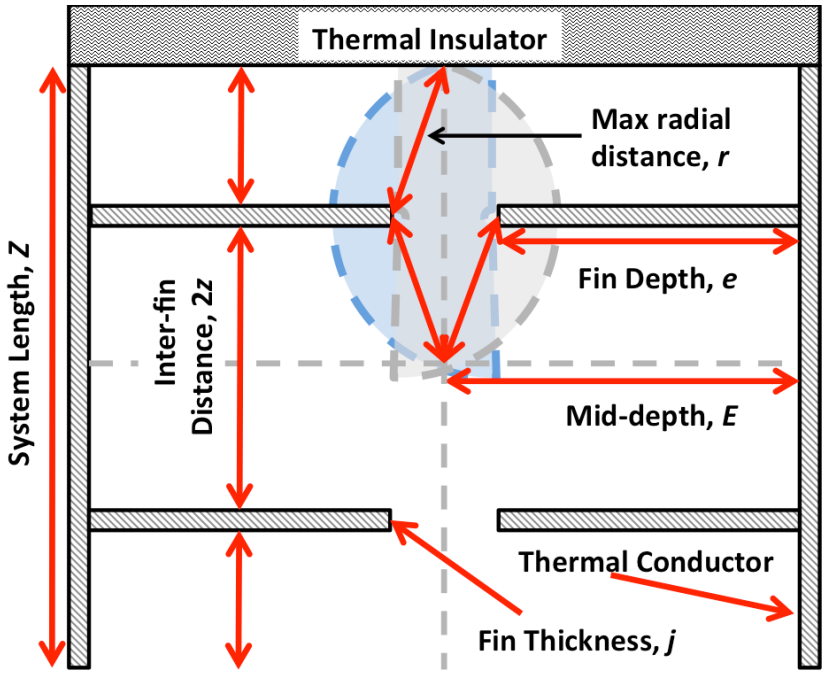

Figure 4-3: Schematic representation of a rectangular enclosure equipped with internal thermally conductive fins that are in thermal communication with the thermally conductive metal sides (i.e., heat exchange plates). The remaining ends of the enclosure consist of a thermally insulating thermoplastic (i.e., heat storage cell base), but only one end is shown. The fins are equally spaced along the metal sides, do not penetrate past the enclosure mid-depth, and are symmetrically assembled on the opposite side.

Two characteristic lengths arise from the fin arrangement in Figure 4-3: planar thermal diffusion (L_1) normal to the fins (parallel to z) and radial thermal diffusion (L_2) emanating from the ends of the fins (parallel to r) into the PCM region not contained in the inter-fin spacing (see Figure 4-4). Their respective characteristic lengths are:

$$L_1 = z, \tag{4.18}$$

and

$$L_2 = \pi r^2/(2j)\ , \tag{4.19}$$

where r and j represent the maximum radial distance obtained between all neighbouring fin ends (as depicted in Figure 4-3) and the fin thickness, respectively. Since $j < r$ and

$$r = \sqrt{(z + j/2)^2 + (E - e)^2}, \tag{4.20}$$

where e represents the fin depth from the heat transfer plate, $L_2 > L_1$ whereby the two can never be made equal without completely traversing the heat storage cell mid-depth ($e = E$). Due to the presence of spring-nucleation triggers, $e >$ outer spring radius, and due to the preference for larger inter-fin spacing needed to promote fin volume fraction minimization, $e \sim (E - z - j/2)$, resulting in:

$$r \approx \sqrt{2(z + j/2)^2}. \tag{4.21}$$

As is shown in Eqs. (4.18) - (4.20), L_2 dominates the overall thermal diffusion performance of the internally finned enclosure in Figure 4-3.

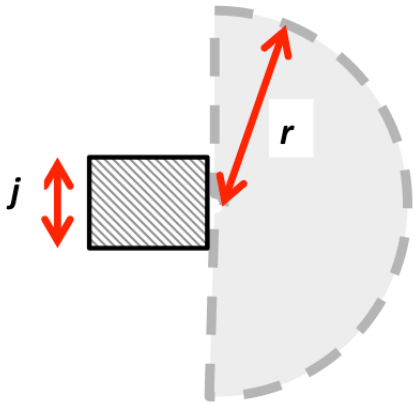

Figure 4-4: Depiction of the radial heat diffusion zones (L_2) at the end of the fins shown in Figure 4-3.

The measure of a useful fin arrangement is determined by its reduction of the overall thermal diffusion process in comparison to the unfinned heat storage cell with $L = E$. Therefore, using Eqs. (4.19) and (4.21), this situation is achieved when

$$r < \sqrt{2Ej\pi^{-1}}, \tag{4.22}$$

and therefore

$$z < \sqrt{Ej\pi^{-1}} - j/2, \tag{4.23}$$

for which $z <$ 2.3 mm for the Marks II and III heat storage cells (E = 25.4 mm) and selecting fins with a thickness, j, of 1 mm; with j = 5 mm, $z <$ 3.9 mm. Consequently, the inter-fin spacings are too restrictive and fin volume fractions (> 16 vol% and > 29 vol%, respectively) are too great in either of these scenarios, therefore showing that the fin arrangement in Figure 4-3 is not suitable for implementation into the heat storage cell designs.

A similar, although asymmetrical fin arrangement (also asymmetrical internal heat transfer and plate heat transfer) is shown Figure 4-5, in which the fins on one side of the heat storage cell are translated to align with the middle of the inter-fin spacing on the opposite side. Furthermore, the fins located on the staggered side have one fewer fin at either end, chosen this way to minimize the risk of autonucleation that would arise due to the physical contact resulting from placing fins adjacent to the heat storage cell base walls at either end.

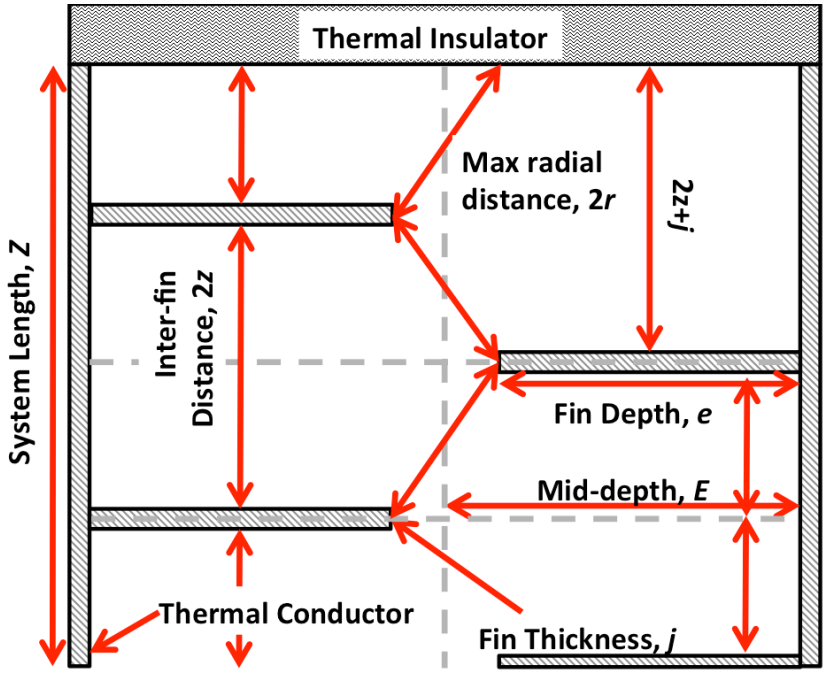

Figure 4-5: Schematic representation of a rectangular enclosure equipped with internal thermally conductive fins that are in thermal communication with the thermally conductive metal sides (i.e., heat exchange plates). The remaining ends of the enclosure consist of a thermally insulating thermoplastic (i.e., heat storage cell base), but only one end is shown. The fins are equally spaced in alternating order of left and right sides and do not penetrate past the enclosure mid-depth.

In the inter-fin zones (excluding the ends of the staggered side), the characteristic length, L_1, remains unchanged from Eq. (4.18), however, the radial distance used to calculate the radial characteristic length, L_2 (Eq. (4.19)), becomes:

$$r \approx \sqrt{(z+j)^2/4 + (E-e)^2}, \tag{4.24}$$

markedly reduced from the result in Eq. (4.20). As was shown above, $e >$ outer spring radius and $e \sim (E - (z+j)/2)$. The staggered side generates an additional characteristic length corresponding to the planar diffusion emanating from the fins at either ends of the

staggered side (e.g., top fin of right side in Figure 4-5), not found in the symmetric fin arrangement in Figure 4-3, is:

$$L_3 = 2z + j. \tag{4.25}$$

Nonetheless, $L_2 > L_3 > L_1$ for the fin arrangement shown in Figure 4-5. As was concluded for the fin arrangement shown in Figure 4-3, the resulting inter-fin spacings, calculated using Eqs. (4.22) and (4.24), and resulting fin volume fractions from the fin arrangement shown in Figure 4-5 are $z < 4.7$ mm and > 8 vol%, for $j = 1$ mm, and $z < 7.7$ mm and > 17 vol%, for $j = 5$ mm, are both unacceptable for implementation into the heat storage cell designs.

As an alternative to the fin arrangements shown in Figure 4-3 and Figure 4-5, the fin arrangement shown in Figure 4-6 uses a staggered fin arrangement wherein the fins located on either side of the heat storage cell penetrate the PCM partially beyond the mid-depth, E. In doing so, the thermal diffusion process occurring in the region at the ends of the fins becomes dominated by the planar diffusion emanating from the heat transfer plate surfaces:

$$L_4 = 2E - e, \tag{4.26}$$

rather than by radial diffusion. Consequently, Eq. (4.26) significantly reduces the resulting local characteristic length and is capable of being made equal to L_1 in order to promote uniform thermal diffusion throughout the heat storage cell. Consequently, the preferred embodiments (i.e., $L_1 = L_4 < E$) would correspond to small j (assumed 1 mm), $e > 25.4$ mm, and $z < 25.4$ mm for which the fin volume fraction > 1 vol%, deemed useful for implementation in heat storage cell designs.

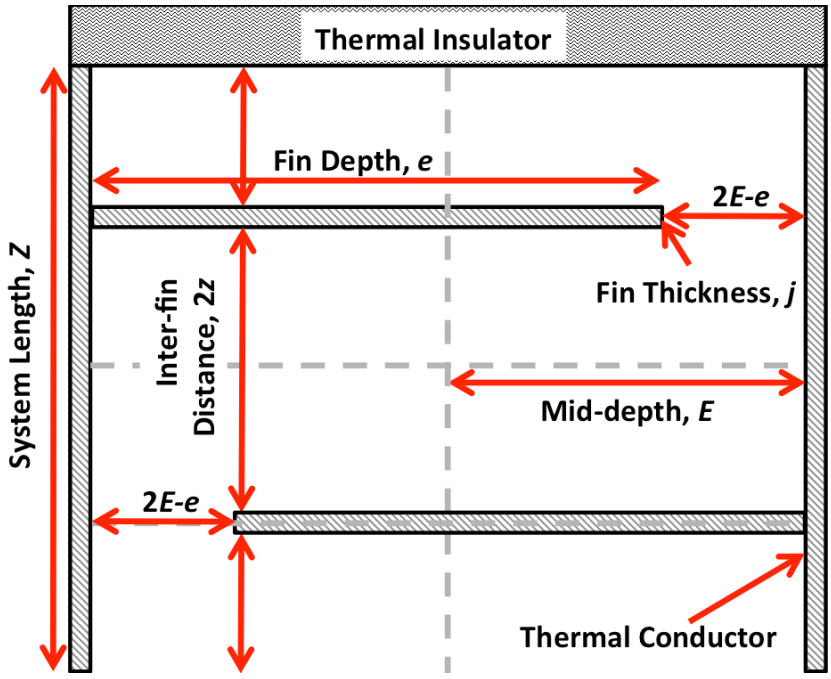

Figure 4-6: Schematic representation of a rectangular enclosure equipped with internal thermally conductive fins that are in thermal communication with the thermally conductive metal sides (i.e., heat exchange plates). The remaining ends of the enclosure consist of a thermally insulating thermoplastic (i.e., heat storage cell base), but only one end is shown. The fins are equally spaced in alternating order of left and right sides and penetrate past the enclosure mid-depth.

In order to achieve similar improvement to the discharge heat transfer process as was estimated for a heat storage cell design with just half the depth of Marks II or III (L = 12.7 mm), the finned arrangement shown in Figure 4-6 would result in just 9 fins (j = 1 mm), each with e = 38.1 mm and z = 12.7 mm, for which the fin volume fraction is 3 vol%.

Figure 4-7 depicts a similar thermal diffusion design to what is shown in Figure 4-6, whereby only one finned plate is fabricated, thereby reducing the cost of fabrication and the material consumption if using subtractive fabrication methods (e.g., milling). Furthermore, in the embodiment shown in Figure 4-7, solidification expansion from a nucleated supercooled liquid PCM would propagate more quickly throughout the heat storage cell than it would in Figure 4-6. However, the former would result in significantly lower HTF heat-transfer rates on the unfinned side vs. the finned side.

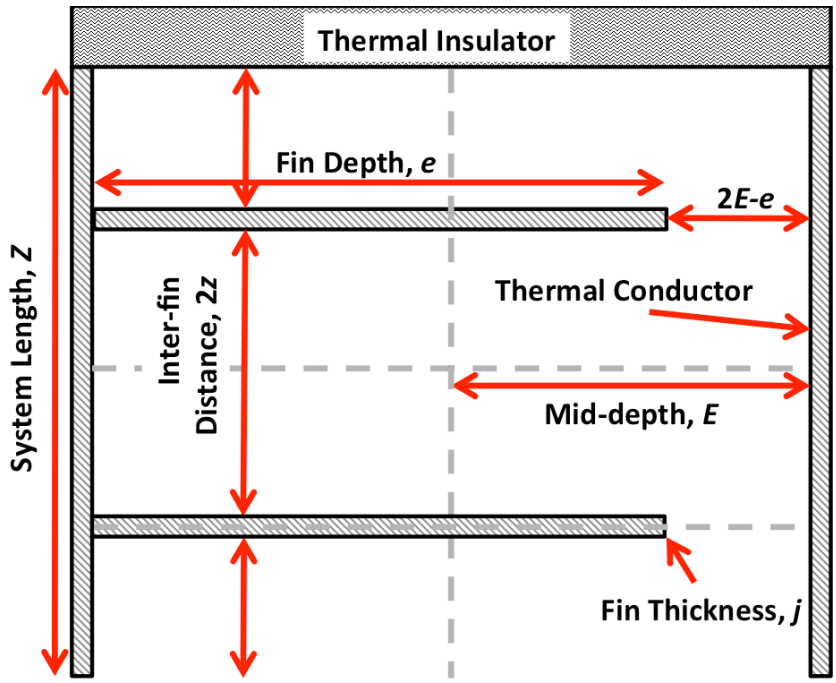

Figure 4-7: Schematic representation of a rectangular enclosure equipped with internal thermally conductive fins that are in thermal communication with the thermally conductive metal sides (i.e., heat exchange plates). The remaining ends of the enclosure consist of a thermally insulating thermoplastic (i.e., heat storage cell base), but only one end is shown. The fins are equally spaced along only one metal side and penetrate past the enclosure mid-depth.

Despite showing promising discharge heat transfer improvements using the Mark II and Mark III heat storage cell designs, neither of the fin arrangements shown in Figure 4-6 and Figure 4-7 were selected to be fabricated and evaluated for the project due to the high anticipated material and fabrication costs associated with milling the finned plate(s) from sheet stock at least 42 mm thick (including ~ 4 mm for the principal heat transfer plate surface). Additive methods (e.g., brazing, soldering, and welding), although more material and cost effective than milling sheet stock to produce the finned plates, risk causing aggressive corrosive attack at the fin-plate joints if the metallurgies differ sufficiently to give rise to dissimilar metal corrosion in the concentrated SAT PCM mixture. Only additive methods capable of guarding against aggressive corrosion at the joints would be acceptable for the implementation of finned heat transfer plates into SAT PCM heat storage cells, e.g., welding with a more cathodic joint material so that the much larger surface area base material can tolerate slow, general corrosion (anode), leaving the joint material unaffected by the galvanic processes.

4.5 EXTERNAL HEAT TRANSFER DESIGN

These next sections detail the design process employed in this project to develop and select the aluminum flow-plate designs that were used in the heat exchange plate assemblies of both Marks II and III. The bases for the individual designs discussed in Sections 4.5.1 and 4.5.2 were to adapt flow pattern design elements used in conventional plate-and-frame heat exchangers (recall Section 1.2.2), whereby emphases were placed on generating turbulence due to flow redirection (i.e., vortex generation), enhanced surface area, and mitigating HTF flow short-circuiting between the HTF inlets and outlets of the individual heat exchange plate assemblies.

Two raised patterns of geometric elements were chosen: diamonds and rectangles. These were chosen over others used in conventional plate-and-frame heat exchangers (e.g., chevrons, serpentine) due to the ease with which to parameterize their designs, ease of fabrication, and their tolerance for flow-over. Serpentine designs are most effective when the HTF flow is channelled within their confines entirely, but require some method of reliably sealing the tops (and bottoms if not machined into the plate base) of the channels to the adjacent channel plate(s) (e.g., PP plate in Marks II and III).

Note that for ease of CNC mill tooling, all of the proposed designs were constrained to minimum feature lengths of 3.2 mm, corresponding to the commonly used 1/8” milling bit. Also, in order to promote high populations of geometric elements for surface area enhancement and to generate turbulence, all of the proposed designs used fixed element spacing of 3.2 mm between neighbouring edges.

4.5.1 DIAMOND PATTERN

Figure 4-8 depicts a repeated, square pattern of diamonds, whereby the centroids of four adjacent diamonds formed a square. The diamonds were equally sized, with all four sides of length W and diagonal width $2F$, and with repeat distance between centroids equal to X. Figure 4-8 also illustrates the anticipated HTF flow paths between the elements (excluding flow-over) using the straight blue arrows, and the curved blue arrows depict anticipated highly turbulent regions.

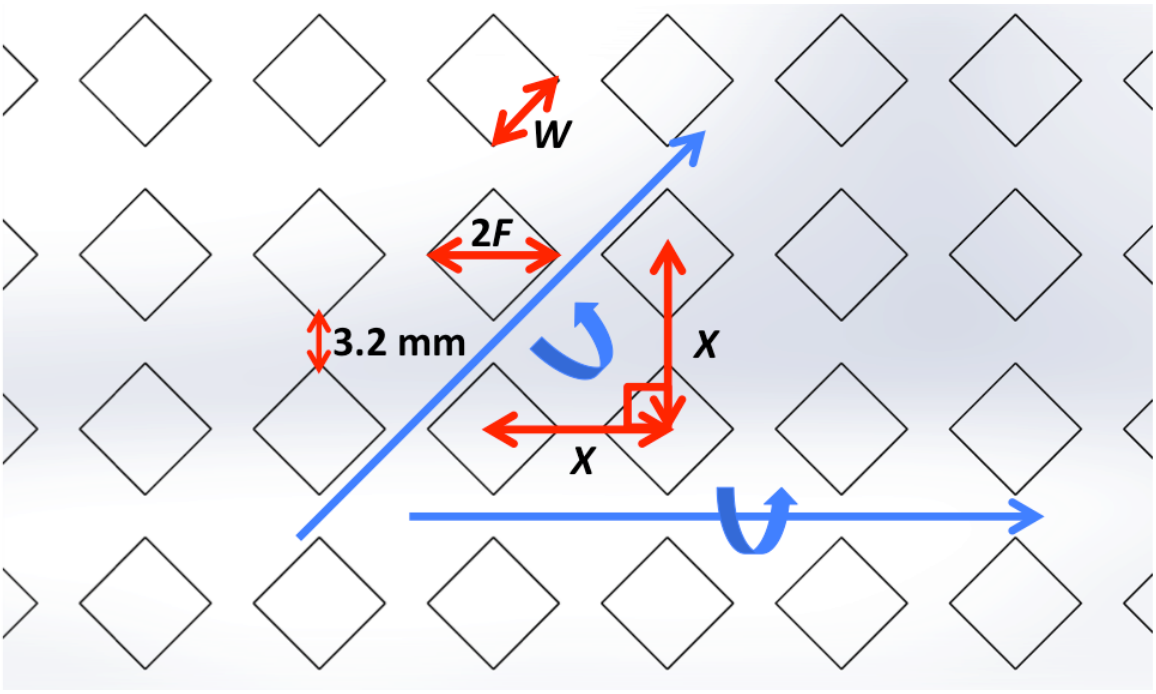

Figure 4-8: Diamond flow-plate schematic, arranged in a square-repeated pattern with repeat distance *X*. Diamonds elements have sides of length *W* and width of 2*F*. Blue arrows depict possible directions for HTF flow. Due to frequent HTF flow-channel expansions and contractions between diamond elements, high vortex generation is anticipated.

The square pattern was chosen for diamond elements due to the frequency with which interstitial HTF flow would encounter channel area contractions and expansions, as well as asymmetric wall friction from the elements and the large amount of surface area projected by the elements normal to the flow directions (causing flow redirection, i.e., vortices (Khoshvaght-Aliabadi, 2015)). In comparison to the square pattern in Figure 4-8, the compact diamond pattern shown in Figure 4-9 neither possesses the same benefits regarding vortex generation from surface area normal to the flow nor frequent channel expansions and contractions as does the square pattern, despite having a higher element population (i.e., extended surface area) than the square pattern. For these reasons, the compact diamond pattern was excluded from design consideration.

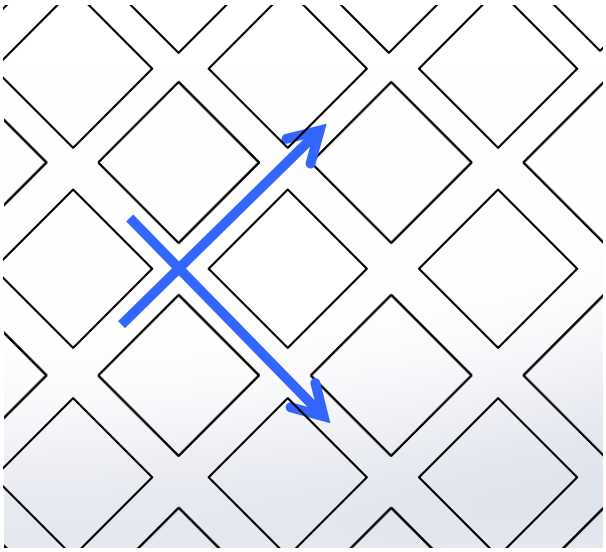

Figure 4-9: Compact diamond flow-plate schematic. Blue arrows depict possible directions for HTF flow, and vortex generation is assumed weak in comparison to the HTF flow depiction in Figure 4-8.

The governing equations for square patterns of diamond elements (Figure 4-8) are:

$$F = W sin(\pi/4), \tag{4.27}$$

and

$$X = 3.2 \text{ mm} + 2F, \tag{4.28}$$

whereby Eqs. (4.27) and (4.28) have been parameterized with respect to W, the equal edge lengths of the diamonds. Therefore, patterns varying in surface area and interstitial channel size can be easily generated from selected values of W.

4.5.2 RECTANGULAR PATTERN

As was shown with the square diamond pattern in Section 4.5.1, staggered patterns of rectangular elements (shown in Figure 4-10) can be generated from parametric governing equations. Eqs. (4.29)-(4.32) were parameterized with respect to the element vertical edge length, W, whereby a variety of patterns could be generated by selecting varying values of W.

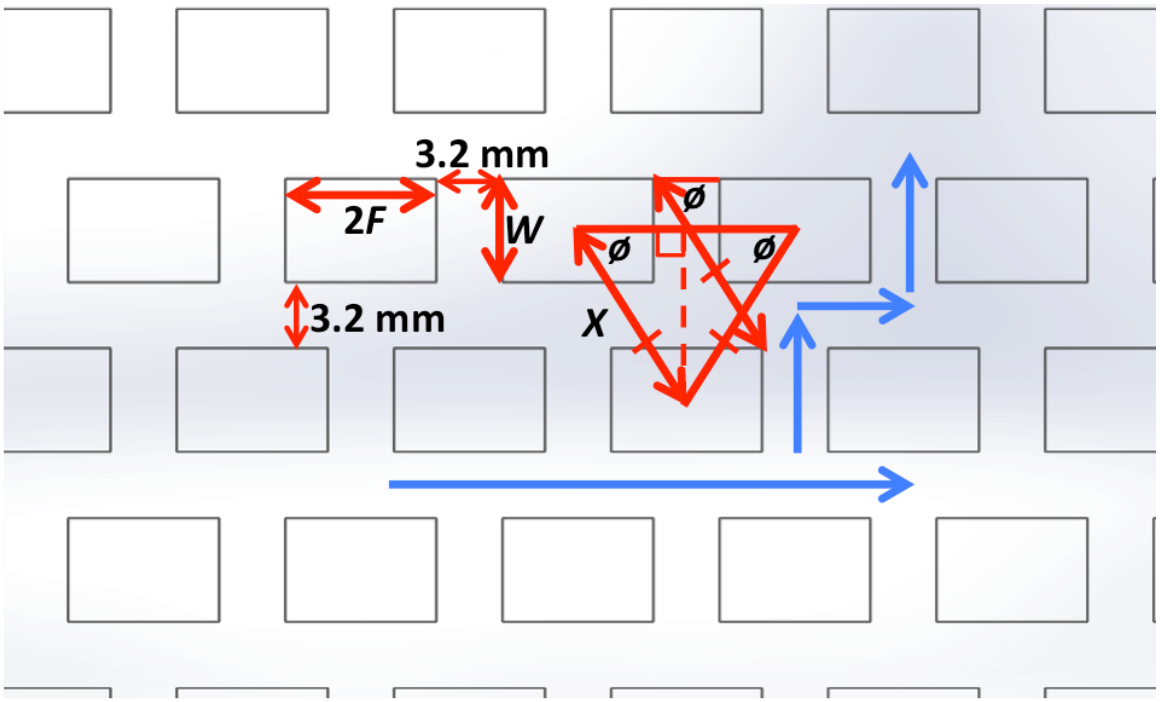

Figure 4-10: Rectangular flow-plate schematic, with repeat distance *X* and pitch angle *ø*. Rectangular elements have sides of height *W* and width of 2*F*. Blue arrows depict possible directions for HTF flow. Due to frequent diagonal flow redirection, high vortex generation is anticipated.

Eqs. (4.29) and (4.30) represent the two similar right-angle triangles with angle ϕ in Figure 4-10, from which Eq. (4.31) was derived. With respect to specifying the pattern parameters, X (Eq. (4.29)) represents the repeat distance between centroids of sequential rows of elements, while ϕ (Eq. (4.32)) represents the pitch angle between them.

$$X = \sqrt{(F + 1.6\ \text{mm})^2 + (W + 3.2\ \text{mm})^2} \tag{4.29}$$

$$WX(W + 3.2\ \text{mm})^{-1} = \sqrt{(3.2\ \text{mm})^2 + W^2} \tag{4.30}$$

$$F = 1.6\ \text{mm} + 10.24\ \text{mm}^2 W^{-1} \tag{4.31}$$

$$\phi = \sin^{-1}((3.2\ \text{mm} + W)\, X^{-1}) \tag{4.32}$$

The rationale for the staggered pattern of rectangular elements was to generate obstacles to all diagonal HTF flow (principal direction of HTF flow between heat exchange plate assembly inlets and outlets), excluding flow-over, whereby flow redirection by element surfaces normal to the flow would generate turbulence. This is illustrated in Figure 4-10 using the blue arrows to represent HTF flow, whereby the red double-arrow line joining the corners of elements in sequential rows, representing the repeat distance X, ensures that no line-of-sight exists diagonally between elements.

Unlike the square pattern of diamond elements, the staggered pattern of rectangular elements does not exhibit changes in interstitial channel cross-sections, but does possess a higher density of element occupation of the heat exchange plate surface area (thus greater potential for extended surface area heat transfer) than does the square pattern of diamond elements.

4.5.3 COMSOL SIMULATIONS

In order to establish a clear selection for the fabrication and evaluation of the Marks II and III heat storage cells, variations of each pattern type were generated in 3-D using SolidWorks 2015 and numerically evaluated using finite element method (FEM) heat transfer and computational fluid dynamics simulations in COMSOL Multiphysics 5.0. The results of the simulations were used to assess the relative importance of the benefits to heat transfer exhibited by each pattern, to allow selection of a single flow plate pattern design. These simulations were strictly for design assistance by comparing the outcomes of the various designs to one-another; therefore, only qualitative validation of the underlying model was required.

4.5.3.1 GEOMETRIES

Three dimensional (3-D) flow-plate geometries used to evaluate heat exchange assembly performance in COMSOL Multiphysics 5.0 were generated from Mark II-based flow-plate layouts only (see Figure 3-10 and Figure B- 5), since the pattern layout would remain largely unchanged for Mark III. However, it was necessary to make one concession with respect to the flow-plate design for import into COMSOL: the two 1/2" NPTF[49] (21 mm diameter) diagonally located flow ports intended for the PP plate were integrated into the flow-plate heat-exchange area. Consequently, pattern elements located in these areas were omitted. Despite the alteration in design, this approach was undertaken in order to generate matching faces throughout each layer of the complete assembly in COMSOL to facilitate meshing.

Figure 4-11 shows the final heat exchange assembly in COMSOL, in which all volume domains outside the designated heat exchange area (embossed area surrounding

[49] NPT stands for National Pipe Taper, with either an M or F suffix to designate male or female connections, respectively.

the pattern elements, measuring 160 mm × 244.8 mm in Figure B- 5) were omitted. Note that the PP plate was also omitted from the model geometry in favour of thermally insulated and zero-slip condition walls. The geometry therefore consisted of only the aluminum flow-plate contained in the heat exchange area as wells as the HTF channel domain enclosed between the aluminum flow-plate and PP end plate, sealed together by a 1/16" thick silicone rubber gasket (measuring 1.3 mm thick under compression). The HTF inlet and outlet ports shown in Figure 4-11 simply acted as open fluid flow boundaries through which fluid could flow in the surface normal directions (downward for inlet and upward for outlet).

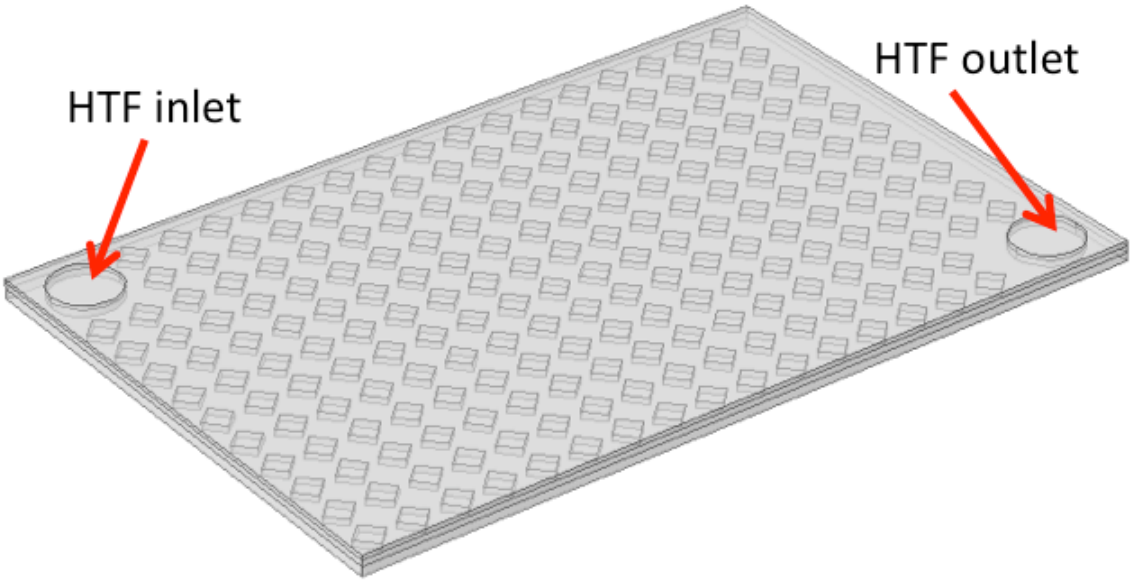

Figure 4-11: Transparent perspective view of model geometry consisting of aluminum, patterned flow-plate (diamond pattern shown), enclosed HTF channel and inlet-outlet ports.

The overall model geometry shown in Figure 3-10 was generated for parametric variations of both the diamond and rectangular patterns, shown in Figure 4-12 and Figure 4-13. Diamond and rectangular patterns were generated for W = [3, 5, 7] mm using Eqs. (4.27)-(4.28) and Eqs. (4.29)-(4.32), respectively.

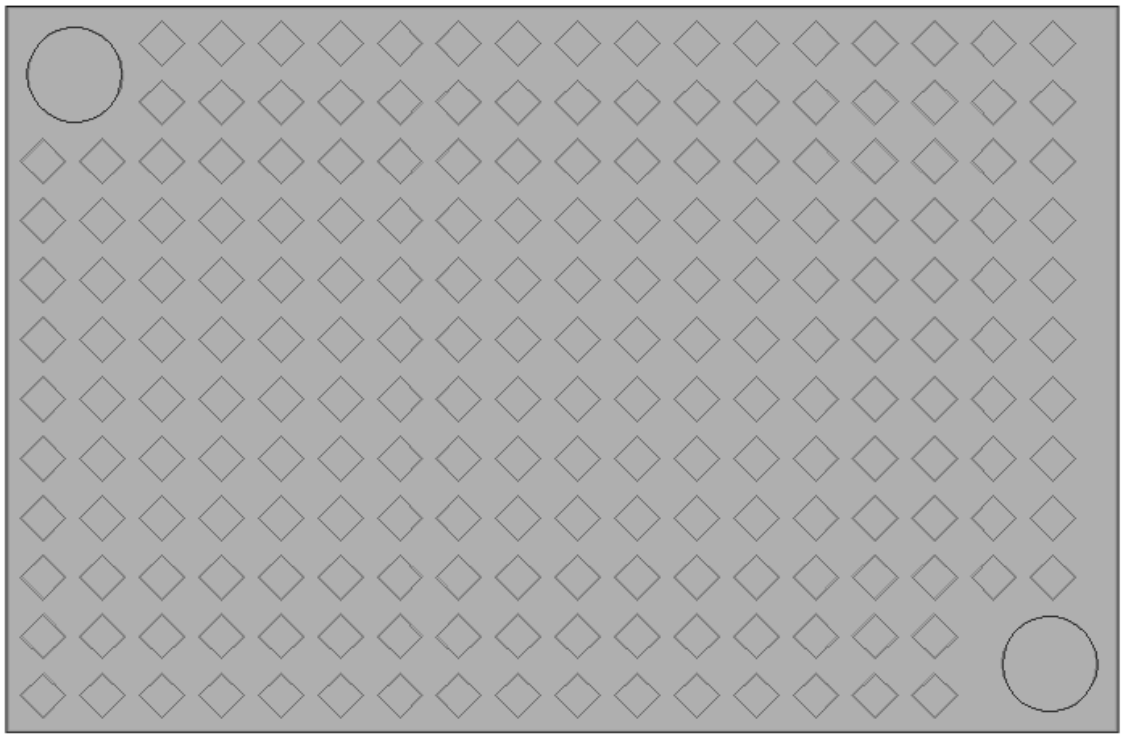

Figure 4-12: Top-view of model geometry shown in Figure 4-12 with transparency.

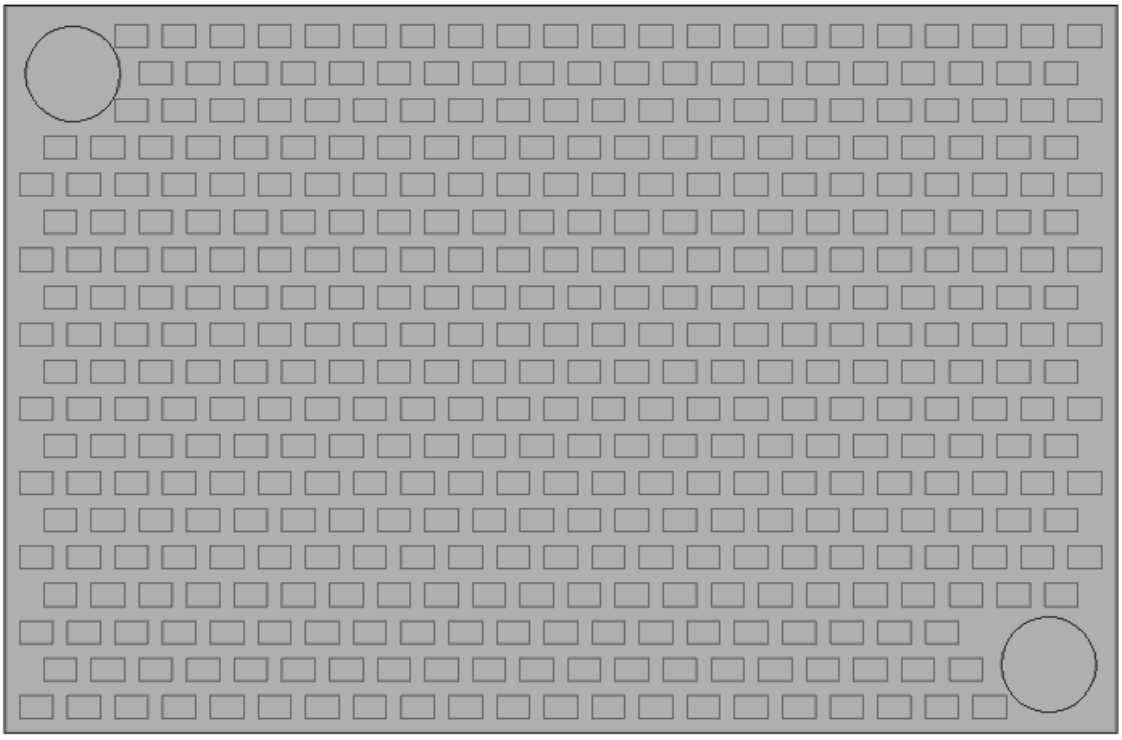

Figure 4-13: Top-view of model geometry showing a rectangular pattern with transparency.

Figure 4-14 shows the layer thicknesses of the overall heat exchange plate assembly model in COMSOL. The aluminum domain, shown in Figure 4-15, represented a 3/16" thick (4.8 mm) aluminum plate machined with the flow plate pattern to a depth of 2 mm (minimum depth typical of plate-and-frame heat exchange plates (McCabe et al., 2005)). The HTF domain, shown in Figure 4-16, consisted of the remaining volume in the 2 mm deep pattern domain and the overhead volume corresponding to the volume enclosed between the gasketted aluminum flow-plate and the PP plate.

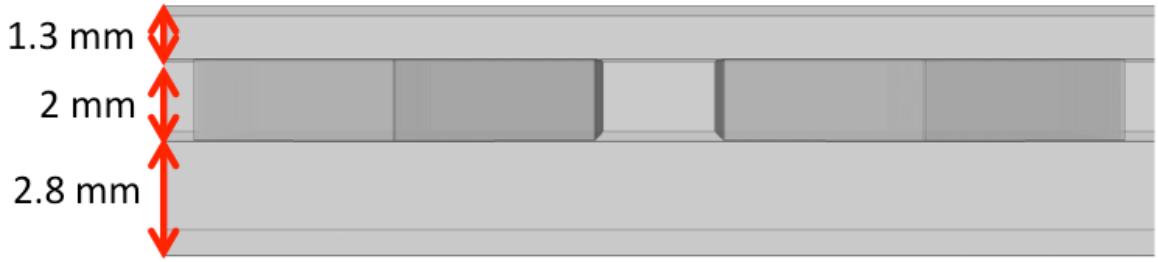

Figure 4-14: Lateral-view of model geometry shown in Figure 4-11 with transparency.

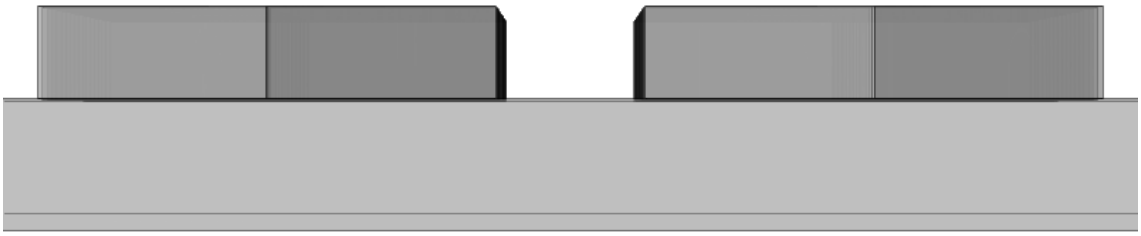

Figure 4-15: Lateral-view from Figure 4-14 showing only the aluminum, patterned flow-plate.

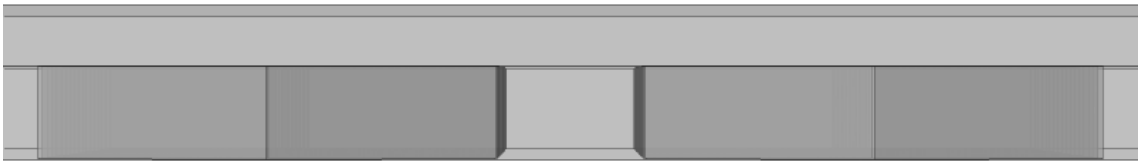

Figure 4-16: Lateral-view from Figure 4-14 showing only the HTF channel. Note the bottom layer consists only of the interstices remaining around the aluminum pattern elements in Figure 4-15 (i.e., embossed pattern).

4.5.3.2 SYSTEM CONDITIONS

In order to evaluate combined fluid flow and heat transfer performance in COMSOL Multiphysics 5.0, heat conduction equations were assigned to the aluminum flow plate domain shown in Figure 4-15, while turbulent flow (RANS and k-ε turbulence modelling selected) and convective heat transfer equations were assigned to the HTF domain shown in Figure 4-16, coupling these physics together in COMSOL using the non-isothermal flow feature. Second-order heat-transfer equation discretization was selected for both domains while second-order velocity field and first-order pressure field discretizations were selected for the momentum transfer equations (fluid flow) in the HTF domain. Only the stationary solutions (steady-state) were obtained since they formed a simple basis for performance comparisons between flow-plate pattern variations.

The thermophysical properties of aluminum and water were selected from the COMSOL built-in material library to represent the aluminum flow-plate and HTF, respectively. Water (Pr ~ 7 at room temperature (McCabe et al., 2005)) was chosen rather than a solution of PG-water (Pr ~ 40 at room temperature for 40 vol% PG in water (ASHRAE, 2013)) for ease of modelling since experimental validation of the COMSOL models was not performed.

The plain bottom surface of the flow-plate domain simulated heat transfer from the SAT PCM as a heat source, remaining constant at T_{trans} = 55 ˚C. The HTF inlet and outlet boundary conditions were 20 ˚C and 1 L/min at the inlet and 0 kPa(g) at the outlet. All remaining external boundaries were modelled as thermally insulated walls, with zero-slip condition wherever HTF was present.

4.5.3.3 MESH

Due to the complex surface geometry formed in the successive layers by the diamond patterns and the circular HTF inlet and outlet ports, free triangular meshes were selected for these surfaces, as shown in Figure 4-17. Although the diamond pattern elements were not shown explicitly in Figure 4-17, their effect on the triangular mesh can be inferred. In order to facilitate a swept mesh, the triangular meshes throughout the layers were made identical to one-another.

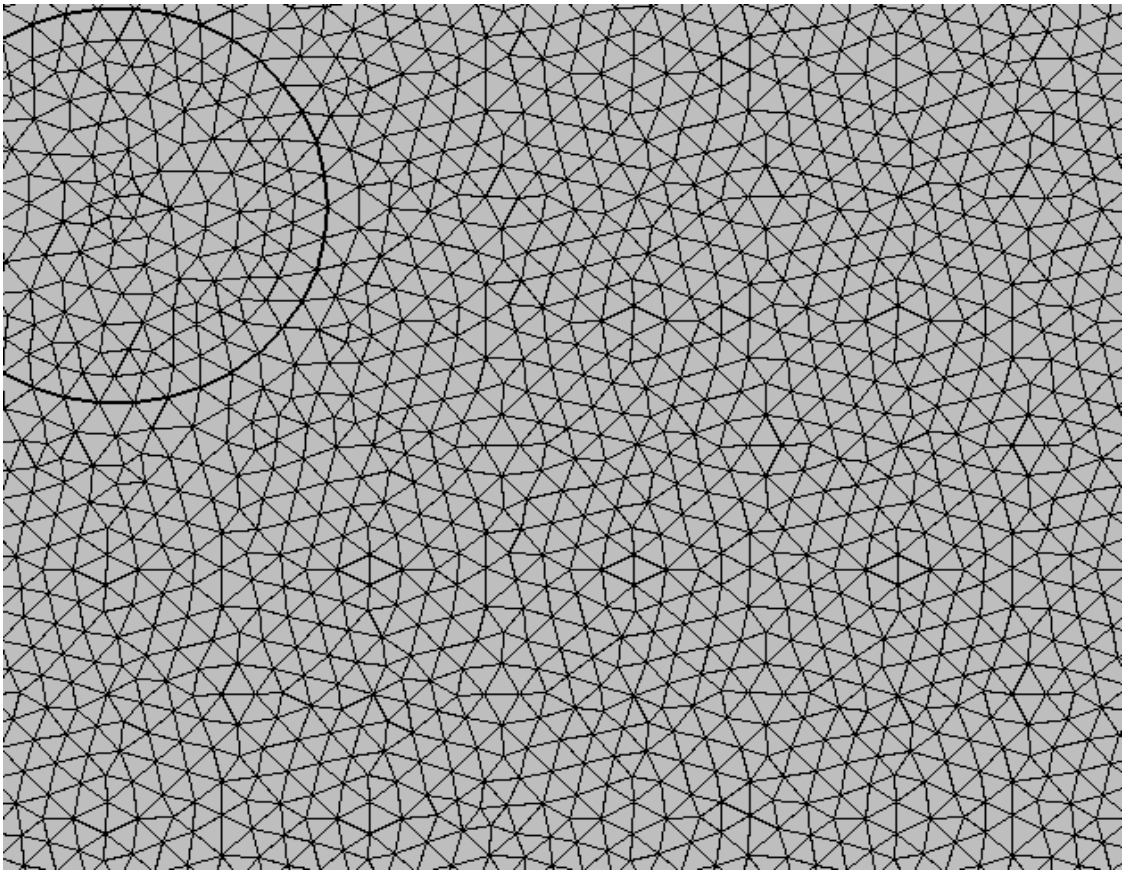

Figure 4-17: Close-up of top-view shown in Figure 4-12 illustrating a fine triangular free surface mesh distribution around HTF inlet port and diamond pattern.

The three dimensional mesh elements were generated from the identical triangular surface meshes using quadrilateral swept meshes distributed in the model geometry's lateral edges (Figure 4-18), forming triangular prism shaped 3-D mesh elements.

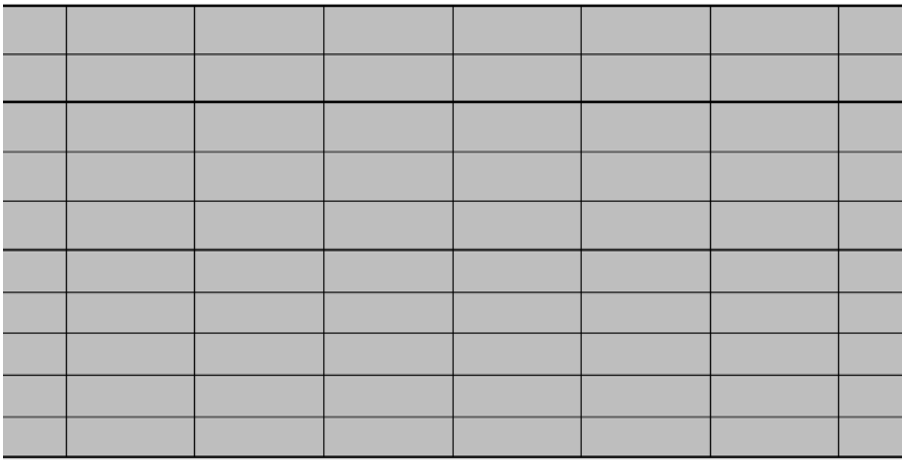

Figure 4-18: Lateral-view of geometry shown in Figure 4-14 showing a vertical quadrilateral swept-mesh element distribution of 0.6 mm/element, nominally.

Various refined meshes were previously evaluated for models wherein the PP plate was equipped with the pattern elements (evaluating turbulent vortex generation only, excluding extended surface area effect) instead of the aluminum plate, but otherwise identical to the model in the present discussion. Consequently, the patterned PP plate mesh convergence study was adopted as proxy for the patterned aluminum flow-plate model. The mesh convergence shown in Figure 4-19 demonstrated that the second-finest mesh (0.6 mm average element size) would be sufficiently converged while improving computational performance in comparison to the finest mesh (6 h vs. 2 days of simulation time on a 2.4 GHz 16-core hyperthreaded Intel i7 computer with 128 GB of RAM). Therefore, all of the pattern variations, both diamond and rectangular, were evaluated using a fine triangular free mesh setting for the layer surfaces and a quadrilateral swept mesh element distribution of 10 elements in the model depth, producing a mesh with an average element size of 0.6 mm, approximately 380,000 3-D mesh elements, and an average mesh quality of 0.72.

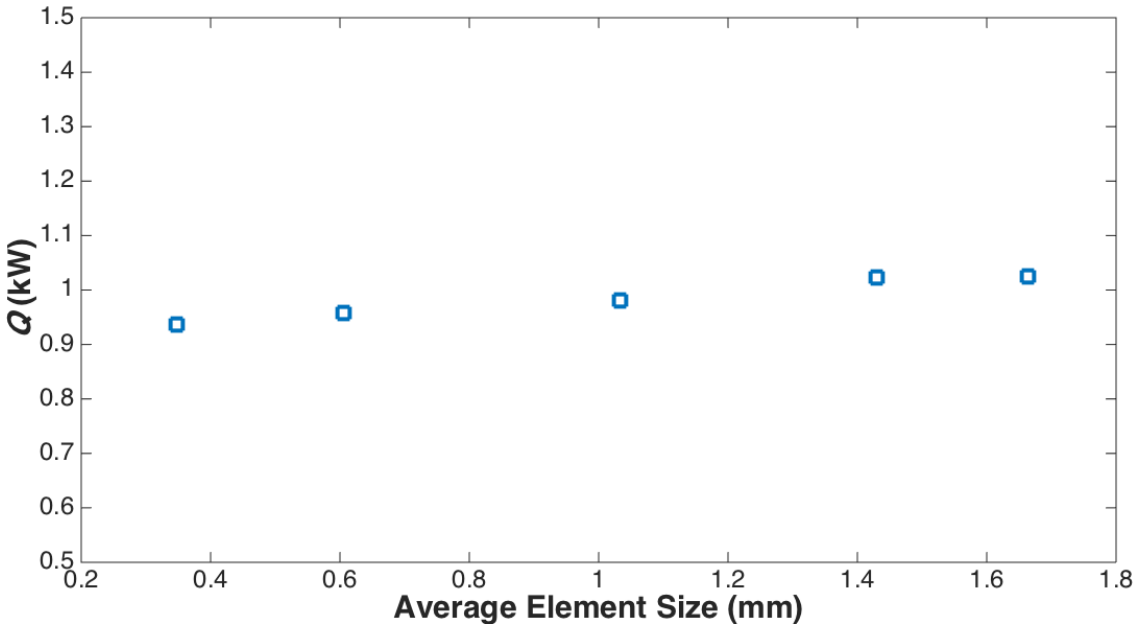

Figure 4-19: Mesh convergence study for the patterned PP plate study (W = 5 mm rectangular pattern) showing the total heat-transfer rates vs. the average 3-D mesh element size. The mesh with average element size of 0.6 mm was selected as the converged mesh for all further model studies with the patterned aluminum flow-plates.

4.5.3.4 RESULTS AND FLOW PATTERN SELECTION

Results pertaining to the heat transfer performances of the various diamond and rectangular patterns are listed in Table 4-1. Results for average heat flux (U_{sup}•$LMTD$) and enthalpy-average HTF outlet temperatures ($T_{ave,out}$) were generated in post-processing from COMSOL, while all other heat transfer values were calculated using Eqs. (4.5) and (4.6). Note that U_{sup} and U_{int} each refer to the superficial (based on flat plate area) and interstitial (based on total heat exchange area) values of the overall heat transfer coefficients and these coefficients correspond only to the HTF and aluminum flow-plate heat transfer characteristics, excluding the thermal conductance from the SAT PCM and the aluminized barrier film used to isolate the aluminum flow-plate from the SAT PCM in Marks II and III, i.e., Eq. (4.13) omitting R_{air}, R_{film}, and R_{PCM}.

Table 4-1: COMSOL Multiphysics heat transfer and computation fluid dynamic Mark II heat exchange plate assembly simulation results.

	Diamonds			Rectangles		
***W* (mm)**	3	5	7	3	5	7
Elements	654	334	208	425	415	371
Extended area (mm^2)	15696	13360	11648	22151	20418	19485
Flat plate area (mm^2)	39168	39168	39168	39168	39168	39168
Total area (mm^2)	54864	52528	50816	61319	59586	58653
% Area increase	40	34	30	57	52	50
***U*$_{sup}$•*LMTD* (kW/m^2)**	34.36	40.25	40.03	35.99	36.83	36.29
***UA* (kW/K)**	0.056	0.072	0.072	0.060	0.062	0.061
***U*$_{int}$ (kW/m^{2}K)**	1.017	1.374	1.407	0.978	1.044	1.036
***U*$_{sup}$ (kW/m^{2}K)**	1.42	1.84	1.83	1.53	1.59	1.55
***T*$_{ave,out}$ (˚C)**	39.22	42.52	42.40	40.14	40.61	40.30
***LMTD* (K)**	24.12	21.84	21.93	23.51	23.19	23.40
***Q* (kW)**	1.35	1.58	1.57	1.41	1.44	1.42

The data in Table 4-1 revealed that the diamond pattern with W = 5 mm generated the most heat transfer, accomplished by generating turbulence in the HTF most effectively. This was observed by examining the respective values of U_{sup} and U_{int} for each pattern, revealing that the majority of U_{sup} remained after compensating for the effect of extended surface area (U_{int}). Based on the scale difference between U_{sup} and $1/R_{plate}$ discussed in Section 4.3, it was also noted that the values of both U_{sup} and U_{int} reported in Table 4-1 were closely representative of $1/R_{HTF}$.

This effect was always most evident with the sparser patterns, $W = [5, 7]$ mm, and greatest for the diamond patterns that were generally more sparsely populated than for the rectangular patterns. The latter suggested that patterns too densely populated and with higher inherent resistance to the passage of flow (i.e., rectangular) generated too much resistance to the passage of flow between elements, causing the HTF to preferentially flow above them instead. Consequently, increased HTF flow-over would generate less turbulence than would HTF flow between the pattern elements and cause the flow to channel diagonally between inlet and outlet. Figure 4-20 and Figure 4-21 depict these differences in HTF flow by showing their proportional velocity field arrow plots. Note that diagonal HTF flow is largely suppressed for the diamond pattern flow-plate with $W = 5$ mm in Figure 4-20 as opposed to the HTF flow for the rectangular pattern flow-plate with $W = 5$ mm in Figure 4-21. The latter confirming the hypothesized origin of the higher values for U_{int} observed in Table 4-1 for diamond vs. rectangular patterns and for sparse vs. densely populated patterns.

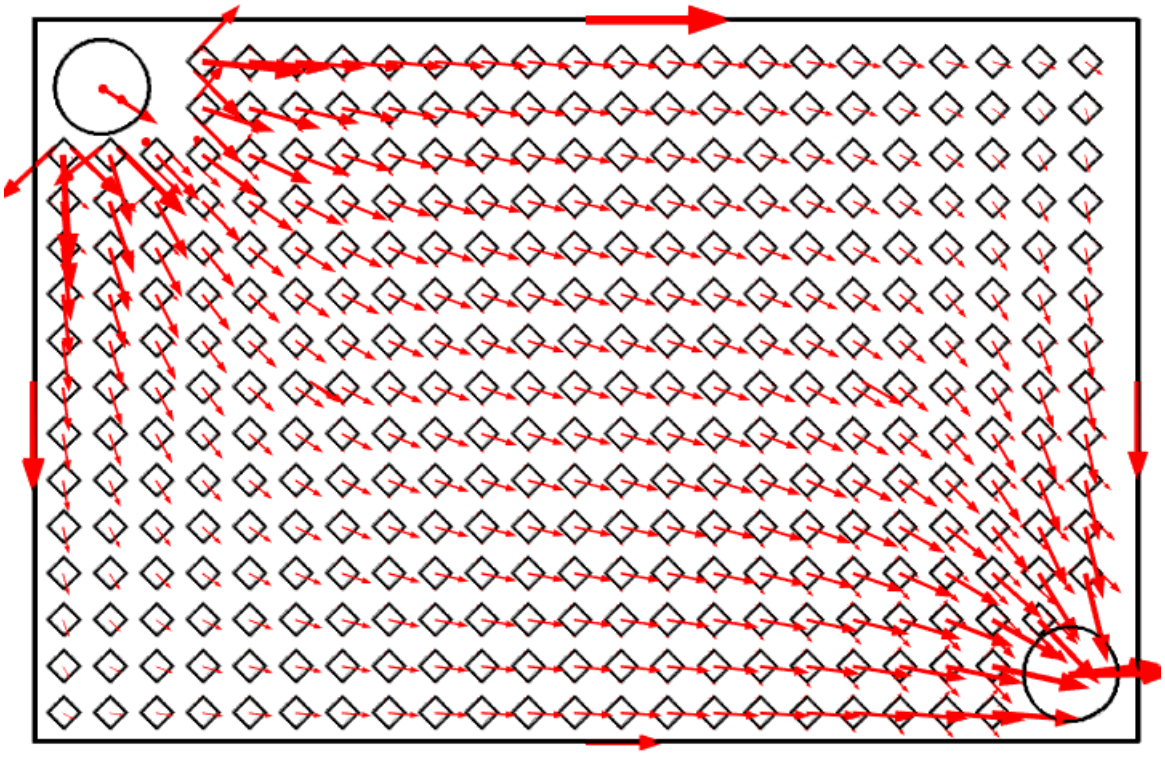

Figure 4-20: Top-view of proportional HTF velocity field (2-D) over 5 mm diamond pattern flow-plate design. Arrows indicate the distribution of HTF flow direction and the relative magnitude of velocity.

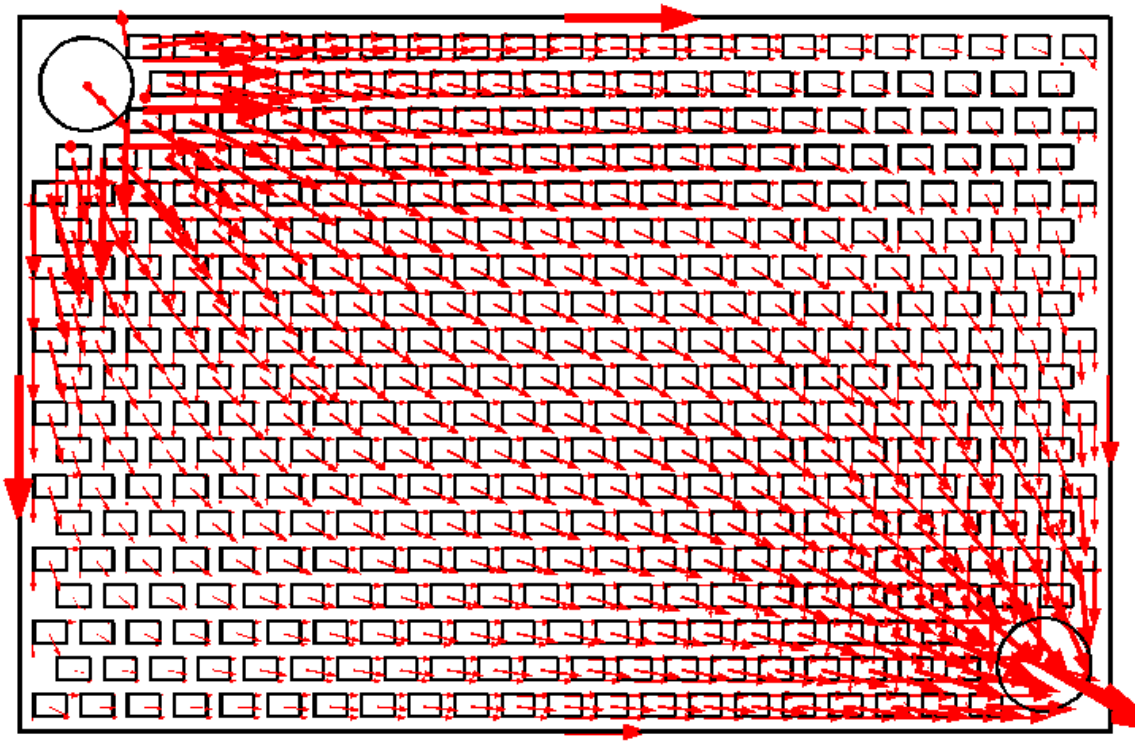

Figure 4-21: Top-view of proportional HTF velocity field (2-D) over 5 mm rectangular pattern flow-plate design. Arrows indicate the distribution of HTF flow direction and the relative magnitude of velocity.

Therefore, for reasons of improved HTF distribution and vortex generation that resulted in the highest values of Q and UA reported in Table 4-1 from COMSOL evaluations, the diamond flow-plate pattern with $W = 5$ mm was chosen for the subsequent fabrication of the Mark II and Mark III aluminum flow-plates.

4.6 HEAT EXCHANGE DESIGN EVALUATION

The selection of the heat exchange plate design having been established from the evaluations executed in Section 4.5.3, and the scale of R_{HTF} having been established using numerical simulations in Section 4.3, the final step was to evaluate the heat exchange performances of the Marks II and III heat storage cells in the experimental circulating HTF system consisting of the ETS and heater-chiller loops. Note that due to the fact that only one Mark II heat storage cell was fabricated, evaluations were largely conducted using the ETS loop due to the lower HTF flow rate requirements. Likewise, the heater-chiller loop was frequently used to evaluate the performances of Mark III heat storage cells '3' and '4' simultaneously due to its capacity to deliver higher HTF flow rates.

Only HTF residence-time average heat transfer rates, Q, log-mean-temperature-differences, $LMTD_{ave}$, and heat transfer capacity rates, UA, were calculated for the evaluations of heat transfer performance of Marks II and III in the following sections. Individually, their values were determined with sufficient accuracy to enable comparisons, however, integral values of Q (i.e., total heat transferred) were not calculated due to the ensuing excessive cumulative uncertainties, also reported by Kabbara (2015). Furthermore, comparisons of total heat transfer would not provide a suitable basis for comparison between Marks II and III since both used the same amount of SAT PCM and both were charged to equivalent states, therefore making comparisons of their energy storage capacities moot.

4.6.1 UNCERTAINTY ANALYSIS

Calculated values of heat-transfer rates, Q, and heat transfer capacity rates, UA, were determined for Mark II and Mark III heat storage cells, respectively, and reported in Sections 4.6.2 and 4.6.3, as well as for liquid-to-air heat exchanger performance in Section 4.7. Their respective uncertainties were quantified and reported to aid gauge the significance of differences between reported results.

For the heat-transfer rates, Q, determined using Eq. (4.1), the resulting error propagation analysis yields (derived in detail in Appendix F):

$$dQ = \sqrt{\left(\frac{\partial Q}{\partial T_2}dT\right)^2 + \left(\frac{\partial Q}{\partial T_1}dT\right)^2 + \left(\frac{\partial Q}{\partial V}dV\right)^2}\,, \tag{4.33}$$

for which only temperature and flow rate measurements constituted linearly independent variables of Q. Note that average values of V were used to calculate Q, due to transient variations of V measured during the heat exchange process residence time (t_f in Appendix F), but are not represented in Eq. (4.33). The result is just the average of the individual error propagation contributions, for which the details are found in Appendix F.

Likewise, the error propagation analysis of the heat transfer capacity rates, UA, yields:

$$dUA = \sqrt{\begin{array}{c}\left(\frac{\partial UA}{\partial T_2}dT\right)^2 + \left(\frac{\partial UA}{\partial T_1}dT\right)^2 + \left(\frac{\partial UA}{\partial V}dV\right)^2 + \left(\frac{\partial UA}{\partial (T_1 - T_2')}2dT\right)^2 + \\ \left(\frac{\partial UA}{\partial (T_2 - T_1')}2dT\right)^2\end{array}}\,, \tag{4.34}$$

where the latter three quantities were time-averaged over the respective heat exchange process residence time. The detailed derivations are all found in Appendix F. However, since *UA* values derived from experimental measurements were inherent to the individual heat transfer processes, the experimental uncertainties of average *UA* values reported in Sections 4.6.2 and 4.6.3 were also supplemented with the magnitudes of their respective 95 % confidence intervals, equal to 2σ (σ = standard deviation of *UA* data).

4.6.2 MARK II

Figure 4-22 and Figure 4-23 show the transient HTF inlet and outlet temperatures and corresponding heat-transfer rates (Q) that were calculated for Mark II in the ETS loop with an HTF flow rate of 3 L/min for one complete cycle, in which positive values correspond to charging and negative values correspond to discharging. As can be seen in Figure 4-23, the heat-transfer rates during charging can only be reliably interpreted in the initial period prior to the 1.5 kW electric heater's repeated on/off cycles used to maintain the HTF set-point temperature. For this reason efforts were made to isolate and omit the frequent on/off periods from the calculations of average heat-transfer rates and *UA* values.

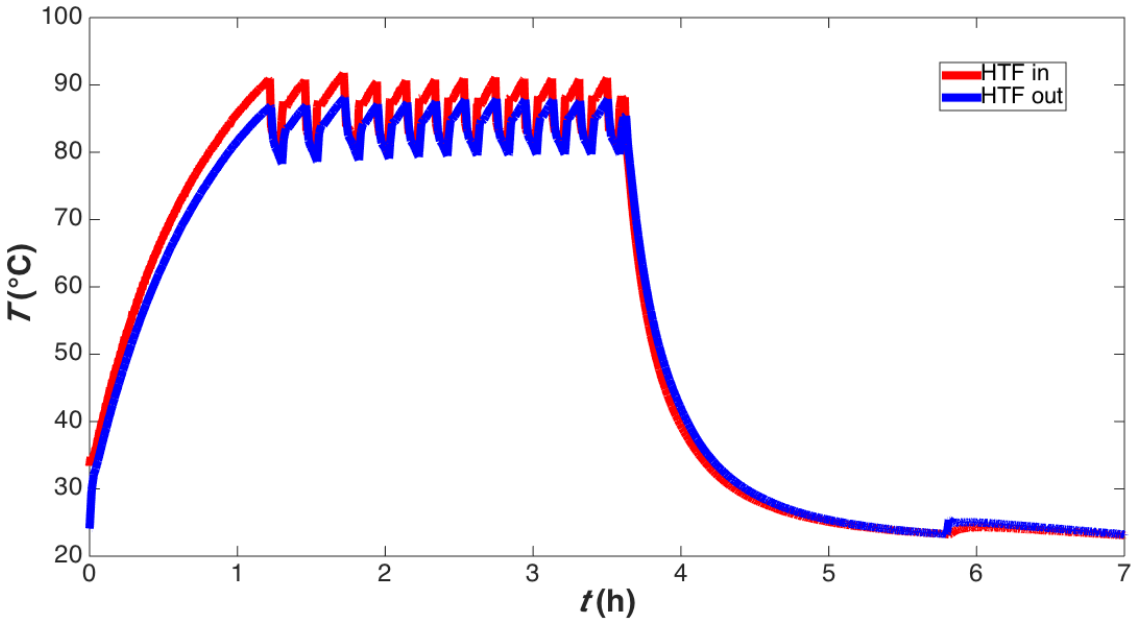

Figure 4-22: Mark II heat storage cell HTF inlet and outlet temperature profile during one complete cycle in the ETS loop, with an average HTF flow rate of 3 L/min and fan power supply set to 100 V. Nucleation triggering occurred shortly before t = 6 h.

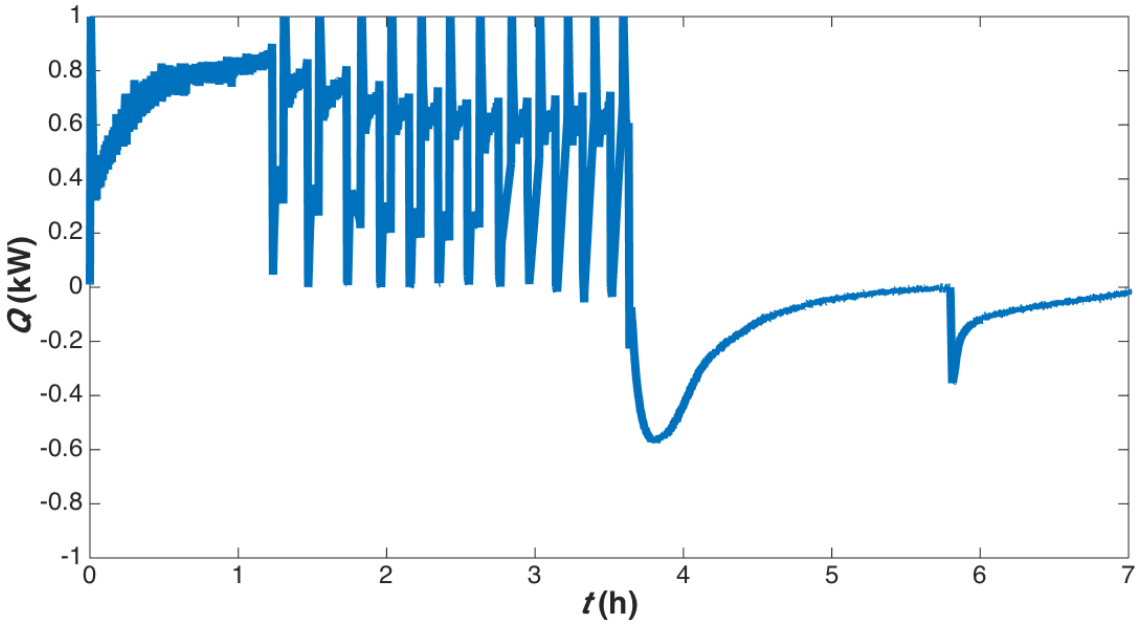

Figure 4-23: Mark II heat storage cell heat-transfer rate (Q) profile corresponding to Figure 4-22. Positive values indicate charging, while negative values indicate discharging. Nucleation triggering occurred shortly before t = 6 h. Values of Q > 1 kW were truncated from the figure range to improve visibility of the profile.

During discharge, however, no such efforts were needed since the resulting heat-transfer rate profiles were smooth. Generally, as was calculated for the heat-transfer rate profile in Figure 4-23, discharge heat-transfer rates did not remain steadily high like they did during charging, and the supercooling peak heat-transfer rates (around t = 3.8 h in Figure 4-23) were approximately double the peak heat-transfer rates occurring at the onset of solidification (i.e., nucleation triggering, shortly before t = 6 h in Figure 4-23).

Although the integrated heat transfer values were not calculated for the separate heat transfer processes shown in Figure 4-23, it was apparent that the resulting heat transferred to the HTF during supercooling (e.g., large, broad peak around t = 4 h) was greater than during solidification (small, narrow peak around t = 6 h). This was in apparent contradiction to their respective heat discharge capacities, approximately equal to one-another as per the results calculated for charging up to 80 ˚C using Eqs. (2.3) to (2.6) in Section 2.3.2.2 and reported in Section 3.3.3.2. However, the apparent excess heat transferred during supercooling was attributed to the sensible energy stored in the heat storage cell's structural materials, for which the PP base alone represents comparable sensible thermal mass to the SAT PCM's sensible heat storage capacity. After supercooling to ≤ 28 ˚C was complete, and solidification heat discharge was initiated

using the nucleation-triggering devices, only the SAT PCM's latent heat storage capacity remained to be transferred to the HTF. Note that this also occurred for discharge heat transfer from Mark III and was also attributed to the excessive amount of structural materials used in the heat storage cell construction.

Figure 4-24 shows the values of *UA* corresponding to the heat-transfer rates in Figure 4-23. The relatively constant values recorded during charging (excluding the heater on/off cycles) suggest that the phase-change process proceeded with relative uniformity during that period, such that internal natural convection (i.e., fully dissolved solution) did not yet occupy the majority of the SAT PCM. With regard to supercooling, however, it can be seen how internal natural convection responds to the heat transfer conditions by gradually decreasing in intensity with decreasing heat-transfer rates. Also, due to the complete occupation of the porous solid SAT PCM during solidification, *UA* is observed to remain relatively constant after the onset of solidification, characteristic of complete heat conduction control of the heat transfer process.

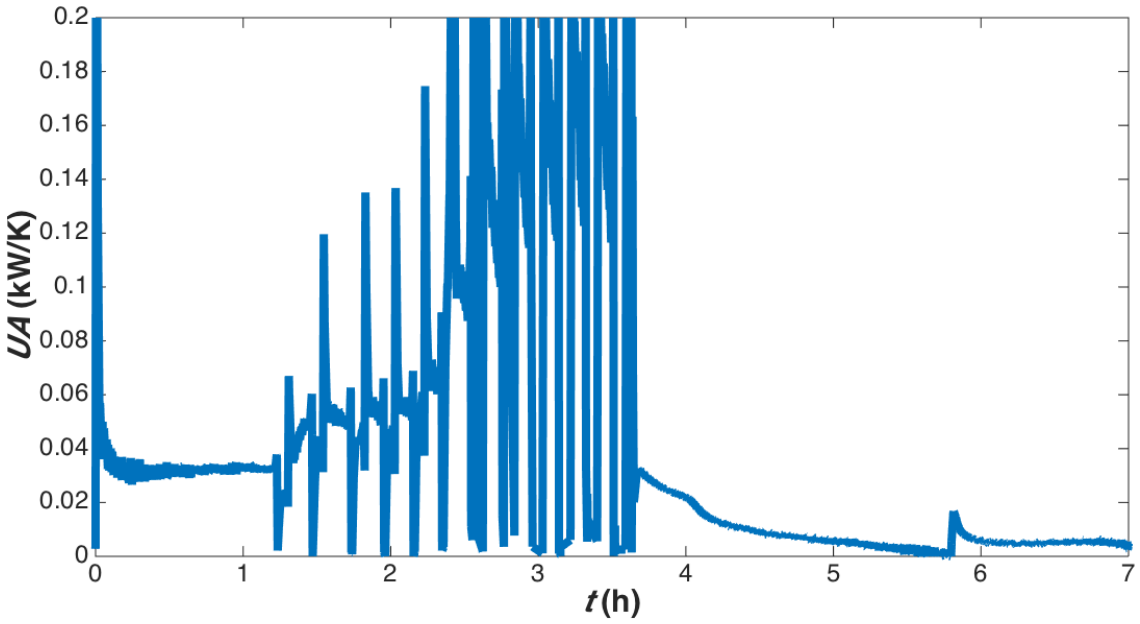

Figure 4-24: Mark II heat transfer capacity rate (*UA*) profile corresponding to Figure 4-23. Values of *UA* above 0.2 kW/K were truncated from the figure to improve visibility of the profile.

To investigate the effect of HTF flow rate on the heat transfer processes, Figure 4-25 shows the average values of Q for charge and discharge during repeated cycling experiments, each conducted at constant HTF flow rate (i.e., fixed needle valve setting) in

the range of 1.5 L/min to 3 L/min. The average heat-transfer rates were chosen to reflect the nominal performance of heat storage systems, as was reported by Medrano et al. (2009) for their heat storage evaluations.

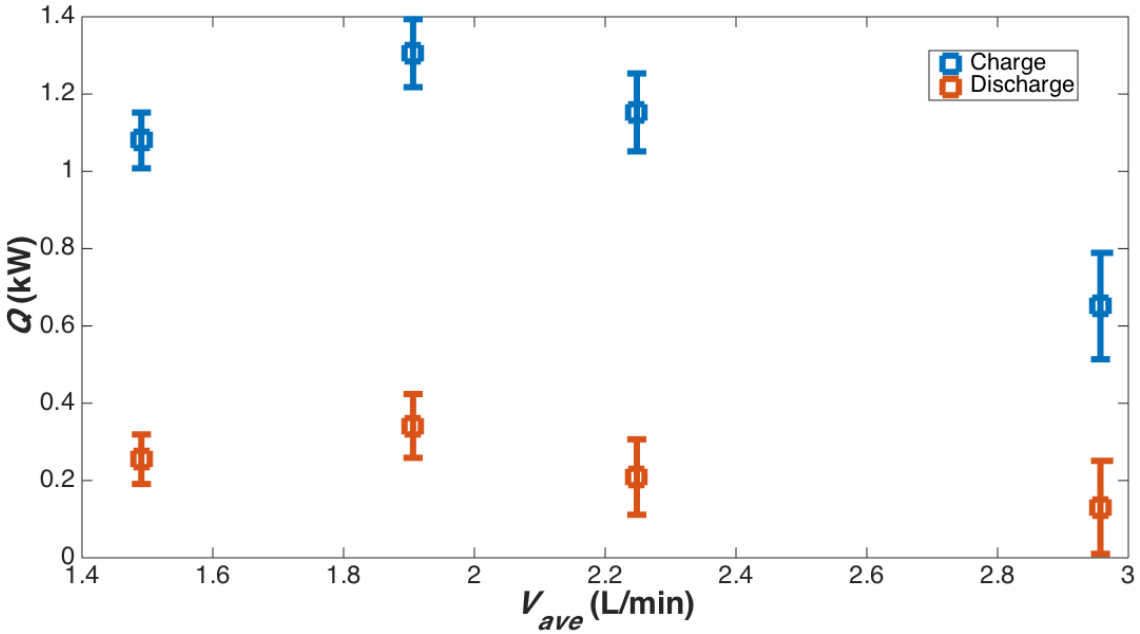

Figure 4-25: Summary of Mark II average charge and discharge (solidification and supercooling) heat-transfer rates (Q) evaluated in the ETS loop at various HTF flow rates. Error bars correspond to the average calculated uncertainties for each experiment.

It was first noted how all values of the discharge heat-transfer rates were relatively invariant to HTF flow rate, all remaining below 0.4 kW, therefore confirming absolute conduction heat transfer control of the heat-discharge process. Charge heat-transfer rates, on the other hand, were observed to decrease at higher HTF flow rates, most notably between 2.2 L/min and 3 L/min for which Q decreased from 1.2 kW to 0.65 kW. Although this trend would appear inconsistent with increasing HTF flow rates, Figure 4-26 demonstrates that temperature differences between the HTF and SAT PCM, represented by the residence-time average *LMTD* profiles of the respective experiments summarized in Figure 4-25, declined in the initial heating periods preceding the heater on/off cycles. Due to the sustained full power operation of the ETS loop's 1.5 kW electric flow-through heater during those periods preceding the heater on/off cycles, Eq. (4.1) dictates that HTF circulation at lower flow rates would result in higher outlet temperatures and quicker rise in HTF temperature than would result from higher HTF flow rates, observed in the rise of the respective *LMTD* profiles in Figure 4-26.

Consequently, the reduced temperature differences between the HTF and the SAT PCM observed in Figure 4-26 at higher HTF flow rate resulted in their decreased heat-transfer rates recorded in Figure 4-25[50] for the period prior to heater on/off cycles. Despite the lower initial *LMTD*s (and resulting heat-transfer rates) exhibited in Figure 4-26 at higher HTF flow rates, consistently elevated *LMTD*s were maintained over longer periods before and after the electric heater's on/off cycles than for lower HTF flow rates, resulting in higher sustained heat-transfer rates (including heater on/off cycles). This result corresponded to the observations of more rapid complete charging of the heat storage cells at higher HTF flow rates for both Marks II and III in Chapter 3.

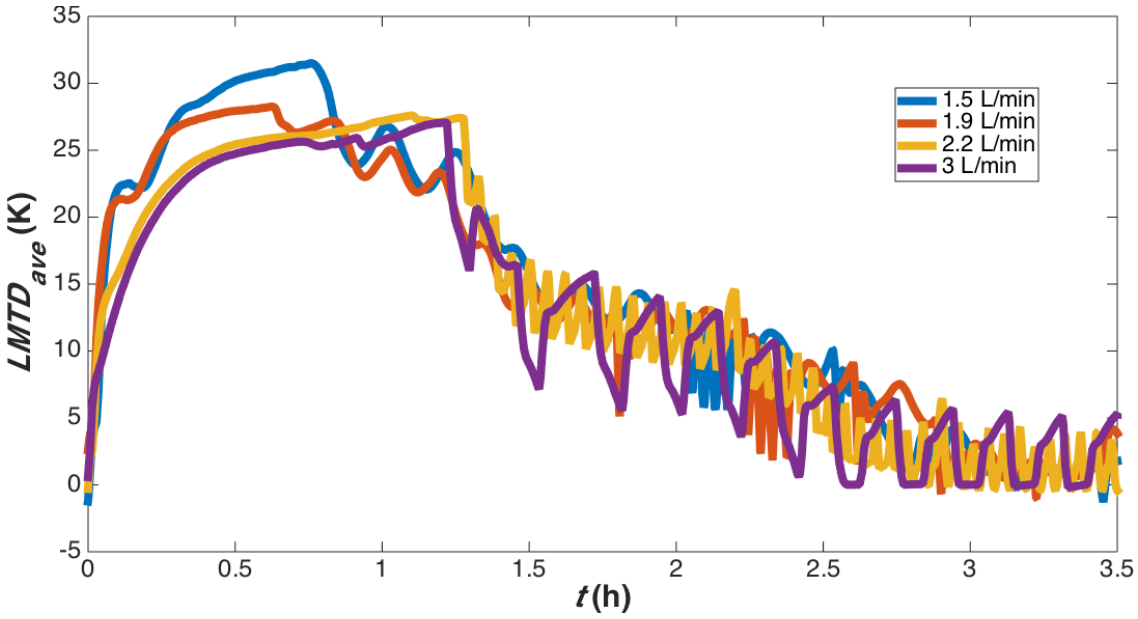

Figure 4-26: Representative Mark II residence time-average *LMTD* charge profiles for all four HTF flow rate experiments summarized in Figure 4-25.

Figure 4-27 shows the average values of *UA* determined using Eq. (4.5) corresponding to the experiments reported in Figure 4-25. The average values of all three processes (charge, supercooling, and solidification) remained generally constant for all HTF flow rates, therefore confirming the absolute control of internal, PCM heat transfer processes. These were ranked in descending order as charge (~ 0.05 kW/K), supercooling (~ 0.02 kW/K), and solidification (~0.01 kW/K), whereas the estimated *UA* for the HTF

[50] Assuming that values of *UA* remained steady, which were later confirmed in Figure 4-27. In general, at constant HTF flow rate and all other heat transfer mechanisms remaining unchanged (or not changing rapidly), *UA* values would remain steady while temperature differences would vary significantly if left uncontrolled.

and aluminum flow plates were estimated to be 0.174 kW/K[51] in Table 4-1. Normalized to the total heat transfer area of 0.078 m^2 for Mark II, the overall heat transfer coefficient values, U, of the respective processes become 0.6 kW m^{-2} K^{-1}, 0.3 kW m^{-2} K^{-1}, and 0.1 kW m^{-2} K^{-1}, respectively, indicating clearly that both of the remaining principal thermal resistances in Eq. (4.13), R_{air} and R_{PCM}, exceeded the minimum value identified for R_{PCM}. The latter further suggests that $R_{PCM} > R_{air}$ since the value of U_{cell} reported for Mark II responded significantly to the heat transfer processes corresponding to the internal processes of the SAT PCM (charge, supercooling, and solidification).

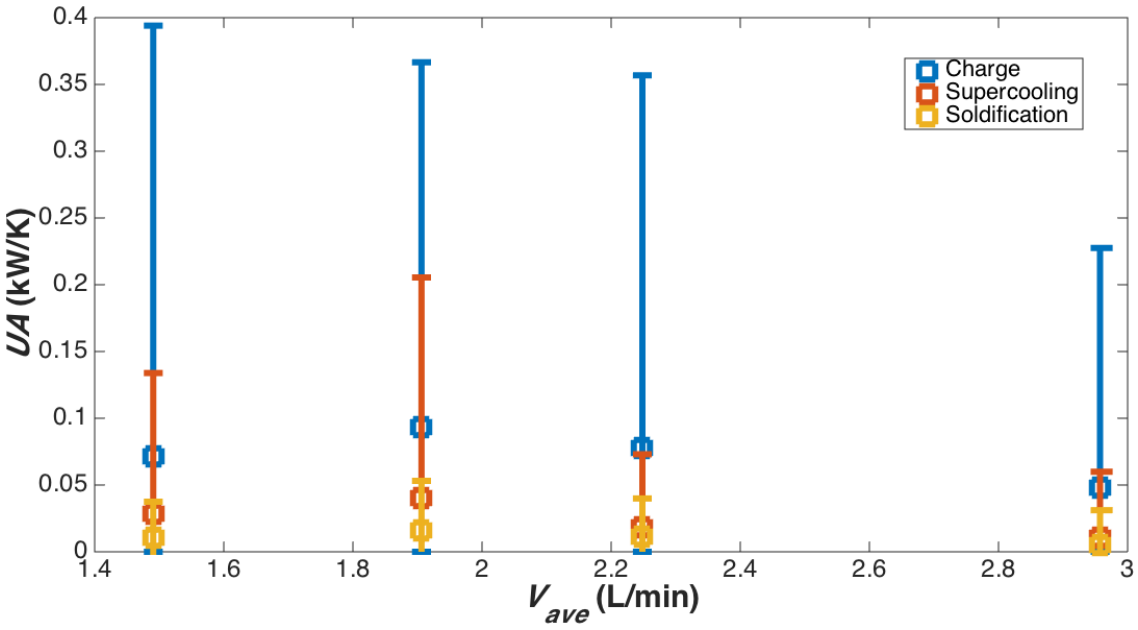

Figure 4-27: Summary of Mark II average charge, supercooling, and solidification heat transfer capacity rates (UA) corresponding to the values of average heat-transfer rates shown in Figure 4-25. Error bars correspond to the sum of the average calculated uncertainties for each experiment and 2σ.

The charge heat-transfer processes for the Mark II heat storage cell were therefore sufficient to support charging in an ETS system using a 1.2 kW to 1.5 kW electric heater, as was noted in Section 3.3.3.2.1. However, both the supercooled liquid and solidification heat-discharge processes were insufficient to support the desired 600 W average heat discharge rate (objectives 11 and E in Section 2.2) from just one heat storage cell. However, when considering only the benchmark literature overall heat transfer coefficient values, U, for SAT PCM heat storage systems (recall Section 1.2.2), expressed

[51] This value was doubled from the value listed in Table 4-1 to correspond to the heat exchange plate pairs used in Marks II and III.

in objective 10 in Section 2.2 as > 30 W m^{-2} K^{-1}, those reported herein for Mark II exceeded this benchmark, therefore achieving the objective.

Since the values of *U* were all sufficiently high to fulfill objective 10, fulfilling objectives 11 and E with a heat storage cell based on the Mark II design would require either increased heat transfer surface area (and PCM volume/mass, affecting all heat transfer processes), reduced heat storage cell depth (and PCM volume/mass, affecting mainly heat discharge processes; recall internal heat transfer discussion in Section 4.4), or both.

4.6.3 MARK III

In order to be compared effectively with the Mark II heat storage cell HTF temperature profiles in Figure 4-22 and heat-transfer rate profile in Figure 4-23, Figure 4-28 and Figure 4-29 show the HTF temperatures and calculated heat-transfer rate profile for Mark III '3' operated in the ETS loop in parallel with Mark III '4' with a total HTF flow rate of 3.6 L/min (partitioned between '3' and '4' at an average of 1.8 L/min). All other reported heat transfer experiments using Mark III '3' and '4' were conducted in the heater-chiller loop due to higher required HTF flow rates to operate both heat storage cells in parallel. Although the charge heat-transfer rates appeared lower in for Mark III '3' in Figure 4-29 than they did for Mark II in Figure 4-23, the discharge heat-transfer rates remained comparable. Unlike the experience for Mark II, the performance reported for Mark III '3' was effectively averaged with '4'.

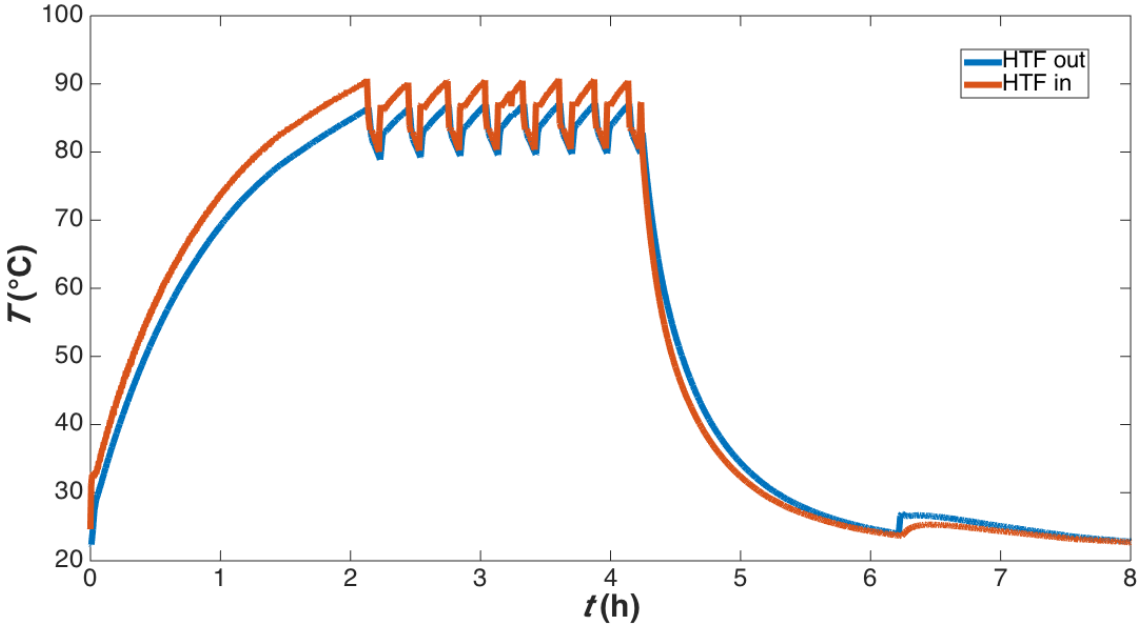

Figure 4-28: Combined Mark III '3' and '4' (in parallel) HTF inlet and outlet temperature profile during one complete cycle in the ETS loop, an average individual heat storage cell HTF flow rate of 1.8 L/min, and fan power supply set to 100 V. Nucleation triggering occurred shortly after t = 6 h.

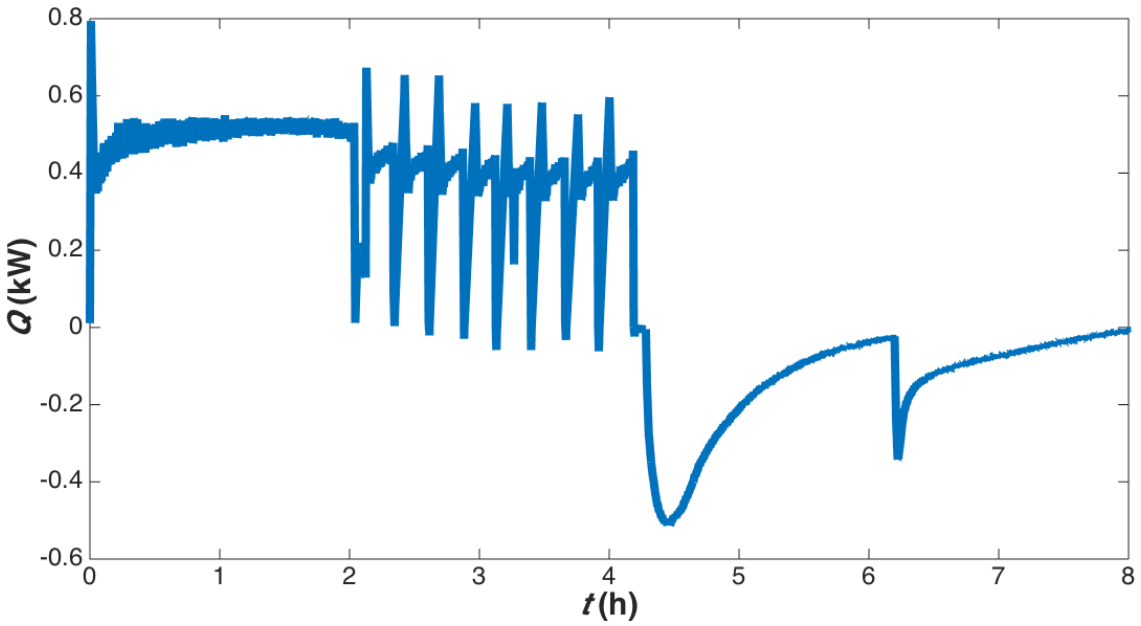

Figure 4-29: Mark III '3' heat storage cell heat-transfer rate (Q) profile corresponding to Figure 4-28. Positive values indicate charging, while negative values indicate discharging. Nucleation triggering occurred shortly after t = 6 h.

Figure 4-30 shows the *UA* profile for Mark III '3' corresponding to Figure 4-29. Note that the value of *UA* increases during charge after t = 1.5 h, which was not observed for

Mark II. The increasing trend in *UA* during charge was maintained until the heater on/off cycles took effect after $t = 2$ h, therefore indicating a persistent effect on the charge heat transfer process that became proportional to the SAT PCM temperature. This likely corresponded to the onset of complete phase change throughout the majority of the heat storage cell, yielding internal natural convection control of the internal heat-transfer process. The discharge processes for Mark III '3' shown in Figure 4-30, on the other hand, remained equivalent to those observed for Mark II. The combinations of these observations suggest that the addition of the HTF channels traversing the bottom of the Mark III heat storage cells affected only the charge process, while yielding no noticeable impact on the discharging processes.

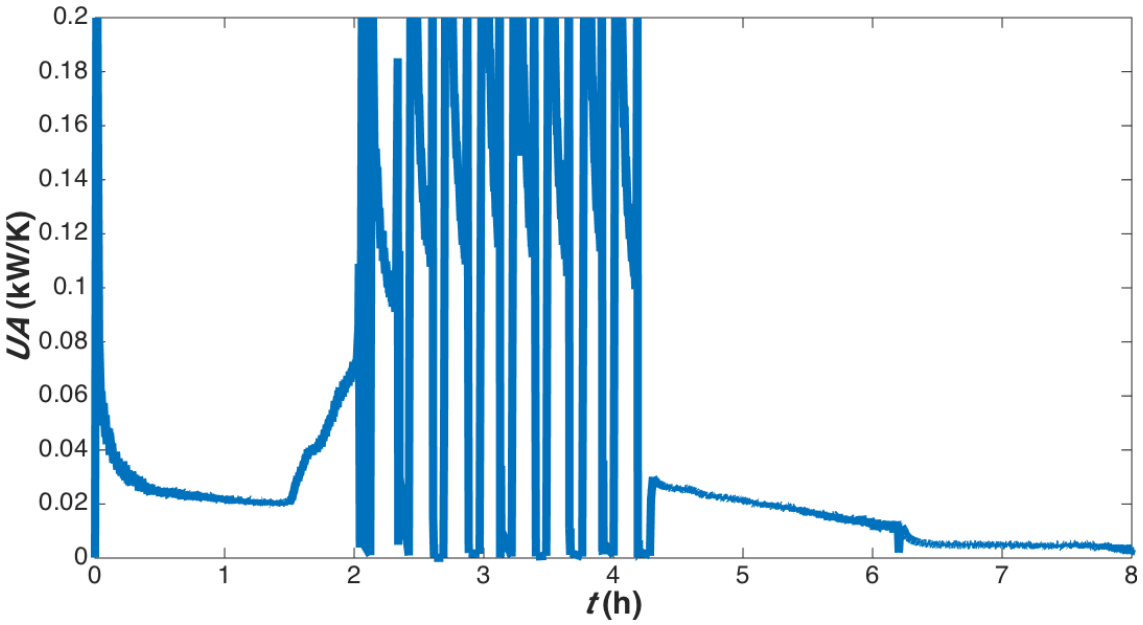

Figure 4-30: Mark III '3' heat transfer capacity rate (*UA*) profile corresponding to Figure 4-29. Values of *UA* above 0.2 kW/K were truncated from the figure to improve visibility of the profile.

The experiment average heat-transfer rates for the Mark III '3' charge and discharge processes at various flow rates are shown in Figure 4-31. As was observed for Mark II, the Mark III charge and discharge heat-transfer rates were invariant to HTF flow rate, with charge heat-transfer rates < 0.6 kW and discharge heat-transfer rates < 0.3 kW. However, it must be noted that maximum heating and cooling rates were not assured using the heater-chiller for the evaluations of Mark III '3' at partitioned HTF flow rates above 2 L/min, possibly generating HTF conditions unsuitable to maintain higher values

of the heat-transfer rate. This was caused by the heater-chiller microcontroller's inability to accept implied maximum heat duty during ramping operations, instead permitting only exact specifications of the required ramp rates. Incidentally, doubling the average heat-transfer rate sustained during charge of Mark III '3' in the ETS loop with the partitioned HTF flow rate at 1.8 L/min to reflect the total heat-transfer rates of Mark III '3' and '4' equalled just less than 1.2 kW, close to the total ETS loop heater power of 1.5 kW and individual Mark II charge rates in Figure 4-25.

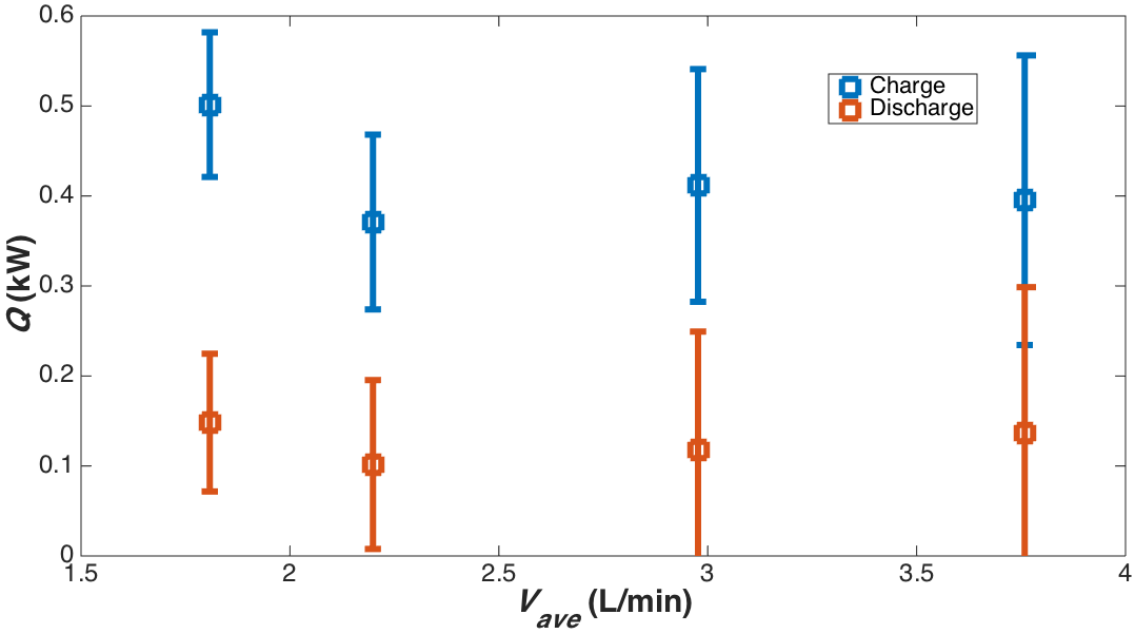

Figure 4-31: Summary of Mark III '3' average charge and discharge (solidification and supercooling) heat-transfer rates (Q) evaluated in either the ETS or heater-chiller loops at various HTF flow rates. Error bars correspond to the average calculated uncertainties for each experiment.

The determinations of *UA*, however, reveal the natures of the respective heat transfer processes that are obscured by observations of the heat-transfer rates alone. Figure 4-32 shows the corresponding average values of *UA* for charge, supercooling, and solidification corresponding to the experiments reported in Figure 4-31. Note that due to their excessive uncertainties, the *UA* values for charge and solidification obtained at the HTF flow rate of 3.8 L/min were identified as outliers, therefore not used in comparisons to the remaining values in Figure 4-32. However, as was reported for Mark II, the average values of *UA* determined for the respective heat transfer processes, remained largely independent of HTF flow rate, thus confirming once again the dominance of

internal heat transfer processes of the SAT PCM with respect to the overall heat transfer behaviour. Ranked in descending order, these were ~ 0.03 kW/K for charge, ~ 0.02 kW/K for supercooling, and ~ 0.003 kW/K for solidification. Normalized to the total heat exchange plate assembly heat transfer area of 0.078 m^2 for Mark III, the overall heat transfer coefficient values, U, of the respective processes were 0.4 kW m^{-2} K^{-1}, 0.3 kW m^{-2} K^{-1}, and 0.04 kW m^{-2} K^{-1}, respectively. With respect to these determinations of UA and U for Mark III, the calculated values of $LMTD_{ave}$ in Mark III '3' using only two thermocouples as opposed to six used in Mark II were likely subject to undervaluation in comparison to Mark II, therefore risking to underestimate the respective values of UA and U. Therefore, for this reason, it was assumed that values of UA and U for Mark III were in fact comparable to those reported for Mark II, especially when considering their heat storage cell design similarities.

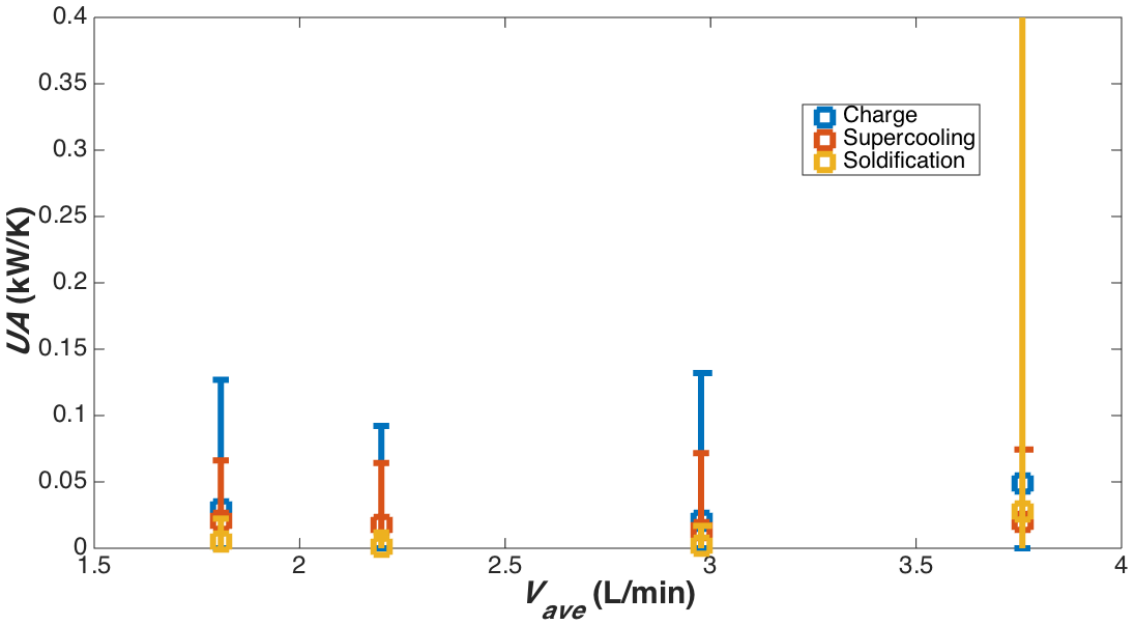

Figure 4-32: Summary of Mark III '3' average charge, supercooling, and solidification heat transfer capacity rates (UA) corresponding to the values of average heat-transfer rates shown in Figure 4-31. Error bars correspond to the sum of the average calculated uncertainties for each experiment and 2σ.

Respecting the comparisons with Mark II, the average values determined for Q and UA were not able to reveal significant differences highlighting the impacts of their external heat transfer designs. These were due largely to the high degrees of uncertainty associated with the calculated values of UA especially (as noted above), but also due to the operational differences between the ETS and heater-chiller loops.

As concluded for Mark II, the charge heat transfer processes for the Mark III heat storage cell were also deemed sufficient to support charging in an ETS system using a 1.2 kW to 1.5 kW electric heater (including in pairs of heat storage cells), as was also noted in Section 3.3.3.2.2. However, both the supercooled liquid and solidification heat discharge processes were still deemed insufficient to support the desired 600 W average heat discharge rate (objectives 11 and E in Section 2.2) from just one heat storage cell, and the average values of U for Mark III exceeded the benchmark threshold identified in objective 10. As also noted for Mark II, the Mark III heat storage design could be improved to deliver the desired heat transfer characteristics in objectives 11 and E either by increasing the heat transfer area (i.e., elongating the heat storage cell design), reducing the heat storage cell depth (i.e., reducing the characteristic length for heat diffusion), or doing both.

4.7 BALANCE-OF-SYSTEM HEAT EXCHANGE EVALUATION

The ETS balance-of-system, regarding heat transfer, consists of the remainder of the HTF circulation system outside of the heat storage cells and the liquid-to-air heat exchanger used to deliver useful indoor heating. The operation and design parameters governing the balance-of-system are the HTF flow rate, liquid-to-air heat exchanger sizing (UA), the liquid-to-air heat-transfer rate, and the rate of airflow through the liquid-to-air heat exchanger. Commensurate with the latter two is the air outlet temperature, which is the manner in which the ETS system operator would perceive heat exchange delivering room heating. Consequently, an emphasis must be placed on the noticeable perception of indoor heat delivery from the ETS by ensuring a noticeably increased air outlet temperature from the liquid-to-air heat exchanger.

Regarding the relationship between liquid-to-air heat exchanger heat-transfer rates, Q, and the flow rates of air and HTF (represented together by C_r), Figure 4-33 shows the resulting average heat-transfer rates from the liquid-to-air heat exchanger determined for series of repeated experiments with HTF flow rate varying between 1.5 L/min to 3.6 L/min and with the fan power supply fixed at 100 V AC[52]. Since the airflow

[52] This fan power supply setting was chosen to reduce fan noise in comparison to operation at 120 V AC and because the experiments conducted using other fan power supply settings could not be reported in this thesis due to malfunctions of the HTF outlet temperature from the liquid-

generated by the fan was not directly measured in the experiment, the capacity ratio, C_r, was used as proxy since the capacity rate of air could be determined using Eqs. (4.1) and (4.10). In all conditions of HTF flow (i.e., C_r), the liquid-to-air heat exchanger delivered average heat-transfer rates ≥ 600 W, therefore fulfilling objectives 11 and E in Section 2.2. Also noted in Figure 4-33 was the appearance of the asymptotic approach of Q with higher C_r, therefore suggesting the liquid-to-air heat exchanger was approaching its maximum value of Q with fixed airflow.

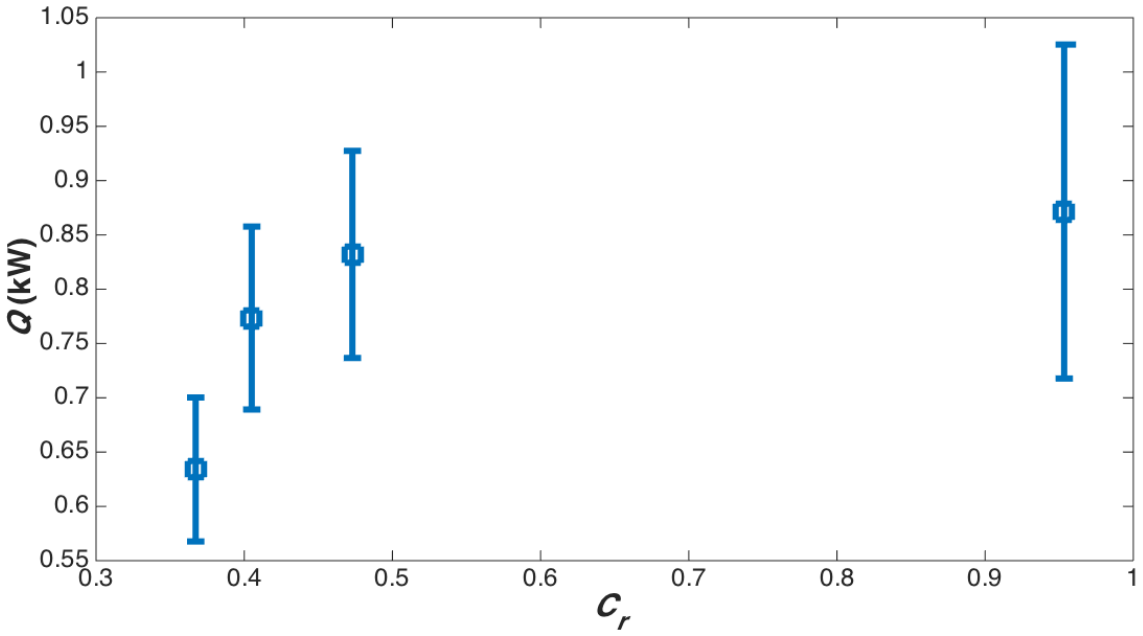

Figure 4-33: Liquid-to-air heat exchanger heat exchange rate (Q) as a function of the capacity ratio (C_r) of HTF and air. The fan power supply was maintained at 100 ± 5 V AC and the HTF flow rate varied nominally between 1.5 L/min to 3.6 L/min. Q and C_r values were averaged for individual experiments. The error bars shown for Q represent the average calculated error propagation uncertainties.

Showing the values of UA for the liquid-to-air heat exchanger corresponding to the values of Q shown in Figure 4-33, Figure 4-34 revealed that the heat exchanger capacity rate was independent of C_r and, by extension, the HTF flow rate, confirming $R_{air,HX} > R_{HTF,HX}$ in Section 4.3. The average UA determined for all values of C_r, uniformly representative of the liquid-to-air heat exchanger with the fan operated at 100 V AC, was UA = 0.2 kW K^{-1}. It was concluded, therefore, that an adequate liquid-to-air heat

to-air heat exchanger. The HTF outlet temperatures were measured by a thermocouple adhered to the surface of the HTF outlet copper tube wall, which had separated from the tube wall throughout some experiments, but was resolved for tests conducted at 100 V AC.

exchanger, independent of its size or airflow rate should have a minimum UA value of 0.2 kW K^{-1} to provide ≥ 600 W of average indoor heating power. Furthermore, as suggested by the results of Figure 4-33 and by virtue of heat transfer efficiency, η (Eq. (4.7)), for counter-current heat exchangers, the maximum value of Q should generally be achieved for C_r approaching one for any liquid-to-air heat exchanger with UA = 0.2 kW K^{-1}.

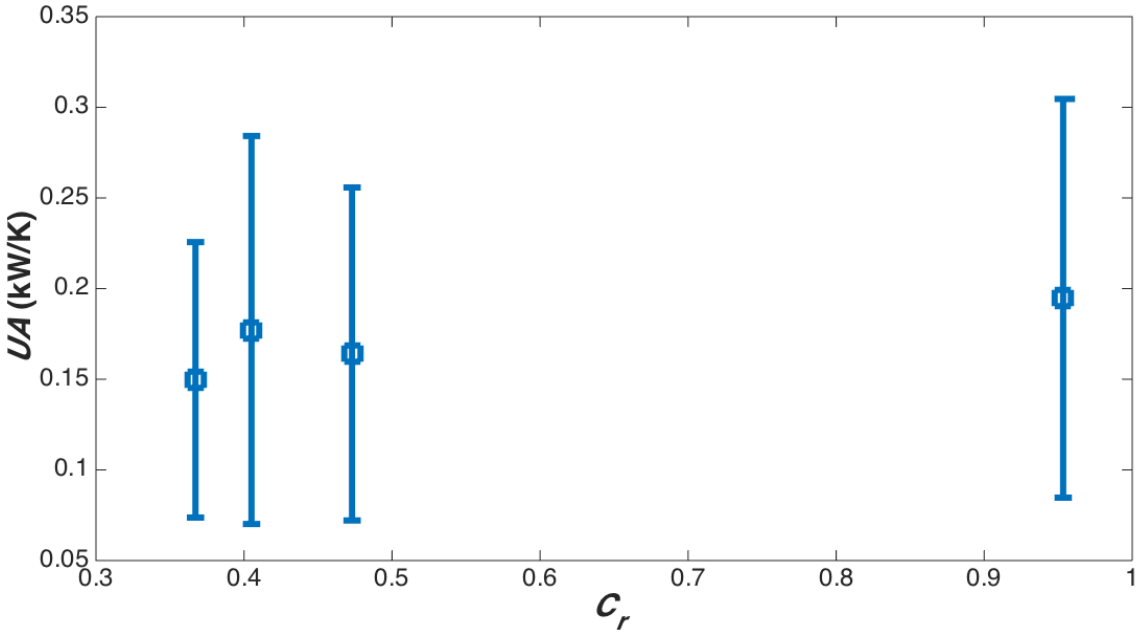

Figure 4-34: Liquid-to-air heat exchanger heat exchange capacity rate (UA) as a function of the capacity ratio (C_r) of HTF and air. The fan power supply was maintained at 100 ± 5 V AC and the HTF flow rate varied nominally between 1.5 L/min to 3.6 L/min. UA and C_r values were averaged for individual experiments. Only UA values for which error propagation uncertainties < 0.6UA were reported in this figure, for which the error bars were calculated from the sum of the average uncertainty and 2σ from the UA distributions.

Figure 4-35 shows the resulting heat transfer efficiency, η, as a function of C_r and residence time-average $LMTD$ values for the liquid-to-air heat exchanger experiments summarized in Figure 4-33 and Figure 4-34. While high values of η were achieved at all values of C_r for high $LMTD$, only the experiment conducted at high C_r (C_r = 0.95) demonstrated uniformly high values of efficiency, $\eta \geq 0.95$, at all values of $LMTD$. High heat-transfer efficiencies imply approaching the heat exchanger's maximum rated heat-transfer rate for a fixed value of UA and also imply generating larger temperature differences in the respective air and HTF flows, based on Eq. (4.1). Therefore, maintaining high values of η at all values of $LMTD$ would therefore be desired to fulfill

the indoor occupants' perceptions of heat discharge from the ETS system as well as fulfilling objectives 11 and E. To do so, for any value of UA would require only that C_r approach unity (i.e., balanced heat exchanger). Since only the values of UA and C_r control the liquid-to-air heat exchanger performance, selecting the desired HTF flow rate ETS system operation would therefore rely on the preferred operating condition with respect to heat exchange from the heat storage cells. Due to their inherently low values of UA, HTF flow rates should therefore be kept low (~ 1.5 L/min) in order to generate higher HTF supply temperatures to the liquid-to-air heat exchanger so as to always promote higher air outlet temperatures, thus maintaining higher heat discharge rates and higher values of the air outlet temperature perceived by the indoor occupants.

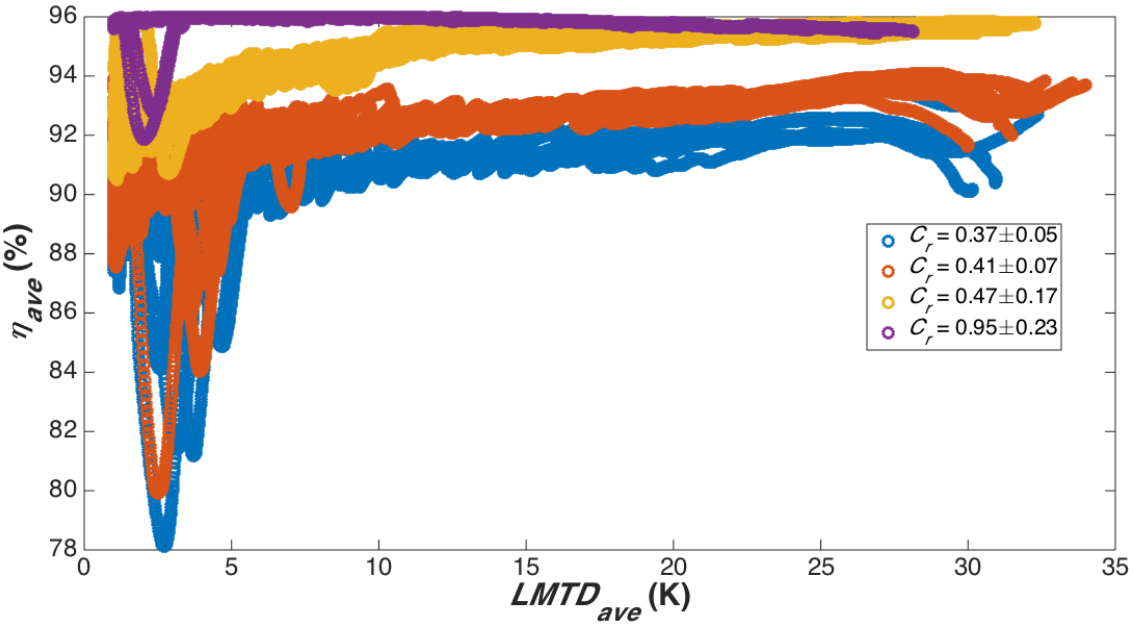

Figure 4-35: Liquid-to-air heat exchanger heat exchange efficiency (η) as a function of the residence-time average *LMTD* and capacity ratio (C_r) of HTF and air. The fan power supply was maintained at 100 ± 5 V AC and the HTF flow rate varied nominally between 1.5 L/min to 3.6 L/min.

Therefore, a suitable complete ETS system that can deliver useful heat discharge from individual heat storage cells while keeping the remaining ones idle (supercooled or kept at high temperature) should have heat storage cells with $UA \geq 0.2$ kW/K during discharge (either supercooling or solidification), a pump capable of delivering HTF flow rates as low as 1.5 L/min during discharge and be equipped with a balanced ($C_r \sim 1$) liquid-to-air heat exchanger with $UA \geq 0.2$ kW/K. While it has been shown that such a liquid-to-air

heat exchanger can be easily procured, further design efforts would be needed to achieve the desired individual heat storage cell performance.

4.8 CONCLUSION

The theoretical bases for internal and external heat transfer processes were discussed for the Marks II and III heat storage cells, and FEM simulations were also used to establish a final selection of the flow-plate pattern used in Marks II and III to generate useful external heat transfer with the circulating HTF.

The ETS and heater-chiller thermal cycling loops were each used to evaluate Mark II and Mark III heat storage cells for their heat transfer performances. With respect to complete ETS operation, the balance-of-system components' ability to deliver useful heat discharge to indoor spaces was also evaluated using the ETS loop.

The aims of developing and evaluating both internal and external heat transfer designs were to fulfill objectives 10, 11, and E in Section 2.2. With respect to the individual topics, the findings were:

1. Internal heat transfer:
    a. Long, staggered internal fin arrangements would be suitable to improve discharge heat transfer performance as much as reducing the heat storage cell depth by 50 %;
    b. Such changes would be expected to improve the average heat discharge performance by as much as a factor of four (objective 10);
    c. Neither was executed due to high cost of raw materials and machining and need to baseline the heat storage cell heat exchange performances;
2. Flow-plate pattern selection:
    a. While FEM simulations for densely distributed, compact rectangular patterns resulted in comparable heat-transfer rates in comparison to diamond elements sparsely distributed in square patterns, rectangular patterns resulted in increased HTF flow-over and reduced flow turbulence;
    b. Diamond patterns simulations produced the highest values of heat-transfer rate and U (both U_{sup} and U_{int}) and generated the least HTF flow-over and highest flow turbulence (vortex generation);

c. The diamond pattern with $W = 5$ mm was selected for the Marks II and III aluminum flow-plate designs, respectively, due to exhibiting the highest values of heat-transfer rate and UA in comparison to all of the other patterns simulated using COMSOL Multiphysics 5.0 (objective 10);

3. Heat transfer evaluations:
    a. Insufficient heat-transfer process data were collected to establish a clear basis for the heat transfer performance differences between Marks II and III;
    b. Marks II and III heat storage cells were able to generate sufficient heat-transfer rates during charging using the 1.5 kW heater supplied in the ETS loop (objective G);
    c. Heat-transfer rates from Marks II and III using single heat storage cells were insufficient to provide the desired discharge heat-transfer rates for ETS operation (objective 11 and E);
    d. The calculated average UA values of Marks II and III during solidification were ≤ 0.01 kW/K, as much as five times lower than their UA charge values and half their UA supercooling values;
    e. The normalized overall heat transfer coefficient values, U, of both Marks II and III exceeded the benchmark threshold listed in objective 10, equal to 30 W m^{-2} K^{-1};
    f. Improvements to Marks II and III could be realized by increasing the heat-transfer surface area, improving the internal heat-diffusion performance, or both;
4. Balance-of-system (i.e., liquid-to-air heat exchange):
    a. In the range of HTF flow rates between 1.5 L/min and 3.6 L/min, the heat-transfer capacity rate, UA, for the liquid-to-air heat exchanger remained independent of the HTF flow rate at an average value of $UA = 0.2$ kW/K, while the fan power supply was kept constant at 100 V AC;

b. Average room-heating heat-transfer rates generated by the liquid-to-air heat exchanger remained above 600 W (objectives 11 and E) at all HTF flow rates;
c. High heat-transfer efficiencies were obtained in the liquid-to-air heat exchanger for all values of *LMTD* for C_r near unity, meaning that airflow and HTF flow balancing should be maintained during ETS system operation, regardless of the HTF flow rate used to operate the ETS system.

Therefore, these findings result in formulating an ETS system fulfilling objectives 11 and E using a liquid-to-air heat exchanger with UA $\geq$ 0.2 kW/K, an HTF circulating pump capable of delivering flow rates $\leq$ 1.5 L/min during discharge ($\geq$ 1.5 L/min during charge), and individual heat storage cells with average UA $\geq$ 0.2 kW/K during discharge. The latter is selected out of the desire for a minimum of balanced heat transfer performance between the heat storage cells and the liquid-to-air heat exchanger.

CHAPTER 5: CONCLUSIONS AND FUTURE WORK

5.1 CONCLUSIONS

Three consecutive design iterations of a supercooling salt hydrate phase-change material (PCM) heat storage cell were proposed and evaluated for the development of a novel, compact and portable electric thermal storage (ETS) system used to deliver time-of-day (TOD) electricity cost savings to indoor heating in homes and businesses. The compactness of the ETS system, its ability to store thermal energy below 110 ˚C with comparable heat storage capacity (475 kJ/kg) to heated bricks in conventional ETS systems as high as 600 ˚C (630 kJ/kg (Romero, 2013)), and the ability to retain ≥ 40 % of the stored thermal energy long-term at room temperature without heat loss are owed to the use of the properties of the supercooling salt hydrate PCM.

The ETS system under development consisted of a circulated heat transfer fluid (HTF), a 120 V AC electric heat source, a circulating pump, a parallel array of heat storage cells, and a liquid-to-air heat exchanger operated using a fan.

This project explored these developments with respect to using sodium acetate trihydrate (SAT) diluted in water in an equimolar ratio (1:1) as the selected PCM. SAT is abundant, low-cost, safe to use, well documented in the scientific literature, and exhibits a suitable maximum transition temperature for indoor heating applications (T_{trans} = 55 ˚C for the equimolar mixture of SAT and water). Dilution of SAT in water (i.e., extra water principle (Sandnes et al., 2006)) was selected to suppress the formation of potentially unrecoverable anhydrous sodium acetate formed at the peritectic point of the hydrated compound in its binary phase equilibrium with water.

The desired design objectives of both the heat storage cell designs and the ETS system under development were outlined in Section 2.2 and addressed throughout Chapters 2 to 4. Table 5-1 lists these objectives and summarizes their respective actions and outcomes. The design objectives for maximum operating temperature and pressure of both the PCM (110 ˚C and 2 atm) and the circulated HTF (112 ˚C and 2 atm) in the ETS system, HTF selection (between 75 mass% and 90 mass% propylene glycol (PG) in water), material compatibility (thermoplastics, silicone rubber, and type 300 series stainless steels), and nucleation-triggering mechanisms (submerged stainless steel extension springs) were addressed using a literature survey in Chapter 2. The remaining,

first-of-its-kind objectives, namely regarding internal phase change processes, nucleation triggering strategy, heat storage cell seal integrity, and heat transfer design were addressed in experiments using the three heat storage cell iterations in Chapters 3 and 4.

Table 5-1: Summary of design objectives in Section 2.2 and respective actions/outcomes.

Objective(s)	Description	Action	Outcome
1	Heat storage cell modularity	Rectangular prism geometry with stacked components	
2/B	Internal pressure < 2 atm	-PCM: 1:1 SAT in water maintained ≤ 110 ˚C -HTF: 75 mass% PG in water maintained ≤ 112 ˚C	-Pressure not measured -Pump discharge observed ≤ 1.3 atm for ≤ 95 ˚C using 40 vol% PG in water
3	Useful heat discharge from PCM ≥ 28 ˚C	-SAT selected as salt hydrate PCM -Phase change occurs to a maximum of 58 ˚C (55 ˚C for 1:1 SAT in water)	-High efficiency for balanced liquid-to-air heat exchange ($C_r \sim 1$)
4	Abundant, low-cost, and safe supercooling salt hydrate PCM	-Retains 40 % of heat when supercooled to 20 ˚C	-Heat storage cells supercooled reliably after charging ≥ 80 ˚C -Achieved 167 days of long-term supercooling
5	≥ 40 % heat storage retained by supercooling	-Assembled without crevices or cyclically strained contacts capable of retaining SAT seed crystals	-Omitted eye-bolts in Mark III to prevent PCM leaks causing the loss of supercooling ability
6	Reliable long-term supercooling at 20 ˚C		
7	Reliable nucleation-triggering mechanism	Internal, linearly actuated, ‘activated’, metal extension spring nucleation trigger selected	Reliable nucleation triggering during 131 cycles using two spring-triggers
8	Total PCM heat storage ≥ 400 kJ/kg	Net heat storage between 425 kJ/kg and 449 kJ/kg from 20 ˚C to 110 ˚C	Remained unaffected by solution stratification
9/H	Heat storage cells achieve full charge << 7 h	≤ 3.5 h for Marks II and III to charge to 95 ˚C, therefore assumed adequate to charge to 110 ˚C << 7 h	
10	Nominal heat transfer coefficient > 30 W($m^{-2}K^{-1}$)	Used combination of patterned flow plates, internal symmetry, and 1D heat diffusion	Between double and twenty times in all heat transfer modes
11/E	Nominal heat discharge power	Liquid-to-air heat exchanger achieved ≥ 600 W in all HTF conditions, but only 200 W achieved for	

	≥ 600 W	individual heat storage cells
12/F	Design life ≥ 10 y for commercial units	Observed material compatibility and operating temperature limits Not measured
13	Heat storage cell structural materials ≤ 20 vol%	Each iteration occupied 49 vol%. Recommend elongating heat storage cells and reducing base wall thicknesses to decrease volume fraction
A	External temperature ≤ 40 ˚C	EPDM foam insulation used on all hot components
C	Total mass ≤ 30 kg	Recommend ≥ 15 kg of SAT PCM and ≤ 15 kg for balance of system
D	Noise generation ≤ 54 dB(A)	Low-noise fan and ≤ 43 dB(A) for pump. Recommend tangential fans for lowest noise to rate of airflow
G	120 V and max 12.5 A for ETS system	Used 1.5 kW heater and remaining components < 250 W. Recommend using 1.2 kW heater instead to avoid overloading household circuits

Repeated cycling was maintained for the final heat storage cell iteration, Mark III, up to 65 cycles and 66 cycles for two individual heat storage cells without noticeable thermal degradation to the SAT PCM or the heat storage cell. Comparisons between the Mark II and Mark III designs proved that SAT PCM charge durations were appreciably reduced due to the presence of HTF inlet channels traversing the bottom of the Mark III design, delivering heat transfer directly to the solid SAT PCM sinking to the bottom of the heat storage cell. Regarding overall heat transfer processes, as determined by the calculated values of *UA* for Marks II and III, respectively, both heat storage cell designs resemble each other closely, therefore not able to clearly distinguish their individual performance attributes using the experimental methods employed in this project. However, for both the Marks II and III, their respective values of *U* each exceeded the design objective of ≥ 0.03 kW m^{-2} K^{-1}, based on literature reports of PCM heat transfer equipment.

The final iteration, Mark III also fared better than either of the two previous iterations for thermal cycling reliability since only the Mark III did not have perforations through the bottom of the heat storage cell base (i.e., threaded eye bolts in used in Marks I and II), causing slow leaks of SAT PCM during charge. These leaks produced external reservoirs of solid SAT PCM that caused unrecoverable autonucleation of the SAT PCM to occur in Marks I and II, but not in Mark III.

Reliable supercooling of the SAT PCM between 28 ˚C and 20 ˚C was achieved using all three heat storage cell iterations and persisted in Mark I for 167 days before autonucleating due to the leaks mentioned above. Due to unavoidable solution stratification occurring in Marks I to III, only cells containing SAT PCM heated above 80 ˚C reliably supercooled, attributed to the dissolution of any anhydrous sodium acetate generated from the peritectic decomposition of the SAT at 58 ˚C.

Regarding the nucleation performance of the spring-nucleation triggering devices, at least two should be present in every heat storage cell since there remains the chance that one spring-trigger does not retain active seed crystals with which to initiate solidification in the supercooled SAT PCM (two were used in Mark III).

Nucleation triggering experiments conducted using Mark I, equipped with five equidistant spring-triggers and a transparent polycarbonate sight-glass on one side, were used to measure and confirm the solidification front expansion rate of the SAT PCM at various supercooling temperatures. The results confirmed the findings reported in the literature that SAT solidification front expansion rates are independent of supercooling temperature (dependent only on the solution concentration of SAT), around 7 mm/s on average for SAT solutions concentrated above 50 mass% sodium acetate. As such, two spring-nucleation triggers should suffice to initiate solidification discharge in heat storage cells as wide as 600 m in 30 s. Although the less stiff springs (lower pre-loading) used in Mark I functioned reliably, stiff springs, like those that were used in Marks II and III were recommended for more reliable nucleation triggering and for resistance to unintended flexure.

The solution stratification that ensued in all three heat storage cell iterations, caused by the separation of the dilute room-temperature equilibrium solution and solid SAT during charge, stabilized with repeated cycling and did not appear to pose a threat to the heat storage function of the SAT PCM. Although it was determined that solution stratification would not detrimentally alter the SAT PCM's heat storage and heat discharge capacities (remaining nearly identical to one-another), it did however reduce the heat exchange surface area directly exposed to the active SAT PCM, since the upper strata was too dilute to generate solidification. Efforts to attenuate solution stratification using only passive techniques, such as charge and discharge heat transfer rates and

ultimate set-point temperatures, proved largely ineffective, with the exception only that higher heat transfer rates during charging improved SAT PCM mixing only slightly.

Overall ETS system design and operating conditions were examined, and a suitable ETS system for pre-commercial development could be conceived using heat storage cells with $UA \geq 0.2$ kW/K and storing up to 32 kg of SAT PCM (4.2 kWh heat storage capacity), a circulating pump capable of generating HTF flows < 4 L/min, a 1.2 kW to 1.5 kW 120V AC electric heater, and a liquid-to-air heat exchanger with $UA = 0.2$ kW/K. It was found that lower flow rates would benefit heat transfer efficiency from the heat storage cells, while the air flow rate generated by the liquid-to-air heat exchanger fan would need to match the capacity rate in the HTF at low flow rates ($C_r \sim 1$) in order to obtain high heat transfer efficiencies in the liquid-to-air heat exchanger. In order to generate the desired average discharge heat transfer rate of 600 W from the ETS system, the heat storage cells would either require increased surface area, internal fins in the SAT PCM, reduced cell depth, or combinations thereof. While the resistance to heat transfer caused by the SAT PCM controlled all the heat storage cell heat transfer processes, it was found that a raised diamond flow plate pattern arranged in a square repeated pattern with sides 5 mm in length generated the most benefit to the HTF heat transfer processes.

5.2 RECOMMENDATIONS AND FUTURE WORK

Further developments to the heat storage cell designs and ETS system design and operating conditions are recommended to achieve commercial viability of the technology.

Regarding the heat storage cell design, type 300 series stainless steel patterned heat exchange plates sealed against the heat storage cell base with a compressible silicone rubber gasket are recommended to replace aluminum plates and aluminized film used in this project in order to improve heat storage cell seal integrity. However, these material choices alter the heat exchange plate's heat transfer properties, and should therefore be evaluated for heat exchange performance vis-à-vis those of Marks II and III in this project.

Heat storage cells with varied aspect ratios of the heat exchange surfaces as well as varied base depths are recommended for evaluations of their impacts on the internal natural convection of the SAT PCM and heat discharge heat transfer characteristics (i.e., UA and U), respectively. The former would be used to further determine the impact of

natural convection ‘soft’ mixing on solution stratification, while the latter would be used to evaluate the impact of decreasing the maximum diffusion length on the resulting discharge heat transfer processes (supercooling and solidification). Likewise, internal fin arrangements using stainless steel patterned heat exchange plates should be evaluated for their anticipated impacts on the overall heat transfer processes, with special consideration given to discharge heat transfer during solidification.

Operation up to 110 ˚C is recommended to generate high heat storage capacity using SAT PCM, however, was not performed due to HTF and equipment limitations, and should therefore be evaluated for heat exchange processes, and supercooling and nucleation triggering reliabilities. The effect of the higher charge temperature should also be evaluated for solution stratification.

Heat storage cells loaded with SAT PCMs of varying dilutions (e.g., $0.5 < w_{SA} < 0.6$) should be evaluated for their resistance to solution stratification compared with the equimolar SAT PCM solution used in this project.

Heat storage cells designed with reduced volume fractions of the materials of construction are recommended in order to reduce fabrication costs and also increase the volumetric fraction of active PCM for heat storage in an ETS system, thereby also reducing the footprint of the ETS system.

Lastly, a heat storage cell design encompassing the most promising heat storage cell attributes regarding the recommended evaluations of the materials of construction, heat exchange surface aspect ratio, heat storage cell depth, internal fin heat transfer design, SAT PCM dilution, and combined heat transfer (UA) and heat storage capacity sizings should be fabricated and evaluated to confirm the combination of desired features. This heat storage cell would constitute a design approaching commercial readiness, confirmed only after evaluating performance in pre-commercial ETS system capable of supplying HTF flows up to 112 ˚C at < 4 L/min using 75 mass% to 90 mass% propylene glycol in water and equipped with a balanced ($C_r = 1$) liquid-to-air heat exchanger and tangential fan with $UA = 0.2$ kW/K.

REFERENCES

Abhat, A. (1983). "Low temperature latent heat thermal energy storage: Heat storage materials." Solar Energy **30**(4): 313-332.

AcrosOrganics (2014). Safety data sheet: Sodium phosphate dibasic, dodecahydrate. CAS number: 10039-32-4, Thermo Fisher Scientific Inc**:** 4, https://www.fishersci.com/shop/msdsproxy?productName=AC271060100&productDescription=SODIUM+PHOSPHATE%2C+DIBASI+10KG&catNo=AC27106-0100+&vendorId=VN00032119&storeId=10652.

AeroflexUSA. (2016). "Aerocell epdm: Epdm high performance rubber." Retrieved April 28, 2016, from http://www.aeroflexusa.net/epdm/.

Agyenim, F., N. Hewitt, P. Eames and M. Smyth (2010). "A review of materials, heat transfer and phase change problem formulation for latent heat thermal energy storage systems (lhtess)." Renewable and Sustainable Energy Reviews **14**(2): 615-628.

Ahmad, J. (2002). "Precipitation of sodium acetate trihydrate from its supersaturated solution." Asian Journal of Chemistry **14**(1): 223-226.

AlfaAesar (2015a). Safety data sheet: Sodium acetate trihydrate. CAS number: 6131-90-4, Thermo Fisher Scientific Inc**:** 4, https://www.alfa.com/en/content/msds/USA/A16230.pdf.

AlfaAesar (2015b). Safety data sheet: Sodium sulfate decahydrate. CAS number: 7727-73-3, Thermo Fisher Scientific Inc**:** 4, https://www.alfa.com/en/content/msds/USA/A15702.pdf.

Anthony, A. E. M., P. F. Barrett and P. K. Dunning (1990). "Verification of a mechanism for nucleating crystallization of supercooled liquids." Materials Chemistry and Physics **25**: 7.

Araki, N., M. Futamura, A. Makino and H. Shibata (1995). "Measurements of thermophysical properties of sodium acetate hydrate." International Journal of Thermophysics **16**: 1455-1466.

Ashby, M. F. (2013). Materials and the environment. Boston, Butterworth-Heinemann.

ASHRAE (2013). 2013 ashrae handbook - fundamentals (si edition), American Society of Heating, Refrigerating and Air-Conditioning Engineers, Inc.

ASME (2013). Asme boiler and pressure vessel code: An international code, ASME**:** 26, go.asme.org/bpvc13.

Byrom, S. (2016). "Economy 7 tariffs." Retrieved June 5, 2016, from https://www.ukpower.co.uk/home_energy/economy-7.

Choi, J. C., S. D. Kim and G. Y. Han (1996). "Heat transfer characteristics in low-temperature latent heat storage systems using salt-hydrates at heat recovery stage." Solar Energy Materials and Solar Cells **40**: 71-87.

Dannemand, M., W. Kong, J. Fan, J. B. Johansen and S. Furbo (2015a). "Laboratory test of a prototype heat storage module based on stable supercooling of sodium acetate trihydrate." Energy Procedia **70**: 172-181.

Dannemand, M., J. M. Schultz, J. B. Johansen and S. Furbo (2015b). "Long term thermal energy storage with stable supercooled sodium acetate trihydrate." Applied Thermal Engineering **91**: 671-678.

Davis, J. R. (1997). Concise metals engineering data book, ASM International.

Desgrosseilliers, L. (2012). Heat transfer enhancement using laminate film encapsulation for phase change heat storage materials. MASc, Dalhousie University.

Desgrosseilliers, L., P. Allred, D. Groulx and M. A. White (2013a). "Determination of enthalpy–temperature–composition relations in incongruent-melting phase change materials." Applied Thermal Engineering **61**(2): 193-197.

Desgrosseilliers, L., D. Groulx and M. A. White (2013b). "Heat conduction in laminate multilayer bodies with applied finite heat source." International Journal of Thermal Sciences **72**: 47-59.

Desgrosseilliers, L., D. Groulx and M. A. White (2014a). "Thermographic validation of a novel, laminate body, analytical heat conduction model." Heat and Mass Transfer: 11.

Desgrosseilliers, L., D. Groulx and M. A. White (2014b). Two-region fin model adjacent temperature profile interactions. 15th Internation Heat Transfer Conference. Kyoto, JP, Begel House.

Desgrosseilliers, L., D. Groulx, M. A. White and L. Swan (2014c). Thermodynamic evaluation of supercooled seasonal heat storage at the drake landing solar community. Eurotherm Seminar #99: Advances in Thermal Energy Storage. Lleida, Spain**:** 1-10.

Desgrosseilliers, L., M. Kabbara, D. Groulx and M. A. White (2016). "Validation of a heat conduction model for finite domain, non-uniformly heated, laminate bodies." Heat and Mass Transfer **52**: 1283–1293.

Desgrosseilliers, L., C. A. Whitman, D. Groulx and M. A. White (2013c). "Dodecanoic acid as a promising phase-change material for thermal energy storage." Applied Thermal Engineering **53**(1): 37-41.

Dimplex (2015). Quantum ets - electric thermal storage heating, Dimplex North America Ltd., http://dimplex.com/cms/publications/Quantum_ConsumerBrochure_LR.pdf.

Dimplex. (2016). "Quantum storage heaters." Retrieved March 14, 2016, from http://dimplex.com/en/renewable_energy/quantum_storage_heaters/products/vfmq40440__vfmq70770/vfmq_storage_heaters.

Dow (2003). A guide to glycols. Dow Chemical Company, http://msdssearch.dow.com/PublishedLiteratureDOWCOM/dh_091b/0901b8038091b508.pdf?filepath=propyleneglycol/pdfs/noreg/117-01682.pdf&fromPage=GetDoc.

Edzwald, J. (2011). Chemical principles, source water composition, and watershed protection. Water Quality & Treatment: A Handbook on Drinking Water, Sixth Edition, McGraw Hill Professional, Access Engineering, http://accessengineeringlibrary.com/browse/water-quality-and-treatment-a-handbook-on-drinking-water-sixth-edition/p2001c2f699703_1001.

Elnur (2015). Ecombi, Elnur Uk Ltd., https://www.elnur.co.uk/wp-content/uploads/2015/12/ecombi-brochure1.pdf.

Fakheri, A. (2007). "Heat exchanger efficiency." Journal of Heat Transfer **129**(9): 1268.

Fan, J., S. Furbo, E. Andersen, Z. Chen, B. Perers and M. Dannemand (2012). "Thermal behavior of a heat exchanger module for seasonal heat storage." Energy Procedia **30**: 244-254.

Farid, M. M., A. M. Kudhair, S. A. K. Razack and S. Al-Hallaj (2004). "A review on phase change energy storage: Materials and applications." Energy Conversion and Management **45**(9-10): 1597-1615.

Felder, R. M. and R. W. Rousseau (2000). Elementary principles of chemical processes, John Wiley & Sons, Inc.

Ferrer, G., A. Solé, C. Barreneche, I. Martorell and L. F. Cabeza (2014). Corrosion of aluminium for use in pcm energy storage. Eurotherm Seminar #99: Advances in Thermal Energy Storage. Lleida, Spain**:** 1-6.

Franzosini, P., W. A. Plautz and E. F. Westrum Jr (1983). "Thermophysics of metal alkanoates i. Heat capacities and thermodynamic properties of sodium methanoate and ethanoate." The Journal of Chemical Thermodynamics **15**(5): 445-456.

Fronczek, F. R., H. N. Kamel and M. Slattery (2003). "Three polymorphs ([alpha], [beta], and [delta]) of d-mannitol at 100 k." Acta Crystallographica Section C **59**(10): o567-o570.

Furbo, S., J. Fan, E. Andersen, Z. Chen and B. Perers (2012). "Development of seasonal heat storage based on stable supercooling of a sodium acetate water mixture." Energy Procedia **30**: 260-269.

G.M. (2010). Chevrolet volt battery, General Motors, http://www.formula-hybrid.org/wp-content/uploads/Chevrolet-Volt-Battery_101.pdf.

Garg, H. P., S. C. Mullick and A. K. Bhargava (1985). Solar thermal energy storage, D. Reidel Publishing Company.

Garverick, L. (1994). Corrosion in the petrochemical industry, ASM International.

Green, D. W. and R. H. Perry (2008). Perry's chemical engineers' handbook, McGraw-Hill.

Green, W. F. (1908). "The melting point of hydrated sodium acetate: Solubility curves." Journal of Physical Chemistry **12**: 655-660.

Grundfos (2014). Alpha variable speed circulators with autoadapt™: Installation and operating instructions. Grundfos A/S. Denmark, Grundfos A/S. **98722880**.

Günther, E., H. Mehling and M. Werner (2007). "Melting and nucleation temperatures of three salt hydrate phase change materials under static pressures up to 800 mpa." Journal of Physics D: Applied Physics **40**(15): 4636-4641.

H.M.Heizkorper (2012). Thermobatterie. H.M. Heizkörper GmbH & Co. KG. Dingelstädt, Germany.

Hammick, D. L., H. K. Goadby and H. Booth (1920). "Clxxv.-disodium hydrogen phosphate dodecahydrate." Journal of the Chemical Society, Transactions **117**(0): 1589-1592.

HAS (2015). Canada's lodging sector: 2015. Hotel Association of Canada.

Hirano, S. and T. S. Saitoh (2002a). "Growth rate of crystallization of disodium hydrogenphosphate dodecahydrate." Journal of Thermophysics and Heat Transfer **16**: 6.

Hirano, S. and T. S. Saitoh (2002b). Influence of operating temperature on efficiency of supercooled salt thermal energy storage. 37th Annual Intersociety Energy Conversion Engineering Conferences.

Hirano, S. and T. S. Saitoh (2009). Long-term performance of latent heat thermal energy storage using supercooling. ISES Solar World Congress 2007: Solar Energy and Human Settlement**:** 2741-2745.

Honeywell (2012). Portable air conditioner: Owner's manual - model: Mm14chcscs. Honeywell International Inc., Honeywell International Inc.

InChem (2004). Polyethylene: Safety data sheet. CAS #: 9002-88-4, InChem, http://www.inchem.org/documents/icsc/icsc/eics1488.htm.

Kabbara, M. (2015). Real time solar and controlled experimental investigation of a latent heat energy storage system. MASc, Dalhousie University.

Kamkari, B., H. Shokouhmand and F. Bruno (2014). "Experimental investigation of the effect of inclination angle on convection-driven melting of phase change material in a rectangular enclosure." International Journal of Heat and Mass Transfer **72**: 186-200.

Kenisarin, M. and K. Mahkamov (2007). "Solar energy storage using phase change materials." Renewable and Sustainable Energy Reviews **11**(9): 1913-1965.

Khoshvaght-Aliabadi, M. (2015). "Thermal performance of plate-fin heat exchanger using passive techniques: Vortex-generator and nanofluid." Heat and Mass Transfer **52**(4): 819-828.

Kravvaritis, E. D., K. A. Antonopoulos and C. Tzivanidis (2010). "Improvements to the measurement of the thermal properties of phase change materials." Measurement Science and Technology **21**(4): pp. 9.

Kravvaritis, E. D., K. A. Antonopoulos and C. Tzivanidis (2011). "Experimental determination of the effective thermal capacity function and other thermal properties for various phase change materials using the thermal delay method." Applied Energy **88**(12): 4459-4469.

Lane, G. A. (1980). "Low temperature heat storage with phase change materials." International Journal of Ambient Energy **1**: 155-168.

Lane, G. A. (1983). Solar heat storage: Background and scientific principles. Baton Rota, CRC Press.

Lane, G. A. (1985). "Pcm science and technology: The essential connection." ASHRAE Transactions **91**(2b).

Lane, G. A., A. C. Kott, G. L. Warner, P. B. Hartwick and H. E. Rossow (1978). Macro-encapsulation of heat storage phase-change materials for use in residential buildings: Report oro/5217-8. Midland, MI., Dow Chemical Company.

LG (2014). Submittal data: Lmn126hvt flex multi-split standard. North York, ON, LG Electronics Canada Inc. **LGECI130501LMN126**.

Liu, C. and D. Groulx (2014). "Experimental study of the phase change heat transfer inside a horizontal cylindrical latent heat energy storage system." International Journal of Thermal Sciences **82**: 100-110.

Marcus, Y. (2013). "Volumetric properties of molten salt hydrates." Journal of Chemical & Engineering Data **58**(2): 488-491.

Mays, L. W. (1999). Environmental hydraulics. Hydraulic Design Handbook, McGraw Hill Professional, Access Engineering, http://accessengineeringlibrary.com/browse/hydraulic-design-handbook/p2000af1299705_1001.

Mays, L. W. (2000). Quality of water in storage. Water Distribution System Handbook, McGraw Hill Professional, Access Engineering, http://accessengineeringlibrary.com/browse/water-distribution-system-handbook/p2000aed999711_1001.

McCabe, W. L., J. Smith and P. Harriott (2005). Unit operations of chemical engineering, McGraw-Hill Education.

McMasterCarr. (2016a). "Type 302 stainless steel extension spring." Retrieved May 12, 2016, from http://www.mcmaster.com/mv1461797376/ - 94135k36/=12dsmsr.

McMasterCarr. (2016b). "Type 302 stainless steel ultra-precision extension spring." Retrieved May 12, 2016, from http://www.mcmaster.com/ - 9065k435/=12dsmtw.

Medrano, M., M. O. Yilmaz, M. Nogués, I. Martorell, J. Roca and L. F. Cabeza (2009). "Experimental evaluation of commercial heat exchangers for use as pcm thermal storage systems." Applied Energy **86**(10): 2047-2055.

Mehling, H. and L. F. Cabeza (2008). Heat and cold storage with pcm. Berlin, Springer.

Meisingset, K. K. and F. Grønvold (1984). "Thermodynamic properties and phase transitions of salt hydrates between 270 and 400 k iii. Ch3co2na·3h2o, ch3co2li·2h2o, and (ch3co2)2mg·4h2o." The Journal of Chemical Thermodynamics **16**(6): 523-536.

Murray, R. E. (2012). Simultaneous charging and discharging of a latent heat energy storage system for use with solar domestic hot water. MASc, Dalhousie University.

Naumann, R. and H. H. Emons (1989). "Results of thermal analysis for investigation of salt hydrates as latent heat-storage materials." Journal of Thermal Analysis **35**: 1009-1031.

NIST. (2016). "Propylene glycol." NIST Chemistry Webbook, from http://webbook.nist.gov/cgi/cbook.cgi?ID=C57556&Mask=4&Type=ANTOINE&Plot=on.

Noël, J. A., S. Kahwaji, L. Desgrosseilliers, D. Groulx and M. A. White (2016). Phase change materials. Storing energy. T. Letcher, Elsevier.

NRCan (2002). Commercial and institutional building energy use survey 2000 detailed statistical report – december 2002. NRCan, Government of Canada.

NRCan (2011). Energy efficiency trends in canada: 1990 to 2009. NRCan, Government of Canada.

NRCan (2012). Energy use data handbook:1990-2009, Government of Canada**:** 169.

NRCan. (2015a). "Air-source heat pumps." Retrieved March 10, 2016, from http://www.nrcan.gc.ca/energy/publications/efficiency/heating-heat-pump/6831.

NRCan. (2015b, Dec 2, 2015). "North american natural gas market: 2015-2016 heating season outlook." Retrieved April 10, 2016, from http://www.nrcan.gc.ca/energy/sources/natural-gas/17894.

NRCan. (2016, March 14, 2016). "Prices, trade and feature articles." Retrieved April 10, 2016, from http://www.neb.gc.ca/nrg/ntgrtd/mrkt/prcstrdrtcl/index-eng.html.

NSPower. (2016). "Time-of-day rates." Retrieved March 14, 2016, from http://www.nspower.ca/en/home/for-my-home/heating-solutions/electric-thermal-storage/tod-rates/default.aspx.

OEB. (2015, November 2, 2015). "Electricity prices." Retrieved March 14, 2016, from http://www.ontarioenergyboard.ca/oeb/Consumers/Electricity/Electricity Prices.

Oxtoby, D. W., H. P. Gillis and N. H. Nachtrieb (2002). Principles of modern chemistry, Thomson/Brooks/Cole.

Pavlov, D. (2011). H2so4 electrolyte - an active material in the leadeacid cell. Lead-acid batteries - science and technology - a handbook of lead-acid battery technology and its influence on the product, Elsevier.

Phillips, B. (2010). "Using portable heat pumps/other portable heating devices." RSES(November 2010): 12-16.

Pinel, P., C. A. Cruickshank, I. Beausoleil-Morrison and A. Wills (2011). "A review of available methods for seasonal storage of solar thermal energy in residential applications." Renewable and Sustainable energy reviews **15**(7): 3341-3359.

PSEG. (2016). "Pse&g's residential electric rates." Retrieved March 14, 2016, from https://www.pseg.com/info/environment/ev/rlm-rs_rates.jsp.

Richards, T. W. and F. T. Gucker (1929). "The heats of dilution of sodium hydroxide, acetic acid and sodium acetate, and their bearing on heat capacities and heat of neutralization." Journal of the American Chemical Society **51**(3): 712-727.

Riddick, J. A., W. B. Bunger and T. K. Sakano (1985). Techniques of chemistry: Organic solvents 4th ed., John Wiley and Sons. **2**.

Rogerson, M. A. and S. S. S. Cardoso (2003a). "Solidification in heat packs: I. Nucleation rate." AIChE Journal **49**(2): 505-515.

Rogerson, M. A. and S. S. S. Cardoso (2003b). "Solidification in heat packs: Ii. Role of cavitation." AIChE Journal **49**(2): 516-521.

Rogerson, M. A. and S. S. S. Cardoso (2003c). "Solidification in heat packs: Iii. Metallic trigger." AIChE Journal **49**(2): 522-529.

Romero, I. B. (2013). An experimental investigation of an electrical storage heater in the context of storage technologies. MSc, University of Strathclyde.

Sandnes, B. (2003). Exergy efficient production, storage and distribution of solar energy. PhD, University of Oslo.

Sandnes, B. (2008). "The physics and the chemistry of the heat pad." American Journal of Physics **76**(6): 546.

Sandnes, B. and J. Rekstad (2006). "Supercooling salt hydrates: Stored enthalpy as a function of temperature." Solar Energy **80**(5): 616-625.

Schultz, J. M. and S. Furbo (2005). Storage based on phase change materials (pcm) selection of concepts. A Report of IEA Solar Heating and Cooling programme - Task 32 "Advanced storage concepts for solar and low energy buildings". Wolfgang Streicher, International Energy Agency.

Schultz, J. M. and S. Furbo (2007). State of development of the work with seasonal pcm heat storage at the department of civil engineering, technical university of denmark (dtu). A Report of IEA Solar Heating and Cooling programme - Task 32 "Advanced storage concepts for solar and low energy buildings". Wolfgang Streicher, International Energy Agency.

Sharma, A., V. V. Tyagi, C. R. Chen and D. Buddhi (2009). "Review on thermal energy storage with phase change materials and applications." Renewable and Sustainable energy reviews **13**(2): 318-345.

Sharma, S. D. and K. Sagara (2005). "Latent heat storage materials and systems: A review." International Journal of Green Energy **2**(1): 1-56.

Shokouhmand, H. and B. Kamkari (2013). "Experimental investigation on melting heat transfer characteristics of lauric acid in a rectangular thermal storage unit." Experimental Thermal and Fluid Science **50**: 201-212.

Sibbitt, B., D. McClenahan, R. Djebbar, J. Thornton, B. Wong, J. Carriere and J. Kokko (2011). Measured and simulated performance of a high solar fraction district heating system with seasonal storage. ISES Solar World Congress 2011. Kassel, Germany**:** 12.

Sidgwick, N. V. and J. A. H. R. Gentle (1922). "The solubilities of the alkali formates and acetates in water." Journal of the Chemical Society, Transactions **121**: 1837.

Smith, E. H. (1998). Mechanical engineer's reference book, Elsevier.

Snider, B. (2006). Home heating and the environment. Statistics Canada**:** 5.

StatCan (2007). 2006 census of population. StatCan, Government of Canada.

StatCan (2013a). 2011 census of population. StatCan, Government of Canada.

StatCan (2013b). Homeownership and shelter costs in canada. StatCan, Government of Canada.

StatCan (2013c). Households and the environment: Energy use (2011). Statistics Canada, Goverment of Canada.

Steffes. (2016a). "Residential hydronic furnace." Retrieved March 14, 2016, from http://www.steffes.com/off-peak-heating/hydronic-furnace.html.

Steffes. (2016b). "Room unit specifications." Retrieved June 23, 2016, 2016, from http://www.steffes.com/off-peak-heating/room-unit-specs.html.

Sturley, K. R. (1932). "Fresh data on the latent heats and heat conductivities of some aquacrystalline compounds." Journal of the Society of Chemical Industry **51**: 271T-273T.

Targray (2012). Pds targray aluminum laminate pouch rev 3. Targray. Kirkland, QC, CAN.

Verma, P., Varun and S. Singal (2008). "Review of mathematical modeling on latent heat thermal energy storage systems using phase-change material." Renewable and Sustainable energy reviews **12**(4): 999-1031.

Wei, L. L. and K. Ohsasa (2010). "Supercooling and solidification behaviour of phase change material." ISIJ International **50**: 1265-1269.

Welty, J. R., G. L. Rorrer and D. G. Foster (2001). Fundamentals of momentum, heat, and mass transfer. New York, Toronto, John Wiley.

Wettermark, G., B. Carlsson and H. Stymne (1979). Storage of heat: A survey of efforts and possibilities. Stockholm, Sweden, Swedish Council for Building Research.

Wood, D. G., M. B. Brown, S. A. Jones and D. Murnane (2011). "Characterization of latent heat-releasing phase change materials for dermal therapies." The Journal of Physical Chemistry C **115**(16): 8369-8375.

Yaws, C. L. (2010). Yaws' thermophysical properties of chemicals and hydrocarbons (electronic edition), Knovel, http://app.knovel.com/hotlink/toc/id:kpYTPCHE02/yaws-thermophysical-properties/yaws-thermophysical-properties.

Yinping, Z., J. Yi and J. Yi (1999). "A simple method, the t-history method, of determining the heat of fusion, specific heat and thermal conductivity of phase-change materials." Measurement Science Technology **10**: 201-205.

Yoon, W. S., Y. G. Shul, J. K. Kim, H. Joo, M. S. Jeon and T. K. Lee (2000). "Encapsulation of sodium acetate trihydrate and stearic acid for thermal energy storage." Journal of the Korean Institute of Chemical Engineers **38**(5).

Zalba, B., J. M. Marín, L. F. Cabeza and H. Mehling (2003). "Review on thermal energy storage with phase change: Materials, heat transfer analysis and applications." Applied Thermal Engineering **23**(3): 251-283.

Zhang, H., R. M. J. Van Wissen, S. V. Nedea and C. C. M. Rindt (2014). Characterization of sugar alcohols as seasonal heat storage media – experimental and

theoretical investigations. Eurotherm Seminar #99: Advances in Thermal Energy Storage. Lleida, Spain**:** 1-11.

Zimmerman, W. B. (1997). "The effect of chemical equilibrium on the formation of stable stratification." Applied scientific research **59**(2-3): 283-298.

APPENDIX A: MARK I MECHANICAL DESIGN DRAWINGS

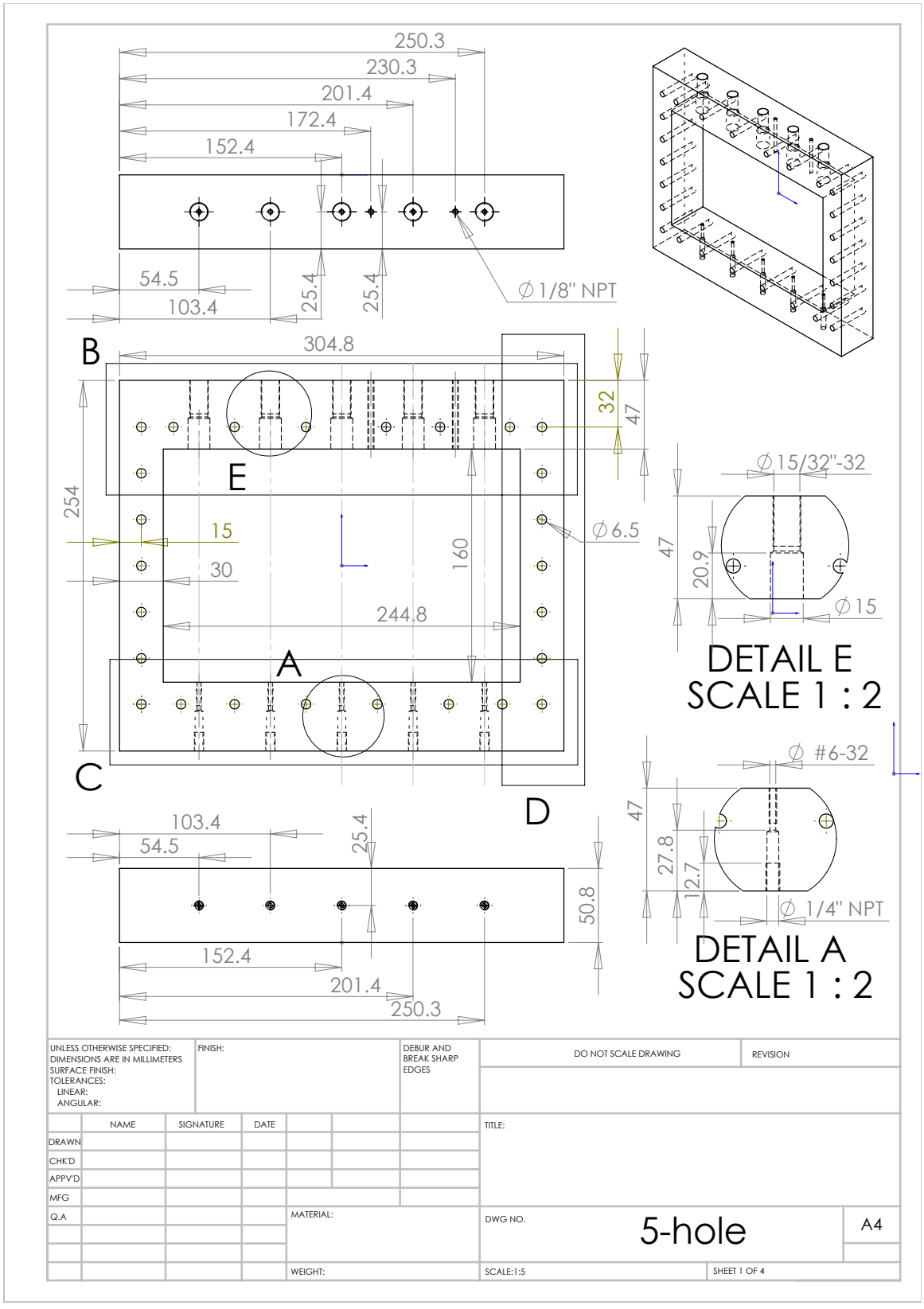

Figure A- 1: Mark I polypropylene base technical drawing page 1.

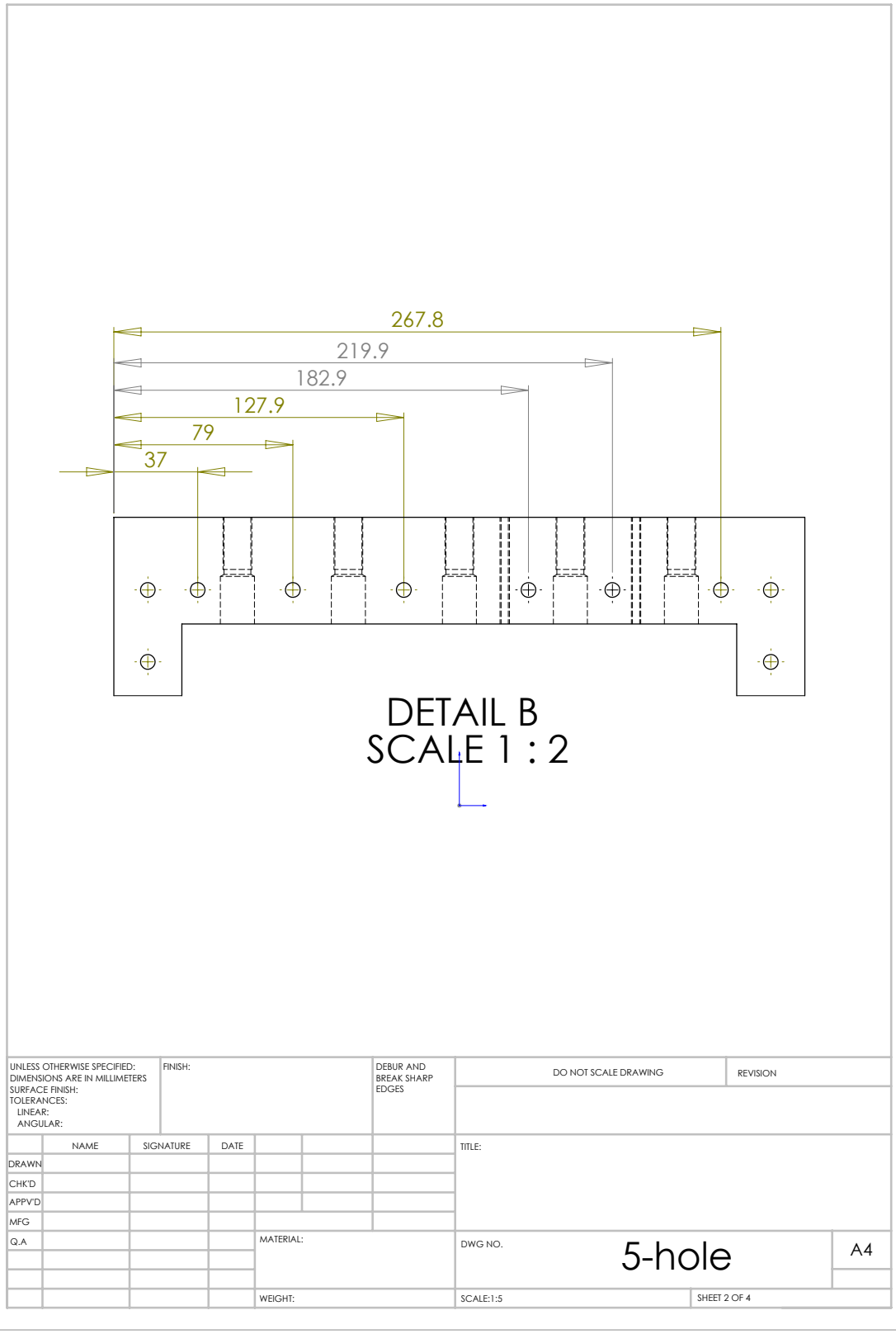

Figure A- 2: Mark I polypropylene base technical drawing page 2.

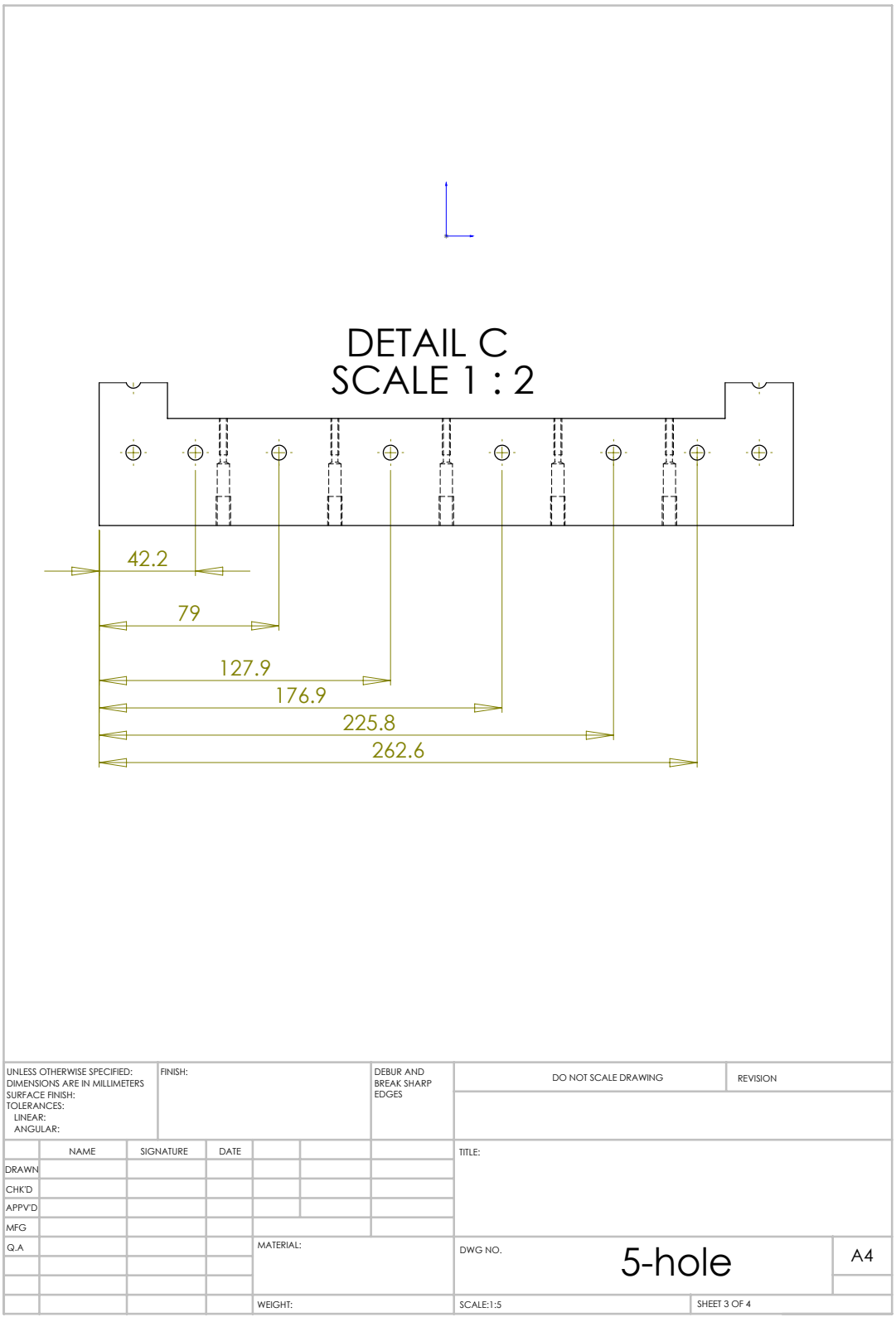

Figure A- 3: Mark I polypropylene base technical drawing page 3.

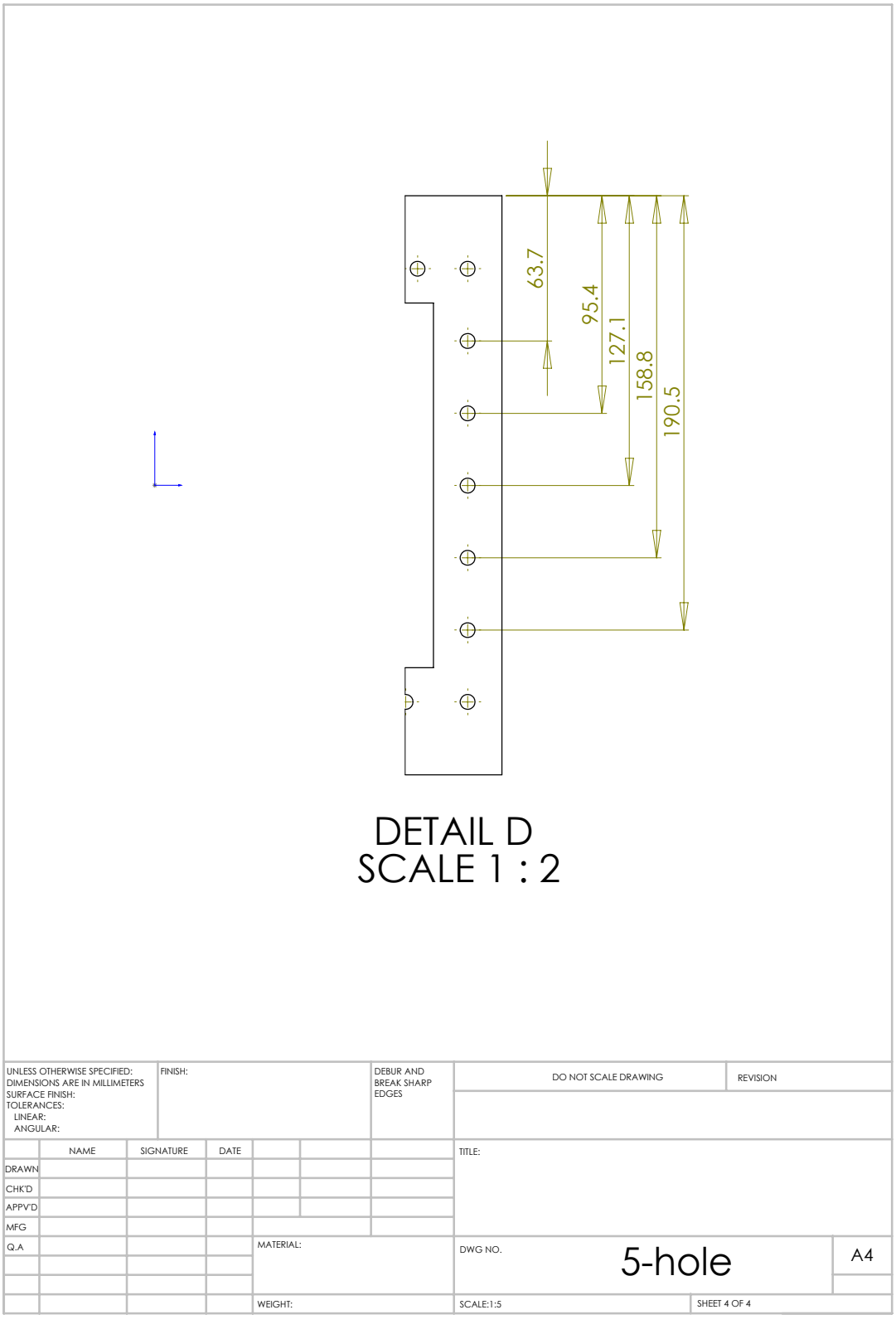

Figure A- 4: Mark I polypropylene base technical drawing page 4.

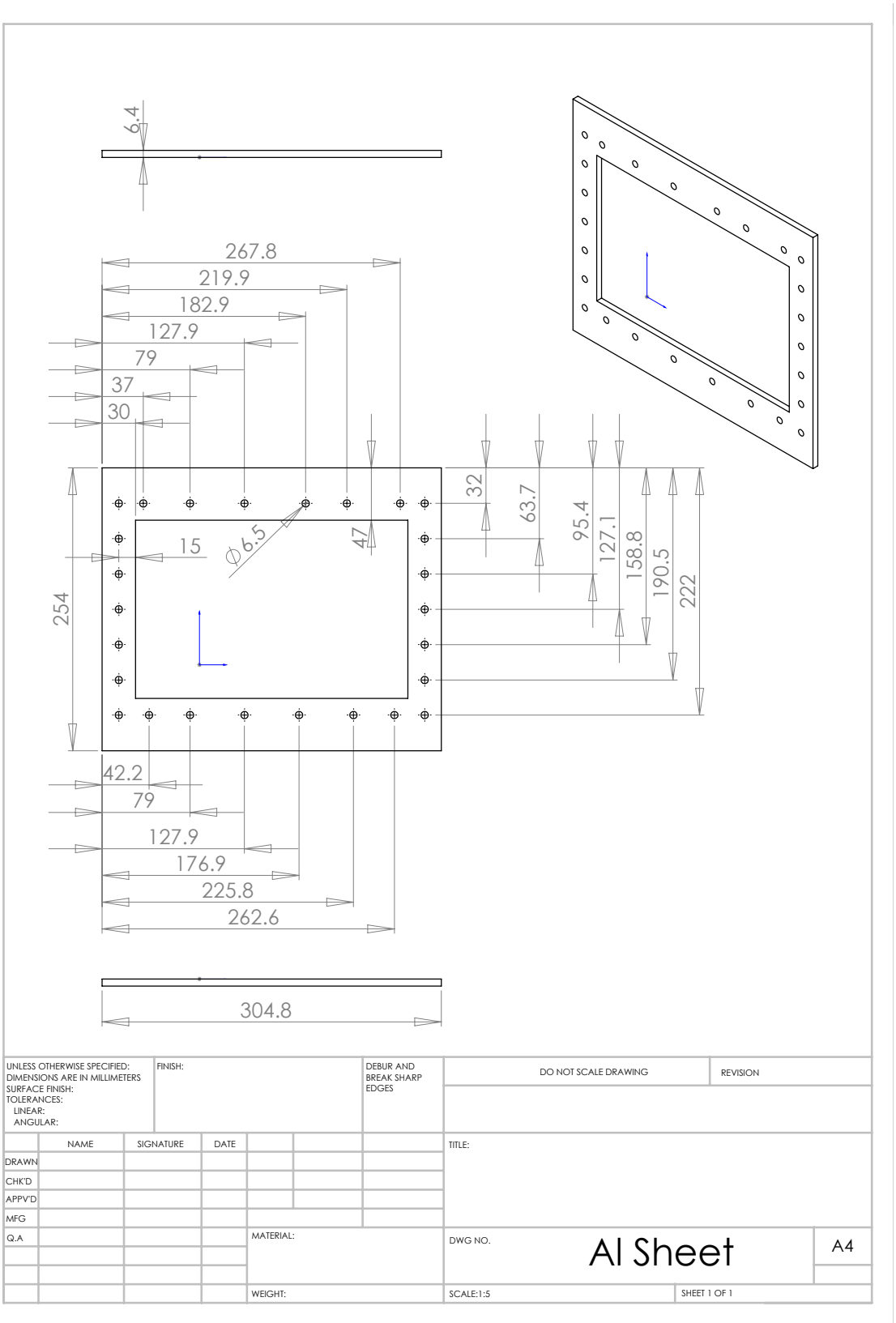

Figure A- 5: Mark I aluminum perimeter sheet technical drawing.

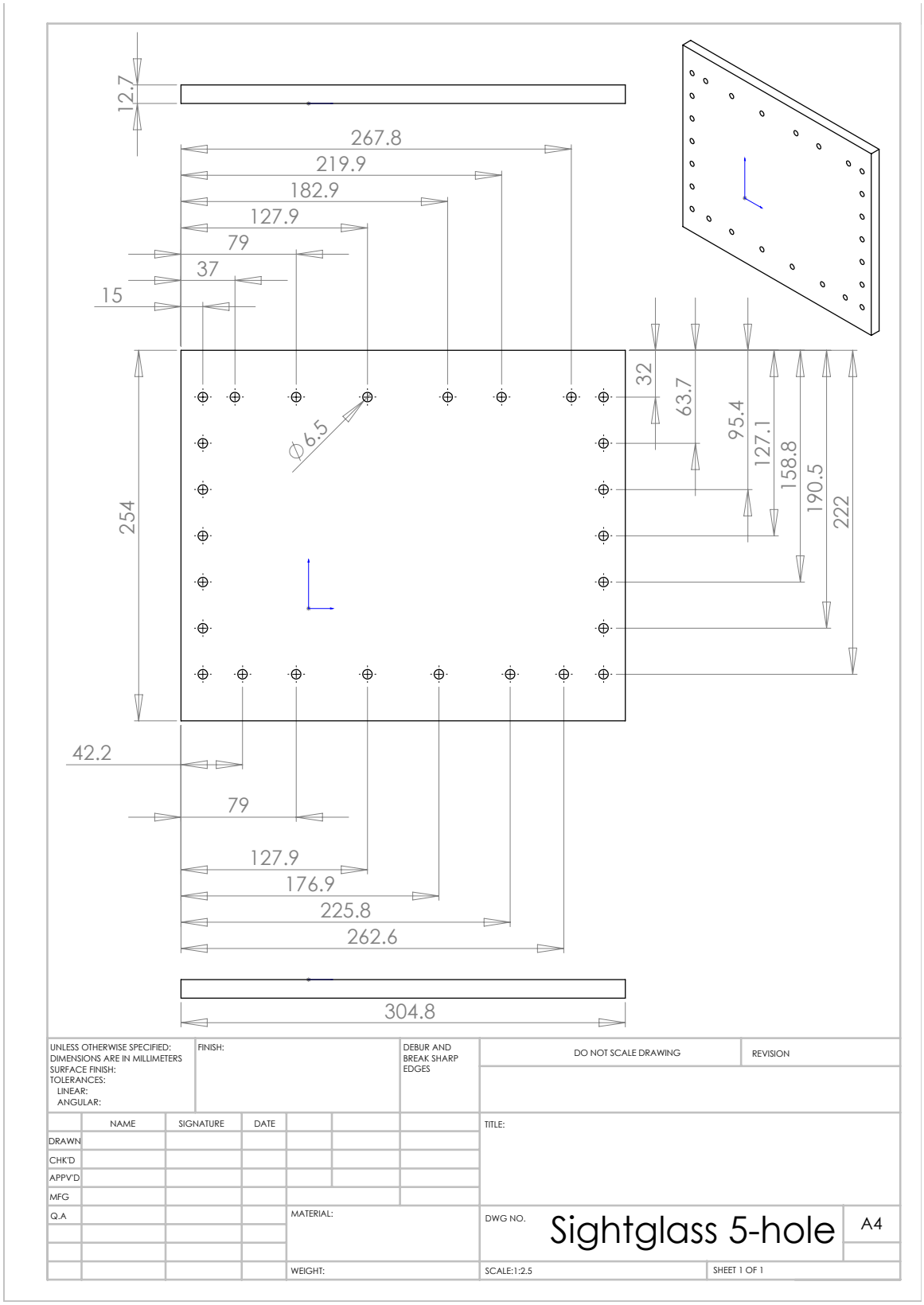

Figure A- 6: Mark I polycarbonate sight-glass technical drawing.

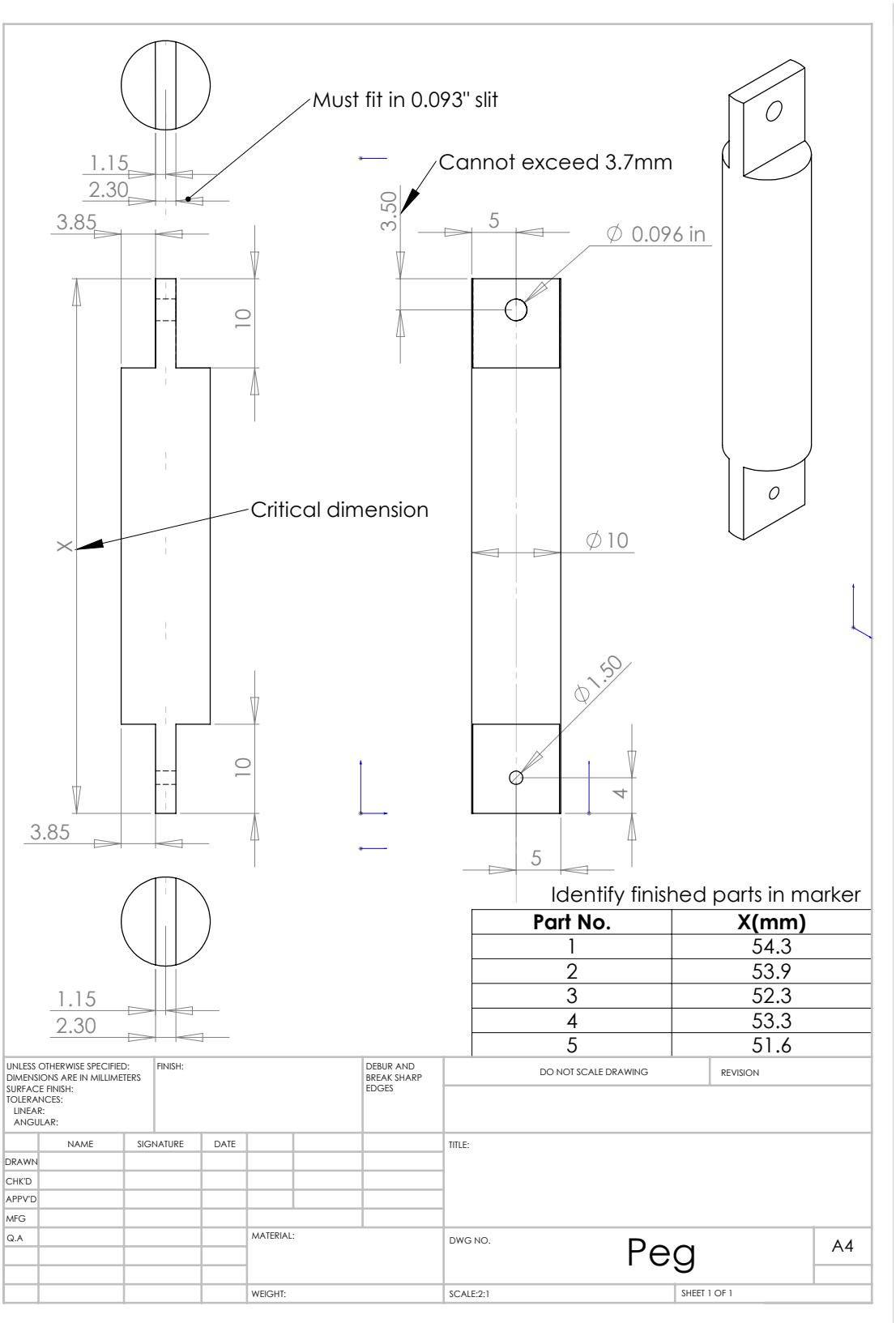

Figure A- 7: Mark I polypropylene peg technical drawing.

APPENDIX B: MARK II MECHANICAL DESIGN DRAWINGS

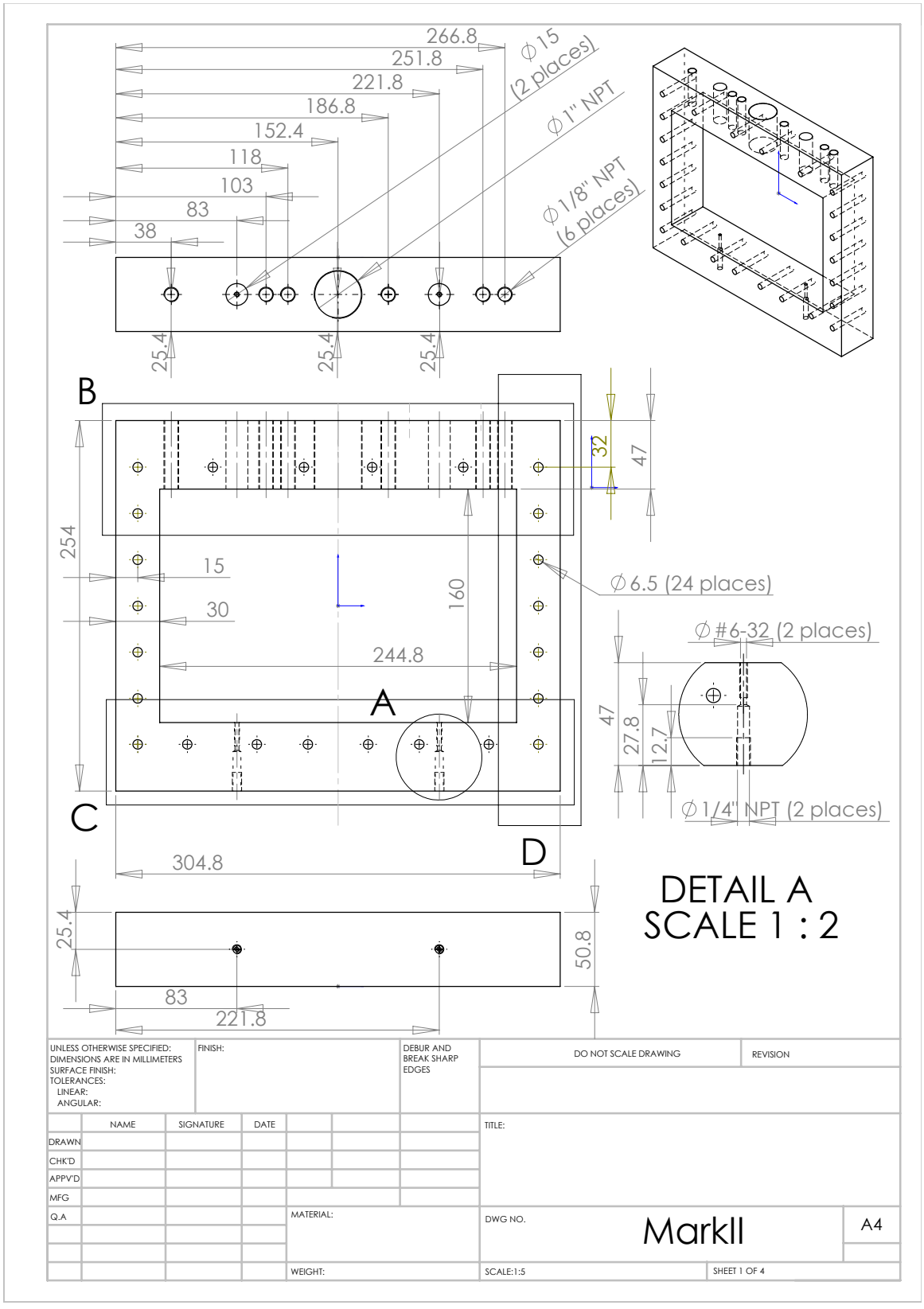

Figure B- 1: Mark II polypropylene base technical drawing page 1.

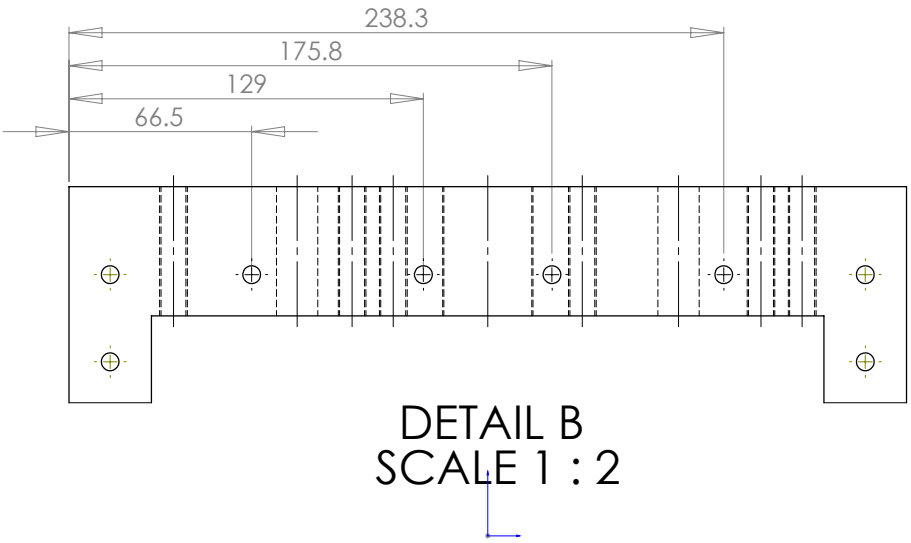

UNLESS OTHERWISE SPECIFIED: DIMENSIONS ARE IN MILLIMETERS SURFACE FINISH: TOLERANCES: LINEAR: ANGULAR:		FINISH:			DEBUR AND BREAK SHARP EDGES		DO NOT SCALE DRAWING	REVISION
	NAME	SIGNATURE	DATE				TITLE:	
DRAWN								
CHK'D								
APPV'D								
MFG								
Q.A				MATERIAL:			DWG NO. MarkII	A4
				WEIGHT:			SCALE:1:5	SHEET 2 OF 4

Figure B- 2: Mark II polypropylene base technical drawing page 2.

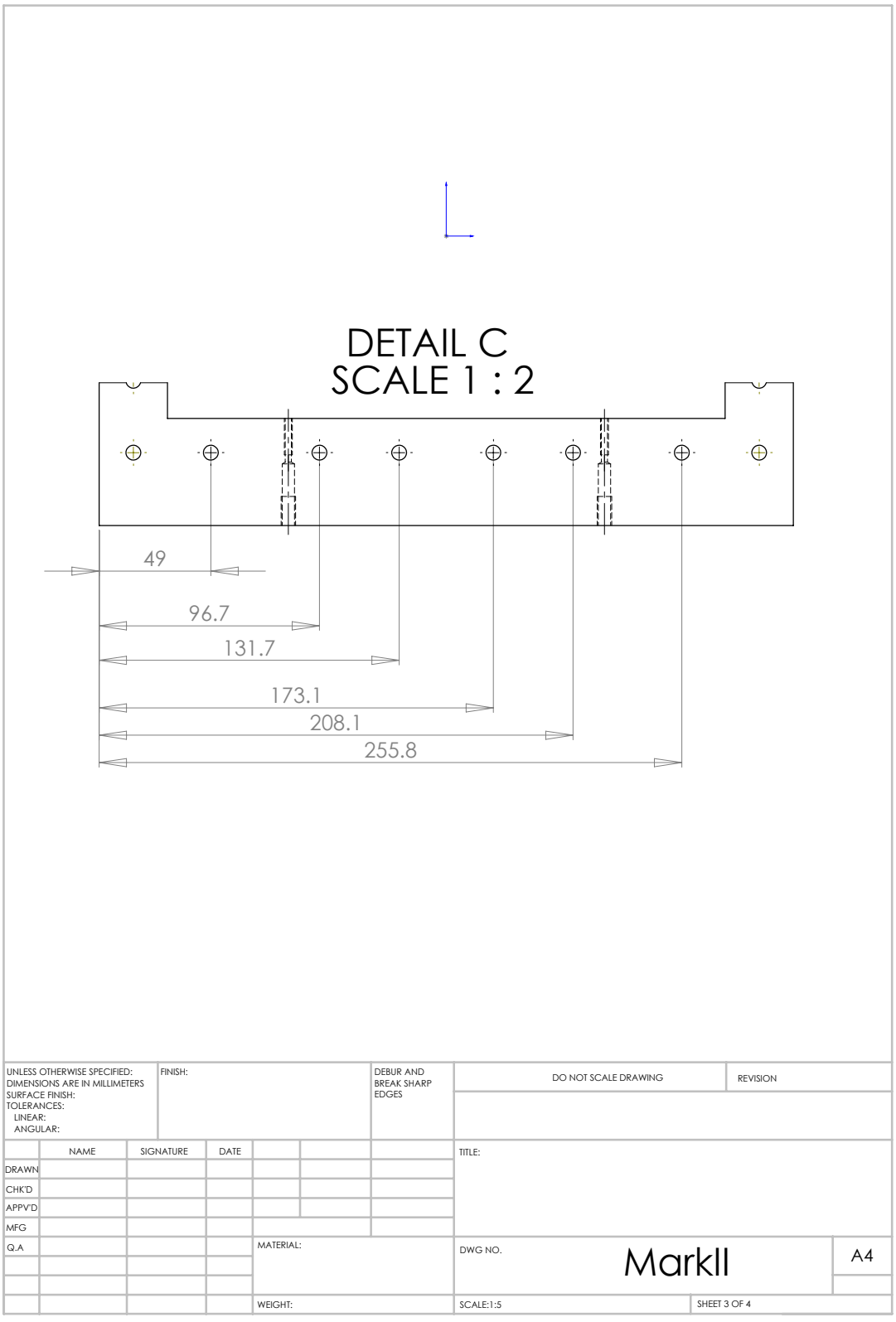

Figure B- 3: Mark II polypropylene base technical drawing page 3.

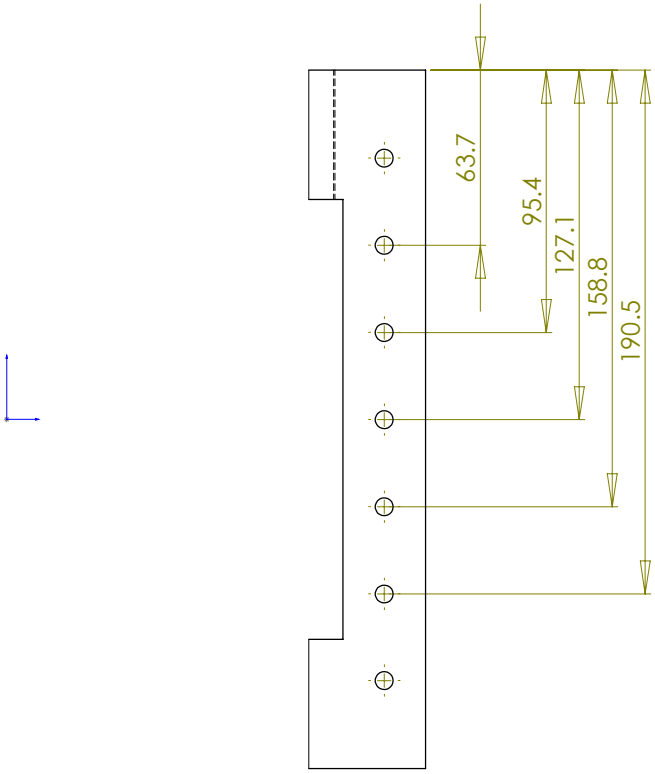

DETAIL D
SCALE 1 : 2

UNLESS OTHERWISE SPECIFIED: DIMENSIONS ARE IN MILLIMETERS SURFACE FINISH: TOLERANCES: LINEAR: ANGULAR:	FINISH:		DEBUR AND BREAK SHARP EDGES		DO NOT SCALE DRAWING	REVISION
	NAME	SIGNATURE	DATE			TITLE:
DRAWN						
CHK'D						
APPV'D						
MFG						
Q.A				MATERIAL:	DWG NO. MarkII	A4
				WEIGHT:	SCALE:1:5	SHEET 4 OF 4

Figure B- 4: Mark II polypropylene base technical drawing page 4.

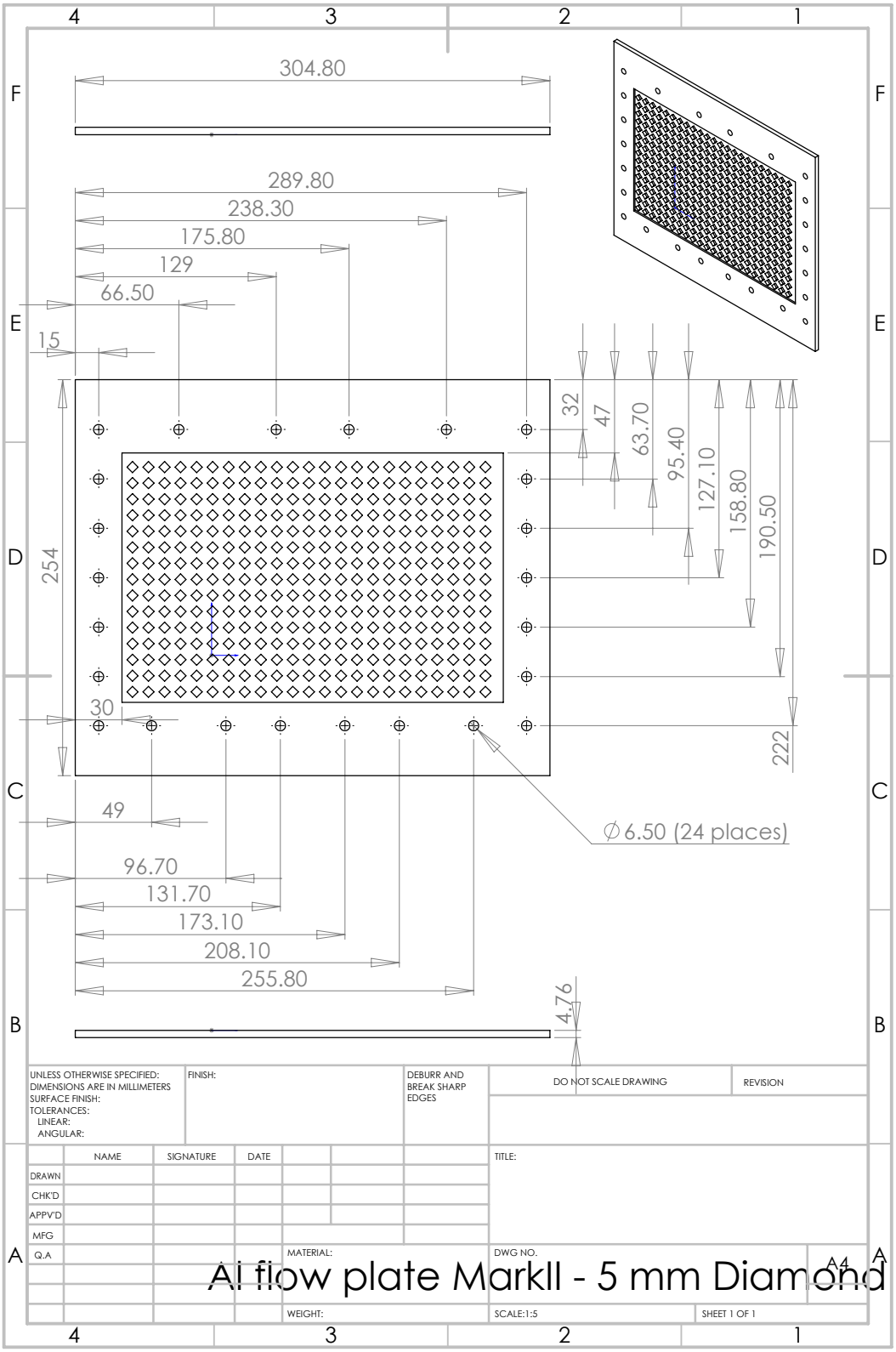

Figure B- 5: Mark II aluminum flow-plate technical drawing.

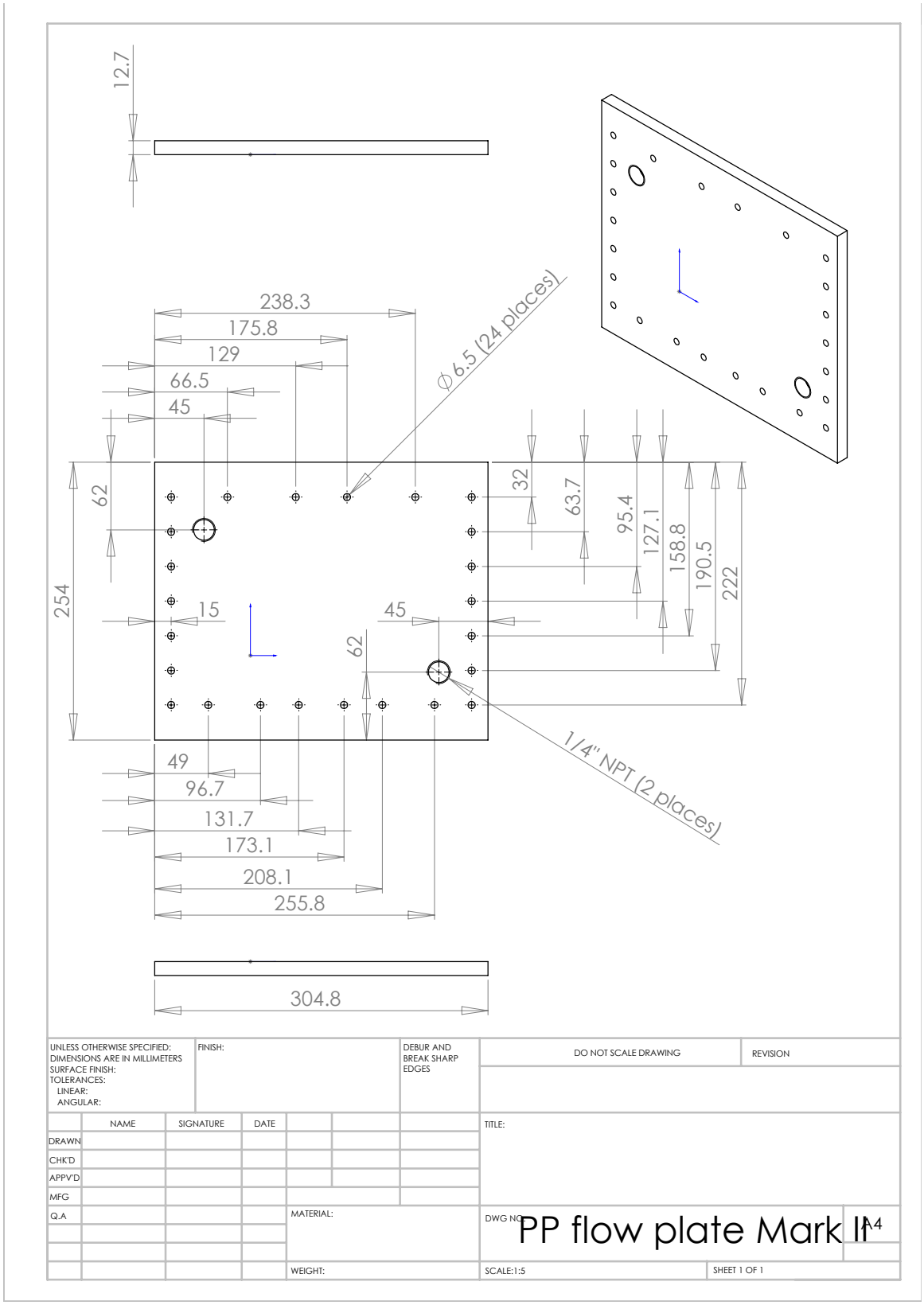

Figure B- 6: Mark II polypropylene plate technical drawing.

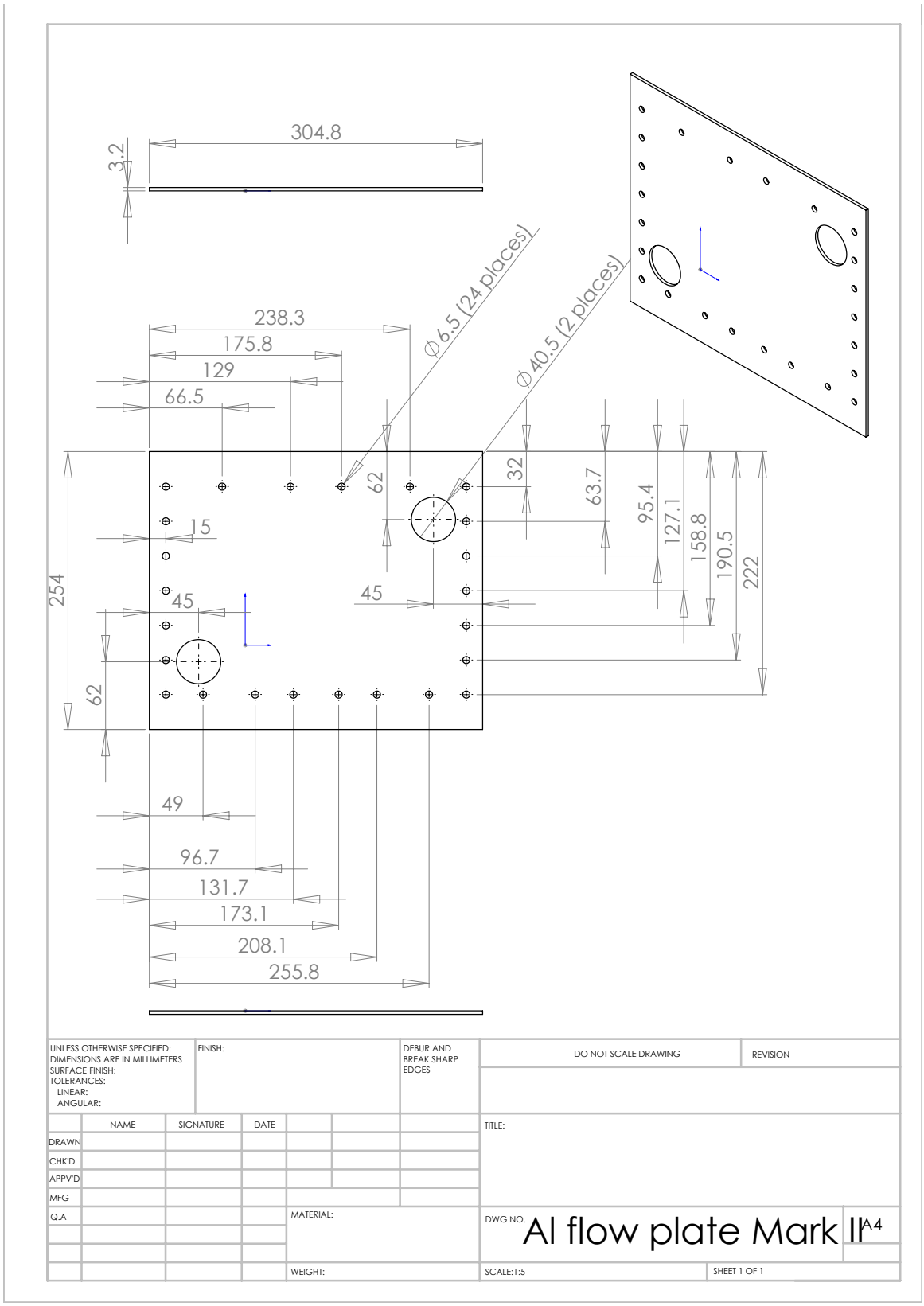

Figure B- 7: Mark II aluminum end-plate technical drawing.

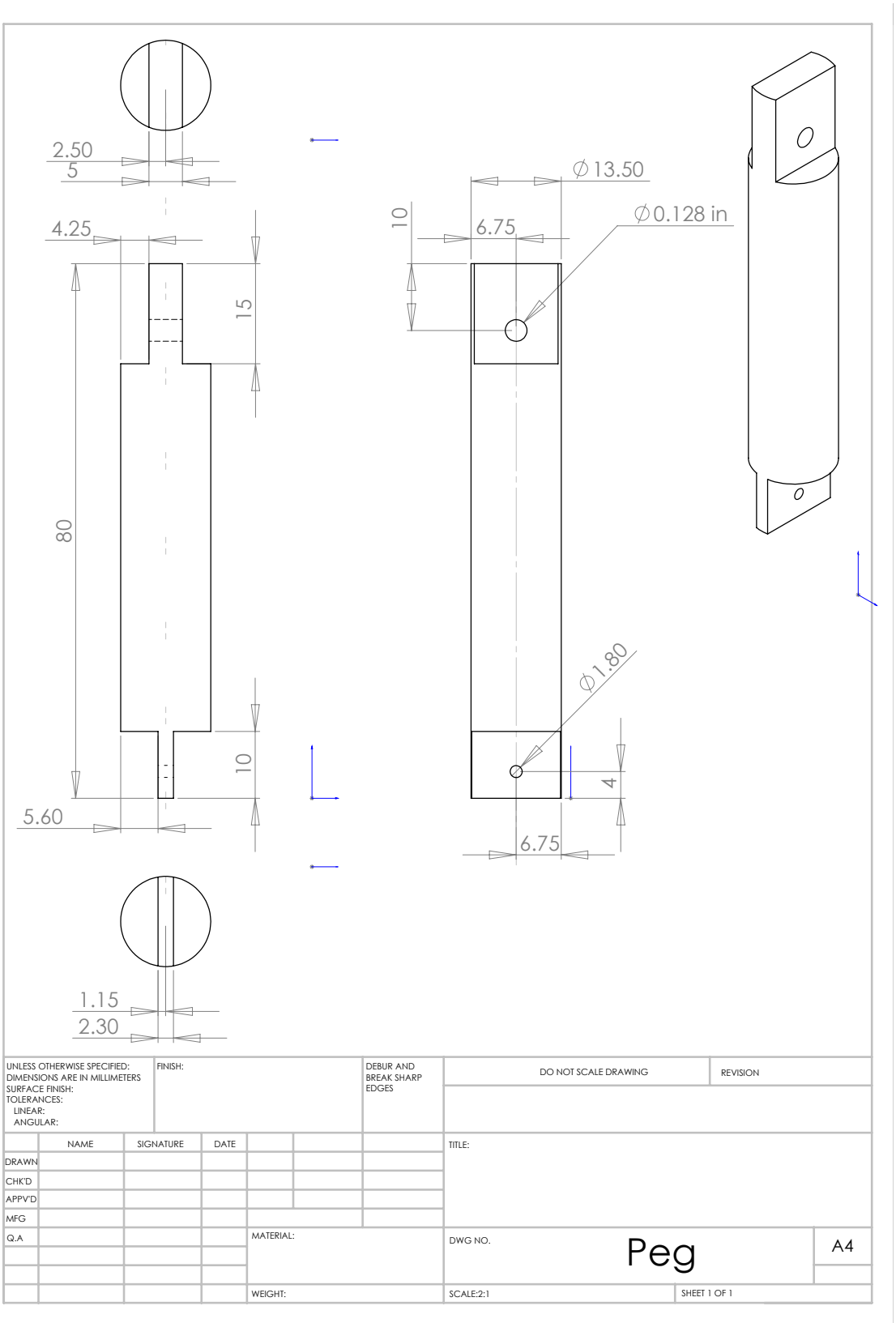

Figure B- 8: Mark II polypropylene peg technical drawing.

APPENDIX C: MARK III MECHANICAL DESIGN DRAWINGS

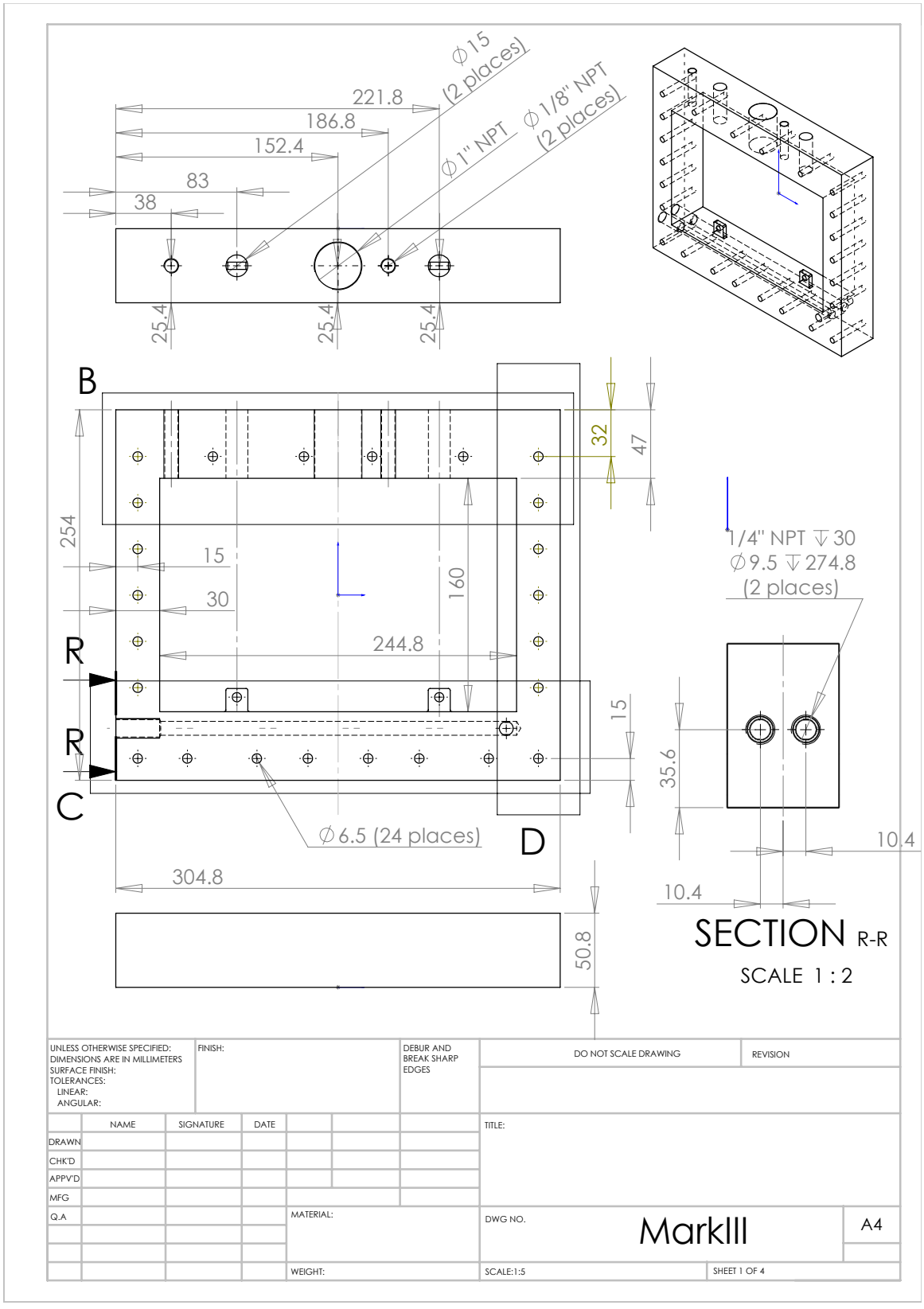

Figure C- 1: Mark III polypropylene base technical drawing page 1.

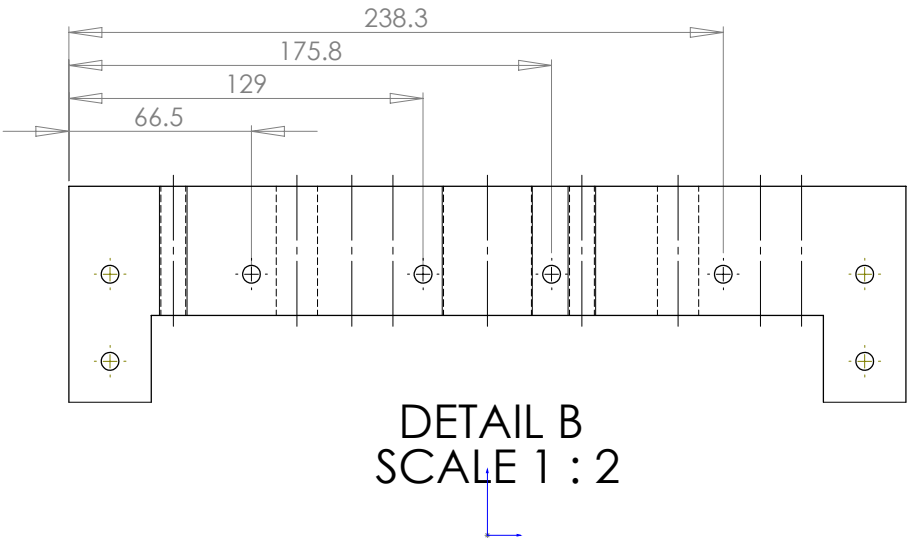

UNLESS OTHERWISE SPECIFIED: DIMENSIONS ARE IN MILLIMETERS SURFACE FINISH: TOLERANCES: LINEAR: ANGULAR:		FINISH:		DEBUR AND BREAK SHARP EDGES		DO NOT SCALE DRAWING		REVISION
	NAME	SIGNATURE	DATE				TITLE:	
DRAWN								
CHK'D								
APPV'D								
MFG								
Q.A				MATERIAL:			DWG NO. MarkIII	A4
				WEIGHT:			SCALE:1:5	SHEET 2 OF 4

Figure C- 2: Mark III polypropylene base technical drawing page 2.

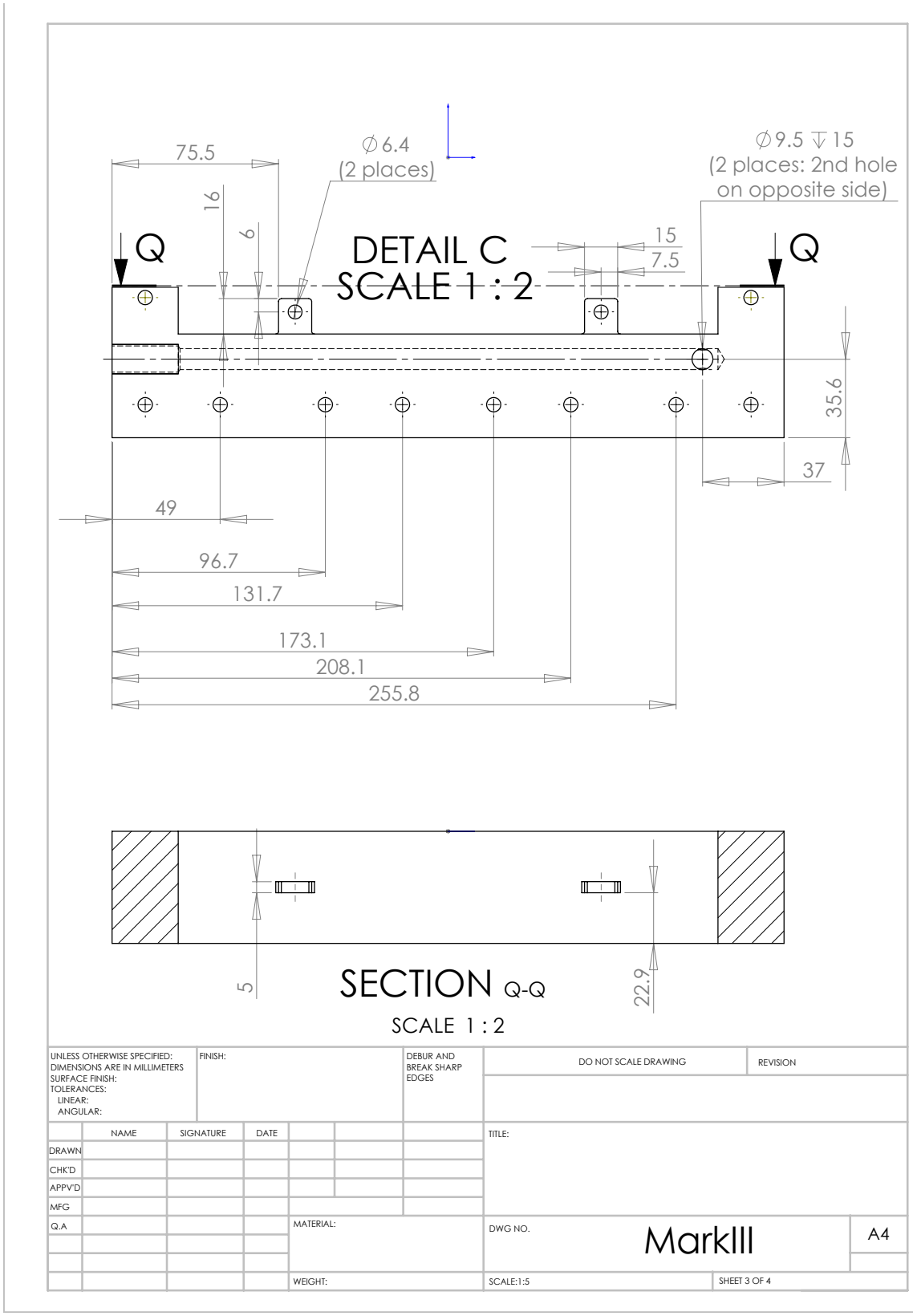

Figure C- 3: Mark III polypropylene base technical drawing page 3.

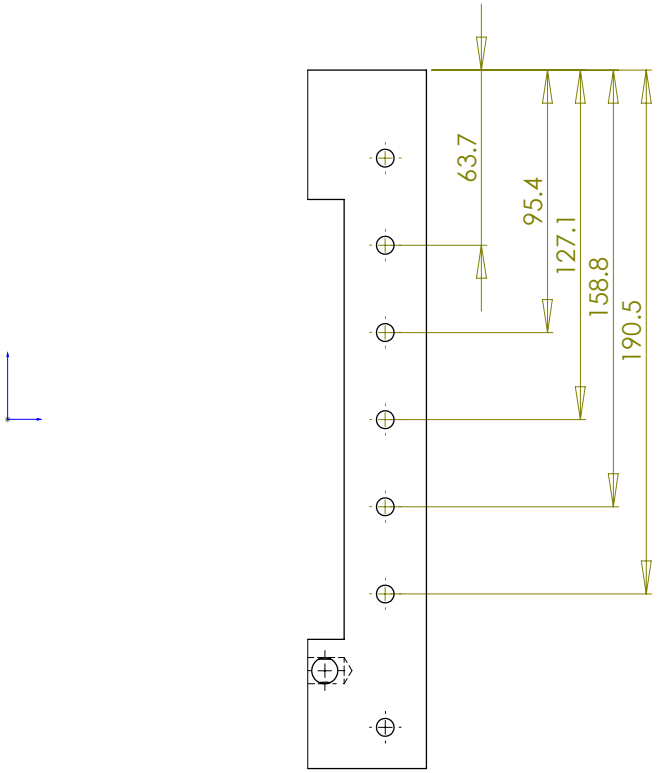

DETAIL D
SCALE 1 : 2

UNLESS OTHERWISE SPECIFIED: DIMENSIONS ARE IN MILLIMETERS SURFACE FINISH: TOLERANCES: LINEAR: ANGULAR:	FINISH:		DEBUR AND BREAK SHARP EDGES		DO NOT SCALE DRAWING	REVISION
	NAME	SIGNATURE	DATE			TITLE:
DRAWN						
CHK'D						
APPV'D						
MFG						
Q.A				MATERIAL:	DWG NO. MarkIII	A4
				WEIGHT:	SCALE:1:5	SHEET 4 OF 4

Figure C- 4: Mark III polypropylene base technical drawing page 4.

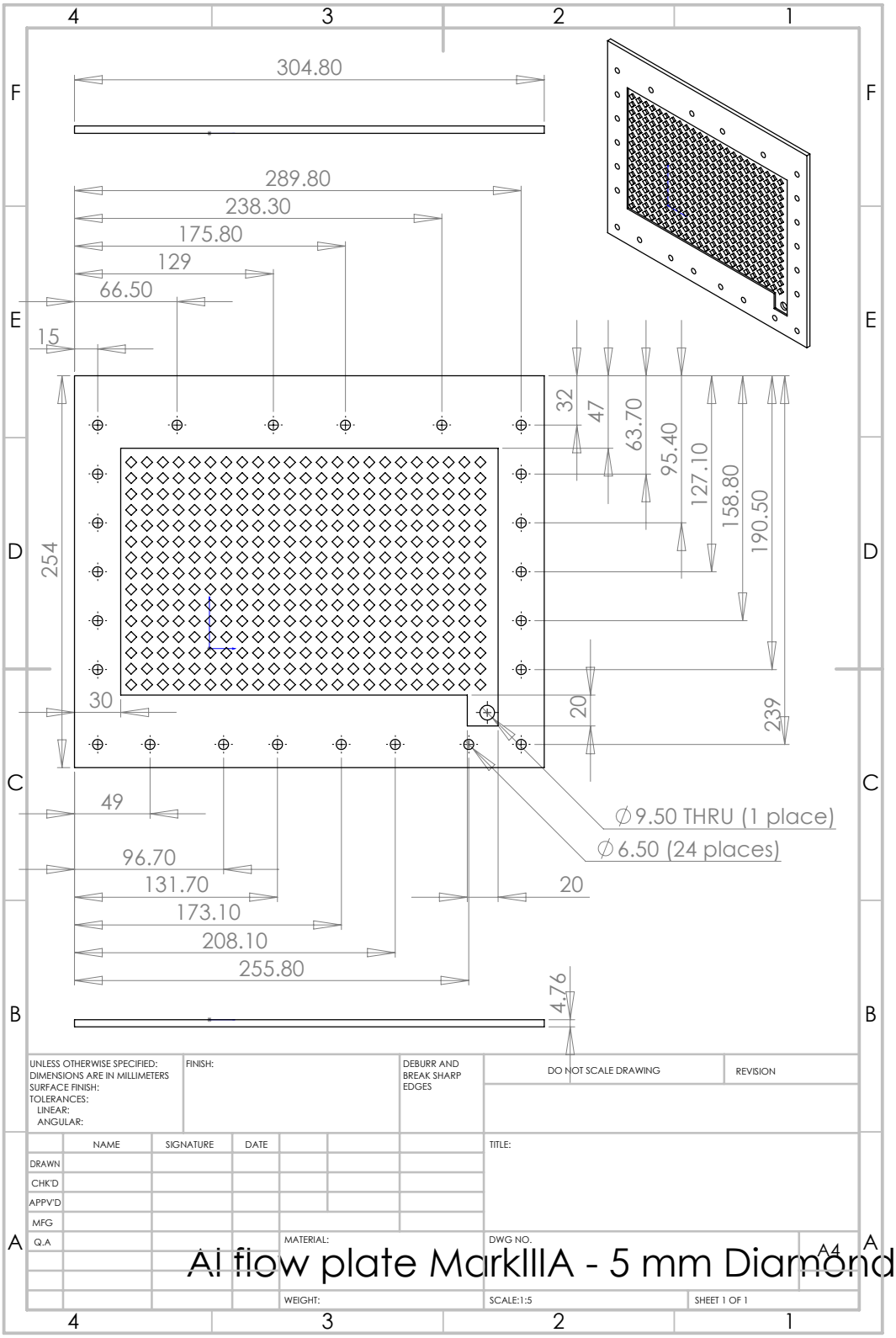

Figure C- 5: Mark III aluminum flow-plate (right-handed) technical drawing.

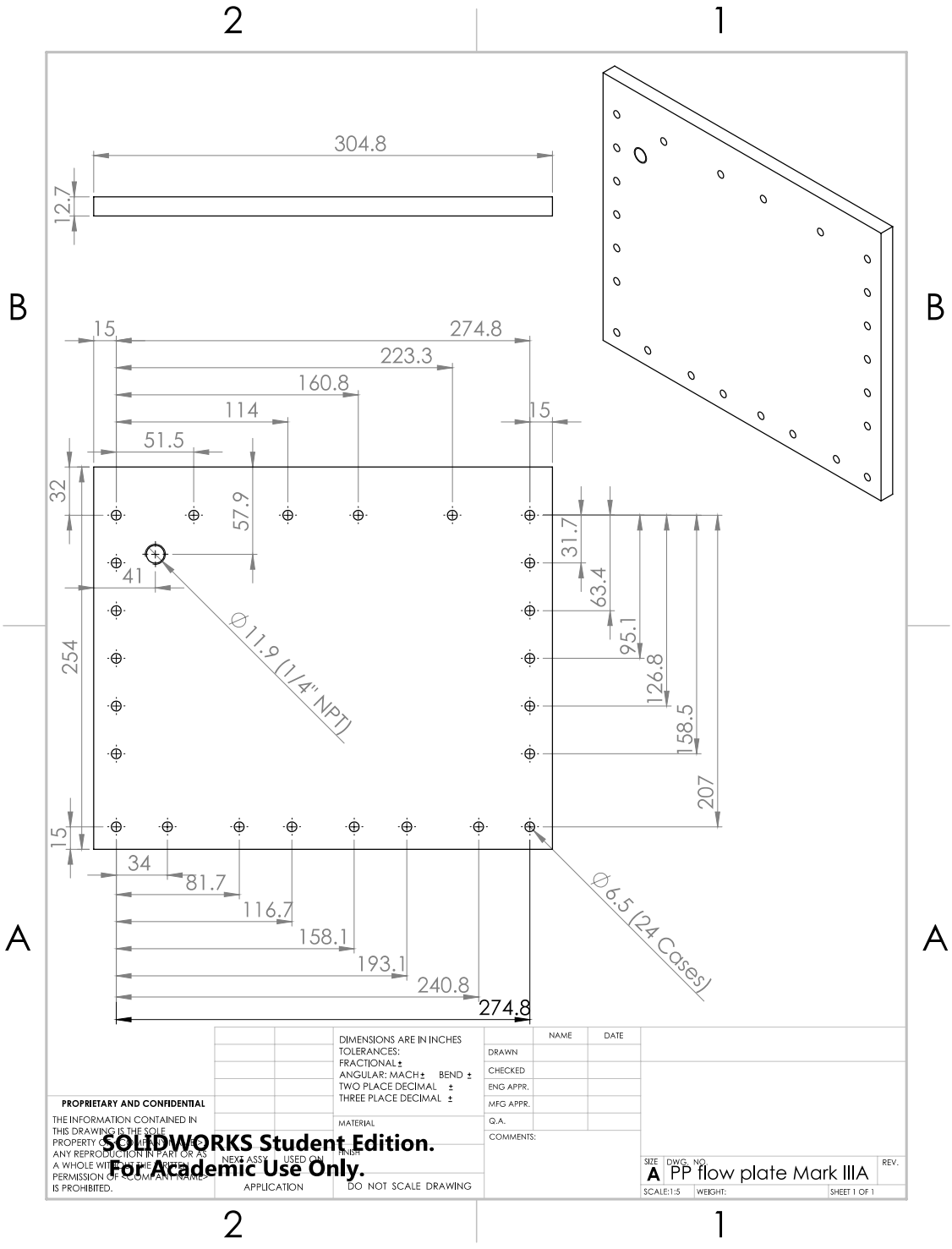

Figure C- 6: Mark III polypropylene plate (right-handed) technical drawing corresponding to Figure C- 5.

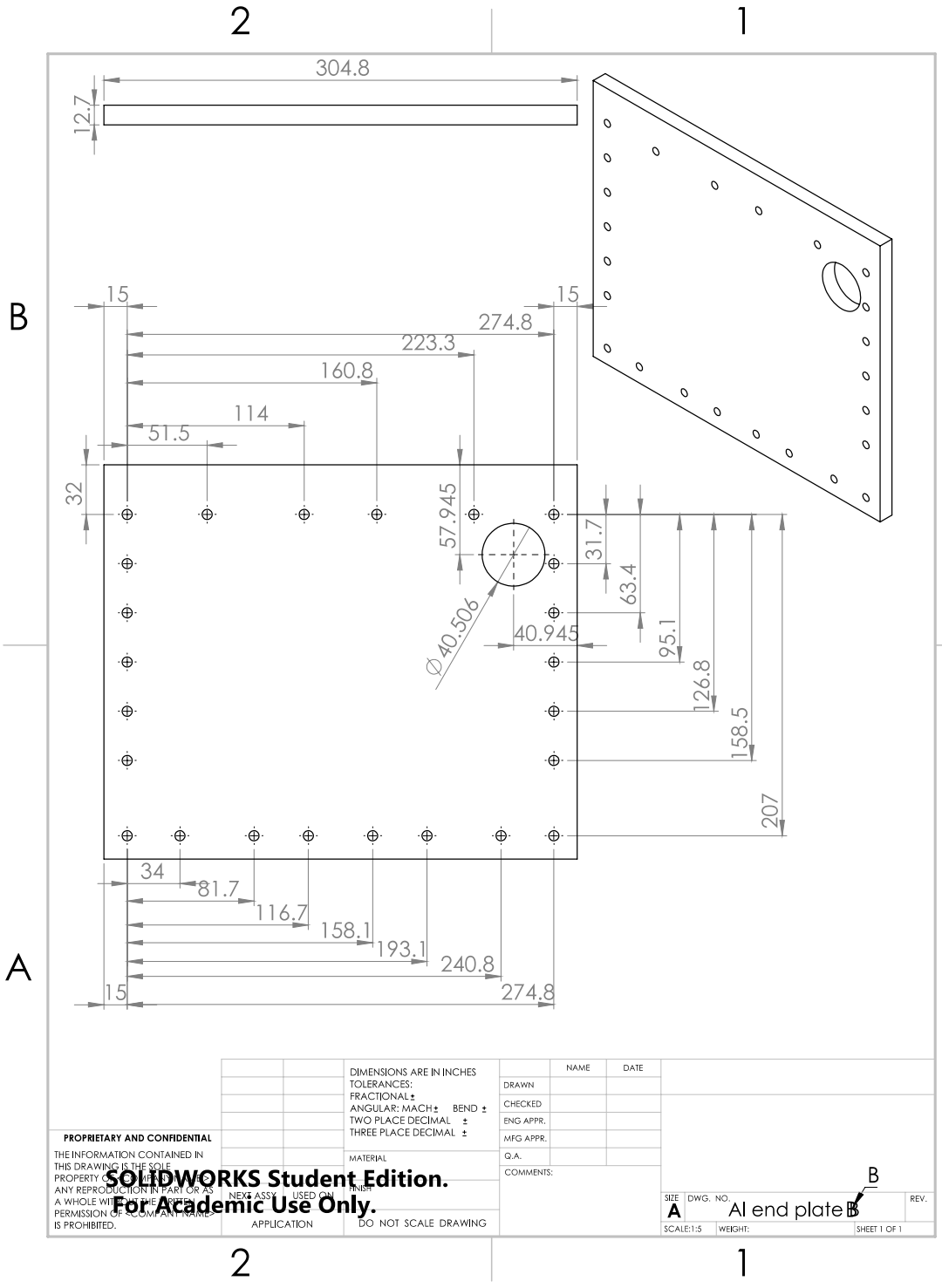

Figure C- 7: Mark III aluminum end-plate technical drawing.

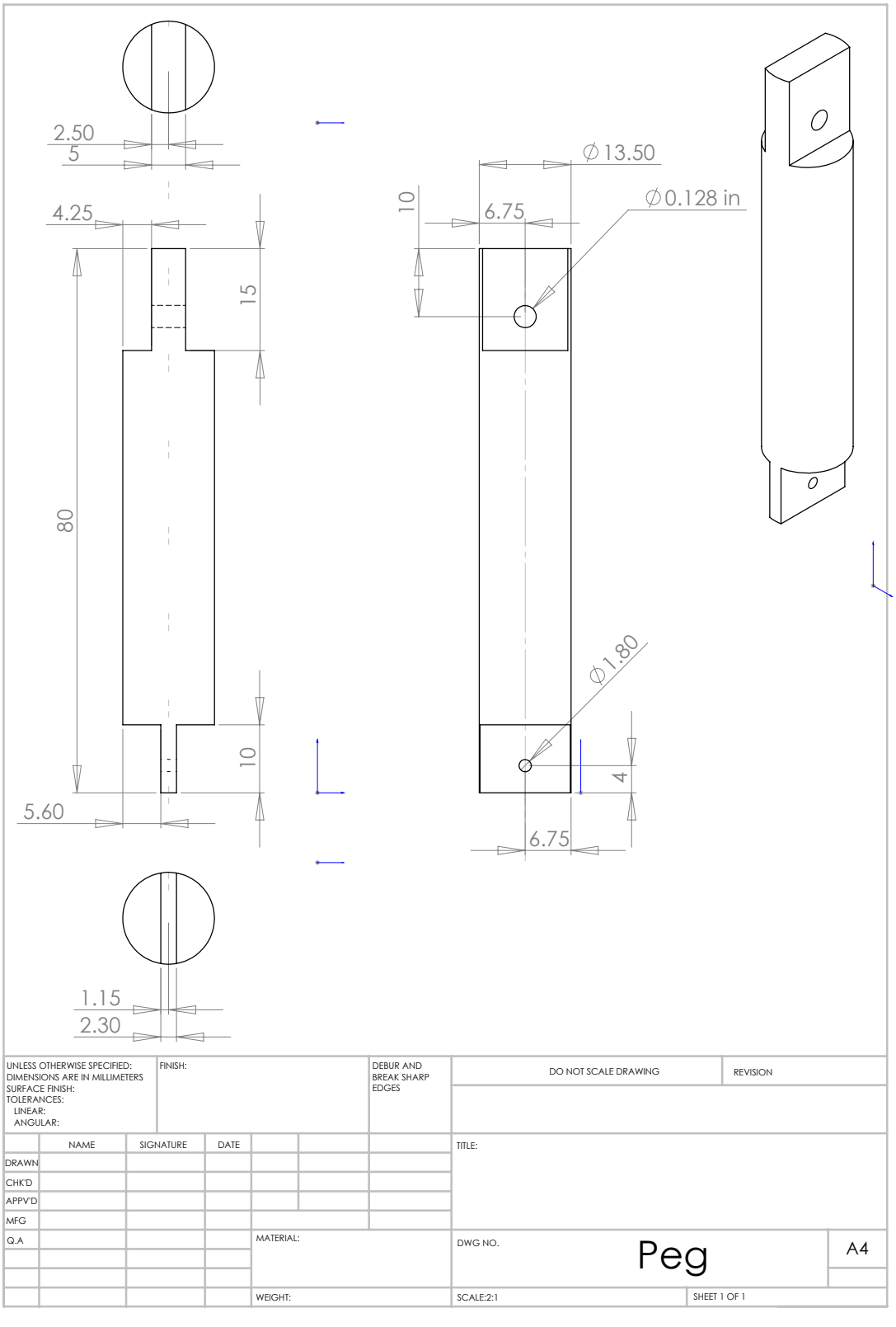

Figure C- 8: Mark III polypropylene peg technical drawing.

APPENDIX D: MATLAB FUNCTIONS AND SCRIPTS

Equivalent Sharp-edged Orifice Diameter Analysis of Pressure Release Data

```
function F = Orifice_dia (F,mode)
% Function calculating the equivalent orifice diameter from pseudo
% steady-state calculations of pressure release experiment data.
% F is the experimental pressure vector in psig recoreded at 1 Hz.
% mode is used to select +ve pressure (==1) or vacuum (==2) tests.
% Output is array of [psig, kPa, kPa/s, kg/L, Y, m^2, m].
% date: April 23rd, 2015
% by: Louis Desgrosseilliers

L = length(F);

% convert to kPa
F(:,2) = F*101.325/14.696 + 101.325;

% dP/dt in kPa/s
F(1:L-1,3) = diff(F(:,2));

% density of air at current pressure and 20 degC in kg/L
F(:,4) = 29e-3*F(:,2)/(8.31451*293.15);

% leakage rate in kg/s for V = 1.99 L
F(:,5) = 29e-3*F(:,3)*1.99/(8.31451*293.15);

% Calculation of Y parameter for compressible flow through an orifice
plate
F(:,6) = 1-0.41*(1-101.325./F(:,2))/1.4;

% Equivalent orifice cross-section area in m^2
F(:,7) = abs(F(:,5)./(0.61*F(:,6).*sqrt(2*(F(:,2)-101.325).*F(:,4))));

if mode == 1
    F(:,7) = F(:,7).*(F(:,3)<0);
else
    F(:,7) = F(:,7).*(F(:,3)>0);
end

% Equivalent orifice diameter in m
F(:,8) = sqrt(F(:,7))*2/pi;
```

HD Video Processing for Solidification Front Analysis

```
% Video Processing Commands
% Imports colour HD video frames and converts first to grayscale, then
% converted to binary in order to identify regions of solid SAT PCM.
% Measures the amount of solid along a horizontal cut-line to track
extent
% of solidification in a linear path.
% By: Louis Desgrosseilliers
% Date: May 7, 2016

vid = VideoReader('MVI_1290.MP4'); % imports the source HD video file

z = [766 296;766 1684];
% horizontal cut-line coordinates, unique to every video file

j = 235; % frame number at beginning of solidification (nucleation)
k = 800; % frame number at end of full horizontal occupation of solid
PCM
s = 4; % number of interfaces present (x2 per spring trigger)

for i = j:k
    img=read(vid,i);
    img = rgb2gray(img);
% grayscale conversion for single-value pixel evaluation
    A (1,:,i-j+1)=img(z(1,1),z(1,2):z(2,2));
% records cut-line grayscale values
end

A = A>=130; % binary evaluation of grayscale values relating to solid
PCM

for q = 1:length(A(1,1,:))
    P(q,1)=length(find(A(:,:,q)==1));
% recording the occupancy of solid PCM in the horizontal cut-line
end

P=P-P(1); % background subtraction

for q = 2:k-j+1
    % data processing
    if P(q)-P(q-1)<0
        P(q)=P(q-1);
        % substitutes data noise (false negatives)
    end
end
P(find(diff(P)==0)+1)=[];
% omits noise to improve data quality
P(:,2)=P(:,1)*d_pix/s;
% converts relative solidification to linear distance (d_pix =
mm/pixel),
% unique to every video file
P(:,3)=linspace(0,length(P(:,1))-1,length(P(:,1)))'/fps;
% generates a corresponding time vector (not real-time) for all of the
% positive solidification front expansion events using the videos frame
```

```
% rate
```

Infrared Image Processing for Solidification Front Analysis

```
% Sequential Infrared Thermographic Processing Commands
% Imports grayscale IR frames using a static, linear calibrated
grayscale
% intensity scale. Converts grayscale frames to their corresponding
% 2-D temperature-fields.
% Measures the amount of solid along a horizontal cut-line to track
extent
% of solidification in a linear path. Solid PCM is interpreted from the
% temperature fields by identifying pixels for which temperature > 50
˚C.
% By: Louis Desgrosseilliers
% Date: May 7, 2016

clear P
clear date

j = 49; % frame number at beginning of solidification (nucleation)
k = 81; % frame number at end of full horizontal occupation of solid PCM

date = zeros(k-j+1,1); % initializes the time-vector
P = zeros(k-j+1,1); % initializes the solidification vector

z = [696 121; 696 1140];
% horizontal cut-line coordinates, unique to every video file

m=0.1569; % slope of the linear temperature-grayscale calibration
c = 20; % y-intercept of the linear temperature-grayscale calibration

for i = j:k
    % Sequential IR-frame import
    if i<10
        A=['Image_0000000' num2str(i) '.tif'];
        f = imread(A)*m+c;
        % converts grayscale image to temperature-field
        if i == j
            f1 = f; % saves background temperature-field
        end

        P(i-j+1,1) = length(find(f(z(1,1),z(1,2):z(2,2))>=50));
        % records the number of pixels interpreted to be solid PCM
        a = imfinfo(A);
        date(i-j+1,:) = datenum(a.FileModDate);
        % saves IR-frame timestamp as Matlab datenumber format
        % note that FileModDate only records the timestamp with a 2
second
        % resolution

    elseif i<100
        A = ['Image_000000' num2str(i) '.tif'];
        f = imread(A)*m+c;
        if i == j
            f1 = f;
        end
```

```
        P(i-j+1,1) = length(find(f(z(1,1),z(1,2):z(2,2))>=50));
        a = imfinfo(A);
        date(i-j+1,:) = datenum(a.FileModDate);

    else
        A = ['Image_00000' num2str(i) '.tif'];
        f = imread(A)*m+c;
        if i == j
            f1 = f;
        end

        P(i-j+1,1) = length(find(f(z(1,1),z(1,2):z(2,2))>=50));
        a = imfinfo(A);
        date(i-j+1,:) = datenum(a.FileModDate);
    end

end

date(:,2)=date(:,1)-date(1,1);
% converts timestamp to relative elapsed time
date(:,2)=date(:,2)*3600*24;
% converts relative elapsed time from days to seconds

n = k-j+1; % number of data points
B = zeros(n,1); % initializes elapsed time processing vector
B (2:n) = diff(date(:,2));
% identifies elapsed time values with insufficient resolution
C = B~=0; % unique time steps
D = find(C==1); %index vector of unique time steps

date(:,3) = date(:,2).*C; % records the unique time steps in a new
column

% corrects for inadequate timescale resolution between IR frames
for i = 1:n
    if C(i)==0
        if i < max(D)
            if i < min(D)
                fps = 9;
                % default 9 frames per second (camera maximum capture
rate)
                date(i,3) = date(min(D),3)-(min(D)-i)/fps;
                % corrected elapsed time values
            else
                fps = (D(find(D>i,1))-D(find(D>i,1)-1))/...
                    (date(D(find(D>i,1)),2)-date(D(find(D>i,1)-1),2));
                % approximates fps for complete 2 second intervals since
                % the IR camera does not maintain 9 fps continuously
                date(i,3) = date(i-1,3)+1/fps;
                % corrected elapsed time values
            end
        else
            % assumes the last calculated fps for the final interval if
not
```

```
            % a complete 2 second interval
            date(i,3) = date(i-1,3)+1/fps; % uses last calculated fps
        end
    end
end

P(:,2) = P(:,1)*dpix/s;
% converts relative solidification to average linear distance
% (d_pix = mm/pixel), unique to every video file, for every interface
% present (s = number of interfaces)
P(:,3) = date(:,3);
% records the elapsed time vector in P for consiceness
P(find(P(:,1)==0),:)=[];
% omits noise to improve data quality
P(:,1)=P(:,1)-P(1,1);
% background subtraction
P(:,2)=P(:,2)-P(1,2);
% background subtraction
P(:,3)=P(:,3)-P(1,3);
% establishes relative timing

Tave = ceil(sum(sum(f1))/numel(f1));
% evaluates surface-average IR-recorded temperature for initial frame
```

APPENDIX E: AUXILIARY FIGURES

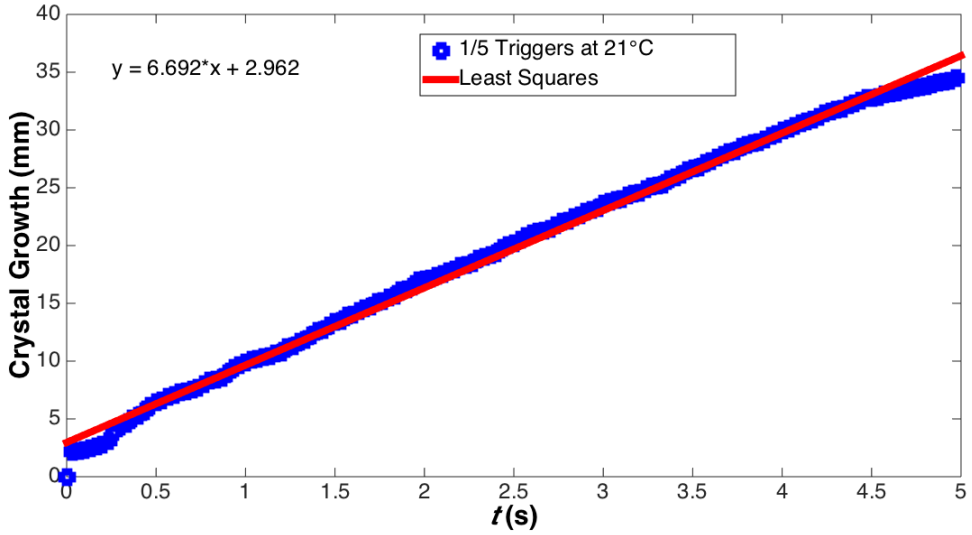

Figure E- 1: Optically measured SAT solidification front expansion from a single actuated spring-trigger. R^2 = 0.996.

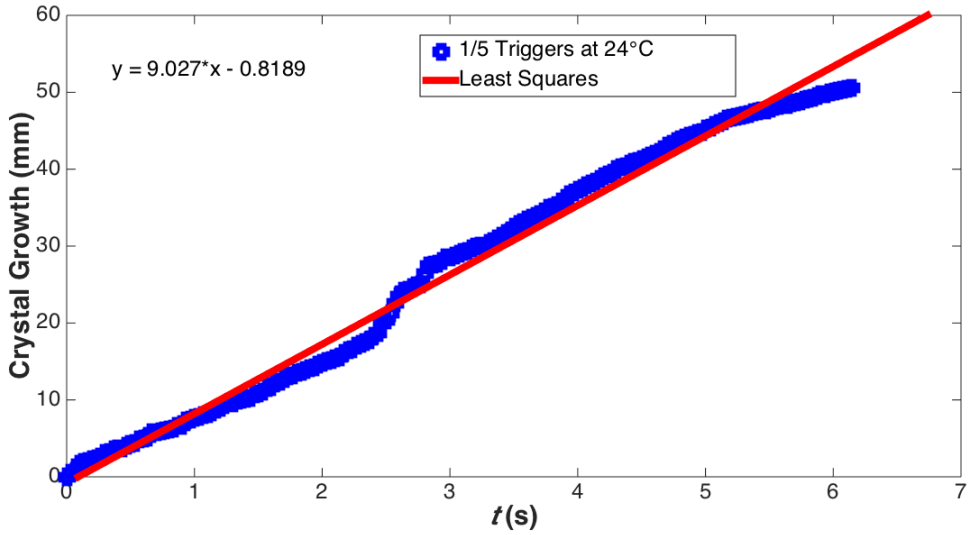

Figure E- 2: Optically measured SAT solidification front expansion from a single actuated spring-trigger. R^2 = 0.988.

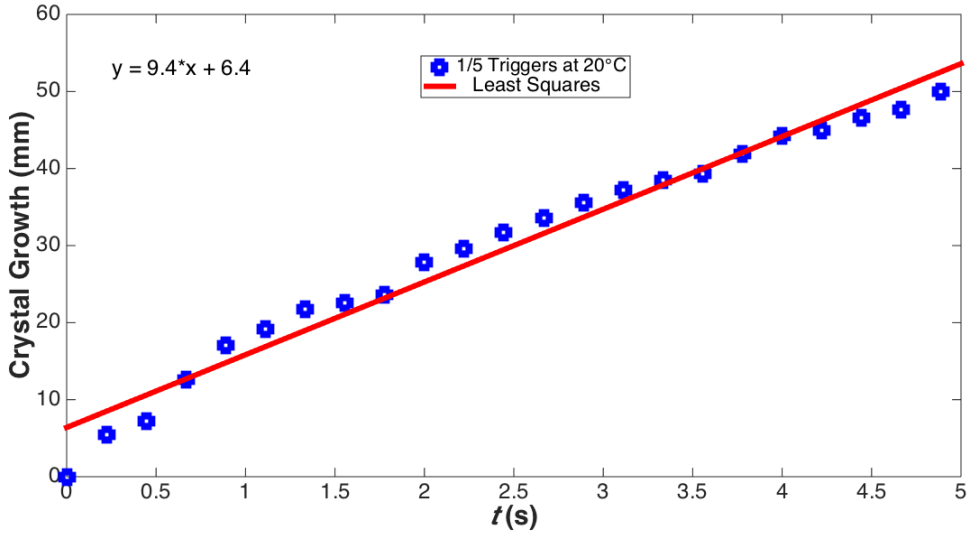

Figure E- 3: IR thermographically measured solidification front expansion from a single actuated spring-trigger. R^2 = 0.972.

APPENDIX F: DIFFERENTIAL EQUATIONS FOR UNCERTAINTY ANALYSES

1.

$$dQ = \sqrt{\begin{array}{c}\left(\frac{\partial Q}{\partial H}\frac{\partial H}{\partial T_2}dT\right)^2 + \left(\frac{\partial Q}{\partial H}\frac{\partial H}{\partial T_1}dT\right)^2 + \\ \left(\frac{\partial Q}{\partial \dot{m}_{ave}}\frac{1}{t_f+1}\right)^2 \sum_{i-t_f}^{i}\left[\left(\frac{\partial \dot{m}}{\partial \rho}\frac{\partial \rho}{\partial T}dT\right)^2 + \left(\frac{\partial \dot{m}}{\partial V}dV\right)^2\right]\end{array}}$$

$$\frac{\partial Q}{\partial H} = \dot{m}_{ave}$$

$$\frac{\partial Q}{\partial \dot{m}_{ave}} = \Delta H$$

$$\frac{\partial H}{\partial T_2} = [0.0033T_2(^{\circ}\mathrm{C})^{-1} + 3.6357]\ \mathrm{kJ\ kg^{-1}\ K^{-1}}$$

$$\frac{\partial H}{\partial T_1} = -[0.0033T_1(^{\circ}\mathrm{C})^{-1} + 3.6357]\ \mathrm{kJ\ kg^{-1}\ K^{-1}}$$

$$\frac{\partial \dot{m}}{\partial \rho} = V$$

$$\frac{\partial \dot{m}}{\partial V} = \rho$$

$$\frac{d\rho}{dT} = [0.0052T(^{\circ}\mathrm{C})^{-1} - 0.3946]\ \mathrm{kg\ m^{-3}}$$

2.

$$dUA = \sqrt{\begin{array}{c}\left(\frac{\partial UA}{\partial T_2}dT\right)^2 + \left(\frac{\partial UA}{\partial T_1}dT\right)^2 + \left(\frac{\partial UA}{\partial V}dV\right)^2 + \left(\frac{\partial UA}{\partial LMTD_{ave}}\frac{1}{t_f+1}\right)^2 \\ \sum_{i-t_f}^{i}\left[\left(\frac{\partial LMTD}{\partial(T_1-T_2')}2dT\right)^2 + \left(\frac{\partial LMTD}{\partial(T_2-T_1')}2dT\right)^2\right]\end{array}}$$

$$\left(\frac{\partial UA}{\partial T_2}dT\right)^2+\left(\frac{\partial UA}{\partial T_1}dT\right)^2+\left(\frac{\partial UA}{\partial V}dV\right)^2=\left(\frac{\partial UA}{\partial Q}dQ\right)^2$$

$$\frac{\partial UA}{\partial Q}=\frac{1}{LMTD_{ave}\Gamma}$$

$$\frac{\partial UA}{\partial LMTD_{ave}}=\frac{Q}{\Gamma}$$

$$\frac{\partial LMTD}{\partial(T_1-T_2')}=\frac{\ln\frac{T_1-T_2'}{T_2-T_1'}-\left(1-\frac{T_2-T_1'}{T_1-T_2'}\right)}{\left(\ln\frac{T_1-T_2'}{T_2-T_1'}\right)^2}$$

$$\frac{\partial LMTD}{\partial(T_2-T_1')}=\frac{-\ln\frac{T_1-T_2'}{T_2-T_1'}+\left(\frac{T_1-T_2'}{T_2-T_1'}-1\right)}{\left(\ln\frac{T_1-T_2'}{T_2-T_1'}\right)^2}$$

APPENDINX G: COPYRIGHT PERMISSIONS

ELSEVIER LICENSE
TERMS AND CONDITIONS

May 02, 2016

This is a License Agreement between Louis Desgrosseilliers ("You") and Elsevier ("Elsevier") provided by Copyright Clearance Center ("CCC"). The license consists of your order details, the terms and conditions provided by Elsevier, and the payment terms and conditions.

All payments must be made in full to CCC. For payment instructions, please see information listed at the bottom of this form.

Supplier	Elsevier Limited The Boulevard,Langford Lane Kidlington,Oxford,OX5 1GB,UK
Registered Company Number	1982084
Customer name	Louis Desgrosseilliers
Customer address	46 Cider Maple Dr Timberlea, NS B3T1K8
License number	3860760767559
License date	May 02, 2016
Licensed content publisher	Elsevier
Licensed content publication	Applied Thermal Engineering
Licensed content title	Determination of enthalpy–temperature–composition relations in incongruent-melting phase change materials
Licensed content author	Louis Desgrosseilliers,Paul Allred,Dominic Groulx,Mary Anne White
Licensed content date	3 November 2013
Licensed content volume number	61
Licensed content issue number	2
Number of pages	5
Start Page	193
End Page	197
Type of Use	reuse in a thesis/dissertation
Portion	figures/tables/illustrations
Number of figures/tables/illustrations	1
Format	both print and electronic

Are you the author of this Elsevier article?	Yes
Will you be translating?	No
Original figure numbers	Figure 3
Title of your thesis/dissertation	Design and Evaluation of a Modular, Supercooling Phase Change Heat Storage Device for Indoor Heating
Expected completion date	Aug 2016
Estimated size (number of pages)	200
Elsevier VAT number	GB 494 6272 12
Permissions price	0.00 USD
VAT/Local Sales Tax	0.00 USD / 0.00 GBP
Total	0.00 USD
Terms and Conditions	

INTRODUCTION

1. The publisher for this copyrighted material is Elsevier. By clicking "accept" in connection with completing this licensing transaction, you agree that the following terms and conditions apply to this transaction (along with the Billing and Payment terms and conditions established by Copyright Clearance Center, Inc. ("CCC"), at the time that you opened your Rightslink account and that are available at any time at http://myaccount.copyright.com).

GENERAL TERMS

2. Elsevier hereby grants you permission to reproduce the aforementioned material subject to the terms and conditions indicated.
3. Acknowledgement: If any part of the material to be used (for example, figures) has appeared in our publication with credit or acknowledgement to another source, permission must also be sought from that source. If such permission is not obtained then that material may not be included in your publication/copies. Suitable acknowledgement to the source must be made, either as a footnote or in a reference list at the end of your publication, as follows:
"Reprinted from Publication title, Vol /edition number, Author(s), Title of article / title of chapter, Pages No., Copyright (Year), with permission from Elsevier [OR APPLICABLE SOCIETY COPYRIGHT OWNER]." Also Lancet special credit - "Reprinted from The Lancet, Vol. number, Author(s), Title of article, Pages No., Copyright (Year), with permission from Elsevier."
4. Reproduction of this material is confined to the purpose and/or media for which permission is hereby given.
5. Altering/Modifying Material: Not Permitted. However figures and illustrations may be altered/adapted minimally to serve your work. Any other abbreviations, additions, deletions and/or any other alterations shall be made only with prior written authorization of Elsevier Ltd. (Please contact Elsevier at permissions@elsevier.com)
6. If the permission fee for the requested use of our material is waived in this instance, please be advised that your future requests for Elsevier materials may attract a fee.
7. Reservation of Rights: Publisher reserves all rights not specifically granted in the

combination of (i) the license details provided by you and accepted in the course of this licensing transaction, (ii) these terms and conditions and (iii) CCC's Billing and Payment terms and conditions.
8. License Contingent Upon Payment: While you may exercise the rights licensed immediately upon issuance of the license at the end of the licensing process for the transaction, provided that you have disclosed complete and accurate details of your proposed use, no license is finally effective unless and until full payment is received from you (either by publisher or by CCC) as provided in CCC's Billing and Payment terms and conditions. If full payment is not received on a timely basis, then any license preliminarily granted shall be deemed automatically revoked and shall be void as if never granted. Further, in the event that you breach any of these terms and conditions or any of CCC's Billing and Payment terms and conditions, the license is automatically revoked and shall be void as if never granted. Use of materials as described in a revoked license, as well as any use of the materials beyond the scope of an unrevoked license, may constitute copyright infringement and publisher reserves the right to take any and all action to protect its copyright in the materials.
9. Warranties: Publisher makes no representations or warranties with respect to the licensed material.
10. Indemnity: You hereby indemnify and agree to hold harmless publisher and CCC, and their respective officers, directors, employees and agents, from and against any and all claims arising out of your use of the licensed material other than as specifically authorized pursuant to this license.
11. No Transfer of License: This license is personal to you and may not be sublicensed, assigned, or transferred by you to any other person without publisher's written permission.
12. No Amendment Except in Writing: This license may not be amended except in a writing signed by both parties (or, in the case of publisher, by CCC on publisher's behalf).
13. Objection to Contrary Terms: Publisher hereby objects to any terms contained in any purchase order, acknowledgment, check endorsement or other writing prepared by you, which terms are inconsistent with these terms and conditions or CCC's Billing and Payment terms and conditions. These terms and conditions, together with CCC's Billing and Payment terms and conditions (which are incorporated herein), comprise the entire agreement between you and publisher (and CCC) concerning this licensing transaction. In the event of any conflict between your obligations established by these terms and conditions and those established by CCC's Billing and Payment terms and conditions, these terms and conditions shall control.
14. Revocation: Elsevier or Copyright Clearance Center may deny the permissions described in this License at their sole discretion, for any reason or no reason, with a full refund payable to you. Notice of such denial will be made using the contact information provided by you. Failure to receive such notice will not alter or invalidate the denial. In no event will Elsevier or Copyright Clearance Center be responsible or liable for any costs, expenses or damage incurred by you as a result of a denial of your permission request, other than a refund of the amount(s) paid by you to Elsevier and/or Copyright Clearance Center for denied permissions.

LIMITED LICENSE

The following terms and conditions apply only to specific license types:
15. **Translation**: This permission is granted for non-exclusive world **English** rights only unless your license was granted for translation rights. If you licensed translation rights you

may only translate this content into the languages you requested. A professional translator must perform all translations and reproduce the content word for word preserving the integrity of the article.
16. **Posting licensed content on any Website**: The following terms and conditions apply as follows: Licensing material from an Elsevier journal: All content posted to the web site must maintain the copyright information line on the bottom of each image; A hyper-text must be included to the Homepage of the journal from which you are licensing at http://www.sciencedirect.com/science/journal/xxxxx or the Elsevier homepage for books at http://www.elsevier.com; Central Storage: This license does not include permission for a scanned version of the material to be stored in a central repository such as that provided by Heron/XanEdu.
Licensing material from an Elsevier book: A hyper-text link must be included to the Elsevier homepage at http://www.elsevier.com . All content posted to the web site must maintain the copyright information line on the bottom of each image.

Posting licensed content on Electronic reserve: In addition to the above the following clauses are applicable: The web site must be password-protected and made available only to bona fide students registered on a relevant course. This permission is granted for 1 year only. You may obtain a new license for future website posting.
17. **For journal authors:** the following clauses are applicable in addition to the above:
Preprints:
A preprint is an author's own write-up of research results and analysis, it has not been peer-reviewed, nor has it had any other value added to it by a publisher (such as formatting, copyright, technical enhancement etc.).
Authors can share their preprints anywhere at any time. Preprints should not be added to or enhanced in any way in order to appear more like, or to substitute for, the final versions of articles however authors can update their preprints on arXiv or RePEc with their Accepted Author Manuscript (see below).
If accepted for publication, we encourage authors to link from the preprint to their formal publication via its DOI. Millions of researchers have access to the formal publications on ScienceDirect, and so links will help users to find, access, cite and use the best available version. Please note that Cell Press, The Lancet and some society-owned have different preprint policies. Information on these policies is available on the journal homepage.
Accepted Author Manuscripts: An accepted author manuscript is the manuscript of an article that has been accepted for publication and which typically includes author-incorporated changes suggested during submission, peer review and editor-author communications.
Authors can share their accepted author manuscript:

- immediately
  - via their non-commercial person homepage or blog
  - by updating a preprint in arXiv or RePEc with the accepted manuscript
  - via their research institute or institutional repository for internal institutional uses or as part of an invitation-only research collaboration work-group
  - directly by providing copies to their students or to research collaborators for their personal use
  - for private scholarly sharing as part of an invitation-only work group on

commercial sites with which Elsevier has an agreement

- after the embargo period
  - via non-commercial hosting platforms such as their institutional repository
  - via commercial sites with which Elsevier has an agreement

In all cases accepted manuscripts should:

- link to the formal publication via its DOI
- bear a CC-BY-NC-ND license - this is easy to do
- if aggregated with other manuscripts, for example in a repository or other site, be shared in alignment with our hosting policy not be added to or enhanced in any way to appear more like, or to substitute for, the published journal article.

Published journal article (JPA): A published journal article (PJA) is the definitive final record of published research that appears or will appear in the journal and embodies all value-adding publishing activities including peer review co-ordination, copy-editing, formatting, (if relevant) pagination and online enrichment.
Policies for sharing publishing journal articles differ for subscription and gold open access articles:
Subscription Articles: If you are an author, please share a link to your article rather than the full-text. Millions of researchers have access to the formal publications on ScienceDirect, and so links will help your users to find, access, cite, and use the best available version.
Theses and dissertations which contain embedded PJAs as part of the formal submission can be posted publicly by the awarding institution with DOI links back to the formal publications on ScienceDirect.
If you are affiliated with a library that subscribes to ScienceDirect you have additional private sharing rights for others' research accessed under that agreement. This includes use for classroom teaching and internal training at the institution (including use in course packs and courseware programs), and inclusion of the article for grant funding purposes.
Gold Open Access Articles: May be shared according to the author-selected end-user license and should contain a CrossMark logo, the end user license, and a DOI link to the formal publication on ScienceDirect.
Please refer to Elsevier's posting policy for further information.
18. **For book authors** the following clauses are applicable in addition to the above:
Authors are permitted to place a brief summary of their work online only. You are not allowed to download and post the published electronic version of your chapter, nor may you scan the printed edition to create an electronic version. **Posting to a repository:** Authors are permitted to post a summary of their chapter only in their institution's repository.
19. **Thesis/Dissertation**: If your license is for use in a thesis/dissertation your thesis may be submitted to your institution in either print or electronic form. Should your thesis be published commercially, please reapply for permission. These requirements include permission for the Library and Archives of Canada to supply single copies, on demand, of the complete thesis and include permission for Proquest/UMI to supply single copies, on demand, of the complete thesis. Should your thesis be published commercially, please reapply for permission. Theses and dissertations which contain embedded PJAs as part of the formal submission can be posted publicly by the awarding institution with DOI links back to the formal publications on ScienceDirect.

Elsevier Open Access Terms and Conditions

You can publish open access with Elsevier in hundreds of open access journals or in nearly 2000 established subscription journals that support open access publishing. Permitted third party re-use of these open access articles is defined by the author's choice of Creative Commons user license. See our open access license policy for more information.

Terms & Conditions applicable to all Open Access articles published with Elsevier:

Any reuse of the article must not represent the author as endorsing the adaptation of the article nor should the article be modified in such a way as to damage the author's honour or reputation. If any changes have been made, such changes must be clearly indicated.

The author(s) must be appropriately credited and we ask that you include the end user license and a DOI link to the formal publication on ScienceDirect.

If any part of the material to be used (for example, figures) has appeared in our publication with credit or acknowledgement to another source it is the responsibility of the user to ensure their reuse complies with the terms and conditions determined by the rights holder.

Additional Terms & Conditions applicable to each Creative Commons user license:

CC BY: The CC-BY license allows users to copy, to create extracts, abstracts and new works from the Article, to alter and revise the Article and to make commercial use of the Article (including reuse and/or resale of the Article by commercial entities), provided the user gives appropriate credit (with a link to the formal publication through the relevant DOI), provides a link to the license, indicates if changes were made and the licensor is not represented as endorsing the use made of the work. The full details of the license are available at http://creativecommons.org/licenses/by/4.0.

CC BY NC SA: The CC BY-NC-SA license allows users to copy, to create extracts, abstracts and new works from the Article, to alter and revise the Article, provided this is not done for commercial purposes, and that the user gives appropriate credit (with a link to the formal publication through the relevant DOI), provides a link to the license, indicates if changes were made and the licensor is not represented as endorsing the use made of the work. Further, any new works must be made available on the same conditions. The full details of the license are available at http://creativecommons.org/licenses/by-nc-sa/4.0.

CC BY NC ND: The CC BY-NC-ND license allows users to copy and distribute the Article, provided this is not done for commercial purposes and further does not permit distribution of the Article if it is changed or edited in any way, and provided the user gives appropriate credit (with a link to the formal publication through the relevant DOI), provides a link to the license, and that the licensor is not represented as endorsing the use made of the work. The full details of the license are available at http://creativecommons.org/licenses/by-nc-nd/4.0.

Any commercial reuse of Open Access articles published with a CC BY NC SA or CC BY NC ND license requires permission from Elsevier and will be subject to a fee.

Commercial reuse includes:

- Associating advertising with the full text of the Article
- Charging fees for document delivery or access
- Article aggregation
- Systematic distribution via e-mail lists or share buttons

Posting or linking by commercial companies for use by customers of those companies.

ELSEVIER LICENSE
TERMS AND CONDITIONS

May 18, 2016

This is a License Agreement between Louis Desgrosseilliers ("You") and Elsevier ("Elsevier") provided by Copyright Clearance Center ("CCC"). The license consists of your order details, the terms and conditions provided by Elsevier, and the payment terms and conditions.

All payments must be made in full to CCC. For payment instructions, please see information listed at the bottom of this form.

Supplier	Elsevier Limited The Boulevard,Langford Lane Kidlington,Oxford,OX5 1GB,UK
Registered Company Number	1982084
Customer name	Louis Desgrosseilliers
Customer address	46 Cider Maple Dr Timberlea, NS B3T1K8
License number	3872100246326
License date	May 18, 2016
Licensed content publisher	Elsevier
Licensed content publication	Experimental Thermal and Fluid Science
Licensed content title	Experimental investigation on melting heat transfer characteristics of lauric acid in a rectangular thermal storage unit
Licensed content author	Hossein Shokouhmand,Babak Kamkari
Licensed content date	October 2013
Licensed content volume number	50
Licensed content issue number	n/a
Number of pages	12
Start Page	201
End Page	212
Type of Use	reuse in a thesis/dissertation
Intended publisher of new work	other
Portion	figures/tables/illustrations
Number of	1

figures/tables/illustrations	
Format	both print and electronic
Are you the author of this Elsevier article?	No
Will you be translating?	No
Original figure numbers	Fig. 4
Title of your thesis/dissertation	Design and Evaluation of a Modular, Supercooling Phase Change Heat Storage Device for Indoor Heating
Expected completion date	Aug 2016
Estimated size (number of pages)	200
Elsevier VAT number	GB 494 6272 12
Permissions price	0.00 CAD
VAT/Local Sales Tax	0.00 CAD / 0.00 GBP
Total	0.00 CAD
Terms and Conditions	

INTRODUCTION

1. The publisher for this copyrighted material is Elsevier. By clicking "accept" in connection with completing this licensing transaction, you agree that the following terms and conditions apply to this transaction (along with the Billing and Payment terms and conditions established by Copyright Clearance Center, Inc. ("CCC"), at the time that you opened your Rightslink account and that are available at any time at http://myaccount.copyright.com).

GENERAL TERMS

2. Elsevier hereby grants you permission to reproduce the aforementioned material subject to the terms and conditions indicated.
3. Acknowledgement: If any part of the material to be used (for example, figures) has appeared in our publication with credit or acknowledgement to another source, permission must also be sought from that source. If such permission is not obtained then that material may not be included in your publication/copies. Suitable acknowledgement to the source must be made, either as a footnote or in a reference list at the end of your publication, as follows:
"Reprinted from Publication title, Vol /edition number, Author(s), Title of article / title of chapter, Pages No., Copyright (Year), with permission from Elsevier [OR APPLICABLE SOCIETY COPYRIGHT OWNER]." Also Lancet special credit - "Reprinted from The Lancet, Vol. number, Author(s), Title of article, Pages No., Copyright (Year), with permission from Elsevier."
4. Reproduction of this material is confined to the purpose and/or media for which permission is hereby given.
5. Altering/Modifying Material: Not Permitted. However figures and illustrations may be altered/adapted minimally to serve your work. Any other abbreviations, additions, deletions and/or any other alterations shall be made only with prior written authorization of Elsevier Ltd. (Please contact Elsevier at permissions@elsevier.com)

6. If the permission fee for the requested use of our material is waived in this instance, please be advised that your future requests for Elsevier materials may attract a fee.
7. Reservation of Rights: Publisher reserves all rights not specifically granted in the combination of (i) the license details provided by you and accepted in the course of this licensing transaction, (ii) these terms and conditions and (iii) CCC's Billing and Payment terms and conditions.
8. License Contingent Upon Payment: While you may exercise the rights licensed immediately upon issuance of the license at the end of the licensing process for the transaction, provided that you have disclosed complete and accurate details of your proposed use, no license is finally effective unless and until full payment is received from you (either by publisher or by CCC) as provided in CCC's Billing and Payment terms and conditions. If full payment is not received on a timely basis, then any license preliminarily granted shall be deemed automatically revoked and shall be void as if never granted. Further, in the event that you breach any of these terms and conditions or any of CCC's Billing and Payment terms and conditions, the license is automatically revoked and shall be void as if never granted. Use of materials as described in a revoked license, as well as any use of the materials beyond the scope of an unrevoked license, may constitute copyright infringement and publisher reserves the right to take any and all action to protect its copyright in the materials.
9. Warranties: Publisher makes no representations or warranties with respect to the licensed material.
10. Indemnity: You hereby indemnify and agree to hold harmless publisher and CCC, and their respective officers, directors, employees and agents, from and against any and all claims arising out of your use of the licensed material other than as specifically authorized pursuant to this license.
11. No Transfer of License: This license is personal to you and may not be sublicensed, assigned, or transferred by you to any other person without publisher's written permission.
12. No Amendment Except in Writing: This license may not be amended except in a writing signed by both parties (or, in the case of publisher, by CCC on publisher's behalf).
13. Objection to Contrary Terms: Publisher hereby objects to any terms contained in any purchase order, acknowledgment, check endorsement or other writing prepared by you, which terms are inconsistent with these terms and conditions or CCC's Billing and Payment terms and conditions. These terms and conditions, together with CCC's Billing and Payment terms and conditions (which are incorporated herein), comprise the entire agreement between you and publisher (and CCC) concerning this licensing transaction. In the event of any conflict between your obligations established by these terms and conditions and those established by CCC's Billing and Payment terms and conditions, these terms and conditions shall control.
14. Revocation: Elsevier or Copyright Clearance Center may deny the permissions described in this License at their sole discretion, for any reason or no reason, with a full refund payable to you. Notice of such denial will be made using the contact information provided by you. Failure to receive such notice will not alter or invalidate the denial. In no event will Elsevier or Copyright Clearance Center be responsible or liable for any costs, expenses or damage incurred by you as a result of a denial of your permission request, other than a refund of the amount(s) paid by you to Elsevier and/or Copyright Clearance Center for denied permissions.

LIMITED LICENSE

The following terms and conditions apply only to specific license types:
15. **Translation**: This permission is granted for non-exclusive world **English** rights only unless your license was granted for translation rights. If you licensed translation rights you may only translate this content into the languages you requested. A professional translator must perform all translations and reproduce the content word for word preserving the integrity of the article.
16. **Posting licensed content on any Website**: The following terms and conditions apply as follows: Licensing material from an Elsevier journal: All content posted to the web site must maintain the copyright information line on the bottom of each image; A hyper-text must be included to the Homepage of the journal from which you are licensing at http://www.sciencedirect.com/science/journal/xxxxx or the Elsevier homepage for books at http://www.elsevier.com; Central Storage: This license does not include permission for a scanned version of the material to be stored in a central repository such as that provided by Heron/XanEdu.
Licensing material from an Elsevier book: A hyper-text link must be included to the Elsevier homepage at http://www.elsevier.com . All content posted to the web site must maintain the copyright information line on the bottom of each image.

Posting licensed content on Electronic reserve: In addition to the above the following clauses are applicable: The web site must be password-protected and made available only to bona fide students registered on a relevant course. This permission is granted for 1 year only. You may obtain a new license for future website posting.
17. **For journal authors:** the following clauses are applicable in addition to the above:
Preprints:
A preprint is an author's own write-up of research results and analysis, it has not been peer-reviewed, nor has it had any other value added to it by a publisher (such as formatting, copyright, technical enhancement etc.).
Authors can share their preprints anywhere at any time. Preprints should not be added to or enhanced in any way in order to appear more like, or to substitute for, the final versions of articles however authors can update their preprints on arXiv or RePEc with their Accepted Author Manuscript (see below).
If accepted for publication, we encourage authors to link from the preprint to their formal publication via its DOI. Millions of researchers have access to the formal publications on ScienceDirect, and so links will help users to find, access, cite and use the best available version. Please note that Cell Press, The Lancet and some society-owned have different preprint policies. Information on these policies is available on the journal homepage.
Accepted Author Manuscripts: An accepted author manuscript is the manuscript of an article that has been accepted for publication and which typically includes author-incorporated changes suggested during submission, peer review and editor-author communications.
Authors can share their accepted author manuscript:

- immediately
  - via their non-commercial person homepage or blog
  - by updating a preprint in arXiv or RePEc with the accepted manuscript
  - via their research institute or institutional repository for internal institutional uses or as part of an invitation-only research collaboration work-group

- directly by providing copies to their students or to research collaborators for their personal use
- for private scholarly sharing as part of an invitation-only work group on commercial sites with which Elsevier has an agreement

- after the embargo period
  - via non-commercial hosting platforms such as their institutional repository
  - via commercial sites with which Elsevier has an agreement

In all cases accepted manuscripts should:

- link to the formal publication via its DOI
- bear a CC-BY-NC-ND license - this is easy to do
- if aggregated with other manuscripts, for example in a repository or other site, be shared in alignment with our hosting policy not be added to or enhanced in any way to appear more like, or to substitute for, the published journal article.

Published journal article (JPA): A published journal article (PJA) is the definitive final record of published research that appears or will appear in the journal and embodies all value-adding publishing activities including peer review co-ordination, copy-editing, formatting, (if relevant) pagination and online enrichment.
Policies for sharing publishing journal articles differ for subscription and gold open access articles:
Subscription Articles: If you are an author, please share a link to your article rather than the full-text. Millions of researchers have access to the formal publications on ScienceDirect, and so links will help your users to find, access, cite, and use the best available version.
Theses and dissertations which contain embedded PJAs as part of the formal submission can be posted publicly by the awarding institution with DOI links back to the formal publications on ScienceDirect.
If you are affiliated with a library that subscribes to ScienceDirect you have additional private sharing rights for others' research accessed under that agreement. This includes use for classroom teaching and internal training at the institution (including use in course packs and courseware programs), and inclusion of the article for grant funding purposes.
Gold Open Access Articles: May be shared according to the author-selected end-user license and should contain a CrossMark logo, the end user license, and a DOI link to the formal publication on ScienceDirect.
Please refer to Elsevier's posting policy for further information.
18. **For book authors** the following clauses are applicable in addition to the above:
Authors are permitted to place a brief summary of their work online only. You are not allowed to download and post the published electronic version of your chapter, nor may you scan the printed edition to create an electronic version. **Posting to a repository:** Authors are permitted to post a summary of their chapter only in their institution's repository.
19. **Thesis/Dissertation**: If your license is for use in a thesis/dissertation your thesis may be submitted to your institution in either print or electronic form. Should your thesis be published commercially, please reapply for permission. These requirements include permission for the Library and Archives of Canada to supply single copies, on demand, of the complete thesis and include permission for Proquest/UMI to supply single copies, on demand, of the complete thesis. Should your thesis be published commercially, please

reapply for permission. Theses and dissertations which contain embedded PJAs as part of the formal submission can be posted publicly by the awarding institution with DOI links back to the formal publications on ScienceDirect.

Elsevier Open Access Terms and Conditions

You can publish open access with Elsevier in hundreds of open access journals or in nearly 2000 established subscription journals that support open access publishing. Permitted third party re-use of these open access articles is defined by the author's choice of Creative Commons user license. See our open access license policy for more information.

Terms & Conditions applicable to all Open Access articles published with Elsevier:

Any reuse of the article must not represent the author as endorsing the adaptation of the article nor should the article be modified in such a way as to damage the author's honour or reputation. If any changes have been made, such changes must be clearly indicated.

The author(s) must be appropriately credited and we ask that you include the end user license and a DOI link to the formal publication on ScienceDirect.

If any part of the material to be used (for example, figures) has appeared in our publication with credit or acknowledgement to another source it is the responsibility of the user to ensure their reuse complies with the terms and conditions determined by the rights holder.

Additional Terms & Conditions applicable to each Creative Commons user license:

CC BY: The CC-BY license allows users to copy, to create extracts, abstracts and new works from the Article, to alter and revise the Article and to make commercial use of the Article (including reuse and/or resale of the Article by commercial entities), provided the user gives appropriate credit (with a link to the formal publication through the relevant DOI), provides a link to the license, indicates if changes were made and the licensor is not represented as endorsing the use made of the work. The full details of the license are available at http://creativecommons.org/licenses/by/4.0.

CC BY NC SA: The CC BY-NC-SA license allows users to copy, to create extracts, abstracts and new works from the Article, to alter and revise the Article, provided this is not done for commercial purposes, and that the user gives appropriate credit (with a link to the formal publication through the relevant DOI), provides a link to the license, indicates if changes were made and the licensor is not represented as endorsing the use made of the work. Further, any new works must be made available on the same conditions. The full details of the license are available at http://creativecommons.org/licenses/by-nc-sa/4.0.

CC BY NC ND: The CC BY-NC-ND license allows users to copy and distribute the Article, provided this is not done for commercial purposes and further does not permit distribution of the Article if it is changed or edited in any way, and provided the user gives appropriate credit (with a link to the formal publication through the relevant DOI), provides a link to the license, and that the licensor is not represented as endorsing the use made of the work. The full details of the license are available at http://creativecommons.org/licenses/by-nc-nd/4.0.

Any commercial reuse of Open Access articles published with a CC BY NC SA or CC BY NC ND license requires permission from Elsevier and will be subject to a fee.

Commercial reuse includes:

- Associating advertising with the full text of the Article
- Charging fees for document delivery or access
- Article aggregation
- Systematic distribution via e-mail lists or share buttons

Creative Commons Legal Code

Attribution-ShareAlike 3.0 Unported

CREATIVE COMMONS CORPORATION IS NOT A LAW FIRM AND DOES NOT PROVIDE LEGAL SERVICES. DISTRIBUTION OF THIS LICENSE DOES NOT CREATE AN ATTORNEY-CLIENT RELATIONSHIP. CREATIVE COMMONS PROVIDES THIS INFORMATION ON AN "AS-IS" BASIS. CREATIVE COMMONS MAKES NO WARRANTIES REGARDING THE INFORMATION PROVIDED, AND DISCLAIMS LIABILITY FOR DAMAGES RESULTING FROM ITS USE.

License

THE WORK (AS DEFINED BELOW) IS PROVIDED UNDER THE TERMS OF THIS CREATIVE COMMONS PUBLIC LICENSE ("CCPL" OR "LICENSE"). THE WORK IS PROTECTED BY COPYRIGHT AND/OR OTHER APPLICABLE LAW. ANY USE OF THE WORK OTHER THAN AS AUTHORIZED UNDER THIS LICENSE OR COPYRIGHT LAW IS PROHIBITED.

BY EXERCISING ANY RIGHTS TO THE WORK PROVIDED HERE, YOU ACCEPT AND AGREE TO BE BOUND BY THE TERMS OF THIS LICENSE. TO THE EXTENT THIS LICENSE MAY BE CONSIDERED TO BE A CONTRACT, THE LICENSOR GRANTS YOU THE RIGHTS CONTAINED HERE IN CONSIDERATION OF YOUR ACCEPTANCE OF SUCH TERMS AND CONDITIONS.

1. Definitions

a. **"Adaptation"** means a work based upon the Work, or upon the Work and other pre-existing works, such as a translation, adaptation, derivative work, arrangement of music or other alterations of a literary or artistic work, or phonogram or performance and includes cinematographic adaptations or any other form in which the Work may be recast, transformed, or adapted including in any form recognizably derived from the original, except that a work that constitutes a Collection will not be considered an Adaptation for the purpose of this License. For the avoidance of doubt, where the Work is a musical work, performance or phonogram, the synchronization of the Work in timed-relation with a moving image ("synching") will be considered an Adaptation for the purpose of this License.
b. **"Collection"** means a collection of literary or artistic works, such as encyclopedias and anthologies, or performances, phonograms or broadcasts, or other works or subject matter other than works listed in Section 1(f) below, which, by reason of the selection and arrangement of their contents, constitute intellectual creations, in which the Work is included in its entirety in unmodified form along with one or more other contributions, each constituting separate and independent works in themselves, which together are assembled into a collective whole. A work that constitutes a Collection will not be considered an Adaptation (as defined below) for the purposes of this License.
c. **"Creative Commons Compatible License"** means a license that is listed at https://creativecommons.org/compatiblelicenses that has been approved by Creative Commons as being essentially equivalent to this License, including, at a minimum, because that license: (i) contains terms that have the same purpose, meaning and effect as the License Elements of this License; and, (ii) explicitly permits the relicensing of adaptations of works made available under that license under this License or a Creative Commons jurisdiction license with the same License

Elements as this License.

d. **"Distribute"** means to make available to the public the original and copies of the Work or Adaptation, as appropriate, through sale or other transfer of ownership.
e. **"License Elements"** means the following high-level license attributes as selected by Licensor and indicated in the title of this License: Attribution, ShareAlike.
f. **"Licensor"** means the individual, individuals, entity or entities that offer(s) the Work under the terms of this License.
g. **"Original Author"** means, in the case of a literary or artistic work, the individual, individuals, entity or entities who created the Work or if no individual or entity can be identified, the publisher; and in addition (i) in the case of a performance the actors, singers, musicians, dancers, and other persons who act, sing, deliver, declaim, play in, interpret or otherwise perform literary or artistic works or expressions of folklore; (ii) in the case of a phonogram the producer being the person or legal entity who first fixes the sounds of a performance or other sounds; and, (iii) in the case of broadcasts, the organization that transmits the broadcast.
h. **"Work"** means the literary and/or artistic work offered under the terms of this License including without limitation any production in the literary, scientific and artistic domain, whatever may be the mode or form of its expression including digital form, such as a book, pamphlet and other writing; a lecture, address, sermon or other work of the same nature; a dramatic or dramatico-musical work; a choreographic work or entertainment in dumb show; a musical composition with or without words; a cinematographic work to which are assimilated works expressed by a process analogous to cinematography; a work of drawing, painting, architecture, sculpture, engraving or lithography; a photographic work to which are assimilated works expressed by a process analogous to photography; a work of applied art; an illustration, map, plan, sketch or three-dimensional work relative to geography, topography, architecture or science; a performance; a broadcast; a phonogram; a compilation of data to the extent it is protected as a copyrightable work; or a work performed by a variety or circus performer to the extent it is not otherwise considered a literary or artistic work.
i. **"You"** means an individual or entity exercising rights under this License who has not previously violated the terms of this License with respect to the Work, or who has received express permission from the Licensor to exercise rights under this License despite a previous violation.
j. **"Publicly Perform"** means to perform public recitations of the Work and to communicate to the public those public recitations, by any means or process, including by wire or wireless means or public digital performances; to make available to the public Works in such a way that members of the public may access these Works from a place and at a place individually chosen by them; to perform the Work to the public by any means or process and the communication to the public of the performances of the Work, including by public digital performance; to broadcast and rebroadcast the Work by any means including signs, sounds or images.
k. **"Reproduce"** means to make copies of the Work by any means including without limitation by sound or visual recordings and the right of fixation and reproducing fixations of the Work, including storage of a protected performance or phonogram in digital form or other electronic medium.

2. Fair Dealing Rights. Nothing in this License is intended to reduce, limit, or restrict any uses free from copyright or rights arising from limitations or exceptions that are provided for in connection with the copyright protection under copyright law or other applicable laws.

3. License Grant. Subject to the terms and conditions of this License, Licensor hereby grants You a worldwide, royalty-free, non-exclusive, perpetual (for the duration of the applicable copyright) license to exercise the rights in the Work as stated below:

a. to Reproduce the Work, to incorporate the Work into one or more Collections, and to Reproduce the Work as incorporated in the Collections;
b. to create and Reproduce Adaptations provided that any such Adaptation, including any translation in any medium, takes reasonable steps to clearly label, demarcate or otherwise identify that changes were made to the original Work. For example, a translation could be marked "The original work was translated from English to Spanish," or a modification could indicate "The original work has been

modified.";
c. to Distribute and Publicly Perform the Work including as incorporated in Collections; and,
d. to Distribute and Publicly Perform Adaptations.

e. For the avoidance of doubt:

i. **Non-waivable Compulsory License Schemes**. In those jurisdictions in which the right to collect royalties through any statutory or compulsory licensing scheme cannot be waived, the Licensor reserves the exclusive right to collect such royalties for any exercise by You of the rights granted under this License;
ii. **Waivable Compulsory License Schemes**. In those jurisdictions in which the right to collect royalties through any statutory or compulsory licensing scheme can be waived, the Licensor waives the exclusive right to collect such royalties for any exercise by You of the rights granted under this License; and,
iii. **Voluntary License Schemes**. The Licensor waives the right to collect royalties, whether individually or, in the event that the Licensor is a member of a collecting society that administers voluntary licensing schemes, via that society, from any exercise by You of the rights granted under this License.

The above rights may be exercised in all media and formats whether now known or hereafter devised. The above rights include the right to make such modifications as are technically necessary to exercise the rights in other media and formats. Subject to Section 8(f), all rights not expressly granted by Licensor are hereby reserved.

4. Restrictions. The license granted in Section 3 above is expressly made subject to and limited by the following restrictions:

a. You may Distribute or Publicly Perform the Work only under the terms of this License. You must include a copy of, or the Uniform Resource Identifier (URI) for, this License with every copy of the Work You Distribute or Publicly Perform. You may not offer or impose any terms on the Work that restrict the terms of this License or the ability of the recipient of the Work to exercise the rights granted to that recipient under the terms of the License. You may not sublicense the Work. You must keep intact all notices that refer to this License and to the disclaimer of warranties with every copy of the Work You Distribute or Publicly Perform. When You Distribute or Publicly Perform the Work, You may not impose any effective technological measures on the Work that restrict the ability of a recipient of the Work from You to exercise the rights granted to that recipient under the terms of the License. This Section 4(a) applies to the Work as incorporated in a Collection, but this does not require the Collection apart from the Work itself to be made subject to the terms of this License. If You create a Collection, upon notice from any Licensor You must, to the extent practicable, remove from the Collection any credit as required by Section 4(c), as requested. If You create an Adaptation, upon notice from any Licensor You must, to the extent practicable, remove from the Adaptation any credit as required by Section 4(c), as requested.
b. You may Distribute or Publicly Perform an Adaptation only under the terms of: (i) this License; (ii) a later version of this License with the same License Elements as this License; (iii) a Creative Commons jurisdiction license (either this or a later license version) that contains the same License Elements as this License (e.g., Attribution-ShareAlike 3.0 US)); (iv) a Creative Commons Compatible License. If you license the Adaptation under one of the licenses mentioned in (iv), you must comply with the terms of that license. If you license the Adaptation under the terms of any of the licenses mentioned in (i), (ii) or (iii) (the "Applicable License"), you must comply with the terms of the Applicable License generally and the following provisions: (I) You must include a copy of, or the URI for, the Applicable License with every copy of each Adaptation You Distribute or Publicly Perform; (II) You may not offer or impose any terms on the Adaptation that restrict the terms of the Applicable License or the ability of the recipient of the Adaptation to exercise the rights granted to that recipient under the terms of the Applicable License; (III) You must keep intact all notices that refer to the

Applicable License and to the disclaimer of warranties with every copy of the Work as included in the Adaptation You Distribute or Publicly Perform; (IV) when You Distribute or Publicly Perform the Adaptation, You may not impose any effective technological measures on the Adaptation that restrict the ability of a recipient of the Adaptation from You to exercise the rights granted to that recipient under the terms of the Applicable License. This Section 4(b) applies to the Adaptation as incorporated in a Collection, but this does not require the Collection apart from the Adaptation itself to be made subject to the terms of the Applicable License.

c. If You Distribute, or Publicly Perform the Work or any Adaptations or Collections, You must, unless a request has been made pursuant to Section 4(a), keep intact all copyright notices for the Work and provide, reasonable to the medium or means You are utilizing: (i) the name of the Original Author (or pseudonym, if applicable) if supplied, and/or if the Original Author and/or Licensor designate another party or parties (e.g., a sponsor institute, publishing entity, journal) for attribution ("Attribution Parties") in Licensor's copyright notice, terms of service or by other reasonable means, the name of such party or parties; (ii) the title of the Work if supplied; (iii) to the extent reasonably practicable, the URI, if any, that Licensor specifies to be associated with the Work, unless such URI does not refer to the copyright notice or licensing information for the Work; and (iv) , consistent with Ssection 3(b), in the case of an Adaptation, a credit identifying the use of the Work in the Adaptation (e.g., "French translation of the Work by Original Author," or "Screenplay based on original Work by Original Author"). The credit required by this Section 4(c) may be implemented in any reasonable manner; provided, however, that in the case of a Adaptation or Collection, at a minimum such credit will appear, if a credit for all contributing authors of the Adaptation or Collection appears, then as part of these credits and in a manner at least as prominent as the credits for the other contributing authors. For the avoidance of doubt, You may only use the credit required by this Section for the purpose of attribution in the manner set out above and, by exercising Your rights under this License, You may not implicitly or explicitly assert or imply any connection with, sponsorship or endorsement by the Original Author, Licensor and/or Attribution Parties, as appropriate, of You or Your use of the Work, without the separate, express prior written permission of the Original Author, Licensor and/or Attribution Parties.
d. Except as otherwise agreed in writing by the Licensor or as may be otherwise permitted by applicable law, if You Reproduce, Distribute or Publicly Perform the Work either by itself or as part of any Adaptations or Collections, You must not distort, mutilate, modify or take other derogatory action in relation to the Work which would be prejudicial to the Original Author's honor or reputation. Licensor agrees that in those jurisdictions (e.g. Japan), in which any exercise of the right granted in Section 3(b) of this License (the right to make Adaptations) would be deemed to be a distortion, mutilation, modification or other derogatory action prejudicial to the Original Author's honor and reputation, the Licensor will waive or not assert, as appropriate, this Section, to the fullest extent permitted by the applicable national law, to enable You to reasonably exercise Your right under Section 3(b) of this License (right to make Adaptations) but not otherwise.

5. Representations, Warranties and Disclaimer

UNLESS OTHERWISE MUTUALLY AGREED TO BY THE PARTIES IN WRITING, LICENSOR OFFERS THE WORK AS-IS AND MAKES NO REPRESENTATIONS OR WARRANTIES OF ANY KIND CONCERNING THE WORK, EXPRESS, IMPLIED, STATUTORY OR OTHERWISE, INCLUDING, WITHOUT LIMITATION, WARRANTIES OF TITLE, MERCHANTIBILITY, FITNESS FOR A PARTICULAR PURPOSE, NONINFRINGEMENT, OR THE ABSENCE OF LATENT OR OTHER DEFECTS, ACCURACY, OR THE PRESENCE OF ABSENCE OF ERRORS, WHETHER OR NOT DISCOVERABLE. SOME JURISDICTIONS DO NOT ALLOW THE EXCLUSION OF IMPLIED WARRANTIES, SO SUCH EXCLUSION MAY NOT APPLY TO YOU.

6. Limitation on Liability. EXCEPT TO THE EXTENT REQUIRED BY APPLICABLE LAW, IN NO EVENT WILL LICENSOR BE LIABLE TO YOU ON ANY LEGAL THEORY FOR ANY SPECIAL, INCIDENTAL, CONSEQUENTIAL, PUNITIVE OR EXEMPLARY DAMAGES ARISING OUT OF THIS LICENSE OR THE USE OF THE WORK, EVEN IF LICENSOR HAS BEEN ADVISED OF THE POSSIBILITY OF SUCH

DAMAGES.

7. Termination

a. This License and the rights granted hereunder will terminate automatically upon any breach by You of the terms of this License. Individuals or entities who have received Adaptations or Collections from You under this License, however, will not have their licenses terminated provided such individuals or entities remain in full compliance with those licenses. Sections 1, 2, 5, 6, 7, and 8 will survive any termination of this License.
b. Subject to the above terms and conditions, the license granted here is perpetual (for the duration of the applicable copyright in the Work). Notwithstanding the above, Licensor reserves the right to release the Work under different license terms or to stop distributing the Work at any time; provided, however that any such election will not serve to withdraw this License (or any other license that has been, or is required to be, granted under the terms of this License), and this License will continue in full force and effect unless terminated as stated above.

8. Miscellaneous

a. Each time You Distribute or Publicly Perform the Work or a Collection, the Licensor offers to the recipient a license to the Work on the same terms and conditions as the license granted to You under this License.
b. Each time You Distribute or Publicly Perform an Adaptation, Licensor offers to the recipient a license to the original Work on the same terms and conditions as the license granted to You under this License.
c. If any provision of this License is invalid or unenforceable under applicable law, it shall not affect the validity or enforceability of the remainder of the terms of this License, and without further action by the parties to this agreement, such provision shall be reformed to the minimum extent necessary to make such provision valid and enforceable.
d. No term or provision of this License shall be deemed waived and no breach consented to unless such waiver or consent shall be in writing and signed by the party to be charged with such waiver or consent.
e. This License constitutes the entire agreement between the parties with respect to the Work licensed here. There are no understandings, agreements or representations with respect to the Work not specified here. Licensor shall not be bound by any additional provisions that may appear in any communication from You. This License may not be modified without the mutual written agreement of the Licensor and You.
f. The rights granted under, and the subject matter referenced, in this License were drafted utilizing the terminology of the Berne Convention for the Protection of Literary and Artistic Works (as amended on September 28, 1979), the Rome Convention of 1961, the WIPO Copyright Treaty of 1996, the WIPO Performances and Phonograms Treaty of 1996 and the Universal Copyright Convention (as revised on July 24, 1971). These rights and subject matter take effect in the relevant jurisdiction in which the License terms are sought to be enforced according to the corresponding provisions of the implementation of those treaty provisions in the applicable national law. If the standard suite of rights granted under applicable copyright law includes additional rights not granted under this License, such additional rights are deemed to be included in the License; this License is not intended to restrict the license of any rights under applicable law.

Creative Commons Notice

Creative Commons is not a party to this License, and makes no warranty whatsoever in connection with the Work. Creative Commons will not be liable to You or any party on any legal theory for any damages whatsoever, including without limitation any general, special, incidental or consequential damages arising in connection to this license. Notwithstanding the foregoing two (2) sentences, if Creative Commons has

expressly identified itself as the Licensor hereunder, it shall have all rights and obligations of Licensor.

Except for the limited purpose of indicating to the public that the Work is licensed under the CCPL, Creative Commons does not authorize the use by either party of the trademark "Creative Commons" or any related trademark or logo of Creative Commons without the prior written consent of Creative Commons. Any permitted use will be in compliance with Creative Commons' then-current trademark usage guidelines, as may be published on its website or otherwise made available upon request from time to time. For the avoidance of doubt, this trademark restriction does not form part of the License.

Creative Commons may be contacted at https://creativecommons.org/.

From: **Grider, Kari (KG)** KLGrider@dow.com
Subject: RE: Propylene Glycols Contact Form {ticketno:[201050947]}
Date: June 7, 2016 at 5:06 PM
To: Louis Desgrosseilliers Louis.D@Dal.Ca
Cc: Grider, Kari (KG) KLGrider@dow.com

GK

Louis,

My apologies for the delay, I had to run this request by the business for review. They have approved your request and you are granted permission to reproduce Figures 6, 11 and A1 from Dow's technical brochure "A Guide to Glycols" in your thesis.

Please be sure to use the figures in a positive light and include the statement "Provided courtesy of The Dow Chemical Company."

Thank you.

Kari L. Grider
Kari Grider, RP® Trademark Paralegal
Office: 317.337.4895 klgrider@dow.com